



Universitat Autònoma de Barcelona

ADVERTIMENT. L'accés als continguts d'aquesta tesi queda condicionat a l'acceptació de les condicions d'ús establertes per la següent llicència Creative Commons:  http://cat.creativecommons.org/?page_id=184

ADVERTENCIA. El acceso a los contenidos de esta tesis queda condicionado a la aceptación de las condiciones de uso establecidas por la siguiente licencia Creative Commons:  <http://es.creativecommons.org/blog/licencias/>

WARNING. The access to the contents of this doctoral thesis it is limited to the acceptance of the use conditions set by the following Creative Commons license:  <https://creativecommons.org/licenses/?lang=en>



Universitat Autònoma
de Barcelona

Synthesis and magnetoelectric properties of Co–Pt based porous materials

Cristina Navarro Senent

Tesi Doctoral

Programa de Doctorat en Ciència de Materials

Jordi Sort Viñas (Director i tutor)

Eva Pellicer Vilà (Directora)

Departament de Física

Facultat de Ciències

2020



**Universitat Autònoma
de Barcelona**

Memòria presentada per aspirar al Grau de Doctor

per

Cristina Navarro Senent

Vist i plau

Dr. Jordi Sort Viñas

(Director i tutor)

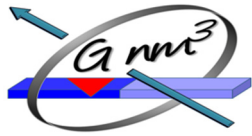
Dra. Eva Pellicer Vila

(Directora)

Bellaterra, 03/11/2020



**Universitat Autònoma
de Barcelona**



Group of smart nanoengineered materials, nanomechanics
and nanomagnetism

El **Dr. Jordi Sort Viñas**, professor ICREA del Departament de Física de la Universitat Autònoma de Barcelona,

i la **Dra. Eva Pellicer Vilà**, Professora Agregada del Departament de Física de la Universitat Autònoma de Barcelona,

CERTIFIQUEN:

Que **Cristina Navarro Senent** ha realitzat sota la seva direcció el treball d'investigació que s'exposa a la memòria titulada "Synthesis and magnetoelectric properties of Co–Pt based porous materials" per optar al grau de **Doctor per la Universitat Autònoma de Barcelona**.

Que el disseny dels experiments, síntesi de mostres, llur caracterització, l'anàlisi dels resultats, la redacció dels articles i d'aquesta memòria són fruit del treball d'investigació realitzat per Cristina Navarro Senent.

I perquè així consti, signen el present certificat,

Dr. Jordi Sort Viñas

Dra. Eva Pellicer Vilà

Bellaterra, 3 de Novembre de 2020

Abstract

This Thesis dissertation focuses on the electrochemical synthesis and investigation of the magnetoelectric properties of cobalt-platinum (Co–Pt) based porous materials. These materials are expected to minimize heat dissipation and power consumption in magnetically actuated devices.

Owing to the interfacial nature of magnetoelectric effects, porosity, roughness and nanostructuring in Co–Pt based materials are expected to promote or enhance their magnetoelectric response due to the increase in the surface-to-volume ratio. For this reason, electrodeposition from aqueous solutions containing P-123 micelle assemblies (referred to as micelle-assisted electrodeposition) was employed to fabricate mesoporous Co–Pt based materials consisting of Co–Pt alloy and Co oxides (Co–Pt+Co_xO_y). In combination with photolithography and the atomic layer deposition (ALD) of HfO_x and AlO_x nanolayers, arrays of circular microstructures and heterostructured films, respectively, were prepared. The magnetoelectric properties of the materials were studied by an electrolyte-gating approach in a polar, water-free, organic solvent. This approach exploits the generation of an electric double layer to create large electric fields at the electrolyte/sample interface.

A reduction of coercivity (by 88%) and an increase of Kerr signal (by 60%) were obtained at room temperature when mesoporous Co–Pt+Co_xO_y arrays of micron-sized disks were subject to electric field. The observed voltage-induced variations were attributed to charge accumulation at the surface of the ultranarrow pore walls of the mesoporous microdisks and voltage-drive oxygen ion migration (i.e., magneto-ionic effects).

In nanostructured Co–Pt+Co_xO_y/HfO_x and Co–Pt+Co_xO_y/AlO_x heterostructures, coercivity and magnetic moment at saturation were effectively modulated after biasing the heterostructured films with negative and positive voltages. The observed electric-field induced changes were ascribed to oxygen migration through the Co–Pt+Co_xO_y/ALD oxide interface.

In parallel, the impact of electrolyte processing on the mesoporosity of fully metallic Co–Pt thin films was investigated. A parametric study using various baths revealed that previous dissolution of the hexachloroplatinate salt and their storage for a few days before the other chemicals (the cobalt salt and the P-123 block-copolymer surfactant) are added is critical for the reproducible formation of the mesoporous network.

Finally, electrodeposition on colloidal crystal templated substrates was pursued to manufacture hard magnetic macroporous Co–Pt films. As-deposited films exhibited tightly packed pores of 200 nm in diameter (which matched the size of the parent colloids) and were structurally composed of a mixture of face-centered cubic A1-disordered nearly equiatomic Co–Pt solid solutions. Upon annealing, partial transformation from A1-disordered into tetragonal L1₀-ordered phase was achieved, resulting in a significant increase of coercivity from 148 Oe to 1328 Oe. Remarkably, the macroporosity in the films was preserved after the thermal treatment.

Resumen

La presente Tesis doctoral abarca la síntesis electroquímica y la investigación de las propiedades magnetoeléctricas de materiales porosos basados en cobalto-platino (Co-Pt). Se espera que estos materiales minimicen la disipación de calor y el consumo de energía en dispositivos operados magnéticamente.

Teniendo en cuenta la naturaleza interfacial de los efectos magnetoeléctricos, es de prever que la porosidad, la rugosidad y la nanoestructuración de los materiales basados en Co-Pt favorezcan o incrementen su respuesta magnetoeléctrica dada su elevada relación superficie/volumen. Por este motivo, en esta Tesis se ha empleado la electrodeposición a partir de soluciones acuosas que contenían micelas de P-123 (denominado electrodeposición asistida por micelas) para fabricar materiales mesoporosos a base de Co-Pt compuestos por una aleación de Co-Pt y óxidos de Co (Co-Pt+Co_xO_y). Asimismo, la electrodeposición se ha combinado con fotolitografía y deposición de capas atómicas (ALD) de HfO_x y AlO_x para la fabricación de matrices de microestructuras circulares y películas heteroestructuradas, respectivamente. Las propiedades magnetoeléctricas de los materiales se han estudiado mediante electrolito líquido como material dieléctrico, utilizando un solvente orgánico polar no acuoso. Este enfoque aprovecha la generación de una doble capa eléctrica para generar grandes campos eléctricos en la interfaz electrolito/muestra.

En primer lugar, mediante la aplicación de campos eléctricos a discos mesoporosos de tamaño micrométrico de Co-Pt+Co_xO_y, se logró una reducción de la coercitividad (88%) y un aumento de la señal de Kerr (60%) a temperatura ambiente. Tales variaciones inducidas por el voltaje se atribuyeron a la acumulación de carga en la superficie de las paredes ultra-estrechas de los poros de los microdiscos mesoporosos, y a la migración de iones de oxígeno impulsada por el voltaje (es decir, a efectos magneto-iónicos).

En un segundo trabajo, la coercitividad y el momento magnético en la saturación de heteroestructuras nanoestructuradas de Co-Pt+Co_xO_y/HfO_x y Co-Pt+Co_xO_y/AlO_x fueron modulados eficazmente después de polarizarlas con voltajes negativos y positivos. Los

cambios inducidos por el voltaje se adscribieron a la migración de oxígeno en la interfaz Co–Pt+Co_xO_y/óxido.

Paralelamente, se ha investigado el impacto del procesamiento del electrolito en la mesoporosidad en capas delgadas Co–Pt totalmente metálicas. Un estudio paramétrico de varios baños reveló que la disolución previa de la sal de hexacloroplatino y su posterior almacenamiento durante unos días, antes de que se añadan los demás reactivos químicos (la sal de cobalto y el surfactante polimérico de bloque P-123) es fundamental para la formación de la red mesoporosa.

Finalmente, la electrodeposición en sustratos estampados con cristales coloidales se ha utilizado para la fabricación de películas macroporosas magnéticamente duras de Co–Pt. Las películas de Co–Pt mostraron una estructura empaquetada de poros de 200 nm de diámetros (coincidiendo con el tamaño de los coloides originales) y, estructuralmente, una mezcla de fases cristalográficas casi equiatómicas de solución sólida de Co–Pt cúbica centrada en las caras (A1 desordenada). Tras el tratamiento térmico, se logró una transformación parcial de la fase desordenada cúbica A1 a la fase ordenada tetragonal L1₀ lo cual produjo un aumento significativo de la coercitividad de 148 Oe a 1328 Oe. Sorprendentemente, la porosidad de las películas se conservó después del tratamiento térmico.

Glossary

- $(BH)_{max}$: Maximum energy product
- ALD: Atomic layer deposition
- BCP: Block-copolymer
- c.m.c: critical micelle concentration
- CE: Counter electrode
- CTAB: hexadecyltrimethylammonium bromide
- CV: cyclic voltammetry
- DEME-TFSI: diethylmethyl(2-methoxyethyl)ammonium bis(trifluoromethylsulfonyl)imide
- DMS: Diluted magnetic semiconductor
- EBL: Electron beam lithography
- EDL: Electric double layer
- EDX: Energy dispersive X-ray (spectroscopy)
- EELS: Electron-energy loss spectroscopy
- E-field: Electric field
- EL: Electrochemical lithography
- EPD: Electrophoretic deposition
- EXAFS: Extended X-ray absorption fine spectroscopy
- fcc: Face-centered cubic
- fct: Face-centered tetragonal
- FE-SEM: Field-emission scanning electron microscopy
- FET: Field-effect transistor
- FIB: Focused ion beam
- FY: Fluorescence yield
- Galfenol: Fe–Ga
- GIXRD: Grazing incidence X-ray diffraction
- H: magnetic field
- $H_{applied}$: Applied external magnetic field
- H_c : Coercivity
- hcp: Hexagonal close packed
- HDD: Hard disk drive
- HRTEM: High resolution transmission electron microscopy
- ICT: Information and communication technology
- IT: Information and communication
- K_u : uniaxial magneto-crystalline anisotropy constant

- LIGA: Lithographie, Galvanoformung and Abformung
- LLC: Lyotropic liquid crystal
- LSMO: $\text{La}_{1-x}\text{Sr}_x\text{MnO}_3$
- M: Magnetization
- MAE: Magnetocrystalline anisotropy energy
- MBE: Molecular beam epitaxy
- ME: Magnetolectric
- MEMS: Microelectromechanical systems
- MF: Multiferroic
- MOKE: Magneto-optical Kerr effect
- M_R/M_S : Squareness ratio
- M_R : Remanent magnetization
- MRAM: Magnetic random-access memory
- M_S : Saturation magnetization
- MTJ: Magnetic tunneling junction
- ORR: Oxygen reduction reaction
- PC: Propylene carbonate
- PEO–PPO–PEO: Oxide-polypropylene oxide-polyethylene oxide
- PI: Polyimide
- PLD: Pulsed laser deposition
- PMA: Perpendicular magnetic anisotropy
- PMMA: poly(methyl methacrylate)
- PS: Polystyrene
- PS-b-PEO: Polystyrene-poly(ethylene oxide)
- PUE: Power usage effectiveness
- PVDF: Polyvinyl fluoride
- PZT: $\text{PbZr}_{1-x}\text{Ti}_x\text{O}_3$
- RE: Reference electrode
- S/V: Surface-to-volume
- SAED: Selective area electron diffraction
- STEM: Scanning transmission electron microscopy
- STT: Spin-transfer-torque
- T_C : Curie temperature
- TEM: Transmission electron microscopy
- Terfenol-D: $\text{Tb}_x\text{Dy}_{1-x}\text{Fe}_2$
- TEY: Total electron yield
- T_N : Néel temperature
- VSM: Vibrating sample magnetometer
- WE: Working electrode

- XANES: X-ray Absorption near edge structure spectroscopy
- XAS: X-ray absorption spectroscopy
- XMCD: X-ray magnetic circular dichroism
- XRD: X-ray diffraction
- λ_{TF} : Thomas-Fermi screening length

Table of contents

Abstract	VII
Resumen	IX
Glossary	XI
Table of contents	XV
1. Introduction	3
1.1. The problem of energy efficiency	3
1.2. Fundamentals of magnetism	6
1.3. Mechanisms to control magnetism with electric field	14
1.4. Configurations to apply electric field. Electrolyte-gated magnetoelectric actuation	23
1.5. Interfacial nature of magnetoelectric effects	26
1.6. Porous and patterned materials by electrodeposition	28
1.7. The Co–Pt system	41
Bibliography	45
2. Objectives	73
3. Experimental techniques	77
3.1. Material synthesis techniques	77
3.2. Characterization techniques	82
Bibliography	92
4. Results as a compilation of articles	97
4.1. Large magnetoelectric effects in electrodeposited nanoporous microdisks driven by effective surface charging and magneto-ionics	99

4.2. Enhancing magneto-ionic effects in magnetic nanostructured films via conformal deposition of nanolayers with oxygen getter/donor capabilities	121
4.3. The order of addition and time matters: impact of electrolyte processing on micelle-assisted electrosynthesis of mesoporous alloys	141
5. Hard-magnetic, macroporous L1₀-ordered Co-Pt electrodeposited films	163
5.1. Introduction	163
5.2. Experimental section	166
5.3. Results & Discussion	168
5.4. Conclusions	178
References	178
6. General discussion	185
7. Conclusions	193
8. Future perspectives	199
9. Curriculum vitae	203



1

Introduction

1. Introduction

1.1. The problem of energy efficiency

Energy is the lifeblood of our civilization. Our lifestyle is unconceivable without reliable, sustainable and affordable supplies of energy. In 2007, the European Council adopted the '20-20-20' climate and energy targets (20% increase in energy efficiency, 20% reduction of CO₂ emissions, and 20% renewables by 2020). With those goals in mind, around 5.9€ billion were allocated to energy research and innovation projects.¹ Such projects have focused on developing new technologies that promote renewable energy sources (solar, wind, bioenergy, hydrogen and tidal energy) and the development of smart energy technologies, such as energy efficient devices, storage, electrified transport, fuel cells and various information and communication technology (ICT) applications, among others. Despite having reached the energy 20-20-20 targets, much more remains to be done within the next decade. For this reason, the 2030 climate and energy framework includes more ambitious goals (cutting greenhouse gas emissions by at least 40%, sharing renewable energies by at least 32% and improving energy efficiency by 32.5%).² The energy system has reached a tipping point in a world becoming depleted in fossil fuel resources and with increased energy consumption. New energy-smart technologies are thus becoming essential.

Within this context, energy efficiency has become the catchphrase of the 21st century. One of the main objectives of the Horizon Europe Programme (2021-2027) is the search for new strategies for the implementation of energy-efficient devices. The growing demand for high-performance ICT is stimulating the search for next generation of highly energy-efficient digital systems.³ According to Moore's law, the number of transistors on a microprocessor chip will double every two years, achieving microprocessor with circuit features of around 14 nanometers across. However, the miniaturization of integrated circuits has already started to falter due to the unavoidable generated heat. Self-heating in current devices arises from the interaction between electrons and lattice vibrations (Joule heating due to electron-phonon scattering).⁴⁻⁶ As a result, an intense research is

being pursued to explore and develop new cooling technologies (i.e. thermoelectric cooling, direct liquid cooling, high-performance air-cooled heat sinks, etc.) in computer and telecommunications systems.⁷ Nevertheless, despite the efforts, heat dissipation and power consumption in micro-/nanoelectronics remains an ongoing challenge.⁴

Among the various areas of the Information and Communication (IT) industry, data centers are one of the main sectors in which energy efficiency issues are continuously addressed. Data centers are energy-hungry infrastructures which consume over 270 TWh of energy with a compound annual growth rate over 4.5%.⁸ In fact, according to the energy forecast (**Figure 1.1a**), electricity use by ICTs is predicted to exceed 20% of the global total by 2030, with data centers using more than one-third of the total amount of electricity.⁹ In addition, the problem of energy consumption does not only affect large storage and data processing companies (e.g. Facebook, Microsoft or Google), this issue is more relevant for small computation systems. This can be verified by comparing the “power usage effectiveness ratio” (PUE) values of both data centers (large and small data centers). PUE is the ratio between the total energy used and the energy delivered to computing equipment, being 1.0 an ideal PUE. A PUE value above 2 implies that more energy is being used for maintenance issues (e.g. cooling) than computing.¹⁰ As shown in **Figure 1.1b**, the PUE values for data center facilities differ at various scales, where the smaller the server, the higher the PUE value and thus, the lower the energy efficiency.

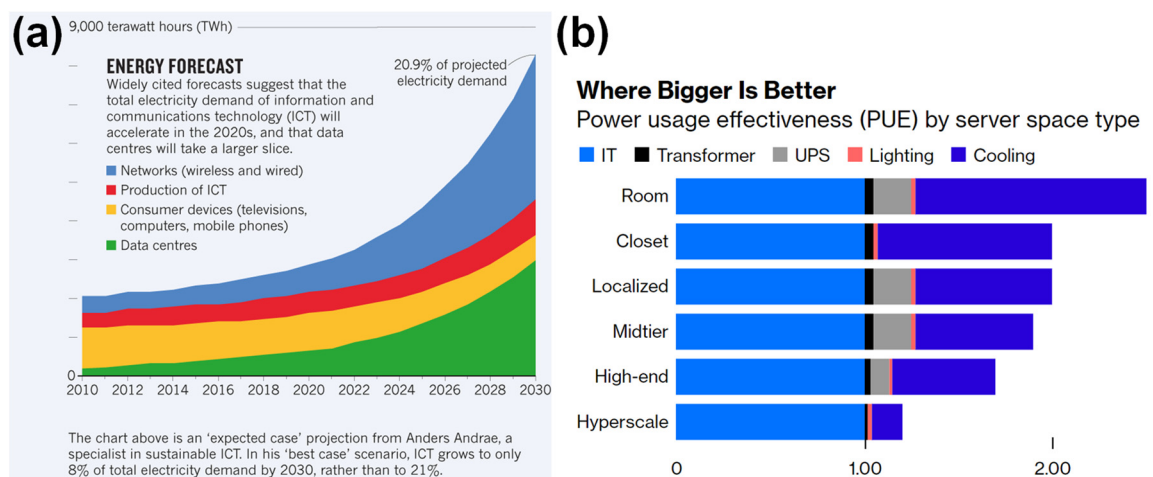


Figure 1.1. (a) Expected case projection of the total electricity demand of ICTs (forecast until 2030). Adapted from reference 9. (b) Power usage effectiveness by data server space type. IT stands for “information technologies” (computing) whereas UPS refers to “uninterruptible power supply”. Adapted from reference 10.

Accordingly, the energy consumed by the data center can be divided in two parts: the use of energy by the infrastructure facilities (cooling and power conditioning systems) and the use of IT equipment (i.e. servers, storage, etc.). IT equipment includes all types of devices, a large part of which comprises magnetically actuated devices such as hard disk drives (HDDs) and magnetic random-access memories (MRAMs). In HDD, information is stored in many binary digital magnetic units (called "bits"). In order to provide stability to the stored data, the bits are made of magnetic material with a high coercive field and a high magnetic anisotropy (**Figure 1.2a**). These bits can have dipole moment "up" or "down" which is represented in the binary code as 1=Up and 0=Down. In order to write information, an external magnetic field is applied locally to induce magnetic switching. MRAMs are also composed of dense arrays of magnetic bits, which comprise multi-layer stacks denoted as "magnetic tunneling junctions" (MTJs). As shown in **Figure 1.2b**, the tunneling junctions are built of a "free" ferromagnetic layer, a spacer oxide layer, a "pinned" ferromagnetic layer and a pinning layer (antiferromagnetic). All these layers are sandwiched between the word (bottom) and bit (above) lines which provide the magnetic field to control the orientation of the free and pinned layers. The magnetization of the free and pinned magnetic layers can be aligned parallel (low resistance) or antiparallel (high resistance) which can be associated to digital signal "0" and "1", respectively. For writing, current pulses are used through one line of each array and only in the intersection of the word and bit lines the magnetic field is high enough to orient the magnetization of the free layer.

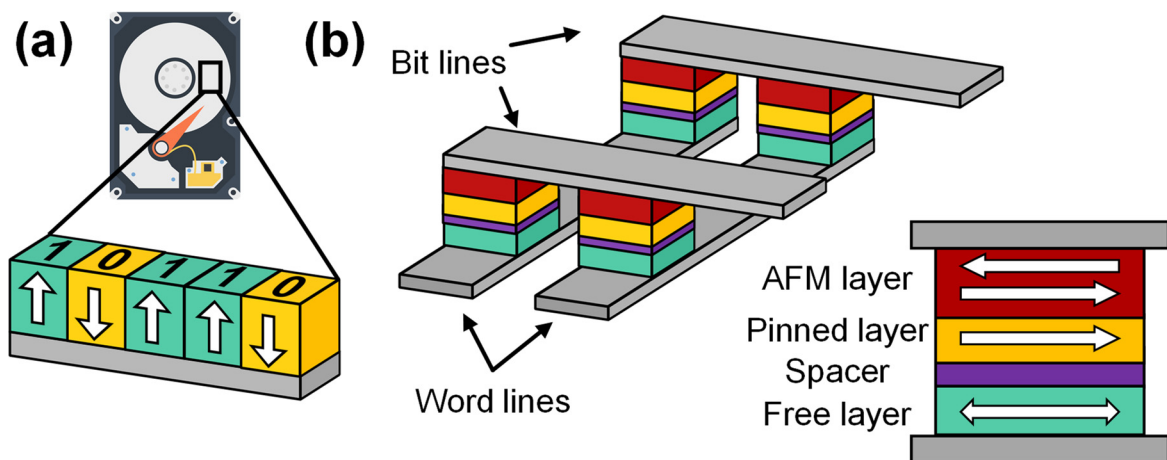


Figure 1.2. Scheme of (a) a hard-disk memory and (b) a magnetic random-access memory with a scheme of a tunneling junction unit.

As can be gleaned from above, in both magnetically actuated memory devices the use of magnetic field for recording process remains an important limitation. Such magnetic fields are produced by miniaturized electromagnets in HDDs and by the currents flowing in the bit and word lines in the MRAMs, involving a relatively high waste of energy (power dissipation) through Joule heating effect. Accordingly, several solutions have been proposed in order to optimize the recording process. In HDD, magnetic switching can be assisted by locally heating the magnetic bit temporarily with a laser which reduces the magnetic anisotropy energy and the coercivity (heat-assisted magnetic recording, HAMR).¹¹ In MRAMs, the usage of magnetic field can be completely avoided by using spin-polarized electric currents which orient the magnetic bit via spin-transfer torque.¹² Despite all the advancements, in spin-transfer-torque RAMs (STT-RAMs), flowing currents are still present, and a fraction of the energy employed in the writing process is consumed through Joule heating. For example, the currents required in MRAMs are of the order of 10 mA, while STT-RAMs need currents of around 0.5 mA, still a factor five times higher than the output currents in metal-oxide-semiconductor-field-effect transistors.^{12,13} In thermally-assisted writing of HDDs, the generation of heat (with a laser) is also a source of energy consumption. For this reason, finding solutions to the magnetic recording problem is a key issue on the way to future energy-efficient spintronics devices.

1.2. Fundamentals of magnetism

The magnetic moment in an atom originates from the intrinsic spinning motion of electrons around their own axis (spin moment) and the electron's orbital movement around the nucleus (orbital moment).¹⁴ All the materials have a response in the presence of an applied external magnetic field (H_{applied}) and depending on that response, materials can be classified into five categories: diamagnetic, paramagnetic, ferromagnetic, antiferromagnetic and ferrimagnetic (**Figure 1.3a**). As shown in **Figure 1.3b**, the magnetization (M) versus H_{applied} curves associated to the various types of materials show a different profile. The response is related with how the magnetic moments are arranged in the material (**Figure 1.3a**).

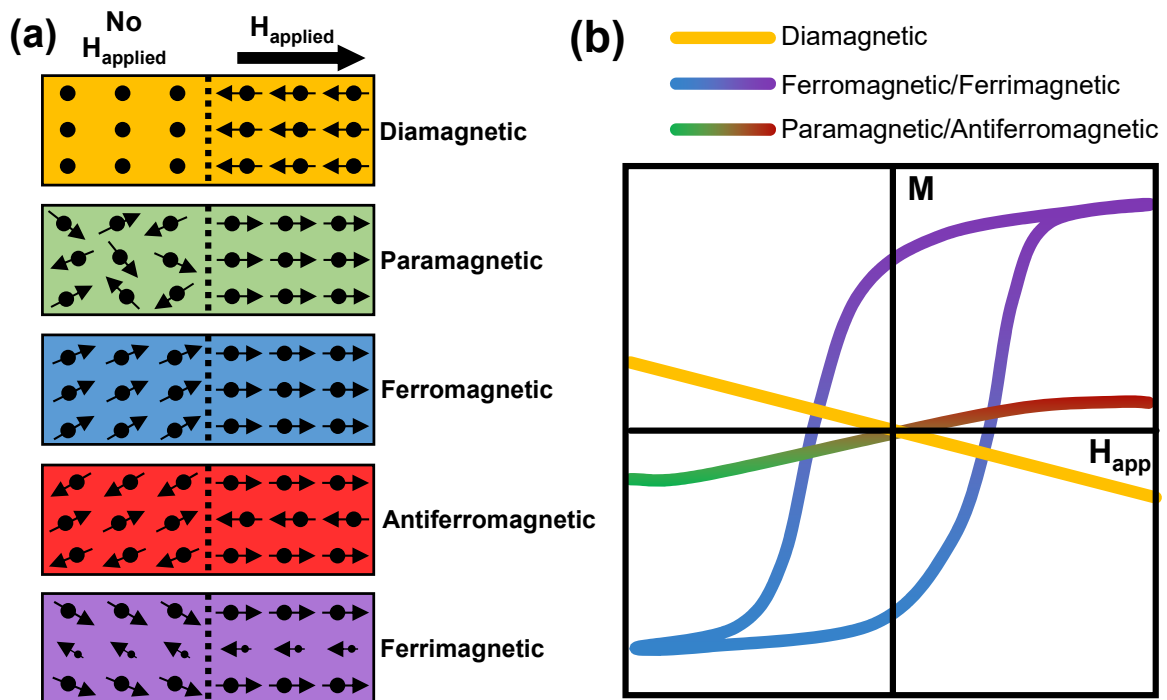


Figure 1.3. (a) Schematic representation of the magnetic moments configuration for diamagnetic, paramagnetic, ferromagnetic, ferrimagnetic and antiferromagnetic materials and (b) the magnetic response of the materials against a strong H_{applied} .

- Diamagnetism.** The origin of diamagnetism arises from the change in the electron orbital motion (Larmor precession) in an atom under H_{applied} , and as a result, a small negative moment is generated (**Figure 1.3a**). The induced magnetic field tends to oppose to the H_{applied} , which is manifested as a linear relationship between M vs. H_{applied} with a negative slope (**Figure 1.3b**). Since diamagnetism arises from bounded electrons, all materials present a diamagnetic response to a H_{applied} . Nevertheless, diamagnetism signal can be overshadowed by other stronger contributions (i.e. ferromagnetism or paramagnetism). Diamagnetic materials are composed of elements with orbitals shells completed without unpaired electrons. Since diamagnetic materials do not exhibit net magnetic moment, the diamagnetism vanishes when the applied external field is removed (**Figure 1.3a**).
- Paramagnetism.** In paramagnetic materials, magnetic moments are uncoupled to each other since thermal fluctuations overcome interaction between the spins (exchange interaction), so magnetic moments are randomly oriented in the

absence of H_{applied} (**Figure 1.3a**). Upon application of H_{applied} , magnetic moments tend to align along the field direction, resulting in a linear relationship with a positive slope between M and H_{applied} (**Figure 1.3b**). Upon removal of H_{applied} , magnetic moments become misaligned, hence, no retention of the net magnetic moment is found in paramagnetic materials.

- **Ferromagnetism.** In ferromagnetic materials, exchange interaction between the spins of neighbouring atoms is positive and very strong. Upon application of H_{applied} , the magnetic moments tend to align along the field direction (**Figure 1.3a**), consequently, when the field is removed, part of the alignment (exhibited spontaneous magnetization) is retained, showing a hysteresis behavior. Ferromagnetic materials become paramagnetic above the so-called Curie temperature (T_C). A detailed explanation of ferromagnetic materials is provided in Section 1.2.1.
- **Antiferromagnetism.** In antiferromagnetic materials, negative exchange interactions cause the antiparallel alignment of the adjacent magnetic moments (**Figure 1.3a**), thus providing a total zero macroscopic net magnetic moment in absence of H_{applied} . When an external magnetic field is applied, the magnetization shows a positive linear behavior as for paramagnetic materials (**Figure 1.3b**). Antiferromagnetic materials become paramagnetic above the Néel temperature (T_N).
- **Ferrimagnetism.** Similar to antiferromagnetism, the negative exchange interaction tends to align the magnetic moments antiparallel to each other, but the two spin sublattices have dissimilar strength (**Figure 1.3a**). Thus, spontaneous magnetization exists leading to a non-zero magnetic moment in absence of H_{applied} . Upon application of H_{applied} , ferrimagnetic materials exhibit hysteresis loops similar to ferromagnetic ones.

1.2.1. Ferromagnetism

Ferromagnetism arises from the spins of electrons from partially filled outer atom shells (3d and 4f electronic bands) which have a net magnetic moment. Positive exchange

interaction causes neighboring electron spins to align parallel to each other over small regions called magnetic domains. Such magnetic domains are microscopic and separated by walls which embrace a gradual reorientation of the individual magnetic moment of the atoms (**Figure 1.4a**). The size of a domain wall depends on the anisotropy and the exchange interaction of the material, but the size may range from tenths to hundreds of nanometers. As shown in **Figure 1.4bi**, in absence of H_{applied} the domains are randomly oriented to each other and the material remains unmagnetized. Upon application of a magnetic field, the magnetic moments of the different domains tend to align along the H_{applied} direction, and, in addition, the domain walls propagate promoting the growth of the magnetic domains aligned with the field at the expenses of the others (**Figure 1.4bii**). These processes continue as the strength of the applied field increases until the ferromagnetic material macroscopically becomes a single domain state, aligned parallel to the H_{applied} , reaching the maximum possible magnetization called "saturation magnetization" (M_S), as depicted in **Figure 1.4biii**. When H_{applied} is reduced to zero, the magnetization decreases with a slower rate without retracing the initial magnetization curve from a zero-field value. This effect is called "hysteresis" and it occurs because the aligned magnetic domains have reached a lower energy configuration and the domain walls show a certain resistance in response to the field reversal. Consequently, even after removing the H_{applied} , a portion of the magnetization is retained, resulting in a remanent magnetization (M_R) (**Figure 1.4biv**). As a result, the magnetization vs. H_{applied} curve describes a hysteresis loop, which is characteristic of ferromagnetic and ferrimagnetic materials (**Figure 1.3b**). As the magnetic field is applied along the reverse direction, the net remaining magnetization in the material can be suppressed at certain magnetic field value, which is called "coercivity" (H_C). Eventually, as H_{applied} is increased further, saturation is reached in the reverse direction. The magnetic properties of magnetic materials depend on several factors such as particle shape, orientation, crystallite size, exchange energy or magnetocrystalline anisotropy, amongst others.

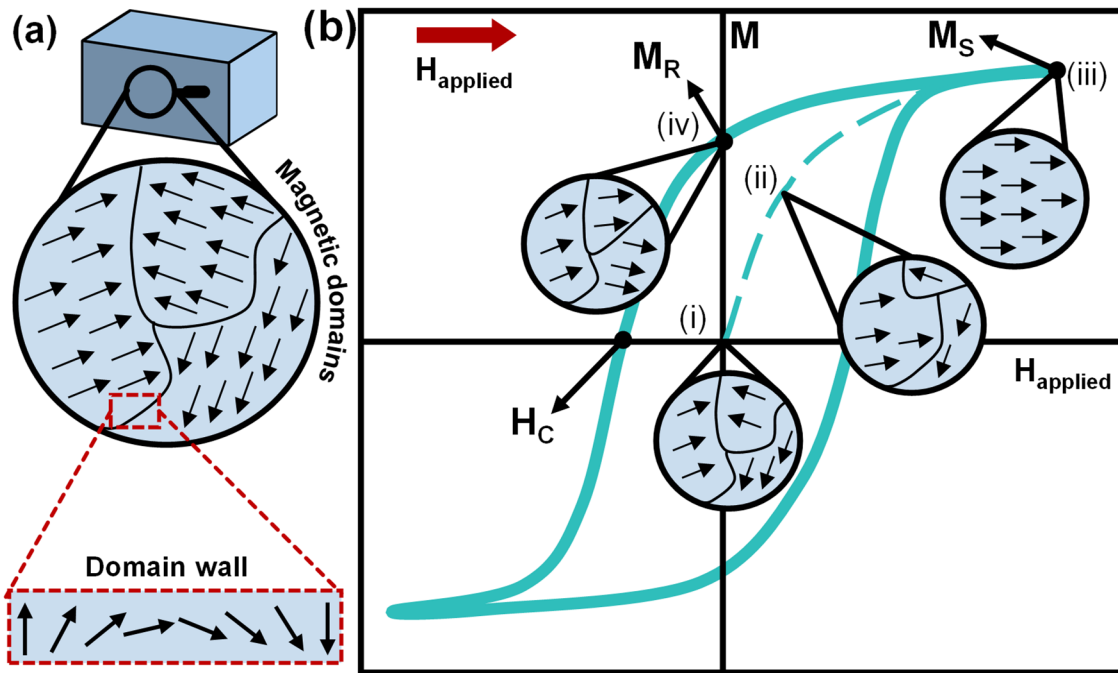


Figure 1.4. (a) Scheme of the magnetic domains and the domain walls on a ferromagnetic material. (b) Schematic representation of a typical hysteresis loop for a ferromagnetic material and the corresponding orientation of the magnetic domain at each point. Magnetic parameters such as M_S , M_R and H_C points are depicted.

1.2.2. Soft and hard magnetic materials

The magnetic properties of ferromagnetic materials are determined by the shape of their hysteresis loops and depending on the magnitude of M_S , M_R and H_C values, ferromagnetic materials can be divided in two categories: soft and hard.

Soft magnetic materials are characterized by low H_C values and typically large M_S , thus resulting in narrow hysteresis loops (blue curve, **Figure 1.5**). Soft magnets are found in applications requiring an increase of the magnetic flux density generated by a magnetic field or a change in the magnetic induction. For this reason, soft magnets are used in electromagnets, transformers cores or motors since these materials can be magnetized and demagnetized with low applied magnetic fields. Some examples of soft magnets are Si steels, Zn or Ni ferrites, Fe–Ni alloys (e.g. permalloy) or Fe-based and Co-based amorphous alloys.¹⁵

Hard magnetic materials, also known as permanent magnets, are characterized by a high H_C value and usually smaller M_S values compared to soft magnetic materials, i.e. broad hysteresis loops (red curve, **Figure 1.5**). These materials are very difficult to magnetize and demagnetize. The figure of merit that describes permanent magnet performance is the maximum energy product, $(BH)_{\max}$ and it is closely related to the total area enclosed by the hysteresis loop (plotting magnetic induction B vs. H_{applied} , where B is given by: $B = \mu_0(H+M)$ where μ_0 is the permeability of free space). Magnetic induction B is thus a function of the internal magnetic field (H) and M . The maximum energy product gives information of the overall energy that can be stored in the permanent magnet. The higher the value of $(BH)_{\max}$, the stronger the magnetic field the permanent magnet can produce.¹⁶ Large H_C , high M_S values and squareness ratio (M_R/M_S) close to 1 are desirable to maximize the $(BH)_{\max}$ parameter. For all these reasons, hard magnetic materials are used to supply a magnetic field or as storage-energy systems, finding applications in motors, generators or high-density recording media, among others.^{17,18} Some examples of hard magnetic materials are: SmCo_5 , Al-Ni-Co , strontium or barium hexagonal ferrites, Nd-Fe-B alloys, $L1_0$ -ordered alloys (Fe-Pt , Co-Pt), and hexagonal close packed (hcp) Co-based alloys.

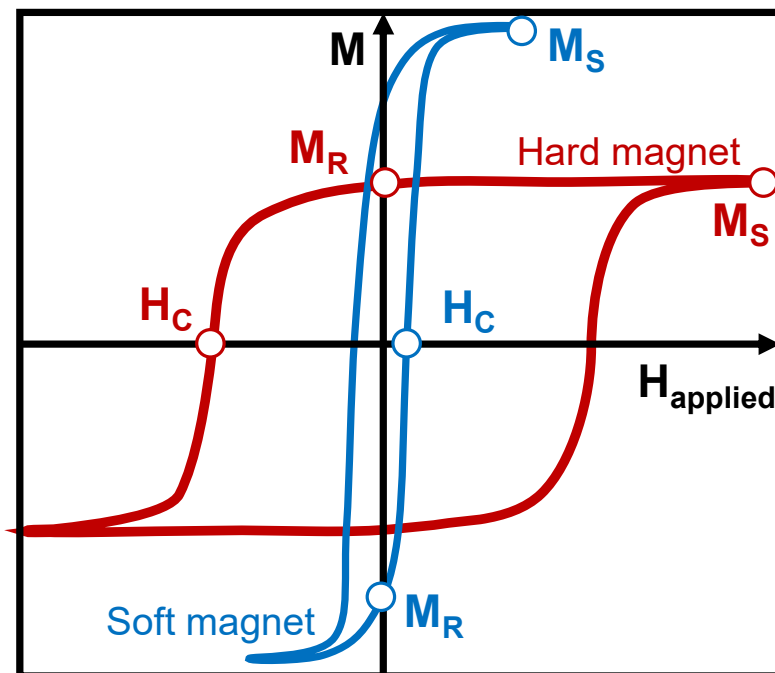


Figure 1.5. Schematic representation of the hysteresis loops of soft (blue curve) and hard (red curve) magnetic materials portraying the M_S , M_R and H_C parameters.

L1₀-ordered intermetallic alloys have gained attention as candidate permanent magnets in the field of magnetic recording media owing to their high (BH)_{max} (407 and 200 kJ/m³ for L1₀-ordered Fe–Pt and Co–Pt, respectively).^{19–21} The tetragonal L1₀ intermetallic family has a general structure that comprises an iron-series 3d transition metal and a heavy transition metal (rare-earth (4f), palladium (4d) and platinum-series elements) which form as stable phases near the equiatomic compositions.²² **Figure 1.6** shows as an example the unit cell of L1₀-ordered Co–Pt, where Co (blue) and Pt (yellow) atoms are alternated in an asymmetric face-centered tetragonal (fct) structure. This asymmetry leads to a large uniaxial magnetocrystalline anisotropy with an easy c-axis (about 5 MJ/m³ for Co–Pt). The Co atoms ensure a high magnetization and T_C, whereas the Pt atoms provide the spin-orbit coupling from which the large anisotropy of the L1₀-ordered Co–Pt structure originates.^{19,23}

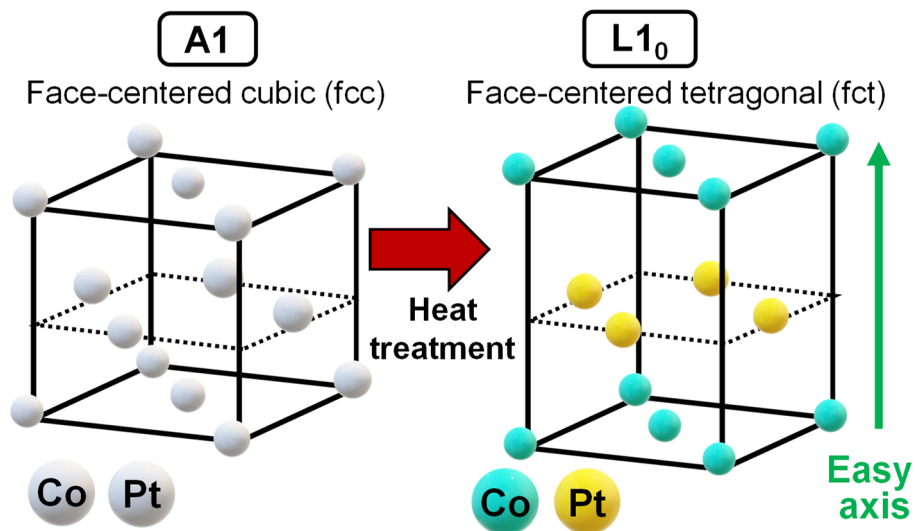


Figure 1.6. Unit cell of Co–Pt alloy before and after heat treatment to induce the A1 → L1₀-ordered phase transformation.

The most common approach to obtain the L1₀-ordered Co–Pt, Co–Pd, Fe–Pt and Fe–Pd phase is heat treating of their corresponding A1-disordered phase (face-centered cubic) (**Figure 1.6**). The A1-disordered structure can be fabricated by several techniques: pulsed laser deposition (PLD),²¹ sputtering,²⁴ molecular beam epitaxy (MBE)²⁵ or electrodeposition among others.^{26,27} L1₀-ordered systems are mostly prepared in the form of thick and thin films owing to the complexity of synthesis which involves high temperature treatments (300–800 °C). The fabrication of L1₀-ordered systems in the form

of nanostructured films²⁸ and micro-/nano-structures such as nanoparticles and pillars^{29–31} has been less studied. Remarkably the fabrication of mesoporous L1₀-ordered alloy films remains unexplored.

1.2.3. Control of magnetism

Proper control of magnetism is of paramount importance for any of the aforementioned applications of ferromagnetic materials. This particularly applies to the field of data storage and data processing in ITCs. As it has been described in Section 1.1, magnetically actuated devices, such as HDDs and MRAMs, rely on the use of magnetism for the storage of information, and application of magnetic fields has been the standard means to switch the magnetization of the magnetic bits. Nevertheless, the ever-increasing demand for energy-efficient and low-power electronic devices has propelled the search for new non-magnetic approaches for manipulating magnetism.

Plastic deformation of magnetic materials has marked effects on their magnetic properties, and it has been explored as a means to tailor magnetism. One example is the cold-work which allows to induce an uniaxial anisotropy by e.g. rolling metals and alloys, such as Ni and Ni-Fe, Fe-Al, Ni-Co alloys.^{32–34} Plastic deformation increases the density of dislocations and lattice defects in the material. The created microstresses affect the domain wall motion, resulting in an increase of the magnetic hardness (and the mechanical hardness). This, in turn, induces several changes in the hysteresis loop: wider shape (higher H_C), bigger area, etc.³⁴ Particularly, magnetostrictive materials have been an object of research due to their ability to transduce magnetic energy into mechanical energy and vice versa. Inverse magnetostrictive effect (or Villari effect) is known as the phenomenon of changing the magnetic properties of a material in response to an externally applied mechanical stress. All magnetic materials exhibit magnetostriction. Nevertheless, certain materials show higher magnetostriction constant than others, for example, Fe-Ga alloy (Galfenol), Fe-Al, Tb_xDy_{1-x}Fe₂ (Terfenol-D) or Fe-Co, among others.

The interplay between light and magnetism is also appealing as a means to control/tailor the magnetic properties of materials. Light can induce magnetization switching without making use of magnetic fields. This approach exploits either the indirect coupling of the

spins with the electric field component of the light (spin-orbit interaction) or the direct coupling between the spins and the magnetic field component.³⁵ Several works have demonstrated that the ultrafast laser pulse excitation of magnetic material can induce spin-reorientation, demagnetization, modification of magnetic structure or even magnetization reversal.³⁶⁻⁴¹

The magnetic and mechanical properties of any material can be altered via irradiation with ions, electrons or gamma rays. Changes in the properties can occur due to the atomic rearrangements caused by the irradiation, where the type of rearrangement depends on the kind of irradiation.³⁴ For example, ion implantation/irradiation can be employed to modify the microstructure, composition and chemical ordering of alloys and consequently, various magnetic parameters become affected, such as magnetization, magnetic anisotropy, H_C or magnetization reversal.⁴²⁻⁴⁶

Another interesting method to induce magnetization switching is to employ spin-polarized electric currents. When a spin-polarized current (i.e. a current with unequal number of spin-up and spin-down electrons) enters a ferromagnet, whose magnetization presents some tilt with respect to the spin direction of the electrons, the mismatch exerts a torque which is transferred from the current to the magnetization itself (spin-transfer torque), resulting in magnetization reorientation and, eventually, switching.⁴⁷ As it has been mentioned above, this approach has been exploited in magnetic storage devices (spin transfer torque MRAMs, STT-MRAMs), increasing the selectivity in the bit's flip and reducing the overall power-consumption during the magnetization reversal process by avoiding the use of magnetic fields.⁴⁸

1.3. Mechanisms to control magnetism with electric field

As evidenced from the above overview, the performance of devices has improved over the years with novel and improved technical advances which do not make use of magnetic fields to manipulate magnetism. Despite the efforts, electrical currents are still the principal means to manipulate the magnetic elements of memory devices, resulting in energy losses through heat dissipation.

In parallel to the above-mentioned strategies, an alternative approach to produce even more efficient devices by completely suppressing the use of electrical currents has been envisaged in the last decade. This promising strategy is the control of magnetism by means of electric field (E-field control of magnetism), which is based on the substitution of electric currents by voltage. E-field control of magnetism relies on the so-called magnetoelectric effect (ME). In general, the ME effect can be defined as the influence of an external magnetic field on the electric polarization of certain materials (direct ME effect) or, vice versa, the effect of an electric polarization on the magnetic properties (converse ME effect). Specifically, the latter is the basis of the E-field control of magnetism.

The classical example of ME materials to be altered by means of electric field are the so-called multiferroics (MFs). These are single-phase materials in which at least two ferroic orders (i.e. (anti)ferromagnetism, ferroelectricity or ferroelasticity), are inherently coupled.⁴⁹ In the case of MFs considered as ME materials (ME MFs), ferromagnetism and ferroelectricity are the two ferroic properties coupled to each other. This means that both ME effects can be observed in such materials; namely the application of a magnetic field induces changes on the electric polarization and, conversely, the magnetic response can be altered upon applying an electric field. Although ME MFs are very appealing for voltage-controlled devices, the scarcity of single-phase multiferroic materials, and their generally weak and low-temperature ME effect hamper, their real application.⁵⁰

To overcome these limitations, a flurry of research has been conducted in the E-field control of magnetism in ME materials different from MFs through various mechanisms. In general terms, the various mechanisms for accomplishing converse ME effect can be categorized into strain-mediated, charge accumulation, and electrochemical processes (**Figure 1.7**). The latter is subdivided in two categories which are described in Section 1.3.3. Such mechanisms do not occur separately and, in most of the cases, various effects occur simultaneously, making their disentangling difficult.^{51,52}

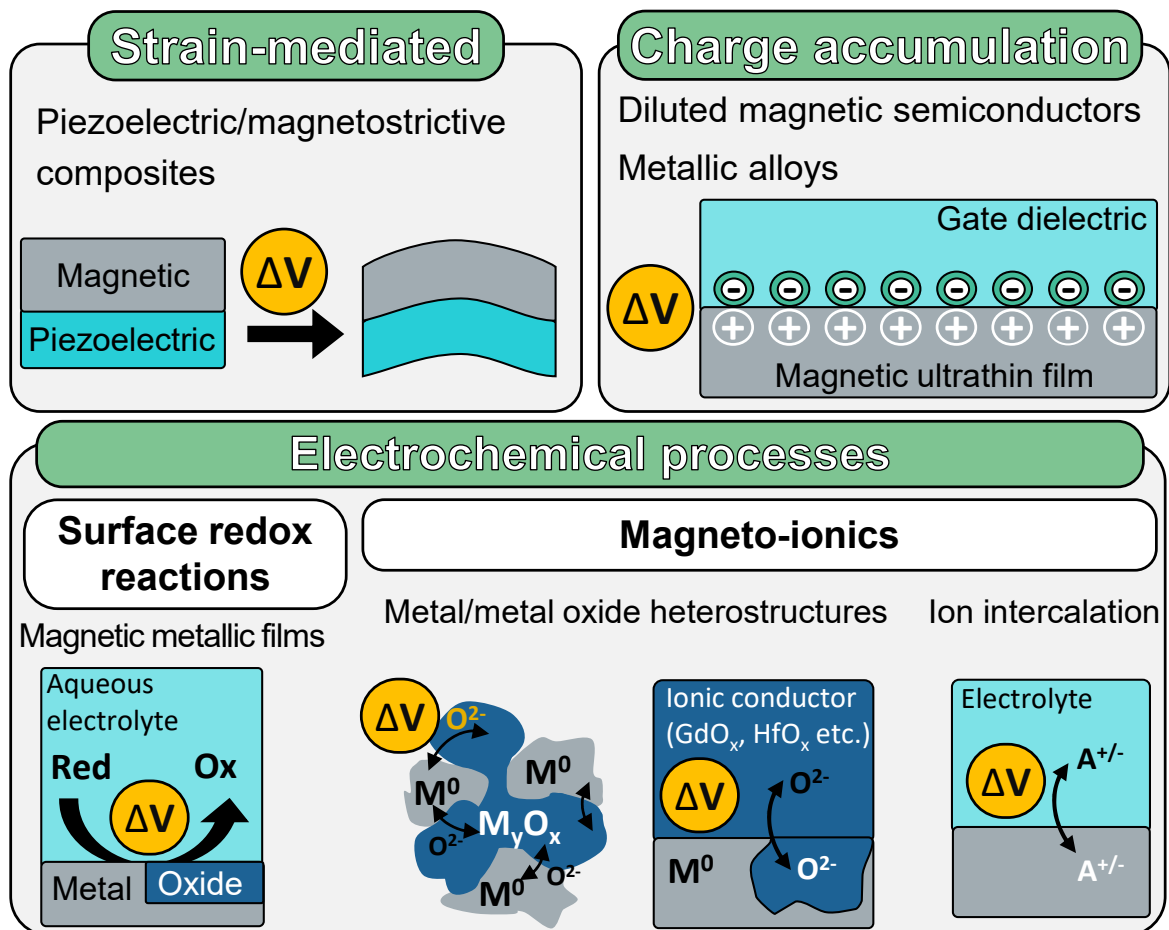


Figure 1.7. Main mechanisms responsible for ME effects. The most representative types of materials for each case are depicted, together with a schematic drawing to describe the physical/physicochemical underlying principles associated to each mechanism.

1.3.1. Magnetolectric coupling via strain

Strain-mediated ME effect relies on inducing inverse magnetostriction (or Villari effect) in a magnetic material by using piezoelectricity. A common configuration consists in combining a single-crystalline piezoelectric material with a magnetic thin film (in some cases magnetostrictive material). The application of voltage induces strain in the piezoelectric component, which is transmitted to the magnetostrictive material, leading to changes in its magnetic properties. The first successful strain-mediated ME effect was realized in 1972, in an eutectic composite obtained by unidirectional solidification which involved ferroelectric piezoelectric BaTiO₃ and ferromagnetic magnetostrictive CoFe₂O₄.⁵³ Since then, several other ME composites consisting of piezoelectric and magnetostrictive materials have been investigated: PbZr_{1-x}Ti_xO₃ (PZT)/ferrites,⁵⁴

PZT/La_{1-x}Sr_xMnO₃ (LSMO),⁵⁵ PZT/Fe_{0.5}Co_{0.5},⁵⁶ and PZT/Terfenol-D.⁵⁷ Besides magnetostrictive systems, there has been a great interest in combining ferromagnetic thin films^{58,59} and multilayers^{60,61} with piezoelectric substrates. In this regard, changes in H_c up to 40% have been reported in Fe/BaTiO₃ heterostructures.⁵⁸

A giant strain-mediated ME effect was observed in FeRh/BaTiO₃ heterostructures, taking advantage of the lattice parameter dependence of the antiferromagnetic-ferromagnetic metamagnetic transition in FeRh.⁶² Changes in the magnetization up to 550 emu·cm⁻³ (corresponding to a shift of T_c ≈ 25 K) were achieved due to the strain transmitted from BaTiO₃ to FeRh by applying an external voltage of about ± 20 V. The magnetic response achieved upon voltage application showed a butterfly-like shape, confirming that strain was the mediator of the ME effect. However, a slight asymmetry in the loop suggested the occurrence of a secondary E-field effect, namely electrostatic charge doping at the FeRh/BaTiO₃ interface. Owing to the fact that many of the employed piezoelectric substrates are also ferroelectric, the occurrence of synergetic effects of both strain and electrostatic charge doping (so-called charge-mediated ME effect) have been reported in several works.⁶³⁻⁶⁵

Despite the remarkable results obtained in the examples above, some non-trivial aspects hinder the practical usage of strain-mediated ME effect. First, a good contact at the interface is crucial for an effective strain coupling. In this regard, the lattice mismatch and the nature of the ferroelectric counterpart play an essential role. Furthermore, most of the ferroelectric substrates are oxide-based, which results in an unavoidable oxidation of the ferromagnetic counterpart when deposited, thus deteriorating the interface and consequently the strain coupling.^{66,67} An additional problem are the clamping effects. When the piezoelectric counterpart is grown in thin film form onto an underlying rigid substrate, the amount of voltage-induced strain that can be transmitted to the magnetic component is severely limited. Another aspect to consider is the limited endurance of the strain-based devices, caused by contact loosening, cracking and sparking after long-term use (mechanical fatigue).⁶⁸

1.3.2. Magnetoelectric effects via charge accumulation

Early studies on E-field manipulation of magnetism via carrier accumulation were pioneered in 2000 by Ohno et al. in diluted magnetic semiconductors (DMS) gated with solid dielectric used to create the E-field.⁶⁹ The group succeeded in switching a thin film of (In, Mn)As from a ferromagnetic to a paramagnetic state due to effective T_C modulation achieved by applying an external voltage of ± 125 V at 20 K. Afterwards, the same group was able to induce reversal of the magnetization in similar (In, Mn)As films by exploiting the change in H_C induced by charge accumulation.⁷⁰ Following the same concept, other works have reported on the E-field control of the magnetic properties of DMS systems like (Ga, Mn)As,⁷¹ (In, Fe)Sb⁷² and $Mn_{0.05}Ge_{0.95}$.⁷³ Despite the remarkable results, the use of magnetic semiconductors in practical applications is limited by their low temperature ferromagnetism. Only a few works have successfully demonstrated the effective manipulation of the magnetic properties in diluted semiconductors (Co-doped TiO_2) with T_C above room temperature.⁷⁴

As alternative magnetic materials, several studies have focused on the ME coupling via charge-accumulation in magnetic transition metals and metallic alloys (e.g. Fe, Co, Ni, Fe–Pt, Fe–Pd, Co–Pt and Co–Pd) owing to their higher T_C compared to most magnetic semiconductors. In 2007, Weisheit et al. reported the first observation of electric field-effect in a metal via surface charging. Specifically, the authors demonstrated a modification of 4.5% and 1% in the H_C of Fe–Pt and Fe–Pd ultrathin films (≈ 2 nm), respectively.⁷⁵ The authors ascribed such changes to the modification of the magnetocrystalline anisotropy energy (MAE) by surface charging, which was subsequently confirmed by density functional calculations for these systems and later for Co–Pt, Co–Pd⁷⁶ and Cu–Ni.⁷⁷ Through theoretical studies, researchers showed that the origin of changes in MAE in response to the electric field is associated to the modulation of unpaired d electrons with energies close to the Fermi level, in addition to the E-field surface screening in ferromagnetic transition metals (e.g. Fe, Ni and Co) being spin dependent.^{78–80} These studies encouraged further investigation of these systems, including Fe and CoFeB, for which electric-field-induced changes of H_C were also reported.^{81,82}

Aside from E-field manipulation of H_c , the electric field control of other magnetic parameters has been studied. For instance, Shimamura and coauthors demonstrated a large tuning of T_c (up to 100 K) in Co ultrathin films by applying ± 2 V using an ionic liquid.⁸³ Electric field control of magnetic anisotropy has been also studied. Maruyama et. al reported changes of up to 40% in the magnetic anisotropy of a few atomic layers of Fe metal. The observed electric-field effects resulted from the electric-field modulation of Fe electron occupancy together with the strong spin-orbit coupling between Au and Fe.⁸⁴ From a microscopic perspective, electric fields can also be used to control domain wall nucleation, and propagation velocity in CoFeB,^{82,85} Fe-Pt,⁸⁶ and Co.⁸⁷ In the last decade, multiple theoretical works have reported the electric control of skyrmions,⁸⁸⁻⁹⁰ which has been experimentally demonstrated at low temperatures.⁹¹ Recently, Givord et al. achieved the effective control of skyrmions in Pt/Co/oxide trilayers via an applied electric field at room temperature.⁹²

It is worth to mention that electric-field effects reported in the aforementioned studies occur mainly at the utmost surface of the metal due to the well-known screening effect. This is considered a limitation in the voltage control of magnetism of magnetic metals and metallic alloys. In contrast to semiconductors, the electric field is effectively screened in metals, and charges are accumulated at the surface within the so-called Thomas-Fermi screening length ($\lambda_{TF} \sim 0.5$ nm) close to the interface with the dielectric material used to create the E-field.⁹³ For this reason, the investigated magnetic materials are typically grown in the form of ultrathin films, in order to enlarge the surface-to-volume (S/V) ratio and consequently optimize the ME effect. More recently, porous magnetic materials, which are characterized by high S/V ratios, have been the subject of a flurry of research because the ME effect can be greatly enhanced. The research in this area is overviewed in Section 1.5.

1.3.3. Magnetoelectric effects via electrochemical processes

Voltage-induced electrochemical processes can be utilized to modify the oxidation state of an element (or elements) in a material and, in turn, its magnetic properties. Contrary to strain and charge-accumulation mechanisms, electrochemical processes are generally non-volatile and are not limited by the electric field screening length. Electrochemical

processes associated to changes in the magnetic properties of a material are classified into: (i) surface redox reactions and (ii) truly ion migration (magneto-ionics).

It should be noted that this classification is adopted throughout this Thesis although other classifications can be found in the literature. The criterion used herein is based on the fact that surface redox reactions employ oxidizing electrolytes to oxidize the magnetic material. Likewise, ion diffusion (or ion intercalation from an ionic conductor) in magneto-ionics causes changes in the oxidation state of the element(s) in the magnetic material. The frontier between these two mechanisms in the literature is unclear since they often act synergistically under the action of an electric field.

1.3.3.1. Surface redox reactions using oxidizing electrolytes

This approach benefits from oxidation-reduction reactions of a magnetic metallic (or metal oxide) material in the presence of an aqueous alkaline electrolyte (commonly, KOH or NaOH). When the material (either a metal or a metal oxide) is subjected to electrical voltage, a charge-transfer reaction takes place between the electrolyte and the material, changing its oxidation state and, consequently, causing a modulation of the magnetic properties.

To date, iron-based materials are the most studied ones in voltage-control of magnetism via surface redox reactions.⁹⁴⁻⁹⁸ For example, Leistner and co-workers achieved a variation of M_s up to 20% in 10 nm thick Fe film in KOH. Changes were attributed to the oxidation-reduction processes of 2 nm of the Fe layer upon voltage application.⁹⁴ Similarly, the same group was able to tune M , M_R/M_s and perpendicular magnetic anisotropy (PMA) in $\text{Fe}_3\text{O}[\text{Fe}_3\text{O}_4/\text{Fe}/(001)]L1_0$ Fe-Pt trilayers and FeO_x/Fe nanoislands using 1 M KOH as alkaline electrolyte.^{94,95}

Besides iron-based systems, ME effects via redox reactions have been also investigated in Pd-Ni, Co and Cu-Ni.⁹⁹⁻¹⁰¹ Magnetic anisotropy of Co ultrathin films was successfully increased by $0.36 \text{ erg}\cdot\text{cm}^{-2}$ by oxidizing the Co surface in 0.01 M KOH. Such variation was attributed to the formation of a Co-OH layer from the initially reduced Co-H state.¹⁰⁰ Interesting results have been reported by Quintana et al. in Cu-Ni alloy films. After subjecting the films to voltage in presence of NaOH aqueous electrolyte, an increase of

up to 33% in M_s was achieved. The observed effect was associated to a selective electrochemical redox reaction, in which the oxidation of the Cu–Ni film affected only the Cu counterpart, causing an enrichment of the Ni content in the Cu–Ni film and, in turn, an increase of the M_s .¹⁰¹

1.3.3.2. Magneto-ionics

Magneto-ionics exploits voltage-driven ionic motion (i.e. ion diffusion) as a means to control the oxidation state of an element (or elements) in a magnetic compound and, hence, to modify its magnetic properties. Magneto-ionic effects are non-volatile and are not limited to the surface either, thereby allowing to significantly affect thick films in their entire thickness. Importantly, ion migration can extend beyond superficial passivation typically achieved by surface redox reactions using alkaline electrolytes.

Most frequently, magneto-ionics effects have been studied in metal/metal-oxide heterostructures, where the motion of O^{2-} is used to tailor the oxidation state of the atoms in the magnetic material. Such heterostructures comprise the magnetic material (e.g., Fe, Co or Ni) and a gate oxide which acts as donor or acceptor of oxygen (e.g. GdO_x ^{102,103} or HfO_x ^{104–107}). The applied voltage displaces O^{2-} ions through the ferromagnet/oxide interface, thereby inducing changes in the magnetic anisotropy, domain wall velocity, H_c and M_s in the ferromagnetic counterpart.^{103–105} The term “magneto-ionic control” was first employed in Bauer and co-worker’s study to describe the voltage-induced oxygen migration in magnetic films. In this work, the PMA was successfully tuned in Co/ GdO_x bilayers by controlling the oxygen migration at the interface. By applying voltage, O^{2-} ions could move back and forth, oxidizing reversibly the Co/ GdO_x , which in turn allowed to modulate the easy axis of magnetization from out-of-plane to in-plane.¹⁰³ Bi et al. and Gilbert et al. found similar results in Co/ GdO_x ¹⁰⁸ and Co/ AlO_x / GdO_x heterostructures, respectively.¹⁰² HfO_2 has been also employed as oxygen source in various magneto-ionic systems due to their high oxygen mobility. For instance, PMA, T_c , H_c , M_s and exchange bias field were shown to change in Co/Ni and $[Co/Ni]_3$ layers in presence of HfO_2 as source of oxygen and an ionic liquid medium to create the electric field.^{104,105}

Alternatively, recent studies have focused on voltage-induced oxygen migration phenomena in certain magnetic materials without the assistance of gate oxide layers, using non-aqueous electrolyte gating. In such cases, the material itself includes the reservoir of oxygen by either containing oxygen in its structure or a surface passivation layer.^{51,109–111} Quintana and co-workers demonstrated that ferromagnetism can be fully suppressed by voltage-driven O and Co redistribution in Co_3O_4 films through nonaqueous electrolyte gating.¹¹¹ The onset of ferromagnetism was also successfully controlled in SrRuO_3 films by electrolyte-gating. In this work, the transition temperature decreased up to around 30 K and recovered by reversing the voltage polarity. The creation and annihilation of oxygen vacancies in the SrRuO_3 lattice was the underlying mechanism.¹¹²

Besides voltage-driven oxygen migration, lithiation (Li^+ ion diffusion) have also been employed for ME purposes. For instance, Dasgupta et al. showed that the voltage-induced Li insertion and extraction can controllably tune the magnetic properties of maghemite ($\gamma\text{-Fe}_2\text{O}_3$).¹¹³ Similarly, Dubraja and co-authors showed that magnetization of nanoporous $\text{Co}_{0.5}\text{Ni}_{0.5}\text{Fe}_2\text{O}_4$ and CoFe_2O_4 can be modified by voltage-driven Li^+ ion intercalation.¹¹⁴

Despite the significant ME results achieved by magneto-ionics, in most cases prolonged operation times and/or high temperature are required during voltage application. Ion migration is a rather slow process which typically require hundreds of seconds, unless high temperatures (or laser-assisted heating) are used since ion diffusion is a thermally activated phenomenon. These drawbacks hamper the potential use of magneto-ionics in energy-efficient devices.^{102,108} Very recently, it has been demonstrated that proton (H^+)-based magneto-ionic devices could significantly overcome such disadvantages.^{115,116} In these studies, H_2O hydrolysis (using atmosphere humidity) is employed to provide a source of mobile H^+ that could be voltage-driven through a gate oxide to reversibly manipulate the magnetic anisotropy. Proton-controlled magneto-ionic devices offer significant capabilities: room temperature operation, fast speed magnetization switching (~ 100 ms), and reversible operation (proton injection and release) for multiple switching cycles.^{115,116} Remarkably, the same authors have demonstrated in a recent study that the speed of the proton-induced magnetization switching largely depends on the

conductivity of the oxide material. Faster (~ 1 ms) and reliable ($>10^3$ cycles) magnetization switching is obtained in yttria-stabilized zirconia gate oxide as solid-oxide proton electrolyte.¹¹⁷

1.4. Configurations to apply electric field. Electrolyte-gated magnetoelectric actuation

Considering the different ME systems described in the previous sections, two different configurations can be used to apply an electric field on a magnetic material. As shown in **Figure 1.8**, the two most common geometries are the field-effect transistor (FET) configuration and the capacitor configuration. The first one is based on a transistor comprising a source, a drain and a gate electrode. In this configuration, the voltage is applied to the gate electrode across the insulating layer (dielectric). Here, the gate voltage modifies the magnetic properties of the magnetic layer, and the current which flows between the source and the drain electrodes is used to indirectly monitor the changes in magnetization (**Figure 1.8a**). This geometry is mostly used to assess measurements by means of resistive Hall Effect (or anomalous Hall effect). The second configuration is the capacitor one (**Figure 1.8b**). Here, the magnetic layer is grown on top (or below) the insulating layer (dielectric) and the voltage is applied between the magnetic material and the counter-electrode located on the other side of the insulating layer.

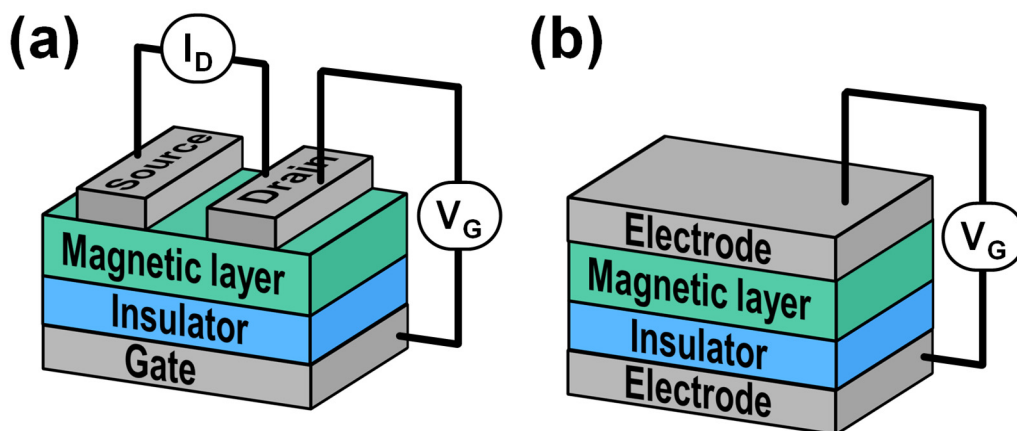


Figure 1.8. Scheme of the (a) field-effect transistor (FET) and (b) capacitor geometries utilized to assess the effect of electric fields on magnetic materials. Drawing adapted from reference 52.

In both geometries, the strength of the electric field is directly proportional to the applied voltage and inversely proportional to the thickness of the dielectric layer. High-quality ultra-thin dielectric layers with high κ (dielectric constant) value (e.g. 1–2 nm HfO_2 , Gd_2O_3 , Al_2O_3) are desirable to produce as much accumulated charge as possible. Unfortunately, the production of all-solid-state ME devices is still a challenge (specially in samples of relatively large area) due to the presence of structural defects in the dielectric layer, which cause pinholes through which the accumulated charge leaks out. Consequently, several approaches have been proposed to surmount this drawback by replacing the conventional solid oxide dielectric layer with: (i) polymer-based dielectric materials, such as polyimide (PI) or polyvinyl fluoride (PVDF) and (ii) liquid electrolytes. This last approach, known as liquid electrolyte-gating, involves the use of different types of electrolytes as a means to generate the electric field, such as aprotic organic solvents (e.g. propylene carbonate (PC)), ionic liquids (e.g. diethylmethyl(2-methoxyethyl)ammonium bis(trifluoromethylsulfonyl)imide (DEME-TFSI)) or other electrolytes (e.g. LiPF_6 -ethylene carbonate or KClO_4 -polyethylene oxide).⁵²

The essence of electrolyte-gating is to exploit the formation of the “electric double layer” (EDL) to generate high electric fields. EDL can be understood as the solid-liquid capacitor formed between a solid electrode and dissolved ions in an ionic medium (electrolyte) which acts as a dielectric.¹¹⁸ As shown in Figure **1.9**, electrode polarization results in migration, and consequently ionic (counter-ions and co-ions) and solvent species are accumulated along the electrode surface at the electrolyte/electrode interface forming the EDL. The key aspect of electrolyte gating is the nanometer-scale thickness of the formed EDL, resulting in a large specific capacitance. Consequently, reasonably higher electric fields (of the order of hundreds of MV/cm) can be achieved upon applying a few volts.^{119–121}

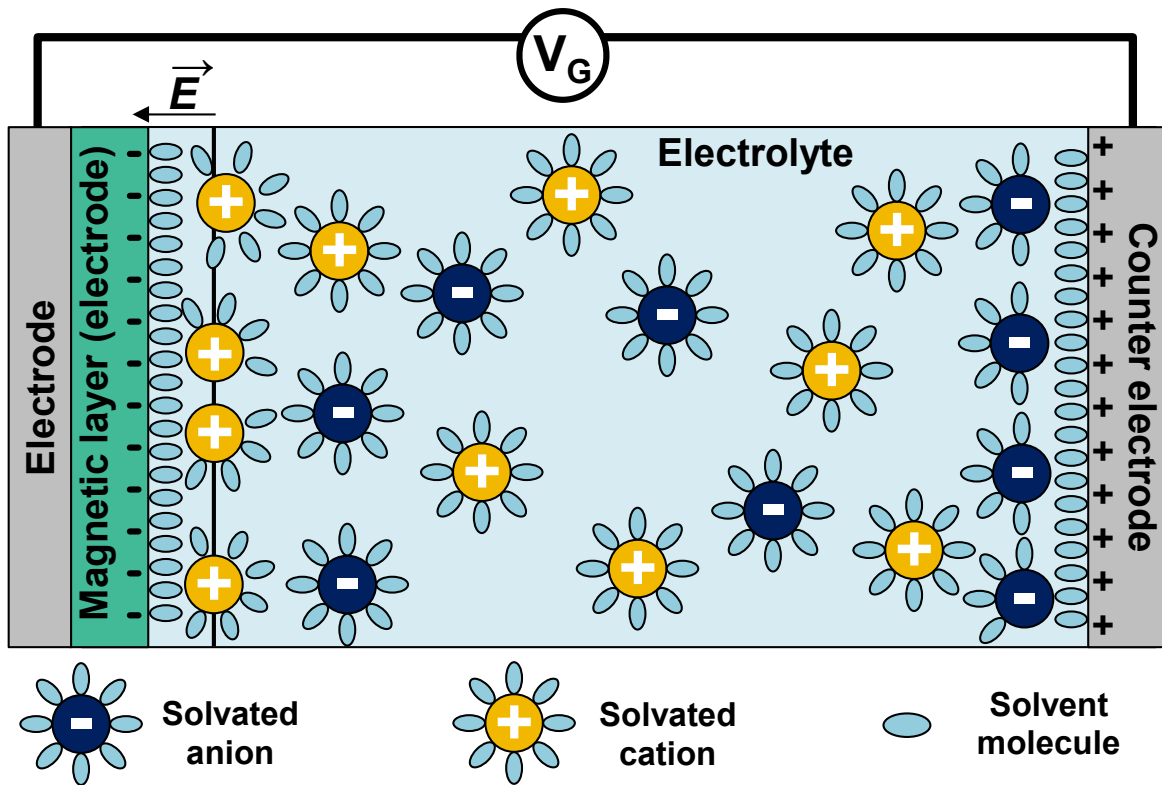


Figure 1.9. Scheme of the capacitor-like geometry using electrolyte-gating as a strategy to generate the electric field. In this configuration, the electric double layer of the solvated ions in the electrolyte creates the electric field at the magnetic layer/electrolyte interface.

Although all-solid-state ME actuation is preferred in most applications, liquid-electrolyte gating ME actuation is rapidly expanding and gaining interest due to its important advantages. First, liquid electrolytes exhibit higher ion mobility compared to solid electrolytes, which promotes the ion intercalation. Moreover, in all-solid-state devices, the electric field propagates through the entire thickness of the dielectric layer while in electrolyte-gating the E-field is confined at the electrolyte/magnetic layer interface. As a result, larger values of electric field are obtained at lower voltages in solid/liquid configuration and, hence, with lower energy consumption.⁵¹ Finally, liquid electrolytes are very much convenient for the E-field actuation of high S/V ratio materials (like mesoporous alloys) since the electrolyte can penetrate in the material and consistently wet the surface of the pore walls. The electrolyte/magnetic interface is greatly maximized and, thus, charge accumulation, redox and magneto-ionics effects can be enhanced. Unfortunately, electrolyte gating is less compatible with the existing production platform of solid-state electronics.

1.5. Interfacial nature of magnetoelectric effects

As explained in the preceding sections, the ME coupling existing in all the different mechanisms has an interfacial origin since the ME interface plays a key role in the response of the magnetic material to an external electrical stimulus. In the case of strain-mediated ME coupling, the quality of the interface between the piezoelectric and the ferromagnetic layers is essential for the propagation of the strain. ME effects via charge accumulation is a surface or near-surface effect limited by the Thomas-Fermi screening length, and thus this mechanism is mainly observable in ultrathin films. Moreover, the dielectric layer employed for generating the electric field is crucial since charges are concentrated at the interface of the dielectric/magnetic heterostructure. Conversely, magneto-ionic effects are not restricted to ultra-thin films, but the interface between the magnetic layer and the adjacent ion reservoir material is crucial for promoting ion diffusion, and thus, changes in the oxidation state of the elements in the magnetic layer. Finally, the ME effect via surface redox reactions is mainly ruled by the interface between the magnetic materials and the aqueous alkaline electrolyte.

As can be gleaned from the above, large S/V ratio materials (nanoporous or roughened materials, etc.) are expected to increase the magnitude of the ME effect. In this framework, porous materials are excellent candidates since they are known as prime examples of high S/V ratio materials.

1.5.1. Magnetoelectric effects in porous materials

Despite the interfacial nature of ME effects, the use of porous materials in this field is still in its infancy. In this regard, the ME response of several mesoporous materials made of metals, metal alloys, metal/metal oxide or all-oxide systems has been studied. Additionally, in most of these studies electrolyte-gating is utilized since it is the most suitable approach to create an effective E-field in porous materials.^{77,109,122–124} Liquid electrolytes can eventually penetrate throughout the whole 3D porous structure of the mesoporous materials, avoiding pinholes and thus leading to exacerbated ME effects.

Among nanoporous metal and metallic alloy systems, first investigations demonstrated the manipulation of the magnetic properties in nanoporous Co–Pd,¹²³ Pd–Ni¹²⁵ and Fe–Au alloys.¹²² In these studies, the ME response was attributed to strain (pressure) induced by the charge accumulation at the nanocrystallites of the porous framework. Similarly, recent studies have reported changes of H_C in relatively thick films (0.5–1 μm) of various mesoporous Cu–Ni⁷⁷ and Fe–Cu¹²⁴ alloys. The H_C values of mesoporous Cu–Ni and Fe–Cu films could be reduced by 25% and 32%, respectively, by applying an external voltage using an anhydrous electrolyte as dielectric. Such reduction of H_C was ascribed to variation in the MAE stemming from the surface charge accumulation (as demonstrated by *ab-initio* calculations⁷⁷). Remarkably, Quintana et al. subjected fully dense Cu–Ni films with same thickness and composition to the same experiment. In that case, negligible changes in H_C were observed. This result corroborated the key role of the porosity in the observed ME effects. Besides anhydrous electrolytes, aqueous alkaline electrolytes can be used to induce reduction-oxidation electrochemical reactions at the surface of porous metal or metal/metal oxide materials. For instance, the superparamagnetic state can be tuned in nanoporous Co–Pd alloys through electrically gating in KOH electrolyte, where the electrochemical hydrogen sorption enhances Ruderman–Kittel–Kasuya–Yoshida type interaction in the Pd matrix.¹²⁶ Similar studies performed in nanoporous $\gamma\text{-Fe}_2\text{O}_3\text{-Pt}$ electrode have reported variations of 4.2% in M_S .⁹⁷

Composite porous materials containing metal oxide and metallic phases have been also investigated. For example, large changes in H_C and M_S were achieved in nanoporous Fe–Cu/FeO_x/CuO_x films by applying an external voltage and using an anhydrous electrolyte. In this work, voltage-induced rearrangements in the structural oxygen (i.e. oxygen from the material itself) caused structural transformations in the metallic counterpart, resulting in H_C and M_S variations of 100% and 20 %, respectively.¹⁰⁹

Electrical control of magnetism in all-oxide porous materials (e.g. CoFe₃O₄, LiFe₅O₈, NiFe₂O₄, etc.) has been also explored.^{114,127–129} Reversible electric-field manipulation of magnetism has been successfully performed in nanoporous CoFe₃O₄ by magneto-ionic means.¹²⁸ The authors demonstrated that by applying an external voltage to the films, partial reduction of the metal ions to zero valence state is achieved due to oxygen ion migration to the surface and eventually out of the films. Interestingly, variations up to

28% and 15% in H_c and M_s , respectively, were achieved in these nanoporous films, whereas analogous films with much lower porosity showed smaller changes, i.e., 2% in H_c and 4% in M_s .

ME actuation in porous materials is an emerging field which has been progressively expanding during the last decade. The increased number of publications in the field have demonstrated that the presence of porosity allows to boost the electrical control of magnetism. Actually, ME porous materials have a huge potential to be implemented in energy-efficient applications: spintronic devices, energy harvesters and computing platforms. Despite the exciting new results, several open challenges need to be overcome before the use of porous ME systems becomes widespread. One of them is the need of liquid electrolytes to generate the electric field, which is the most frequently used approach in the abovementioned studies. For marketable devices, liquid electrolytes should be replaced by solid dielectric materials, such as FE nanolayers or an ionic conductor. For example, GdO_x , HfO_x are solid dielectric materials which can be fabricated by atomic layer deposition (ALD), resulting in a conformal nanocoating of the porous structure of the ME material. In fact, magneto-ionic effects have been recently observed in nanoporous cobalt ferrite coated with HfO_2 .¹²⁹ An enhanced magnetic response was observed compared to uncoated films. However, a liquid electrolyte was still used to avoid the occurrence of electric pinholes in the HfO_2 layer.

1.6. Porous and patterned materials by electrodeposition

1.6.1. Fundamentals of electrodeposition

Electrodeposition is one of the most useful methods to produce a broad spectrum of materials (metals, alloys, oxides and even polymers), with electrically conducting or semiconducting properties, in a variety of different shapes and forms (thin and thick films, nanowires, nanorods, three-dimensional micro-/nanostructures, etc.) Contrary to most fabrication techniques (physical vapor deposition, atomic layer deposition, vacuum hot-pressing sintering, etc.), electrodeposition offers unique advantages: simple setup, no

vacuum system required, fast growth rate, cost-effectiveness and industrial scalability.¹³⁰⁻

132

Electrodeposition is an electrochemical process by which the deposition of a target material occurs onto a conductive substrate by means of reduction-oxidation (redox) reactions. In cathodic electrodeposition, the electrochemical reduction of metal ions in an electrolyte takes place on the conductive substrate (also referred to as working electrode, WE) by the action of an external electric current. Besides the WE, either a counter electrode (CE) (in the two-electrode configuration) or a CE plus a reference electrode (RE) (in the three-electrode configuration) are required. Aqueous, organic, mixed aqueous-organic or molten salt-based electrolytes can be employed. More recently, ionic liquids and deep eutectic solvents have also gained much interest as solvents. In this section, water-based electrolytes (i.e., water plus compounds dissolved in it) are considered. Therefore, the minimum constituents for electrodeposition to take place are the electrolyte, two conductive electrodes and a power supply, which altogether constitute the electrochemical cell or, more precisely, the electrolytic cell.

As aforementioned, the reaction of interest in cathodic electrodeposition is a reduction, wherein the WE is negatively charged, acting as the cathode (**Figure 1.10**) and providing the electrons required to discharge the metal ions into their metallic form:



Obviously, Eq. 1.1 is a simplified version of what is actually occurring in electrodeposition since metal ions coming from dissociated metal salts in water form metal complexes consisting of a central metal ion surrounded by molecules (like water molecules or some complexing species added on purpose) or ions (e.g. chloride).

The term 'electrolytic cell' implies that electrodeposition is not a reversible process. In order to have a non-spontaneous cell reaction to occur, an overpotential η (in V) needs to be applied:

$$\eta = E(I) - E_{rev} \quad (1.2)$$

where $E(l)$ is the applied potential at the WE resulting in a net current (l) flowing through the external circuit towards the WE, whereas E_{rev} is the reversible equilibrium potential or Nernst potential. When an overpotential exists, or has been set, we say that the electrode is 'polarized'. There are different types of polarization, namely charge transfer (CT), mass transfer (MT), reaction (Rx), and crystallization (Cryst). Therefore, the experimentally determined overpotential values are in fact the sum of these four contributing processes:

$$\eta = \eta_{CT} + \eta_{MT} + \eta_{Rx} + \eta_{Cryst} \quad (1.3)$$

For small η , the relation between l and η is linear. For $\eta \geq 100$ mV, the current depends exponentially on η as described by the Volmer-Butler equation. In this case, the charge transfer of the electroactive species is the rate-determining (slow) process. At even larger η values, the mass transfer of ions from the bulk of the electrolyte to the electrode surface becomes the limiting factor. The current reaches a limit referred to as limiting current density and denoted as i_L , which can be derived from the Fick's first law.¹³³

According to Faraday's laws of electrolysis, the current flow, time and equivalent weight of the metal can be related to the weight of the deposit. The first law states that the total mass of ions liberated in grams (deposited material) is proportional to the total electric charge. The second law states that the mass of the deposited material is proportional to its atomic weight and inversely proportional to its valency. Both laws are summarized as follows:

$$m = \left(\frac{Q \cdot M}{F \cdot z} \right) \quad (1.4)$$

where m is the mass of the deposited material (in g), Q is the total electric charge (in C), M is the molar mass (in g/mol), F is the Faraday's constant and z is the valence number of the ions. Nevertheless, Faraday's laws assume a current efficiency of 100%, i.e. other secondary reactions are not considered. However, during the electrodeposition process, a certain amount of the charge is often consumed by secondary reactions that occur in parallel with the metal deposition such as hydrogen evolution reaction (**Figure 1.10**), partial reduction of metal species or other secondary reaction (even non-electrolytic

reactions). Therefore, Faraday's laws are considered an approximation of the mass of the deposited material. The current efficiency is defined as the ratio between the total mass deposited and the theoretical value calculated from Faraday's laws.

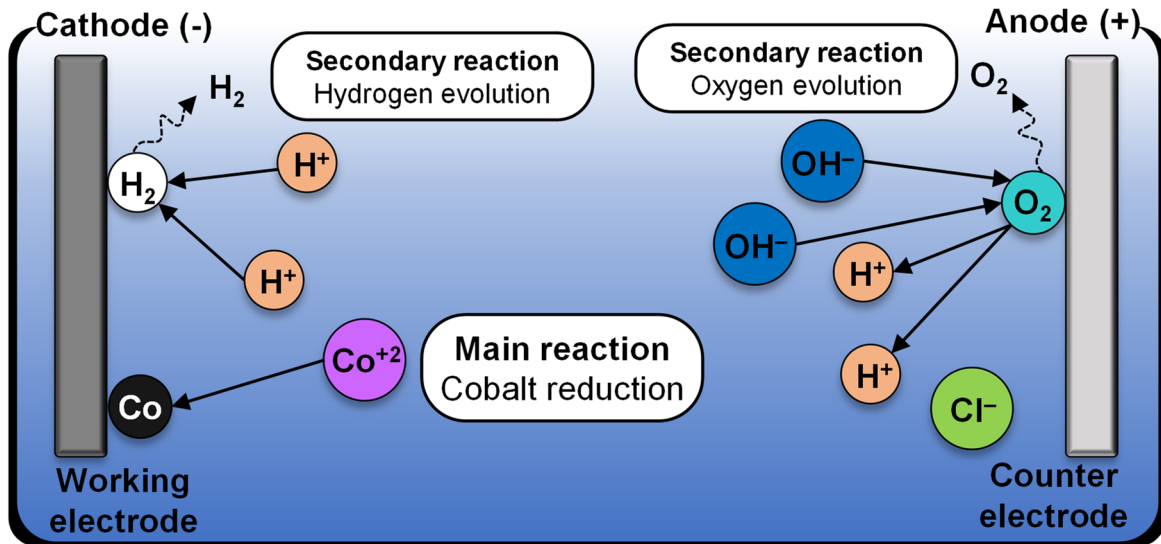


Figure 1.10. Schematic drawing of the electrochemical reactions occurring at the cathode (working electrode) and the anode (counter electrode) during cathodic electrodeposition.

Electrodeposition of more than one metal simultaneously (codeposition of metals) is pursued to grow binary, ternary or even quaternary alloys with superior or synergistic properties that are not achievable with single metals alone. For codeposition to happen, the electrolyte should contain the corresponding metal ions and their deposition potentials should be sufficiently close to each other. In practice, this means that many metals cannot be simultaneously electroplated because of the large difference in their deposition potentials. However, if the difference is acceptable, complexing agents (e.g. carboxylic acids, aminoacids) can be added to the electrolyte to bring the deposition potentials further close to one another. Once this is secured, the electrolyte composition, the concentration of electroactive species, temperature and pH, together with the applied electrodeposition parameters (deposition mode, potential, current density, stirring etc.), can be varied at will to tune the properties of the alloy (composition, morphology, microstructure and, in turn, their physical and physico-chemical properties).

The electrodeposition of a single metal or alloy onto a conductive substrate can be performed either potentiostatically or galvanostatically. In potentiostatic mode, the

potential between the WE the RE is kept constant, while the current density is recorded continuously. The overpotential is a key parameter in alloy electrodeposition. At low polarization, the more noble metal is preferentially deposited, whereas at higher polarization the less noble metal is preferentially discharged. If the relative proportion of the metals in the electrodeposited alloy is as expected on the basis of the equilibrium potentials of the metals against the solution, the deposition is termed 'normal'. When the less noble metal is preferentially deposited, the deposition is then referred to as 'anomalous' codeposition. Generally, the potentiostatic mode allows to tune the relative proportion of the metals in the deposited alloys or in multilayered structures by selectively adjusting the applied potential. In galvanostatic mode, a constant current is applied between the WE and the CE and the potential between the WE and RE is measured. In this mode, the surface area of the WE should be precisely known, which might be difficult when non-flat substrates (e.g. alumina membranes or e-beam patterned substrates) are used. In contrast to the potentiostatic mode, the galvanostatic mode offers a constant growth rate, allowing for a better control of the amount, and hence thickness, of deposited material by adjusting the deposition time. Moreover, since it does not necessarily involve a reference electrode (unless accurate monitoring of the potential is required), the galvanostatic mode is used preferably in industrial applications.

For certain applications, a composite deposit consisting of a metal (or an alloy) and a metal oxide might be desired. A particulate composite microstructure can be achieved by suspending micron- or nanosized metal oxide particles in the electrolyte. These particles can become engulfed or entrapped in the growing metallic deposit during electrodeposition.¹³⁴ In this case, research in the field is commonly oriented towards achieving a fine and uniform distribution of the filler within the coating. Alternatively, composites might grow from particle-free solutions under conditions favoring the formation of metal oxides on the electrode.¹³⁵

1.6.2. Methods for introducing porosity into electrodeposited materials

Porous metals and alloys have gained increased importance over the last decades due to their suitability to be utilized in a wealth of applications including sensing, heterogeneous catalysis, or energy conversion.^{136–139} Template electrosynthesis has been widely employed as an effective pathway to fabricate low-dimensional materials (nanoparticles, nanowires, nanotubes etc.) and, more recently, porous materials.¹⁴⁰ Compared to other wet chemistry approaches, electrodeposition yields the products attached to a substrate, which can be advantageous in, for example, electrocatalysis.¹⁴¹ The production of porous materials via electrodeposition is based on the use of hard and soft templates. The former directly serve as working electrodes whereas soft-templating relies on the action of compounds dissolved or present in the electrolyte. Depending on the nature of the parent template and the resulting pore size of the electrodeposited material, macroporous (with pore diameters beyond 50 nm), mesoporous (with pore diameters between 2 nm and 50 nm) and mixed macro/mesoporous materials can be obtained. Silica opal template, biological samples, mesoporous zeolites, and colloidal spheres can be used as hard templates to induce macro/meso-porosity in electrodeposited materials.^{142–144} Since these materials are insulating or low conductive, their prior metallization or attachment to an electrically-conducting surface is required. Regarding soft-template electrodeposition, the otherwise unwanted reduction of protons (i.e., hydrogen evolution) that accompanies metal ions discharge in aqueous electrolytes can be utilized, if sufficiently intensified, as a means to introduce porosity in the deposit. This method, referred to as 'hydrogen bubble dynamic template', produces macroporous deposits since the pore diameter is defined by the size of hydrogen bubbles (hundreds of micrometers). Alternatively, water-in-ionic-liquid or ionic-liquid-in-water microemulsions have been proposed as soft-template for electrodeposition of porous materials. This method benefits from the nanometer-size of the droplets (of ionic liquid or water) where the electrodeposition of the metal species only occurs at the water/ionic liquid interface, resulting in well-defined porous structure.^{145–147} In the case that smaller pores are targeted, ionic and non-ionic amphiphilic surfactants are added to

the electrolyte to serve as structure-directing agents.^{148–151} In the following, the two strategies utilized throughout this Thesis to endow the electrodeposited materials with macro- and mesoporosity are described.

1.6.2.1. Mesoporosity via micelle-assisted electrodeposition

Lyotropic liquid crystal (LLC) templating has been utilized in combination with electrodeposition to fabricate various mesoporous metals such as Pd, Co, Ni, Cu and their alloys.^{152–154} LLC is based on the self-assembly of amphiphilic (or amphiphatic) molecules in a solvent, which results in different LLC phases with regular arrays of pores ranging from 2 to 15 nm. Typically, LLC phases are obtained by dissolving high concentrations of surfactant, which can be ionic (e.g. hexadecyltrimethylammonium bromide, CTAB) or non-ionic (e.g. block-copolymers), in water. The formation of the different LLC phases depends mainly on the concentration of the surfactant and the temperature. At low concentrations, the amphiphilic molecules are just dissolved in the solvent; however, above a certain concentration (known as 'critical micelle concentration', c.m.c), the molecules tend to arrange forming micelles (with the hydrophilic head regions being in contact with the surrounding water molecules while sequestering the hydrophobic single-tail regions in the interior of the micelle). At higher concentration, such micelles self-organize forming cylindrical aggregates and these, in turn, arrange into a long-range hexagonal lattice referred to as hexagonal phase. Finally, at higher concentrations, the so-called 'lamellar phase' forms through the layered arrangement of the amphiphilic molecules.

The main drawback associated to the use of complex LLC phases as soft template is the viscosity of the solution. As the surfactant concentration increases, the electrolyte becomes more viscous, which prevents an efficient stirring of the electrolyte. Alternatively, several works have exploited the concept of micelle-assisted electrodeposition for the synthesis of mesoporous single metals and alloys. In these works, block-copolymers (BCPs) are employed at concentrations above c.m.c, but below the concentration threshold for complex LLC phases formation.^{77,155–163} Interestingly, the resulting average pore size can be conveniently tuned by employing BCPs with different molecular weights. In the micelle-assisted electrodeposition process, BCP micelles

spontaneously form in the electrolyte (Step 1, **Figure 1.11**). The metallic cations present in solution interact with the hydrophilic shell domain of the micelle. Upon negatively polarizing the WE, the entities migrate towards it (Step 2, **Figure 1.11**). Once they adsorb onto the WE, the cations are reduced (Step 3, **Figure 1.11**), resulting in the formation of a mesostructured solid after removing the BCP micelles (Step 4, **Figure 1.11**). Thus, the micelles act as structure-directing agent, where the interaction between the metal ions and the polymeric micelles is critical for the formation of a mesoporous structure. Among BCPs, the tri-block polyethylene oxide-polypropylene oxide-polyethylene oxide (PEO-PPO-PEO) with the BASF trademark name of Pluronic® is one of the most employed due to its structure-directing ability and greater stability.¹⁴³ The use of commercial diblock copolymers (e.g. polystyrene-poly(ethylene oxide), PS-*b*-PEO) or in-house synthesized BCPs have been reported in the literature, providing greater flexibility in the size of the pores.

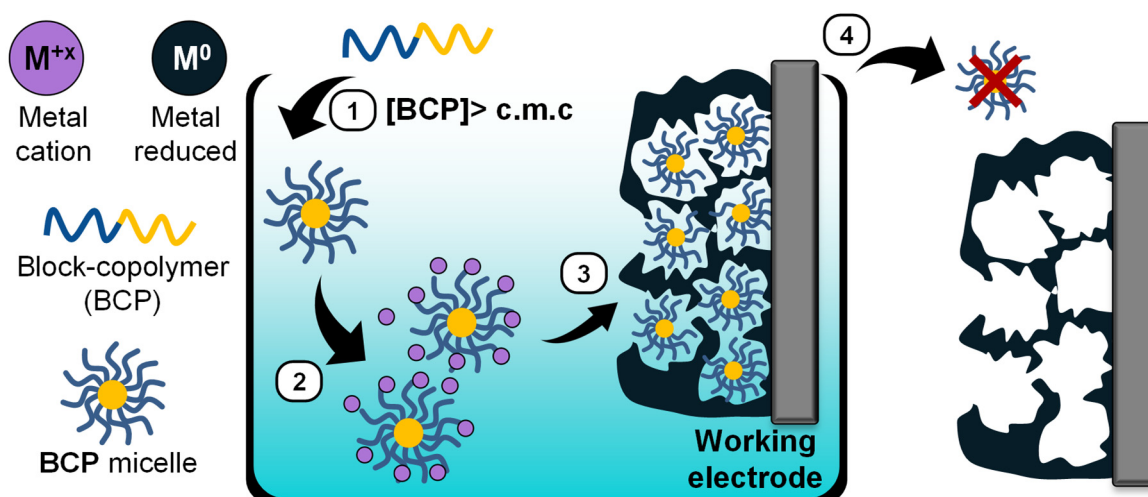


Figure 1.11. Scheme of the micelle-assisted electrodeposition process. Step 1: BCP micelles form spontaneously in the electrolyte. Step 2: the metal ions coordinate to the outer hydrophilic shell of the BCP micelles. Step 3: the metallic ions reduce at the cathode by virtue of the applied potential. Step 4: BCP micelles are removed, leaving the mesoporous metallic film behind.

1.6.2.2. Macroporosity via colloidal template-assisted electrodeposition

Colloidal lithography is a widely used technique which, combined with electrodeposition, allows to fabricate three-dimensional pseudo-ordered macroporous materials. In contrast to other lithography techniques, colloidal lithography is a straightforward and inexpensive technique since it does not involve neither a complex and expensive fabrication process nor a sophisticated lab equipment.^{164,165} Colloidal lithography relies on the self-assembly of colloidal particles (e.g. polystyrene (PS) beads) to create a pattern of colloidal crystals onto a substrate in a face-centered or hexagonal close-packed structure. Common deposition techniques used to create the colloidal template are dip-coating, sedimentation, electrophoretic deposition, evaporation, and spin coating.^{166,167}

Electrophoretic deposition (EPD) is an attractive option to create 3D assemblies of colloidal particles with a homogeneous coverage and a well-defined arrangement over a large area.¹⁶⁸⁻¹⁷⁰ As shown in **Figure 1.12**, EPD is a process by which the particles suspended in a solution are collected on a conductive substrate using an electric field. Deposition is performed in a two-electrode cell filled with a colloidal suspension of particles (e.g. PS beads) which are conveniently functionalized (e.g. PS-COOH, PS-NH₂ or PS-SO₄) to endow them with surface charge. When a potential is applied, the suspended particles are polarized and forced to move toward an electrode, thus forming a coherent deposit (**Figure 1.12a**). Typically, this process is followed by an additional step (sintering or curing) to obtain a fully dense coverage. Subsequently, the coated electrode can be used as WE for the electrodeposition of various metal and alloys (**Figure 1.12b**). In this step, the material grows within the voids or interstices existing between the particles. Finally, the selective removal of the latter results in a pseudo-ordered porous framework (**Figure 1.12b**). Electrodeposition possesses an important advantage over physical deposition methods like sputtering or evaporation since all the interstitial voids existing between the particles can be filled with the deposited material provided that the electrolyte is capable to penetrate down to the electrode surface. Conversely, in sputtering and evaporation, shadowing effects are typically encountered, which preclude the formation of a continuous network. Moreover, the porous structure obtained by

electrodeposition is a true cast of the colloidal crystal template where the dimension of the particles determines the pitch and pore size of the replica.

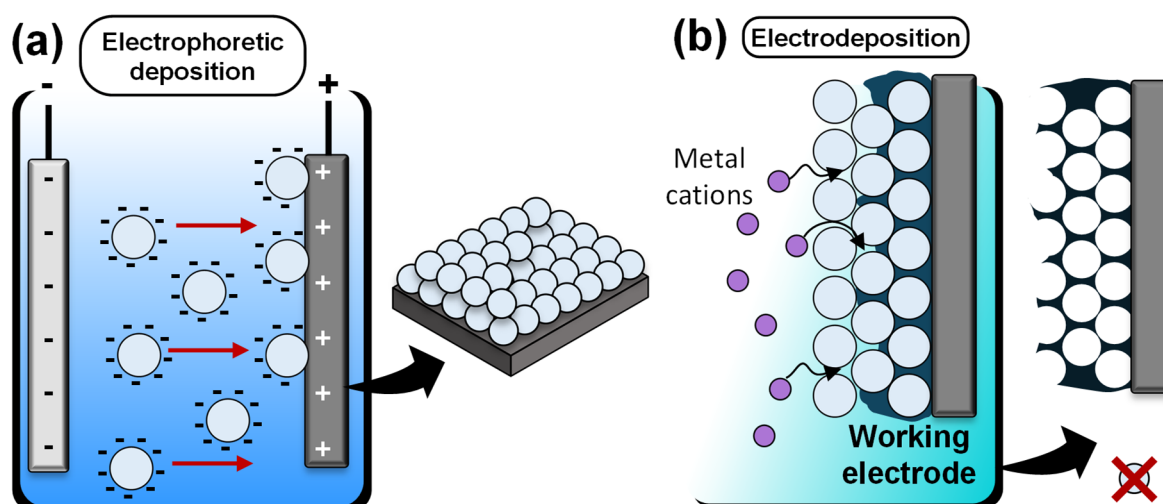


Figure 1.12. (a) Schematic drawing depicting the EPD deposition. By applying an electric field, polarized particles are forced to move towards the anode, resulting in the assembly of the particles onto the substrate. Subsequently, (b) the substrate coated with the particles is used as WE for the electrodeposition of metals and alloys. Finally, the spheres are selectively removed, leaving the pseudo-ordered macroporous film behind.

The combination of both, colloidal lithography and electrodeposition, is a versatile method since polymeric colloidal crystal templates are compatible with aqueous electrolytes in a wide range of depositions conditions. Macro-/mesoporous films of various metals,^{171,172} alloys,¹⁷³ oxides,¹⁷⁴ and polymers¹⁷⁵ with (electro)catalytic activity and superhydrophobic properties,^{176,177} have been successfully obtained by electrodeposition on colloidal crystal templates. Furthermore, the combination of micelle-assisted electrodeposition and colloidal templating can lead to hierarchically structured materials with exotic architectures (**Figure 1.13**), as it will be shown in the Results Section 5 of this Thesis.

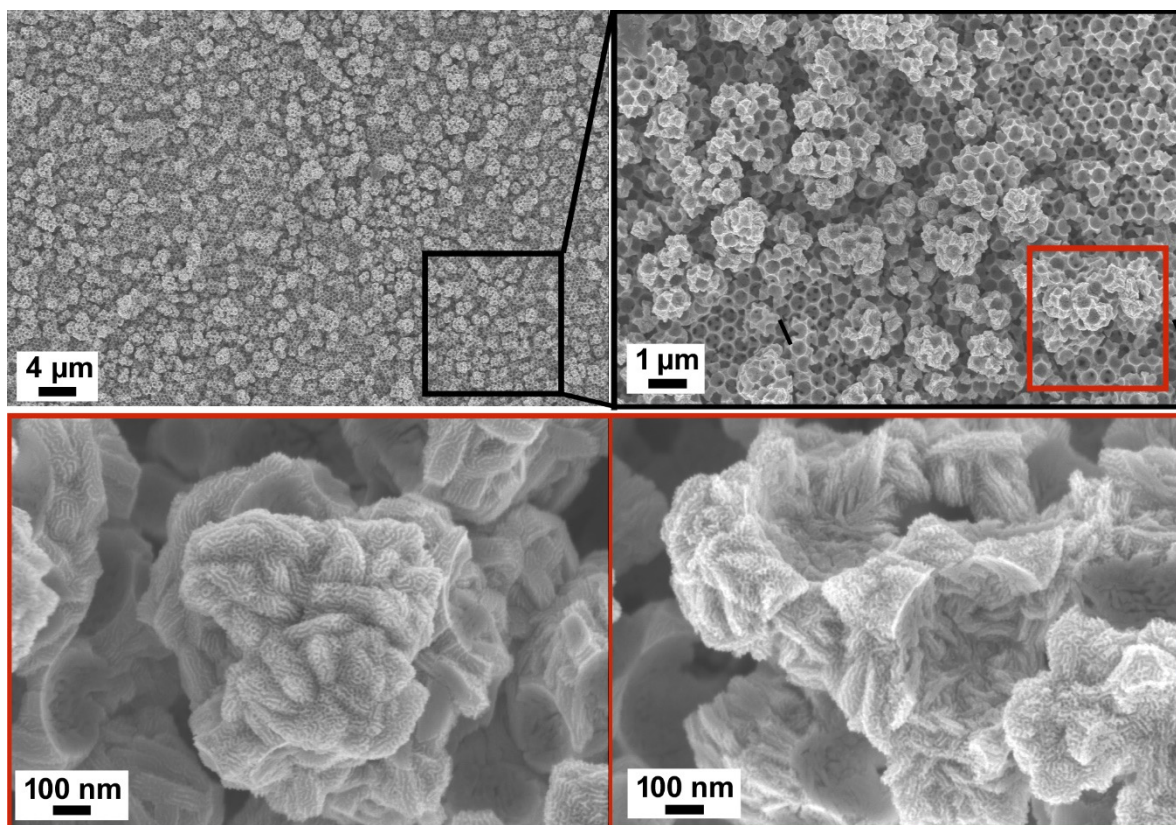


Figure 1.13. Low (top) and high (bottom) magnification field-emission scanning electron microscopy images of hierarchically porous Co-Pt films fabricated by micelle-assisted electrodeposition on colloidal crystal templated substrates.

1.6.3. Electrodeposition on photolithographed substrates

The combination of lithography and electroplating started in the early 1980s, under the name of LIGA, the German acronym for Lithographie, Galvanoformung and Abformung (Lithography, electroplating and molding).¹⁷⁸ This technique was a breakthrough in the microelectromechanical systems (MEMS) fabrication technology as it enabled the fabrication of 3D microstructures with high aspect ratios. As its name denotes, LIGA involves the following steps: lithography, electrodeposition and molding. Originally, lithography was performed using X-rays usually generated by a synchrotron source, which yielded high aspect ratio microstructures with great precision. However, the lack of access to a synchrotron source and, in turn, the associated high costs, triggered the development of UV lithography. UV lithography, also known as photolithography or optical lithography, employs ultraviolet radiation instead of X-rays to transfer a pattern from a mask to a photosensitive resist.^{179,180}

An example of UV-LIGA process is shown in **Figure 1.14**. First, a photoresist (negative or positive) is deposited onto the conductive substrate usually by spin-coating, which ensures the formation of very smooth and homogeneous resist films (**Figure 1.14a**). Second, a prebake step is performed to dry and stabilize the photoresist. Then, the photoresist layer is exposed to UV light through a mask where, depending on the photoresist type (negative or positive), the pattern transmitted to the photoresist is a direct or inverse image of the mask (**Figure 1.14b**). After exposure, a selected developer is used to remove the exposed areas (positive photoresist) or unexposed areas (negative photoresist) (**Figure 1.14c**). In the case of a negative photoresist, the areas exposed to UV become cross-linked and, therefore, they remain on the substrate after the development step. As a result, the inverse pattern of the mask is obtained (**Figure 1.14ci**). On the contrary, the exposed areas of a positive photoresist to UV become more soluble and washed away with the developer solvent, yielding an identical copy of the mask pattern (**Figure 1.14cii**). The latter is the most commonly employed in microsystems fabrication. Subsequently, electrodeposition is performed into the patterned areas by using the photolithographed substrates as WE (provided that the bottom of the cavities is conductive). Finally, the photoresist is stripped commonly with mild organic solvents (e.g. acetone), obtaining well-defined electrodeposited microstructures (**Figure 1.14d**).

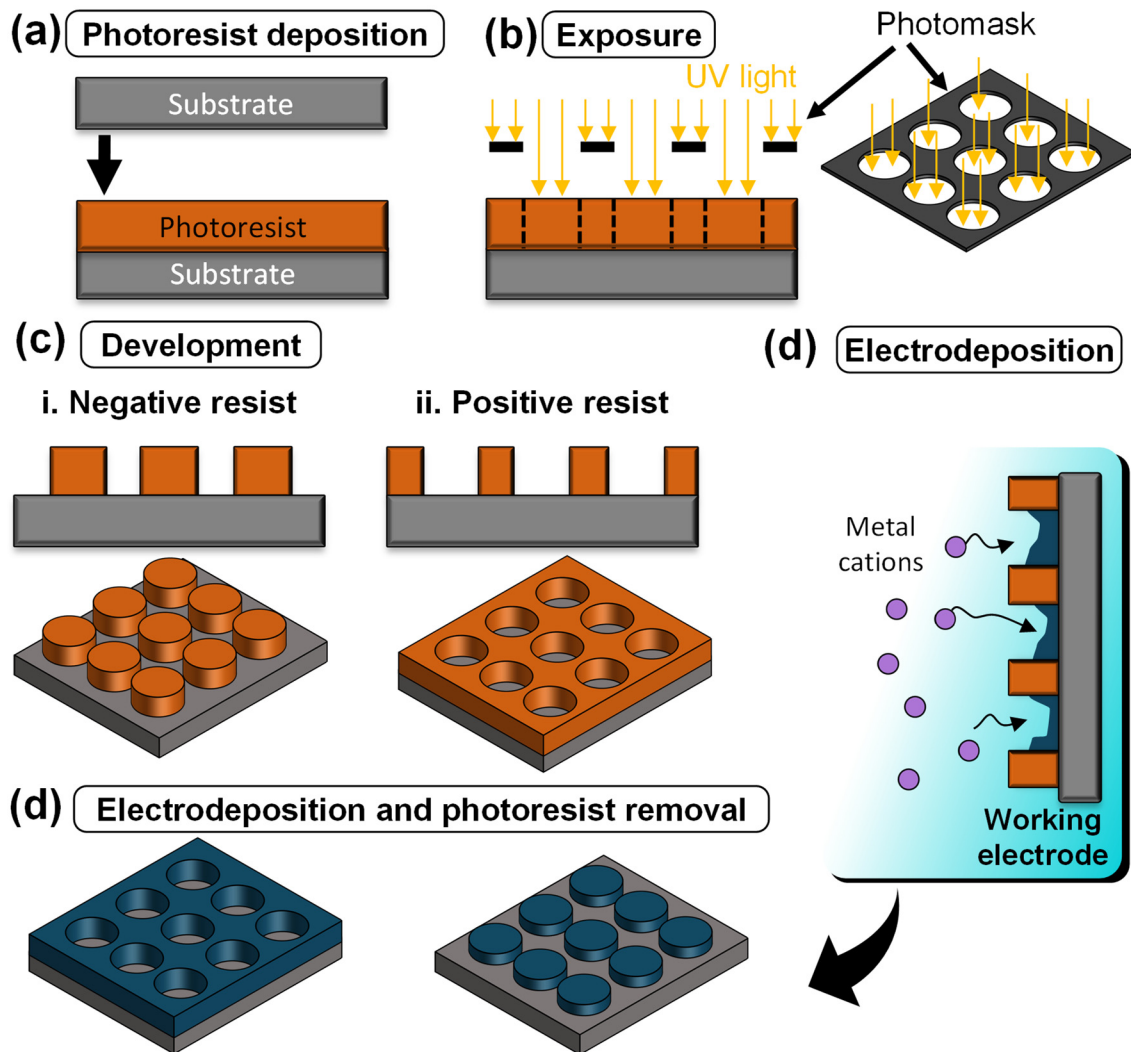


Figure 1.14. Schematic representation of UV-LIGA process. (a) A layer of photoresist is spin-coated on a conductive substrate. (b) The photoresist is exposed to UV radiation through a photomask which has the desired patterns to transfer. (c) The substrate with the photoresist is soaked in a developer which removes (i) the non-exposed areas in the case of negative resist or (ii) the exposed areas in the case of positive resist. (d) The patterned areas are used as templates for the electrodeposition of metallic, polymeric, semiconductor or composite materials, followed by the removal of the photoresist.

The combination of both, electrodeposition and optical lithography, is one of the most effective bottom-up fabrication techniques. Photolithography allows the manufacture of well-defined shapes and geometries with high aspect ratio, while electrodeposition enables the synthesis of a wide variety of materials, including metals, alloys, semiconductors, and even polymers. Together, they offer the possibility of fabricating multiple types of micro/nano-structures (e.g. wires, stripes, disks, cylinders, cubes, rods

or more complex structures) with variable compositions such as Cu,¹⁸¹ Co–Ni,¹⁸² Au¹⁸³ and Ni.^{184,185} In addition, both techniques are compatible with the approaches to introduce porosity in the deposits described above. Therefore, the production of arrays of porous micro-/nanostructures is in principle feasible. More recently, two-photon and even multi-photon direct laser writing has been used to pattern substrates, giving rise to 3D structures like helices or springs with resolutions from a few microns to the sub-micron range.^{186,187}

Aside from photolithography, electrodeposition has also been combined with other lithographic techniques such as electron-beam lithography (EBL) –to produce arrays of nanometer-sized motifs–, interference lithography and electrochemical lithography (EL) for the fabrication of miniaturized components (e.g. integrated circuits, biomedical devices, data storage devices and sensors).¹⁸⁸

1.7. The Co–Pt system

Cobalt is a transition metal with ferromagnetic properties known as one of the three room-temperature ferromagnets. Co mainly crystallizes in the face-centered cubic (fcc) and hexagonal close-packed (hcp) structures.^{189,190} The latter is preferred in permanent magnetic applications owing to its intrinsic uniaxial anisotropy. Co-based alloys have been extensively investigated due to their excellent magnetic properties, corrosion resistance, high temperature resistance and wear resistance. Among various Co-based systems, Co–Pt alloys have gained interest in the field of ultra-high-density magnetic recording because of their high magnetic anisotropy, chemical stability, and large coercivity (particularly in the tetragonal phase).^{191,192} Besides patterned magnetic recording media applications, Co–Pt has also been studied for electrocatalytic purposes. Interestingly, Co–Pt alloys are structurally more stable than other platinum alloys (with Ni, Fe or V) due to the higher mutual solubility.^{193,194} For this reason, owing to its remarkable electrocatalytic activity and durability, Co–Pt has been recognized as one of the most efficient systems for oxygen reduction reaction (ORR) among Pt-based bimetallic catalysts.^{145,195–198}

Cobalt-platinum system forms a solid solution from pure hcp cobalt to pure fcc platinum with an order/disorder transformation.^{199,200} According to the phase diagram (**Figure 1.15**), the alloy exists in three forms, namely A1 (fcc), L1₀ (fct) and L1₂ (fcc). At high temperatures, the Co–Pt alloy exists in the A1 phase, while at specific atomic compositions and for low temperatures, it crystallizes in the L1₀ and L1₂ phases. As aforementioned, Co–Pt alloys are of major interest owing to their magnetic properties which, in turn, depend on the relative amount between Co and Pt. For example, the intermetallic Co₃Pt compound exhibits perpendicular magnetic anisotropy.^{201–203} Meanwhile, equiatomic Co–Pt alloy can undergo a structural phase transition from A1-disordered to L1₀-ordered phase. L1₀-ordered Co–Pt alloy exhibits strong magneto-crystalline anisotropy ($K_u = 4.9 \text{ MJ/m}^3$) which results in large coercivity values.^{204–206} In general, as-synthesized equiatomic Co–Pt possesses the magnetically soft disordered A1 phase. For this reason, high-temperature deposition or post-deposition annealing is typically required to induce a structural transformation from the A1 to L1₀ phase, which has been extensively investigated in the literature.^{28,30,207–210}

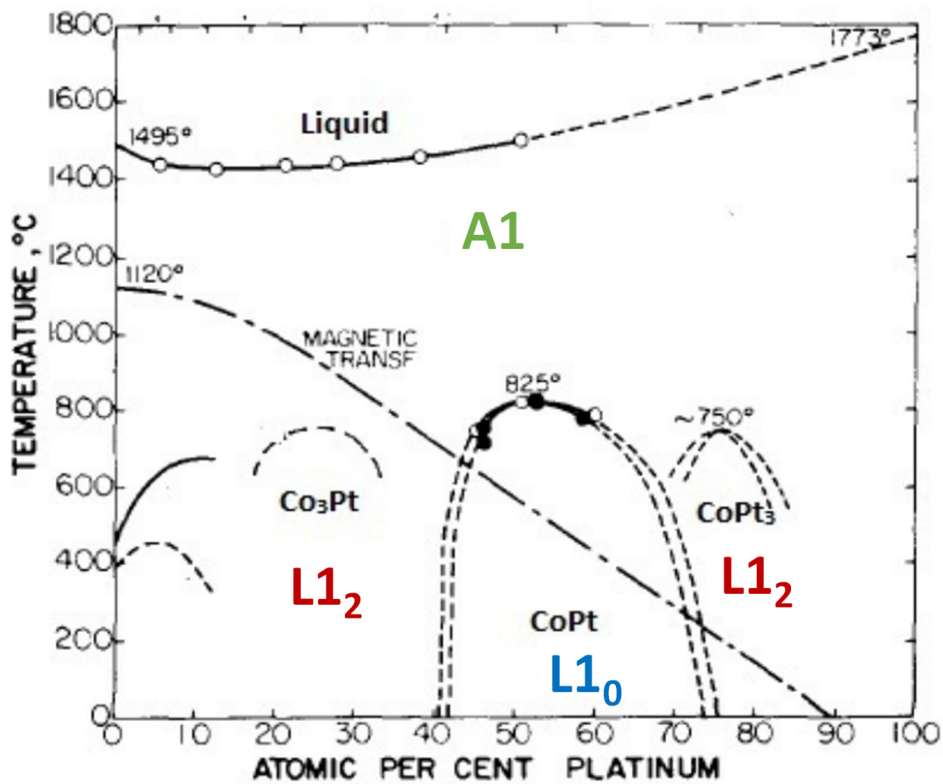


Figure 1.15. Equilibrium phase diagram of cobalt-platinum. Figure adapted from reference 211.

So far, several techniques have been utilized for the deposition of Co–Pt based materials in thin film form. The most commonly used are sputtering,^{212,213} molecular beam epitaxy,^{214,215} electron beam lithography,²⁰³ and electrodeposition.^{28,216,217}

Compared to vacuum-based fabrication methods, electrodeposition offers several advantages (high deposition rates under optimized conditions, low equipment cost, scalability to large substrates and ability to grow the material inside the narrow cavities of templates – i.e., for the growth of nanowires) which contribute to the facile integration of the Co–Pt system in technological applications.¹³² Co–Pt electrodeposition has been demonstrated from a variety of baths. Generally, electrolytes for Co–Pt electrodeposition include Co^{2+} ions (as chloride, sulfate or sulfamate salts) as the source of cobalt and Pt^{2+} or Pt^{4+} ions (dinitrodiammine platinum (II) or hexachloroplatinate salts) as the source of platinum.^{217–222} Representative electrolytes employed for Co–Pt electrodeposition are summarized in **Table 1.1**. According to the literature, most of the electrolytes based on hexachloroplatinate salts (e.g. Na_2PtCl_6 , H_2PtCl_6 or K_2PtCl_6) combined with either chloride or sulfate cobalt salts (e.g. CoCl_2 , CoSO_4) operate in the acidic range (**Table 1.1**). In addition, most of chloride-based electrolytes do not involve complexing agents, except for a few which employ sodium citrate (or citric acid) or ammonium chloride. Moreover, the formation of metal oxides (CoO , Co_3O_4 and PtO) has been frequently reported in deposits obtained from these electrolytes. The formation of metal oxide phases results either from the transformation of the corresponding as-deposited hydroxides or the residual oxygen remaining in the electrolyte.^{145,220,223} Although the formation of oxides is normally considered an issue in the electrodeposition community, the possibility of fabricating metal/metal oxide composite films can be an attractive option for certain applications (e.g. in magneto-ionics, as it will be shown in this Thesis). Besides chloride-based electrolytes, other widely studied electrolytes contain the dinitrodiammineplatinum complex ($\text{Pt}(\text{NH}_3)_2(\text{NO}_2)_2$) and sulfate or sulphamate cobalt salts (i.e., CoSO_4 , $\text{Co}(\text{NH}_2)_2(\text{SO}_3)_2$). In general, these electrolytes operate under mild alkaline or mild acid pH, and ammonium citrate is often added as complexing agent to bring the reduction potentials of Co and Pt near one another.

Table 1.1. Representative metal salts, additives and pH of electrolytes employed for Co–Pt electrodeposition as reported in the literature.

Metal salts	Additives	pH	Reference
CoCl₂ K₂PtCl₆	H ₃ BO ₄	4	224
CoCl₂ Na₂PtCl₆	Na ₃ C ₆ H ₅ O ₇ NH ₄ Cl H ₃ BO ₃	4.5	225
CoCl₂ PtCl₄	NaCl	2.5	226,227
CoSO₄ H₂PtCl₆	CH ₃ COOH	3.5	228
CoSO₄ PtCl₄	H ₃ BO ₃	3	229
CoSO₄ H₂PtCl₆	H ₃ BO ₃ MgSO ₄	-	30
Co(NH₂)₂(SO₃)₂ Pt(NH₃)₂(NO₂)₂	(NH ₄) ₂ C ₆ H ₆ O ₇ NH ₂ CH ₂ COOH	8	216
CoSO₄ Pt(NH₃)₂(NO₂)₂	(NH ₄) ₂ C ₆ H ₆ O ₇ NH ₂ CH ₂ COOH	5.2	230
CoSO₄ Pt(NH₃)₂(NO₂)₂	(NH ₄) ₂ C ₆ H ₆ O ₇ NH ₂ CH ₂ COOH CH ₃ (CH ₂) ₁₀ CH ₂ OSO ₃ Na	5.2	231
Co(NH₂)₂(SO₃)₂ Pt(NH₃)₂(NO₂)₂	(NH ₄) ₂ C ₆ H ₆ O ₇	7	26
Co(NH₂)₂(SO₃)₂ Pt(NH₃)₂(NO₂)₂	(NH ₄) ₂ C ₆ H ₆ O ₇	5	206
CoSO₄ Pt(NH₃)₂(NO₂)₂	(NH ₄) ₂ C ₆ H ₆ O ₇	8	232

Electrodeposition of Co–Pt micro/nanostructures has been the object of intensive research. A great variety of structures such as nanowires,^{216,224,228} nanoparticles,²²⁵ dot arrays,^{230,231} and multilayered structures,²³³ have been successfully electrodeposited, as well as most common ultra-thick films,^{26,206,226} and thin films.^{28,217} Nevertheless, whilst electroplated Co–Pt micro/nanostructures have been widely explored due to their application in magnetic patterned media,²³⁴ the electrodeposition of porous Co–Pt based materials for applications different from electrocatalytic ones has been seldom addressed. The few studies available have reported on the direct electrodeposition of

mesoporous films²³⁵ or nanowires/rods into anodic alumina or polycarbonate membranes from microemulsions (water-in-oil or ionic-liquid-in water)^{145–147} or the electrodeposition of dense Co-rich nanowires followed by dealloying.²³⁶ So far, the electrodeposition of mesoporous Co–Pt based materials from micelle-assisted aqueous electrodeposition has not been reported. Likewise, the growth of pseudo-ordered macroporous Co–Pt on colloidal crystal templates has been seldom exploited, and only few publications have investigated the electrodeposition of Co and Pt macroporous films separately.¹⁷¹

Bibliography

1. https://ec.europa.eu/clima/policies/strategies/2020_en.
2. https://ec.europa.eu/clima/policies/strategies/2030_en.
3. Sabry Aly, M. M., Gao, M., Hills, G., Lee, C., Pitner, G., Shulaker, M. M., Wu, T. F., Asheghi, M., Bokor, J., Franchetti, F., Goodson, K. E., Kozyrak, C., Markov, I., Olukotun, K., Pileggi, L., Pop, E., Rabaey, J., Re, C., Wong, H.-S. P. & Mitra, S. Energy-efficient abundant-data computing: The n3xt 1,000x. *Computer*. **48**, 24–33 (2015).
4. Garimella, S. V., Fleischer, A. S., Murthy, J. Y., Keshavarzi, A., Prasher, R., Patel, C., Bhavnani, S. H., Venkatasubramanian, R., Mahajan, R., Joshi, Y., Sammakia, B., Myers, B. A., Chorosinski, L., Baelmans, M., Sathyamurthy, P. & Raad, P. E. Thermal challenges in next-generation electronic systems. *IEEE Trans. Components Packag. Technol.* **31**, 801–815 (2008).
5. Pop, E., Sinha, S. & Goodson, K. E. Heat generation and transport in nanometer-scale transistors. *Proc. IEEE* **94**, 1587–1601 (2006).
6. Krishnan, S., Garimella, S. V., Chrysler, G. M. & Mahajan, R. V. Towards a thermal moore's law. *IEEE Trans. Adv. Packag.* **30**, 462–474 (2007).
7. Chu, R. C., Simons, R. E., Ellsworth, M. J., Schmidt, R. R. & Cozzolino, V. Review of cooling technologies for computer products. *IEEE Trans. Device Mater. Reliab.* **4**, 568–585 (2004).
8. Dayarathna, M., Wen, Y. & Fan, R. Data center energy consumption modeling: a

- survey. *IEEE Commun. Surv. Tutorials* **18**, 732–794 (2016).
9. Jones, N. How to stop data centres from gobbling up the world's electricity. *Nature* **561**, 163–166 (2018).
 10. Arman Shehabi, Sarah Josephine Smith, Dale A Sartor, Richard E Brown, Magnus Herrlin, Jonathan G Koomey, Eric R Masanet, Nathaniel Horner, Inês Lima Azevedo & William Lintner. *United States Data Center Energy Usage Report | Energy Technologies Area*. (2016). at <<https://eta.lbl.gov/publications/united-states-data-center-energy>>
 11. Moser, A., Takano, K., Margulies, D. T., Albrecht, M., Sonobe, Y., Ikeda, Y., Sun, S. & Fullerton, E. E. Magnetic recording: advancing into the future. *J. Phys. D. Appl. Phys.* **35**, R157–R167 (2002).
 12. Dieny, B., Sousa, R. C., Herault, J., Papisoi, C., Prenat, G., Ebels, U., Houssameddine, D., Rodmacq, B., Auffret, S., Buda-Prejbeanu, L. D., Cyrille, M. C., Delaet, B., Redon, O., Ducruet, C., Nozieres, J.-P. & Prejbeanu, I. L. Spin-transfer effect and its use in spintronic components. *Int. J. Nanotechnol.* **7**, 591–614 (2010).
 13. Ralph, D. C., Cui, Y.-T., Liu, L. Q., Moriyama, T., Wang, C. & Buhrman, R. A. Spin-transfer torque in nanoscale magnetic devices. *Philos. Trans. R. Soc. A Math. Phys. Eng. Sci.* **369**, 3617–3630 (2011).
 14. Buschow, K. H. J. & de Boer, F. R. *Physics of Magnetism and Magnetic Materials*. (Springer US, 2003).
 15. Strnat, K. J. Modern permanent magnets for applications in electro-technology. *Proc. IEEE* **78**, 923–946 (1990).
 16. Kuhrt, C. Processing of permanent magnet materials based on rare earth-transition metal intermetallics. *Intermetallics* **3**, 255–263 (1995).
 17. Jiles, D. C. Recent advances and future directions in magnetic materials. *Acta Mater.* **51**, 5907–5939 (2003).
 18. Coey, J. M. D. Hard magnetic materials: A Perspective. *IEEE Trans. Magn.* **47**, 4671–4681 (2011).

19. Skomski, R., Kashyap, A. & Sellmyer, D. J. Finite-temperature anisotropy of PtCo magnets. *IEEE Trans. Magn.* **39**, 2917–2919 (2003).
20. Skomski, R. Nanomagnetism. *J. Phys. Condens. Matter* **15**, R841–R896 (2003).
21. Dempsey, N. M. in *Nanoscale Magn. Mater. Appl.* 661–683 (Springer US, 2009).
22. Kashyap, A., Skomski, R., Solanki, A. K., Xu, Y. F. & Sellmyer, D. J. Magnetism of L1₀ compounds with the composition MT (M=Rh, Pd, Pt, Ir and T=Mn, Fe, Co, Ni). *J. Appl. Phys.* **95**, 7480–7482 (2004).
23. Skomski, R.; Coey, J. M. D. *Permanent magnetism*. (Institute of Physics Publishing, 1999).
24. Ristau, R. A., Barmak, K., Lewis, L. H., Coffey, K. R. & Howard, J. K. On the relationship of high coercivity and L1₀ ordered phase in CoPt and FePt thin films. *J. Appl. Phys.* **86**, 4527–4533 (1999).
25. Cebollada, A., Weller, D., Sticht, J., Harp, G. R., Farrow, R. F. C., Marks, R. F., Savoy, R. & Scott, J. C. Enhanced magneto-optical Kerr effect in spontaneously ordered FePt alloys: Quantitative agreement between theory and experiment. *Phys. Rev. B* **50**, 3419–3422 (1994).
26. Oniku, O. D., Qi, B. & Arnold, D. P. Electroplated thick-film cobalt platinum permanent magnets. *J. Magn. Magn. Mater.* **416**, 417–428 (2016).
27. Berkh, O., Rosenberg, Y., Shacham-Diamand, Y. & Gileadi, E. Electrodeposited Near-Equiatomic CoPt Thick Films. *Electrochem. Solid-State Lett.* **11**, D38–D41 (2008).
28. Wang, F., Hosoiri, K., Doi, S., Okamoto, N., Kuzushima, T., Totsuka, T. & Watanabe, T. Nanostructured L1₀ Co–Pt thin films by an electrodeposition process. *Electrochem. commun.* **6**, 1149–1152 (2004).
29. Kang, S., Shi, S., Jia, Z., Thompson, G. B., Nikles, D. E., Harrell, J. W., Li, D., Poudyal, N., Nandwana, V. & Liu, J. P. Microstructures and magnetic alignment of L1₀ FePt nanoparticles. *J. Appl. Phys.* **101**, 09J113 (2007).
30. Yasui, N., Imada, A. & Den, T. Electrodeposition of (001) oriented CoPt L1₀ columns

- into anodic alumina films. *Appl. Phys. Lett.* **83**, 3347–3349 (2003).
31. Hannour, A., Bardotti, L., Prével, B., Tournus, F., Mailly, D., Bucher, J.-P. & Nafidi, A. Nanostructured L1₀-CoPt dot arrays with perpendicular magnetic anisotropy. *Mater. Lett.* **193**, 108–111 (2017).
 32. Custers, J. F. H. & Rathenau, G. W. Recrystallization in rolled nickel-iron. *Physica* **8**, IN2-1179 (1941).
 33. Krause, R. F. & Cullity, B. D. Formation of uniaxial magnetic anisotropy in nickel by plastic deformation. *J. Appl. Phys.* **39**, 5532–5537 (1968).
 34. Cullity, B. D. & Graham, C. D. *Introduction to Magnetic Materials*. (John Wiley & Sons, Inc., 2008).
 35. Mikhaylovskiy, R. V., Hendry, E., Secchi, A., Mentink, J. H., Eckstein, M., Wu, A., Pisarev, R. V., Kruglyak, V. V., Katsnelson, M. I., Rasing, T. & Kimel, A. V. Ultrafast optical modification of exchange interactions in iron oxides. *Nat. Commun.* **6**, 8190 (2015).
 36. Kimel, A. V., Kirilyuk, A., Tsvetkov, A., Pisarev, R. V. & Rasing, T. Laser-induced ultrafast spin reorientation in the antiferromagnet TmFeO₃. *Nature* **429**, 850–853 (2004).
 37. Beaurepaire, E., Merle, J.-C., Daunois, A. & Bigot, J.-Y. Ultrafast spin dynamics in ferromagnetic nickel. *Phys. Rev. Lett.* **76**, 4250–4253 (1996).
 38. Thiele, J.-U., Buess, M. & Back, C. H. Spin dynamics of the antiferromagnetic-to-ferromagnetic phase transition in FeRh on a sub-picosecond time scale. *Appl. Phys. Lett.* **85**, 2857–2859 (2004).
 39. Ju, G., Hohlfeld, J., Bergman, B., van de Veerdonk, R. J. M., Mryasov, O. N., Kim, J.-Y., Wu, X., Weller, D. & Koopmans, B. Ultrafast generation of ferromagnetic order via a laser-induced phase transformation in FeRh thin films. *Phys. Rev. Lett.* **93**, 197403 (2004).
 40. Stanciu, C. D., Hansteen, F., Kimel, A. V., Kirilyuk, A., Tsukamoto, A., Itoh, A. & Rasing, T. All-optical magnetic recording with circularly polarized light. *Phys. Rev.*

- Lett.* **99**, 047601 (2007).
41. Kirilyuk, A., Kimel, A. V. & Rasing, T. Laser-induced magnetization dynamics and reversal in ferrimagnetic alloys. *Reports Prog. Phys.* **76**, 026501 (2013).
 42. Martín-González, M. S., Briones, F., García-Martín, J. M., Montserrat, J., Vila, L., Faini, G., Testa, A. M., Fiorani, D. & Rohrmann, H. Nano-patterning of perpendicular magnetic recording media by low-energy implantation of chemically reactive ions. *J. Magn. Magn. Mater.* **322**, 2762–2768 (2010).
 43. Maziewski, A., Mazalski, P., Kurant, Z., Liedke, M. O., McCord, J., Fassbender, J., Ferré, J., Mougín, A., Wawro, A., Baczewski, L. T., Rogalev, A., Wilhelm, F. & Gemming, T. Tailoring of magnetism in Pt/Co/Pt ultrathin films by ion irradiation. *Phys. Rev. B* **85**, 054427 (2012).
 44. Devolder, T., Chappert, C., Mathet, V., Bernas, H., Chen, Y., Jamet, J. P. & Ferré, J. Magnetization reversal in irradiation-fabricated nanostructures. *J. Appl. Phys.* **87**, 8671–8681 (2000).
 45. Balk, A. L., Kim, K.-W., Pierce, D. T., Stiles, M. D., Unguris, J. & Stavis, S. M. Simultaneous control of the Dzyaloshinskii-Moriya interaction and magnetic anisotropy in nanomagnetic trilayers. *Phys. Rev. Lett.* **119**, 077205 (2017).
 46. Borschel, C., Messing, M. E., Borgström, M. T., Paschoal, W., Wallentin, J., Kumar, S., Mergenthaler, K., Deppert, K., Canali, C. M., Pettersson, H., Samuelson, L. & Ronning, C. A new route toward semiconductor nanospintronics: highly mn-doped GaAs nanowires realized by ion-implantation under dynamic annealing conditions. *Nano Lett.* **11**, 3935–3940 (2011).
 47. Brataas, A., Kent, A. D. & Ohno, H. Current-induced torques in magnetic materials. *Nat. Mater.* **11**, 372–381 (2012).
 48. Bhatti, S., Sbiaa, R., Hirohata, A., Ohno, H., Fukami, S. & Piramanayagam, S. N. Spintronics based random access memory: a review. *Mater. Today* **20**, 530–548 (2017).
 49. Schmid, H. Multi-ferroic magnetoelectrics. *Ferroelectrics* **162**, 317–338 (1994).

50. Hill, N. A. Why are there so few magnetic ferroelectrics? *J. Phys. Chem. B* **104**, 6694–6709 (2000).
51. Molinari, A., Hahn, H. & Kruk, R. Voltage-control of magnetism in all-solid-state and solid/liquid magnetoelectric composites. *Adv. Mater.* **31**, 1806662 (2019).
52. Navarro-Senent, C., Quintana, A., Menéndez, E., Pellicer, E. & Sort, J. Electrolyte-gated magnetoelectric actuation: phenomenology, materials, mechanisms, and prospective applications. *APL Mater.* **7**, 030701 (2019).
53. Suchtelen, J. van. Product properties: a new application. *Philips Res. Rep.* **27**, 28–37 (1972).
54. Bichurin, M. I., Petrov, V. M., Petrov, R. V., Kiliba, Y. V., Bukashev, F. I., Smirnov, A. Y. & Eliseev, D. N. Magnetolectric sensor of magnetic field. *Ferroelectrics* **280**, 199–202 (2002).
55. Srinivasan, G., Rasmussen, E. T., Levin, B. J. & Hayes, R. Magnetolectric effects in bilayers and multilayers of magnetostrictive and piezoelectric perovskite oxides. *Phys. Rev. B* **65**, 134402 (2002).
56. Laletsin, U., Padubnaya, N., Srinivasan, G. & DeVreugd, C. P. Frequency dependence of magnetolectric interactions in layered structures of ferromagnetic alloys and piezoelectric oxides. *Appl. Phys. A* **78**, 33–36 (2004).
57. Ryu, J., Carazo, A. V., Uchino, K. & Kim, H.-E. Magnetolectric properties in piezoelectric and magnetostrictive laminate composites. *Jpn. J. Appl. Phys.* **40**, 4948–4951 (2001).
58. Brivio, S., Petti, D., Bertacco, R. & Cezar, J. C. Electric field control of magnetic anisotropies and magnetic coercivity in Fe/BaTiO₃(001) heterostructures. *Appl. Phys. Lett.* **98**, 092505 (2011).
59. Venkataiah, G., Shirahata, Y., Itoh, M. & Taniyama, T. Manipulation of magnetic coercivity of Fe film in Fe/BaTiO₃ heterostructure by electric field. *Appl. Phys. Lett.* **99**, 102506 (2011).
60. Ghidini, M., Pellicelli, R., Prieto, J. L., Moya, X., Soussi, J., Briscoe, J., Dunn, S. &

- Mathur, N. D. Non-volatile electrically-driven repeatable magnetization reversal with no applied magnetic field. *Nat. Commun.* **4**, 1453 (2013).
61. Lei, N., Park, S., Lecoeur, P., Ravelosona, D., Chappert, C., Stelmakhovych, O. & Holý, V. Magnetization reversal assisted by the inverse piezoelectric effect in Co-Fe-B/ferroelectric multilayers. *Phys. Rev. B* **84**, 012404 (2011).
 62. Cherifi, R. O., Ivanovskaya, V., Phillips, L. C., Zobelli, A., Infante, I. C., Jacquet, E., Garcia, V., Fusil, S., Briddon, P. R., Guiblin, N., Mougín, A., Ünal, A. A., Kronast, F., Valencia, S., Dkhil, B., Barthélémy, A. & Bibes, M. Electric-field control of magnetic order above room temperature. *Nat. Mater.* **13**, 345–351 (2014).
 63. Ahn, C. H., Bhattacharya, A., Di Ventra, M., Eckstein, J. N., Frisbie, C. D., Gershenson, M. E., Goldman, A. M., Inoue, I. H., Mannhart, J., Millis, A. J., Morpurgo, A. F., Natelson, D. & Triscone, J.-M. Electrostatic modification of novel materials. *Rev. Mod. Phys.* **78**, 1185–1212 (2006).
 64. Singh, K. & Kaur, D. Quantification of charge-to-strain mediated interface coupling transfiguration in FE/FSMA multiferroic heterostructures. *J. Phys. D: Appl. Phys.* **49**, 035004 (2016).
 65. Nan, T., Zhou, Z., Liu, M., Yang, X., Gao, Y., Assaf, B. A., Lin, H., Velu, S., Wang, X., Luo, H., Chen, J., Akhtar, S., Hu, E., Rajiv, R., Krishnan, K., Sreedhar, S., Heiman, D., Howe, B. M., Brown, G. J. & Sun, N. X. Quantification of strain and charge co-mediated magnetoelectric coupling on ultra-thin Permalloy/PMN-PT interface. *Sci. Rep.* **4**, 3688 (2015).
 66. Regan, T. J., Ohldag, H., Stamm, C., Nolting, F., Lüning, J., Stöhr, J. & White, R. L. Chemical effects at metal/oxide interfaces studied by X-ray-absorption spectroscopy. *Phys. Rev. B* **64**, 214422 (2001).
 67. Bisht, M., Couet, S., Lazenka, V., Modarresi, H., Ruffer, R., Locquet, J.-P., Van Bael, M. J., Vantomme, A. & Temst, K. Electric Polarity-Dependent Modification of the Fe/BaTiO₃ Interface. *Adv. Mater. Interfaces* **3**, 1500433 (2016).
 68. Eerenstein, W., Wiora, M., Prieto, J. L., Scott, J. F. & Mathur, N. D. Giant sharp and persistent converse magnetoelectric effects in multiferroic epitaxial

- heterostructures. *Nat. Mater.* **6**, 348–351 (2007).
69. Ohno, H., Chiba, D., Matsukura, F., Omiya, T., Abe, E., Dietl, T., Ohno, Y. & Ohtani, K. Electric-field control of ferromagnetism. *Nature* **408**, 944–946 (2000).
 70. Chiba, D. Electrical manipulation of magnetization reversal in a ferromagnetic semiconductor. *Science*. **301**, 943–945 (2003).
 71. Liu, X., Lim, W. L., Titova, L. V., Dobrowolska, M., Furdyna, J. K., Kutrowski, M. & Wojtowicz, T. Perpendicular magnetization reversal, magnetic anisotropy, multistep spin switching, and domain nucleation and expansion in $\text{Ga}_{1-x}\text{Mn}_x\text{As}$ films. *J. Appl. Phys.* **98**, 063904 (2005).
 72. Tu, N. T., Hai, P. N., Anh, L. D. & Tanaka, M. Electrical control of ferromagnetism in the n-type ferromagnetic semiconductor (In,Fe)Sb with high Curie temperature. *Appl. Phys. Lett.* **112**, 122409 (2018).
 73. Xiu, F., Wang, Y., Kim, J., Hong, A., Tang, J., Jacob, A. P., Zou, J. & Wang, K. L. Electric-field-controlled ferromagnetism in high-Curie-temperature $\text{Mn}_{0.05}\text{Ge}_{0.95}$ quantum dots. *Nat. Mater.* **9**, 337–344 (2010).
 74. Yamada, Y., Ueno, K., Fukumura, T., Yuan, H. T., Shimotani, H., Iwasa, Y., Gu, L., Tsukimoto, S., Ikuhara, Y. & Kawasaki, M. Electrically induced ferromagnetism at room temperature in cobalt-doped titanium dioxide. *Science*. **332**, 1065–1067 (2011).
 75. Weisheit, M., Fahler, S., Marty, A., Souche, Y., Poinignon, C. & Givord, D. Electric field-induced modification of magnetism in thin-film ferromagnets. *Science*. **315**, 349–351 (2007).
 76. Zhang, H., Richter, M., Koepf, K., Opahle, I., Tasnádi, F. & Eschrig, H. Electric-field control of surface magnetic anisotropy: a density functional approach. *New J. Phys.* **11**, 043007 (2009).
 77. Quintana, A., Zhang, J., Isarain-Chávez, E., Menéndez, E., Cuadrado, R., Robles, R., Baró, M. D., Guerrero, M., Pané, S., Nelson, B. J., Müller, C. M., Ordejón, P., Nogués, J., Pellicer, E. & Sort, J. Voltage-induced coercivity reduction in nanoporous alloy

- films: a boost toward energy-efficient magnetic actuation. *Adv. Funct. Mater.* **27**, 1701904 (2017).
78. Duan, C.-G., Velev, J. P., Sabirianov, R. F., Zhu, Z., Chu, J., Jaswal, S. S. & Tsymbal, E. Y. Surface magnetoelectric effect in ferromagnetic metal films. *Phys. Rev. Lett.* **101**, 137201 (2008).
79. Nakamura, K., Shimabukuro, R., Fujiwara, Y., Akiyama, T., Ito, T. & Freeman, A. J. Giant modification of the magnetocrystalline anisotropy in transition-metal monolayers by an external electric field. *Phys. Rev. Lett.* **102**, 187201 (2009).
80. Tsujikawa, M. & Oda, T. Finite electric field effects in the large perpendicular magnetic anisotropy surface Pt/Fe/Pt(001): a first-principles study. *Phys. Rev. Lett.* **102**, 247203 (2009).
81. Bauer, U., Przybylski, M., Kirschner, J. & Beach, G. S. D. Magnetoelectric charge trap memory. *Nano Lett.* **12**, 1437–1442 (2012).
82. Liu, Y. T., Agnus, G., Ono, S., Ranno, L., Bernard-Mantel, A., Soucaille, R., Adam, J.-P., Langer, J., Ocker, B., Ravelosona, D. & Herrera Diez, L. Ionic-liquid gating of perpendicularly magnetised CoFeB/MgO thin films. *J. Appl. Phys.* **120**, 023901 (2016).
83. Shimamura, K., Chiba, D., Ono, S., Fukami, S., Ishiwata, N., Kawaguchi, M., Kobayashi, K. & Ono, T. Electrical control of Curie temperature in cobalt using an ionic liquid film. *Appl. Phys. Lett.* **100**, 122402 (2012).
84. Maruyama, T., Shiota, Y., Nozaki, T., Ohta, K., Toda, N., Mizuguchi, M., Tulapurkar, A. A., Shinjo, T., Shiraishi, M., Mizukami, S., Ando, Y. & Suzuki, Y. Large voltage-induced magnetic anisotropy change in a few atomic layers of iron. *Nat. Nanotechnol.* **4**, 158–161 (2009).
85. Liu, Y. T., Ono, S., Agnus, G., Adam, J.-P., Jaiswal, S., Langer, J., Ocker, B., Ravelosona, D. & Herrera Diez, L. Electric field controlled domain wall dynamics and magnetic easy axis switching in liquid gated CoFeB/MgO films. *J. Appl. Phys.* **122**, 133907 (2017).

86. Herrera Diez, L., Bernand-Mantel, A., Vila, L., Warin, P., Marty, A., Ono, S., Givord, D. & Ranno, L. Electric-field assisted depinning and nucleation of magnetic domain walls in FePt/Al₂O₃ /liquid gate structures. *Appl. Phys. Lett.* **104**, 082413 (2014).
87. Bernand-Mantel, A., Herrera-Diez, L., Ranno, L., Pizzini, S., Vogel, J., Givord, D., Auffret, S., Boulle, O., Miron, I. M. & Gaudin, G. Electric-field control of domain wall nucleation and pinning in a metallic ferromagnet. *Appl. Phys. Lett.* **102**, 122406 (2013).
88. Nakatani, Y., Hayashi, M., Kanai, S., Fukami, S. & Ohno, H. Electric field control of Skyrmions in magnetic nanodisks. *Appl. Phys. Lett.* **108**, 152403 (2016).
89. Fook, H. T., Gan, W. L. & Lew, W. S. Gateable skyrmion transport via field-induced potential barrier modulation. *Sci. Rep.* **6**, 21099 (2016).
90. Kang, W., Huang, Y., Zheng, C., Lv, W., Lei, N., Zhang, Y., Zhang, X., Zhou, Y. & Zhao, W. Voltage controlled magnetic skyrmion motion for racetrack memory. *Sci. Rep.* **6**, 23164 (2016).
91. Hsu, P.-J., Kubetzka, A., Finco, A., Romming, N., von Bergmann, K. & Wiesendanger, R. Electric-field-driven switching of individual magnetic skyrmions. *Nat. Nanotechnol.* **12**, 123–126 (2017).
92. Schott, M., Bernand-Mantel, A., Ranno, L., Pizzini, S., Vogel, J., Béa, H., Baraduc, C., Auffret, S., Gaudin, G. & Givord, D. The skyrmion switch: turning magnetic skyrmion bubbles on and off with an electric field. *Nano Lett.* **17**, 3006–3012 (2017).
93. Black, C. T. & Welser, J. J. Electric-field penetration into metals: consequences for high-dielectric-constant capacitors. *IEEE Trans. Electron Devices* **46**, 776–780 (1999).
94. Duschek, K., Uhlemann, M., Schlörb, H., Nielsch, K. & Leistner, K. Electrochemical and in situ magnetic study of iron/iron oxide films oxidized and reduced in KOH solution for magneto-ionic switching. *Electrochem. commun.* **72**, 153–156 (2016).
95. Duschek, K., Petr, A., Zehner, J., Nielsch, K. & Leistner, K. All-electrochemical voltage-control of magnetization in metal oxide/metal nanoislands. *J. Mater.*

- Chem. C* **6**, 8411–8417 (2018).
96. Duschek, K., Pohl, D., Fähler, S., Nielsch, K. & Leistner, K. Research Update: Magnetoionic control of magnetization and anisotropy in layered oxide/metal heterostructures. *APL Mater.* **4**, 032301 (2016).
 97. Topolovec, S., Jerabek, P., Szabó, D. V., Krenn, H. & Würschum, R. SQUID magnetometry combined with in situ cyclic voltammetry: A case study of tunable magnetism of γ -Fe₂O₃ nanoparticles. *J. Magn. Magn. Mater.* **329**, 43–48 (2013).
 98. Traußnig, T., Topolovec, S., Nadeem, K., Vinga Szabó, D., Krenn, H. & Würschum, R. Magnetization of Fe-oxide based nanocomposite tuned by surface charging. *Phys. status solidi - Rapid Res. Lett.* **5**, 150–152 (2011).
 99. Ghosh, S. Switching magnetic order in nanoporous Pd–Ni by electrochemical charging. *J. Mater. Res.* **28**, 3010–3017 (2013).
 100. Di, N., Kubal, J., Zeng, Z., Greeley, J., Maroun, F. & Allongue, P. Influence of controlled surface oxidation on the magnetic anisotropy of Co ultrathin films. *Appl. Phys. Lett.* **106**, 122405 (2015).
 101. Quintana, A., Menéndez, E., Isarain-Chávez, E., Fornell, J., Solsona, P., Fauth, F., Baró, M. D., Nogués, J., Pellicer, E. & Sort, J. Tunable magnetism in nanoporous CuNi alloys by reversible voltage-driven element-selective redox processes. *Small* **14**, 1704396 (2018).
 102. Gilbert, D. A., Grutter, A. J., Arenholz, E., Liu, K., Kirby, B. J., Borchers, J. A. & Maranville, B. B. Structural and magnetic depth profiles of magneto-ionic heterostructures beyond the interface limit. *Nat. Commun.* **7**, 12264 (2016).
 103. Bauer, U., Yao, L., Tan, A. J., Agrawal, P., Emori, S., Tuller, H. L., van Dijken, S. & Beach, G. S. D. Magneto-ionic control of interfacial magnetism. *Nat. Mater.* **14**, 174–181 (2015).
 104. Zhou, X., Yan, Y., Jiang, M., Cui, B., Pan, F. & Song, C. Role of Oxygen Ion Migration in the Electrical Control of Magnetism in Pt/Co/Ni/HfO₂ Films. *J. Phys. Chem. C* **120**, 1633–1639 (2016).

105. Yan, Y. N., Zhou, X. J., Li, F., Cui, B., Wang, Y. Y., Wang, G. Y., Pan, F. & Song, C. Electrical control of Co/Ni magnetism adjacent to gate oxides with low oxygen ion mobility. *Appl. Phys. Lett.* **107**, 122407 (2015).
106. Herrera Diez, L., Liu, Y. T., Gilbert, D. A., Belmeguenai, M., Vogel, J., Pizzini, S., Martinez, E., Lamperti, A., Mohammedi, J. B., Laborieux, A., Roussigné, Y., Grutter, A. J., Arenholtz, E., Quarterman, P., Maranville, B., Ono, S., Hadri, M. S. El, Tolley, R., Fullerton, E. E., Sanchez-Tejerina, L., Stashkevich, A., Chérif, S. M., Kent, A. D., Querlioz, D., Langer, J., Ocker, B. & Ravelosona, D. Nonvolatile ionic modification of the Dzyaloshinskii-moriya interaction. *Phys. Rev. Appl.* **12**, 034005 (2019).
107. Jiang, M., Chen, X. Z., Zhou, X. J., Cui, B., Yan, Y. N., Wu, H. Q., Pan, F. & Song, C. Electrochemical control of the phase transition of ultrathin FeRh films. *Appl. Phys. Lett.* **108**, 202404 (2016).
108. Bi, C., Liu, Y., Newhouse-Illige, T., Xu, M., Rosales, M., Freeland, J. W., Mryasov, O., Zhang, S., te Velthuis, S. G. E. & Wang, W. G. Reversible control of Co magnetism by voltage-induced oxidation. *Phys. Rev. Lett.* **113**, 267202 (2014).
109. Robbenolt, S., Quintana, A., Pellicer, E. & Sort, J. Large magnetoelectric effects mediated by electric-field-driven nanoscale phase transformations in sputtered (nanoparticulate) and electrochemically dealloyed (nanoporous) Fe–Cu films. *Nanoscale* **10**, 14570–14578 (2018).
110. Zhao, S., Zhou, Z., Peng, B., Zhu, M., Feng, M., Yang, Q., Yan, Y., Ren, W., Ye, Z.-G., Liu, Y. & Liu, M. Quantitative determination on ionic-liquid-gating control of interfacial magnetism. *Adv. Mater.* **29**, 1606478 (2017).
111. Quintana, A., Menéndez, E., Liedke, M. O., Butterling, M., Wagner, A., Sireus, V., Torruella, P., Estradé, S., Peiró, F., Dendooven, J., Detavernier, C., Murray, P. D., Gilbert, D. A., Liu, K., Pellicer, E., Nogues, J. & Sort, J. Voltage-controlled ON–OFF ferromagnetism at room temperature in a single metal oxide film. *ACS Nano* **12**, 10291–10300 (2018).
112. Yi, H. T., Gao, B., Xie, W., Cheong, S.-W. & Podzorov, V. Tuning the metal-insulator crossover and magnetism in SrRuO₃ by ionic gating. *Sci. Rep.* **4**, 6604 (2015).

113. Dasgupta, S., Das, B., Knapp, M., Brand, R. A., Ehrenberg, H., Kruk, R. & Hahn, H. Intercalation-driven reversible control of magnetism in bulk ferromagnets. *Adv. Mater.* **26**, 4639–4644 (2014).
114. Dubraja, L. A., Reitz, C., Velasco, L., Witte, R., Kruk, R., Hahn, H. & Brezesinski, T. Electrochemical tuning of magnetism in ordered mesoporous transition-metal ferrite films for micromagnetic actuation. *ACS Appl. Nano Mater.* **1**, 65–72 (2018).
115. Tan, A. J., Huang, M., Sheffels, S., Büttner, F., Kim, S., Hunt, A. H., Waluyo, I., Tuller, H. L. & Beach, G. S. D. Hydration of gadolinium oxide (GdO_x) and its effect on voltage-induced Co oxidation in a Pt/Co/GdO_x/Au heterostructure. *Phys. Rev. Mater.* **3**, 064408 (2019).
116. Tan, A. J., Huang, M., Avci, C. O., Büttner, F., Mann, M., Hu, W., Mazzoli, C., Wilkins, S., Tuller, H. L. & Beach, G. S. D. Magneto-ionic control of magnetism using a solid-state proton pump. *Nat. Mater.* **18**, 35–41 (2019).
117. Lee, K.-Y., Jo, S., Tan, A. J., Huang, M., Choi, D., Park, J. H., Ji, H.-I., Son, J.-W., Chang, J., Beach, G. S. D. & Woo, S. Fast magneto-ionic switching of interface anisotropy using yttria-stabilized zirconia gate oxide. *Nano Lett.* **20**, 3435–3441 (2020).
118. Zhan, H., Cervenka, J., Prawer, S. & Garrett, D. J. Electrical double layer at various electrode potentials: a modification by vibration. *J. Phys. Chem. C* **121**, 4760–4764 (2017).
119. Kim, S. H., Hong, K., Xie, W., Lee, K. H., Zhang, S., Lodge, T. P. & Frisbie, C. D. Electrolyte-gated transistors for organic and printed electronics. *Adv. Mater.* **25**, 1822–1846 (2013).
120. Du, H., Lin, X., Xu, Z. & Chu, D. Electric double-layer transistors: a review of recent progress. *J. Mater. Sci.* **50**, 5641–5673 (2015).
121. Leighton, C. Electrolyte-based ionic control of functional oxides. *Nat. Mater.* **18**, 13–18 (2019).
122. Mishra, A. K., Bansal, C., Ghafari, M., Kruk, R. & Hahn, H. Tuning properties of nanoporous Au-Fe alloys by electrochemically induced surface charge variations.

- Phys. Rev. B* **81**, 155452 (2010).
123. Ghosh, S., Lemier, C. & Weissmuller, J. Charge-dependent magnetization in nanoporous Pd-Co alloys. *IEEE Trans. Magn.* **42**, 3617–3619 (2006).
 124. Dislaki, E., Robbenolt, S., Campoy-Quiles, M., Nogués, J., Pellicer, E. & Sort, J. Coercivity modulation in Fe-Cu pseudo-ordered porous thin films controlled by an applied voltage: a sustainable, energy-efficient approach to magnetoelectrically driven materials. *Adv. Sci.* **5**, 1800499 (2018).
 125. Ghosh, S. Charge-response of magnetization in nanoporous Pd–Ni alloys. *J. Magn. Mater.* **323**, 552–556 (2011).
 126. Göbller, M., Albu, M., Klinser, G., Steyskal, E., Krenn, H. & Würschum, R. Magneto-ionic switching of superparamagnetism. *Small* **15**, 1904523 (2019).
 127. Reitz, C., Suchomski, C., Wang, D., Hahn, H. & Brezesinski, T. In situ tuning of magnetization via topotactic lithium insertion in ordered mesoporous lithium ferrite thin films. *J. Mater. Chem. C*, **4**, 8889–8896 (2016).
 128. Robbenolt, S., Menéndez, E., Quintana, A., Gómez, A., Auffret, S., Baltz, V., Pellicer, E. & Sort, J. Reversible, electric-field induced magneto-ionic control of magnetism in mesoporous cobalt ferrite thin films. *Sci. Rep.* **9**, 10804 (2019).
 129. Robbenolt, S., Yu, P., Nicolenco, A., Mercier Fernandez, P., Coll, M. & Sort, J. Magneto-ionic control of magnetism in two-oxide nanocomposite thin films comprising mesoporous cobalt ferrite conformally nanocoated with HfO₂. *Nanoscale* **12**, 5987–5994 (2020).
 130. Schlesinger, M. & Paunovic, M. *Modern Electroplating: Fifth Edition*. (2011).
 131. Mohanty, U. S. Electrodeposition: A versatile and inexpensive tool for the synthesis of nanoparticles, nanorods, nanowires, and nanoclusters of metals. *J. Appl. Electrochem.* **41**, 257–270 (2011).
 132. Ruythooren, W., Attenborough, K., Beerten, S., Merken, P., Fransaer, J., Beyne, E., Hoof, C. Van, Boeck, J. De & Celis, J. P. Electrodeposition for the synthesis of microsystems. *J. Micromechanics Microengineering* **10**, 101–107 (2000).

133. Fick, A. Ueber Diffusion. *Ann. der Phys. und Chemie* **170**, 59–86 (1855).
134. Nicolenco, A., Mulone, A., Imaz, N., Tsyntсарu, N., Sort, J., Pellicer, E., Klement, U., Cesiulis, H. & García-Lecina, E. Nanocrystalline electrodeposited Fe-W/Al₂O₃ composites: Effect of alumina sub-microparticles on the mechanical, tribological, and corrosion properties. *Front. Chem.* **7**, 241 (2019).
135. Sivaraman, K. M., Ergeneman, O., Pané, S., Pellicer, E., Sort, J., Shou, K., Suriñach, S., Baró, M. D. & Nelson, B. J. Electrodeposition of cobalt–yttrium hydroxide/oxide nanocomposite films from particle-free aqueous baths containing chloride salts. *Electrochim. Acta* **56**, 5142–5150 (2011).
136. Warren, S. C. & Wiesner, U. Self-assembled ordered mesoporous metals. *Pure Appl. Chem.* **81**, 73–84 (2009).
137. Paul, M. T. Y. & Gates, B. D. Mesoporous platinum prepared by electrodeposition for ultralow loading proton exchange membrane fuel cells. *Sci. Rep.* **9**, 4161 (2019).
138. Pal, N. & Bhaumik, A. Mesoporous materials: versatile supports in heterogeneous catalysis for liquid phase catalytic transformations. *RSC Adv.* **5**, 24363–24391 (2015).
139. Li, W., Liu, J. & Zhao, D. Mesoporous materials for energy conversion and storage devices. *Nat. Rev. Mater.* **1**, 16023 (2016).
140. Bera, D., Kuiry, S. C. & Seal, S. Synthesis of nanostructured materials using template-assisted electrodeposition. *JOM* **56**, 49–53 (2004).
141. Golvano-Escobal, I., Suriñach, S., Baró, M. D., Pané, S., Sort, J. & Pellicer, E. Electrodeposition of sizeable and compositionally tunable rhodium-iron nanoparticles and their activity toward hydrogen evolution reaction. *Electrochim. Acta* **194**, 263–275 (2016).
142. Lai, M. & Riley, D. J. Templated electrosynthesis of nanomaterials and porous structures. *J. Colloid Interface Sci.* **323**, 203–212 (2008).
143. Pérez-Page, M., Yu, E., Li, J., Rahman, M., Dryden, D. M., Vidu, R. & Stroeve, P. Template-based syntheses for shape controlled nanostructures. *Adv. Colloid*

- Interface Sci.* **234**, 51–79 (2016).
144. Petkovich, N. D. & Stein, A. Controlling macro- and mesostructures with hierarchical porosity through combined hard and soft templating. *Chem. Soc. Rev.* **42**, 3721–3739 (2013).
 145. Serrà, A., Gómez, E. & Vallés, E. Facile electrochemical synthesis, using microemulsions with ionic liquid, of highly mesoporous CoPt nanorods with enhanced electrocatalytic performance for clean energy. *Int. J. Hydrogen Energy* **40**, 8062–8070 (2015).
 146. Serrà, A., Grau, S., Gimbert-Suriñach, C., Sort, J., Nogués, J. & Vallés, E. Magnetically-actuated mesoporous nanowires for enhanced heterogeneous catalysis. *Appl. Catal. B Environ.* **217**, 81–91 (2017).
 147. Serrà, A., Montiel, M., Gómez, E. & Vallés, E. Electrochemical Synthesis of Mesoporous CoPt Nanowires for Methanol Oxidation. *Nanomaterials* **4**, 189–202 (2014).
 148. Esteves, M. C., Sumodjo, P. T. A. & Podlaha, E. J. Electrodeposition of CoNiMo thin films using glycine as additive: anomalous and induced codeposition. *Electrochim. Acta* **56**, 9082–9087 (2011).
 149. Guerrero, M., Zhang, J., Altube, A., García-Lecina, E., Roldan, M., Baró, M. D., Pellicer, E. & Sort, J. Room-temperature synthesis of three-dimensional porous ZnO@CuNi hybrid magnetic layers with photoluminescent and photocatalytic properties. *Sci. Technol. Adv. Mater.* **17**, 177–187 (2016).
 150. Pal, N. & Bhaumik, A. Soft templating strategies for the synthesis of mesoporous materials: Inorganic, organic–inorganic hybrid and purely organic solids. *Adv. Colloid Interface Sci.* **189–190**, 21–41 (2013).
 151. Guerrero, M., Pané, S., Nelson, B. J., Baró, M. D., Roldán, M., Sort, J. & Pellicer, E. 3D hierarchically porous Cu–BiOCl nanocomposite films: one-step electrochemical synthesis, structural characterization and nanomechanical and photoluminescent properties. *Nanoscale* **5**, 12542–12550 (2013).

152. Attard, G. S. Mesoporous platinum films from lyotropic liquid crystalline phases. *Science*. **278**, 838–840 (1997).
153. Foyet, A., Hauser, A. & Schäfer, W. Double template electrochemical deposition and characterization of NiCo and NiCu alloys nanoparticles and nanofilms. *J. Solid State Electrochem.* **12**, 47–55 (2008).
154. Bender, F., Mankelow, R. K., Hibbert, D. B. & Gooding, J. J. Lyotropic liquid crystal templating of groups 11 and 12 metal films. *Electroanalysis* **18**, 1558–1563 (2006).
155. Baba, D., Kim, J., Henzie, J., Li, C., Jiang, B., Dag, Ö., Yamauchi, Y. & Asahi, T. Electrochemical deposition of large-sized mesoporous nickel films using polymeric micelles. *Chem. Commun.* **54**, 10347–10350 (2018).
156. Isarain-Chávez, E., Baró, M. D., Pellicer, E. & Sort, J. Micelle-assisted electrodeposition of highly mesoporous Fe–Pt nodular films with soft magnetic and electrocatalytic properties. *Nanoscale* **9**, 18081–18093 (2017).
157. Isarain-Chávez, E., Baró, M. D., Alcantara, C., Pané, S., Sort, J. & Pellicer, E. Micelle-assisted electrodeposition of mesoporous Fe–Pt smooth thin films and their electrocatalytic activity towards the hydrogen evolution reaction. *ChemSusChem* **11**, 367–375 (2018).
158. Wang, H., Wang, L., Sato, T., Sakamoto, Y., Tominaka, S., Miyasaka, K., Miyamoto, N., Nemoto, Y., Terasaki, O. & Yamauchi, Y. Synthesis of mesoporous Pt films with tunable pore sizes from aqueous surfactant solutions. *Chem. Mater.* **24**, 1591–1598 (2012).
159. Iqbal, M., Li, C., Wood, K., Jiang, B., Takei, T., Dag, Ö., Baba, D., Nugraha, A. S., Asahi, T., Whitten, A. E., Hossain, M. S. A., Malgras, V. & Yamauchi, Y. Continuous mesoporous Pd films by electrochemical deposition in nonionic micellar solution. *Chem. Mater.* **29**, 6405–6413 (2017).
160. Tao, F., Guan, M., Jiang, Y., Zhu, J., Xu, Z. & Xue, Z. An easy way to construct an ordered array of nickel nanotubes: the triblock-copolymer-assisted hard-template method. *Adv. Mater.* **18**, 2161–2164 (2006).

161. Zhang, J., Quintana, A., Menéndez, E., Coll, M., Pellicer, E. & Sort, J. Electrodeposited ni-based magnetic mesoporous films as smart surfaces for atomic layer deposition: an "All-chemical" deposition approach toward 3D nanoengineered composite layers. *ACS Appl. Mater. Interfaces* **10**, 14877–14885 (2018).
162. Eiler, K., Fornell, J., Navarro-Senent, C., Pellicer, E. & Sort, J. Tailoring magnetic and mechanical properties of mesoporous single-phase Ni–Pt films by electrodeposition. *Nanoscale* **12**, 7749–7758 (2020).
163. Li, C., Jiang, B., Chen, H., Imura, M., Sang, L., Malgras, V., Bando, Y., Ahamad, T., Alshehri, S. M., Tominaka, S. & Yamauchi, Y. Superior electrocatalytic activity of mesoporous Au film templated from diblock copolymer micelles. *Nano Res.* **9**, 1752–1762 (2016).
164. Hu, J., Abdelsalam, M., Bartlett, P., Cole, R., Sugawara, Y., Baumberg, J., Mahajan, S. & Denuault, G. Electrodeposition of highly ordered macroporous iridium oxide through self-assembled colloidal templates. *J. Mater. Chem.* **19**, 3855 (2009).
165. Yuan, Y. F., Xia, X. H., Wu, J. B., Chen, Y. B., Yang, J. L. & Guo, S. Y. Enhanced electrochromic properties of ordered porous nickel oxide thin film prepared by self-assembled colloidal crystal template-assisted electrodeposition. *Electrochim. Acta* **56**, 1208–1212 (2011).
166. Yang, S.-M., Jang, S. G., Choi, D.-G., Kim, S. & Yu, H. K. Nanomachining by colloidal lithography. *Small* **2**, 458–475 (2006).
167. Zhang, G. & Wang, D. Colloidal lithography-The art of nanochemical patterning. *Chem. - An Asian J.* **4**, 236–245 (2009).
168. Dziomkina, N. V. & Vancso, G. J. Colloidal crystal assembly on topologically patterned templates. *Soft Matter* **1**, 265 (2005).
169. Rogach, A. L., Kotov, N. A., Koktysh, D. S., Ostrander, J. W. & Ragoisha, G. A. Electrophoretic deposition of latex-based 3D colloidal photonic crystals: a technique for rapid production of high-quality opals. *Chem. Mater.* **12**, 2721–2726 (2000).

170. Van der Biest, O. O. & Vandeperre, L. J. Electrophoretic deposition of materials. *Annu. Rev. Mater. Sci.* **29**, 327–352 (1999).
171. Bartlett, P. N., Birkin, P. R. & Ghanem, M. A. Electrochemical deposition of macroporous platinum, palladium and cobalt films using polystyrene latex sphere templates. *Chem. Commun.* **17**, 1671–1672 (2000).
172. Wijnhoven, J. E. G. J., Zevenhuizen, S. J. M., Hendriks, M. A., Vanmaekelbergh, D., Kelly, J. J. & Vos, W. L. Electrochemical assembly of ordered macropores in gold. *Adv. Mater.* **12**, 888–890 (2000).
173. Ke, F.-S., Huang, L., Cai, J.-S. & Sun, S.-G. Electroplating synthesis and electrochemical properties of macroporous Sn–Cu alloy electrode for lithium-ion batteries. *Electrochim. Acta* **52**, 6741–6747 (2007).
174. Bartlett, P. N., Dunford, T. & Ghanem, M. A. Templated electrochemical deposition of nanostructured macroporous PbO₂. *J. Mater. Chem.* **12**, 3130–3135 (2002).
175. Luo, X., Killard, A. J., Morrin, A. & Smyth, M. R. Electrochemical preparation of distinct polyaniline nanostructures by surface charge control of polystyrene nanoparticle templates. *Chem. Commun.* **30**, 3207–3209 (2007).
176. Bartlett, P. N., Ghanem, M. A., El Hallag, I. S., de Groot, P. & Zhukov, A. Electrochemical deposition of macroporous magnetic networks using colloidal templates. *J. Mater. Chem.* **13**, 2596–2602 (2003).
177. Xu, L., Wiley, J. B., Zhou, W. L., Frommen, C., Malkinski, L., Wang, J.-Q., Baughman, R. H. & Zakhidov, A. A. Electrodeposited nickel and gold nanoscale metal meshes with potentially interesting photonic properties. *Chem. Commun.* **1**, 997–998 (2000).
178. Karlsruhe, D.-, Betz, H., Heuberger, A. & Pongratz, S. Production of separation-nozzle systems of X-ray lithography and galvanoplastics. *Naturwissenschaften* **69**, 520–523 (1982).
179. Roth, S., Dellmann, L., Racine, G.-A. & Rooij, N. F. de. High aspect ratio UV photolithography for electroplated structures. *J. Micromechanics Microengineering*

- 9**, 105–108 (1999).
180. Landolt, D. Electrodeposition science and technology in the last quarter of the twentieth century. *J. Electrochem. Soc.* **149**, S9–S20 (2002).
181. Zhang, B., Weng, Y.-Y., Huang, X.-P., Wang, M., Peng, R.-W., Ming, N.-B., Yang, B., Lu, N. & Chi, L. Creating in-plane metallic-nanowire arrays by corner-mediated electrodeposition. *Adv. Mater.* **21**, 3576–3580 (2009).
182. Hu, C., Aeschlimann, F., Chatzipirpiridis, G., Pokki, J., Chen, X., Puigmarti-Luis, J., Nelson, B. J. & Pané, S. Spatiotemporally controlled electrodeposition of magnetically driven micromachines based on the inverse opal architecture. *Electrochem. commun.* **81**, 97–101 (2017).
183. Liu, H.-H., Liang, Y. & Liu, H.-J. Regular microarray of Au flower-like structure formed by template-assisted electrodeposition: Influence factors and their electrochemical behavior. *Electrochim. Acta* **54**, 7514–7518 (2009).
184. Kim, M., Kim, J. & Allen, M. Nanopatterned surfaces based on template-assisted multilayer electrodeposition. *Small* **11**, 1912–1918 (2015).
185. Guiliani, J., Cadena, J. & Monton, C. Template-assisted electrodeposition of Ni and Ni/Au nanowires on planar and curved substrates. *Nanotechnology* **29**, 075301 (2018).
186. Zeeshan, M. A., Grisch, R., Pellicer, E., Sivaraman, K. M., Peyer, K. E., Sort, J., Özkale, B., Sakar, M. S., Nelson, B. J. & Pané, S. Hybrid helical magnetic microrobots obtained by 3D template-assisted electrodeposition. *Small* **10**, 1284–1288 (2014).
187. Schürch, P., Pethö, L., Schwiedrzik, J., Michler, J. & Philippe, L. Additive manufacturing through galvanofarming of 3D nickel microarchitectures: simulation-assisted synthesis. *Adv. Mater. Technol.* **3**, 1800274 (2018).
188. Sun, I.-W. & Chang, J.-K. in *Springer Handb. Electrochem. Energy* 835–895 (Springer Berlin Heidelberg, 2017).
189. Gómez, E. & Vallés, E. Thick cobalt coatings obtained by electrodeposition. *J. Appl. Electrochem.* **32**, 693–700 (2002).

190. Du, X., Inokuchi, M. & Toshima, N. Preparation and characterization of Co–Pt bimetallic magnetic nanoparticles. *J. Magn. Magn. Mater.* **299**, 21–28 (2006).
191. Park, J.-I., Kang, An.-J., Lee, S.-M., Kim, S., Oh, S. J., Ri, H. C. & Cheon, J. Enhanced magnetic transition of core-shell cobalt-platinum nanoalloys. *MRS Proc.* **721**, 235–240 (2002).
192. Kumbhar, A., Spinu, L., Agnoli, F., Wang, K.-Y., Zhou, W. & O'Connor, C. J. Magnetic properties of cobalt and cobalt-platinum alloy nanoparticles synthesized via microemulsion technique. *IEEE Trans. Magn.* **37**, 2216–2218 (2001).
193. Cao, M., Wu, D. & Cao, R. Recent advances in the stabilization of Platinum electrocatalysts for fuel-cell reactions. *ChemCatChem* **6**, 26–45 (2014).
194. Antolini, E., Salgado, J. R. C. & Gonzalez, E. R. The stability of Pt–M (M=first row transition metal) alloy catalysts and its effect on the activity in low temperature fuel cells. *J. Power Sources* **160**, 957–968 (2006).
195. Zhao, H., Xing, T., Li, L., Geng, X., Guo, K., Sun, C., Zhou, W., Yang, H., Song, R. & An, B. Synthesis of cobalt and nitrogen co-doped carbon nanotubes and its ORR activity as the catalyst used in hydrogen fuel cells. *Int. J. Hydrogen Energy* **44**, 25180–25187 (2019).
196. Domínguez, C., Pérez-Alonso, F. J., Abdel Salam, M., Gómez de la Fuente, J. L., Al-Thabaiti, S. A., Basahel, S. N., Peña, M. A., Fierro, J. L. G. & Rojas, S. Effect of transition metal (M: Fe, Co or Mn) for the oxygen reduction reaction with non-precious metal catalysts in acid medium. *Int. J. Hydrogen Energy* **39**, 5309–5318 (2014).
197. Baronia, R., Goel, J., Tiwari, S., Singh, P., Singh, D., Singh, S. P. & Singhal, S. K. Efficient electro-oxidation of methanol using PtCo nanocatalysts supported reduced graphene oxide matrix as anode for DMFC. *Int. J. Hydrogen Energy* **42**, 10238–10247 (2017).
198. Wang, D., Xin, H. L., Hovden, R., Wang, H., Yu, Y., Muller, D. A., DiSalvo, F. J. & Abruña, H. D. Structurally ordered intermetallic platinum–cobalt core–shell nanoparticles with enhanced activity and stability as oxygen reduction

- electrocatalysts. *Nat. Mater.* **12**, 81–87 (2013).
199. Kim, D., Saal, J. E., Zhou, L., Shang, S., Du, Y. & Liu, Z.-K. Thermodynamic modeling of fcc order/disorder transformations in the Co–Pt system. *Calphad* **35**, 323–330 (2011).
 200. Sharma, N., Jones, G. A., Casey, S. M. & Grundy, P. J. The microstructure and magnetic properties of cobalt-rich Co-Pt alloy thin films grown using ion-beam-assisted deposition. *J. Phys. D. Appl. Phys.* **31**, 3020–3027 (1998).
 201. Yamada, Y., Suzuki, T., Kanazawa, H. & Österman, J. C. The origin of the large perpendicular magnetic anisotropy in Co₃Pt alloy thin films. *J. Appl. Phys.* **85**, 5094–5096 (1999).
 202. Y. Yamada, T. Suzuki, E. N. A. Magnetic properties of electron beam evaporated CoPt alloy thin films. *IEEE Trans. Magn.* **33**, 3622–3624 (1997).
 203. Lauhoff, G., Yamada, Y., Itoh, Y. & Suzuki, T. Order dependent magneto-optical spectroscopy of Co₃Pt alloy films. *J. Magn. Soc. Japan* **23**, 43–46 (1999).
 204. Eagleton, T. S., Mallet, J., Cheng, X., Wang, J., Chien, C.-L. & Searson, P. C. Electrodeposition of Co_xPt_{1-x} Thin Films. *J. Electrochem. Soc.* **152**, C27 (2005).
 205. Barmak, K., Kim, J., Lewis, L. H., Coffey, K. R., Toney, M. F., Kellock, A. J. & Thiele, J.-U. On the relationship of magnetocrystalline anisotropy and stoichiometry in epitaxial L1₀ CoPt (001) and FePt (001) thin films. *J. Appl. Phys.* **98**, 033904 (2005).
 206. Rhen, F. M. F., Backen, E. & Coey, J. M. D. Thick-film permanent magnets by membrane electrodeposition. *J. Appl. Phys.* **97**, 113908 (2005).
 207. Agostinelli, E., Laureti, S., Varvaro, G., Generosi, A., Paci, B., Rossi-Albertini, V., Scavia, G. & Testa, A. M. Study of structural microstructural and magnetic properties of very thin Co₅₀Pt₅₀ films deposited by PLD. *Mater. Sci. Eng. C* **27**, 1466–1469 (2007).
 208. Ersen, O., Parasote, V., Pierron-Bohnes, V., Cadeville, M. C. & Ulhaq-Bouillet, C. Growth conditions to optimize chemical order and magnetic properties in molecular-beam-epitaxy-grown CoPt/MgO(001) thin films. *J. Appl. Phys.* **93**, 2987–

- 2995 (2003).
209. Reichel, L., Fähler, S., Schultz, L. & Leistner, K. Initial preorder as condition for L1₀ ordering in ultrathin CoPt films. *J. Appl. Phys.* **114**, 093909 (2013).
 210. Byrne, F. N., Monzon, L. M. A., Stamenov, P., Venkatesan, M. & Coey, J. M. D. Influence of an Au capping layer on the magnetic properties of CoPt nanowires. *Appl. Phys. Lett.* **98**, 252507 (2011).
 211. Massalski, T. B., Okamoto, H., Subramanian, P. R. & Kacprzak, L. *Binary Alloy Phase Diagrams*. (ASM international, 1996).
 212. Liou, S. H., Liu, Y., Malhotra, S. S., Yu, M. & Sellmyer, D. J. Magnetic properties of nanometer-size CoPt particles. *J. Appl. Phys.* **79**, 5060–5062 (1996).
 213. Panagiotopoulos, I., Stavroyiannis, S., Niarchos, D., Christodoulides, J. A. & Hadjipanayis, G. C. Granular CoPt/C films for high-density recording media. *J. Appl. Phys.* **87**, 4358–4361 (2000).
 214. Uba, L., Uba, S., Horpynyuk, O., Antonov, V. N. & Yaresko, A. N. Influence of the crystal structure and chemical order on the magnetic and magneto-optical properties of equiatomic CoPt alloy. *J. Appl. Phys.* **91**, 775–779 (2002).
 215. Albrecht, M., Maier, A., Treubel, F., Maret, M., Poinso, R. & Schatz, G. Self-assembled magnetic nanostructures of CoPt₃ with favoured chemical ordering. *Europhys. Lett.* **56**, 884–890 (2001).
 216. Khatri, M. S., Schlörb, H., Fähler, S., Schultz, L., Nandan, B., Böhme, M., Krenek, R. & Stamm, M. Electrodeposition of Co–Pt continuous films and nanowires within diblock copolymer template. *Electrochim. Acta* **54**, 2536–2539 (2009).
 217. Zana, I. & Zangari, G. Electrodeposition of Co–Pt films with high perpendicular anisotropy. *Electrochem. Solid-State Lett.* **6**, C153–C156 (2003).
 218. Žužek Rožman, K., Krause, A., Leistner, K., Fähler, S., Schultz, L. & Schlörb, H. Electrodeposition and hard magnetic properties of Co–Pt films in comparison to Fe–Pt films. *J. Magn. Magn. Mater.* **314**, 116–121 (2007).
 219. Sirtori, V., Cavallotti, P. L., Rognoni, R., Xu, X., Zangari, G., Fratesi, G., Trioni, M. I. &

- Bernasconi, M. Unusually large magnetic anisotropy in electrochemically deposited Co-rich Co–Pt films. *ACS Appl. Mater. Interfaces* **3**, 1800–1803 (2011).
220. Martín, A. J., Chaparro, A. M. & Daza, L. Electrochemical quartz crystal microbalance study of the electrodeposition of Co, Pt and Pt–Co alloy. *J. Power Sources* **169**, 65–70 (2007).
221. Cortés, M., Gómez, E. & Vallés, E. Magnetic CoPt (60–70 wt%Pt) microstructures fabricated by the electrochemical method. *J. Micromechanics Microengineering* **22**, 055016 (2012).
222. Tabakovic, I., Qiu, J.-M. & Riemer, S. Electrodeposition of CoPt alloys from the stable hexachloroplatinate solution: electrochemical studies. *J. Electrochem. Soc.* **162**, D291–D299 (2015).
223. Tabakovic, I., Qiu, J.-M. & Dragos, O. Electrodeposition of thin CoPt films with very high perpendicular anisotropy from hexachloroplatinate solution: effect of saccharin additive and electrode substrate. *J. Electrochem. Soc.* **163**, D287–D294 (2016).
224. Hnida, K. E., Żywczak, A., Gajewska, M., Marciszko, M., Sulka, G. D. & Przybylski, M. Tuning the magnetic properties of multilayered CoPt–Pt nanowires via thickness of magnetic segments. *Electrochim. Acta* **205**, 29–37 (2016).
225. Cortés, M., Serrà, A., Gómez, E. & Vallés, E. CoPt nanoscale structures with different geometry prepared by electrodeposition for modulation of their magnetic properties. *Electrochim. Acta* **56**, 8232–8238 (2011).
226. Wu, P. L., Li, X. H., Li, W., Sun, H. Y., Chen, Y. & Zhang, X. Y. Microstructure and magnetic behavior of electrodeposited CoPt thick films upon annealing. *Mater. Lett.* **62**, 309–312 (2008).
227. Mallett, J. J., Svedberg, E. B., Sayan, S., Shapiro, A. J., Wielunski, L., Madey, T. E., Chen, P. J., Egelhoff, W. F. & Moffat, T. P. Compositional control in electrodeposited $\text{Co}_x\text{Pt}_{1-x}$ films. *Electrochem. Solid-State Lett.* **8**, C15 (2005).
228. Chu, S. Z., Inoue, S., Wada, K. & Kurashima, K. Fabrication of integrated arrays of

- ultrahigh density magnetic nanowires on glass by anodization and electrodeposition. *Electrochim. Acta* **51**, 820–826 (2005).
229. Shamaila, S., Sharif, R., Riaz, S., Ma, M., Khaleeq-ur-Rahman, M. & Han, X. F. Magnetic and magnetization properties of electrodeposited fcc CoPt nanowire arrays. *J. Magn. Magn. Mater.* **320**, 1803–1809 (2008).
230. Wodarz, S., Abe, J. & Homma, T. Analysis and control of the initial electrodeposition stages of Co-Pt nanodot arrays. *Electrochim. Acta* **197**, 330–335 (2016).
231. Ouchi, T., Arikawa, Y., Konishi, Y. & Homma, T. Fabrication of magnetic nanodot array using electrochemical deposition processes. *Electrochim. Acta* **55**, 8081–8086 (2010).
232. Berkh, O., Shacham-Diamand, Y. & Gileadi, E. Stability of the electrodeposition process for CoPt alloy formation. *J. Appl. Electrochem.* **38**, 1275–1283 (2008).
233. Jyoko, Y. & Schwarzacher, W. Characterization of electrodeposited magnetic Co/Pt multilayered nanostructures. *Electrochim. Acta* **47**, 371–378 (2001).
234. Wang, N. & Arnold, D. P. Thick electroplated Co-rich Co-Pt micromagnet arrays for magnetic MEMS. in *IEEE Trans. Magn.* **44**, 3969–3972 (2008).
235. Serrà, A., Gómez, E., Golosovsky, I. V., Nogués, J. & Vallés, E. Effective ionic-liquid microemulsion based electrodeposition of mesoporous Co–Pt films for methanol oxidation catalysis in alkaline media. *J. Mater. Chem. A* **4**, 7805–7814 (2016).
236. Liu, L., Pippel, E., Scholz, R. & Gösele, U. Nanoporous Pt–Co alloy nanowires: fabrication, characterization, and electrocatalytic properties. *Nano Lett.* **9**, 4352–4358 (2009).



2

Objectives

2. Objectives

This thesis is mostly aimed at studying three-dimensional (3D) porous Co–Pt based materials from two viewpoints, namely their synthesis through electrochemical pathways and the analysis of their magnetoelectric properties. Owing to the interface nature of magnetoelectric effects, porosity and nanostructuring of the Co–Pt based materials are expected to boost charge accumulation and magneto-ionic effects due to the resulting increase of the S/V ratio. To this end, electrodeposition using soft templates (i.e. micelle-assisted electrodeposition) was combined with other fabrication techniques such as photolithography and ALD. Detailed investigations of the electrochemical fabrication of meso- and macroporous Co–Pt based materials have been carried out.

The main goals are summarized as follows:

- Growth of porous Co–Pt+Co_xO_y based materials from aqueous electrolytes by micelle-assisted electrodeposition. The main goal is to achieve the appropriate chemical composition and morphology, with special emphasis on the development of porosity, to obtain suitable Co–Pt based materials for magnetoelectric purposes.
- Combination of micelle-assisted electrodeposition with photolithography to achieve Co–Pt+Co_xO_y patterned structures exhibiting mesoporosity and investigation of their magnetoelectric properties via non-aqueous electrolyte gating approach.
- Combination of micelle-assisted electrodeposition with ALD to fabricate nanostructured Co–Pt+Co_xO_y/ALD oxide heterostructures and assessment of their magneto-ionic effects via non-aqueous electrolyte gating approach.
- Improvement of magnetoelectric effects through charge accumulation and magneto-ionics in mesoporous Co–Pt+Co_xO_y based materials with the introduction of porosity and nanostructuring to maximize the S/V ratio.

- Investigation of the impact of electrolyte processing on the reproducible formation of a homogenous mesoporosity in fully metallic Co–Pt films prepared by micelle-assisted electrodeposition.
- Fabrication of hard magnetic macroporous Co–Pt thin films by electrodeposition on colloidal crystal templated substrates. Analysis of the dependence of the magnetic properties with the annealing temperature.



3

Experimental techniques

3. Experimental techniques

This chapter describes the experimental details and provides a brief overview of the fundamentals of the main techniques used throughout the thesis. Theoretical concepts of conventional techniques are not given, as we consider they can be found in advanced textbooks. Conversely, the fundamentals of other, less common, techniques are provided in order to show key concepts for an unfamiliar reader.

3.1. Material synthesis techniques

3.1.1. Electrodeposition

a) Apparatus and cell

Electrochemical experiments were performed in a one-compartment thermostated three-electrode cell connected to PGSTAT302N or PGSTAT204 Autolab potentiostat/galvanostat (Metrohm-Autolab) (**Figure 3.1a and Figure 3.1b**, respectively). A double junction Ag|AgCl ($E = +0.210$ V/SHE) reference electrode (Metrohm AG) was used with 3 M potassium chloride (KCl) as the inner solution and 1 M sodium chloride (NaCl) or 1 M sodium sulfate (Na_2SO_4) as the outer solution. A platinum spiral served as the counter electrode and the temperature was set by making water circulate through the external jacket of the electrochemical cell, whose temperature was controlled by an F12 Julabo Thermostat (**Figure 3.2a**). Different substrates were used as working electrodes depending on the electrochemical experiment (**Figure 3.2b**).

a) Types of working electrode/substrates

(i) Si/Ti(10 nm)/Cu(200 nm) 5 mm x 10 mm. For the growth of continuous films, Si substrates with sputtered Ti/Cu adhesion/seed layers were used as working electrode. Prior to electrodeposition, the substrates were cleaned with acetone, isopropanol, followed by Milli-Q water, and finally dried with N_2 . The working area was always 0.25 ± 0.01 cm².

(ii) Photolithographed Si/Ti(10 nm)/Cu (70 nm) 5 mm x 10 mm. For the growth of the metal-metal oxide microdisks, photolithographed Si/Ti/Cu substrates were used. Arrays of cylindrical holes of 50 μm in diameter and 5 μm in height were patterned by optical lithography using AZ-9260 photoresist and AZ-400K developer.

(iii) Colloidal templated Si/Ti(150 nm) substrates with amidine functionalized PS spheres. For the growth of macroporous metallic films, positively charged amidine-terminated polystyrene spheres of 200 nm were electrophoretically assembled on Si/sputtered Ti substrates. Electrophoretic deposition was performed using an Agilent B2902A power supply as voltage source connected to a home-made cell consisting of a poly(methyl methacrylate) (PMMA) chamber attached to a counter electrode made of platinized titanium sheet (**Figure 3.3**). The Ti-coated substrate (cathode) was fixed at 0.5 cm from the counter electrode (anode). The positively charged amidine PS spheres were deposited by applying an electric field of 60 $\text{V}\cdot\text{cm}^{-1}$ during 5 min.

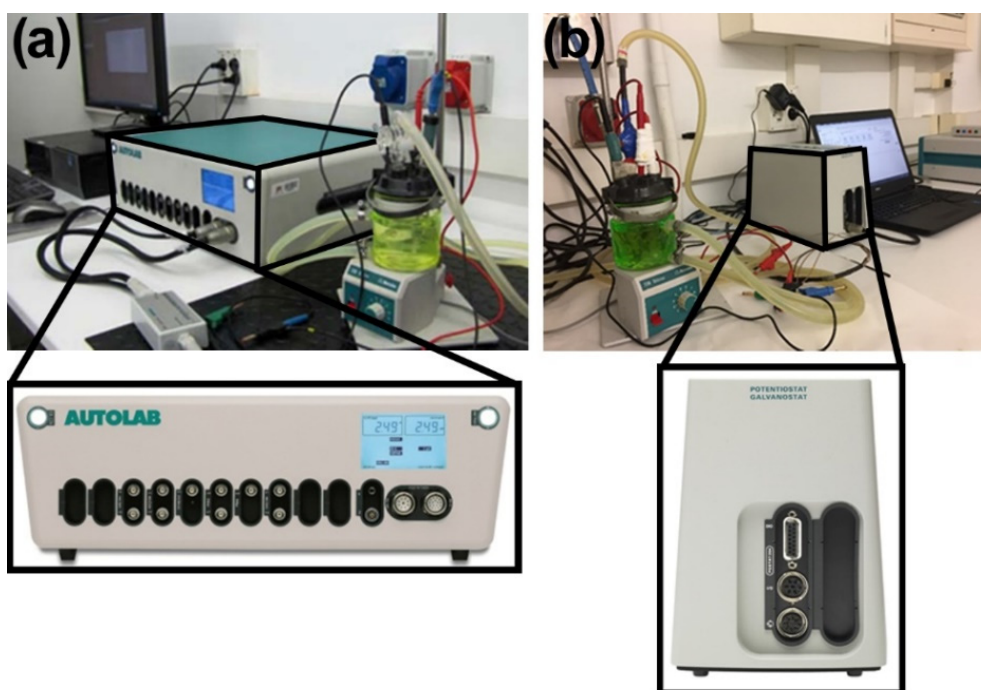


Figure 3.1. Pictures of the three-electrode cell connected to an Autolab Potentiostat/Galvanostat model (a) PGSTAT302N and (b) PGSTAT204 (Metrohm-Autolab).

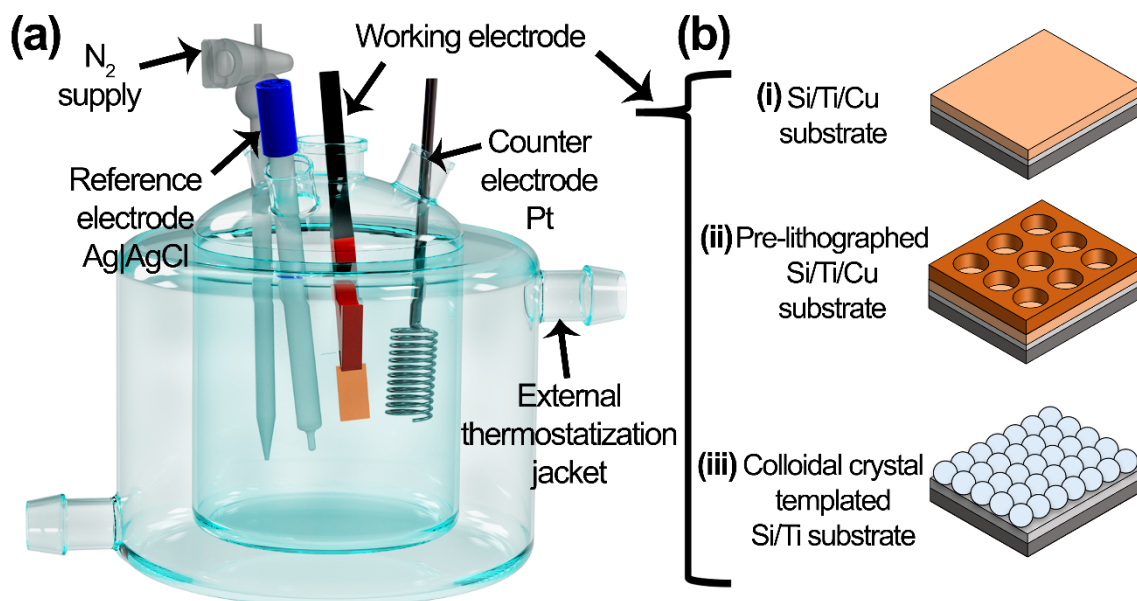


Figure 3.2. (a) Scheme of the electrochemical cell in three-electrode configuration and (b) drawings of the different types of substrates used as working electrode: (i) Si substrate with sputtered Ti/Cu adhesion/seed layers (denoted as Si/Ti/Cu), (ii) photolithographed Si/Ti/Cu substrates and (iii) colloidal templated Si/Ti substrates with amidine functionalized polystyrene spheres.

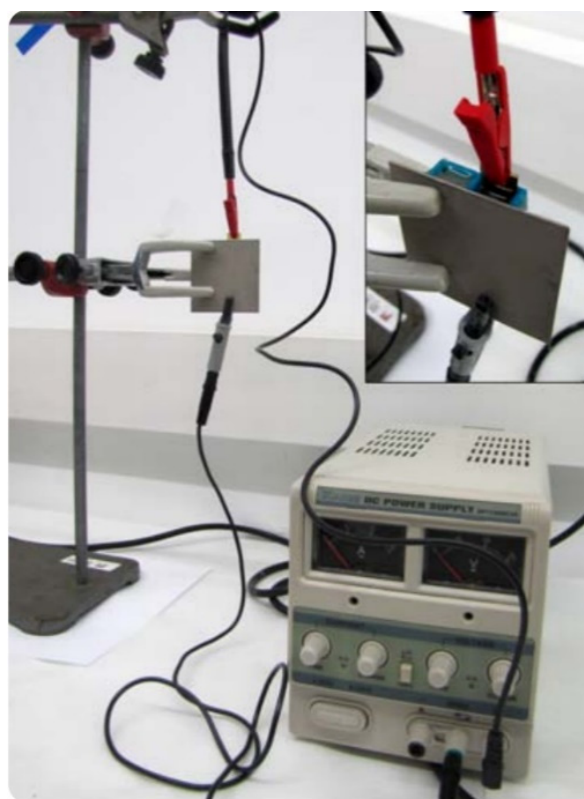


Figure 3.3. Picture of the home-made electrophoresis set-up.

b) Potentiostatic deposition

The fundamentals of electrodeposition have been already explained in Section 1.6 and the specific details for each type of Co–Pt deposit can be found in the articles presented in Section 3. Nevertheless, common parameters related to the electrodeposition of Co–Pt are briefly outlined below.

Analytical grade reagents and Millipore Milli-Q water were used to prepare the electrolytes. The electrolyte volume was typically between 50-100 mL. Bath formulations are detailed in each article. Depositions were conducted potentiostatically at potentials ranging between -0.5 and -1.4 V and during 300-600 s depending on the experiment, at 25 °C and under mild stirring ($\omega = 100$ rpm). In some cases, nitrogen gas was bubbled through the electrolyte during the electrodeposition.

c) Cyclic voltammetry

Voltammetry is an electroanalytical technique used to study the redox processes of the bath species within a potential window. Cyclic voltammetry (CV) involves sweeping the applied potential at the working electrode between two potential limits in both directions (forward and reverse) at a fixed scan rate while measuring the current. In our case CV was used to examine the optimum range of working potentials from each bath for the deposition of Co–Pt. CVs were carried out in the three-electrode cell described above using a vitreous carbon cylindrical rod (Metrohm) with 0.0314 cm² surface area as the working electrode. A single cycle was recorded in each experiment with different lower and upper limits, at a scan rate of 50 mV·s⁻¹. The potential was initially swept from a value in which no current was recorded towards different lower limits and then reversed towards the positive direction.

3.1.2. Atomic Layer Deposition

Atomic layer deposition (ALD) is a gas-phase deposition technique characterized by an alternating surface-limited reaction from the chemical precursors to produce ultrathin coatings with an excellent conformality. ALD was employed to conformally coat the electrodeposited Co–Pt films with HfO_x and AlO_x nanolayers. The deposition of HfO_x and

AlO_x nanocoatings was carried out on a Cambridge NanoTech Savannah 100 reactor by Mariona Coll's group at Institut de Ciència de Materials de Barcelona (ICMAB). HfO_x deposits were prepared by combining tetrakis(dimethylamido)hafnium(IV) (TDMAH) heated at 75-80 °C and deionized water as co-reactant. Nitrogen served as carrier and purging gas (40 and 20 sccm, respectively). The deposition of AlO_x was achieved by alternate pulsing of trimethylaluminum (TMA) and ozone in exposure mode. In both cases, the temperature was set at 200 °C. The number of ALD cycles was varied to obtain varying nanocoating thicknesses.

3.1.3. Annealing treatment

Heat treatments of the Co–Pt deposits were performed in a home-made furnace set-up at different annealing temperatures ranging from 550 to 650 °C under vacuum conditions (pressure 10^{-6} mbar). The home-made set-up consists of a high-vacuum system connected to a quartz tube containing the sample, which is located inside of a 653.03 high-Temperature Furnace (**Figure 3.4**). The system was properly purged with argon several times before heating was initiated. The furnace was first heated up to the target temperature, and then the quartz tube containing the sample was pushed into the furnace.



Figure 3.4. Picture of the home-made high-vacuum annealing set-up.

3.2. Characterization techniques

3.2.1. Electron microscopy

a) Scanning electron microscopy

Morphological characterization of the nanostructured Co–Pt films was characterized by field emission scanning electron microscopy (FE-SEM) with a Zeiss Merlin FE-SEM operated between 1 and 5 kV us for imaging purposes. Compositional analyses were done by energy-dispersive X-ray (EDX) using the FE-SEM operated between 15-20 kV. No special preparation of the films was required for their observation.

b) Transmission electron microscopy

The crystal structure of the samples was studied by high-resolution transmission electron microscopy (HRTEM) and selected area electron diffraction (SAED) on a JEOL-JEM 2011 system with a field emission gun operating at 200 kV.

Further compositional and morphological characterization was investigated by scanning transmission electron microscopy (STEM) on a Tecnai F20 HRTEM/STEM microscope operated in STEM mode at 200 kV.

TEM and STEM analyses were carried out on the cross-section of the nanostructured films from a lamella fabricated by focused ion beam (FIB) using a Crossbeam 1560XB from Zeiss equipped with an ion column Canion from Orsay Physics. The lamellae were firstly capped with 2 μm of tetraethyl orthosilicate (TEOS) and then thin slices of $1 \times 10 \mu\text{m}^2$ were cut and glued onto a TEM grid. Finally, the slices were further thinned down to 100 nm using 5 kV and a current of 50 pA.

c) Energy electron loss spectroscopy

Energy electron loss spectroscopy (EELS) is an analytical technique used in TEM. When the incident electron beam passes through the sample, some of the electrons transfer energy to the electrons in atomic inner shells from the sample, resulting in the ionization

of the atom. Thus, these electrons, which ionized the atom, lose some energy (inelastic scattering) and are slightly deflected from their path (**Figure 3.5**). EELS is based on measuring the energy distribution of these inelastic-scattered electrons after interacting with the sample. Such amount of electron-energy loss is directly related to the ionization energy, which is characteristic for a given element, hence, information about elemental composition, chemical bonding, and electronic properties can be acquired from EELS. Owing to the high resolution of TEM, EELS constitutes a highly localized and sensitive technique that provides structural and chemical information with a spatial resolution at the atomic level.¹⁻³

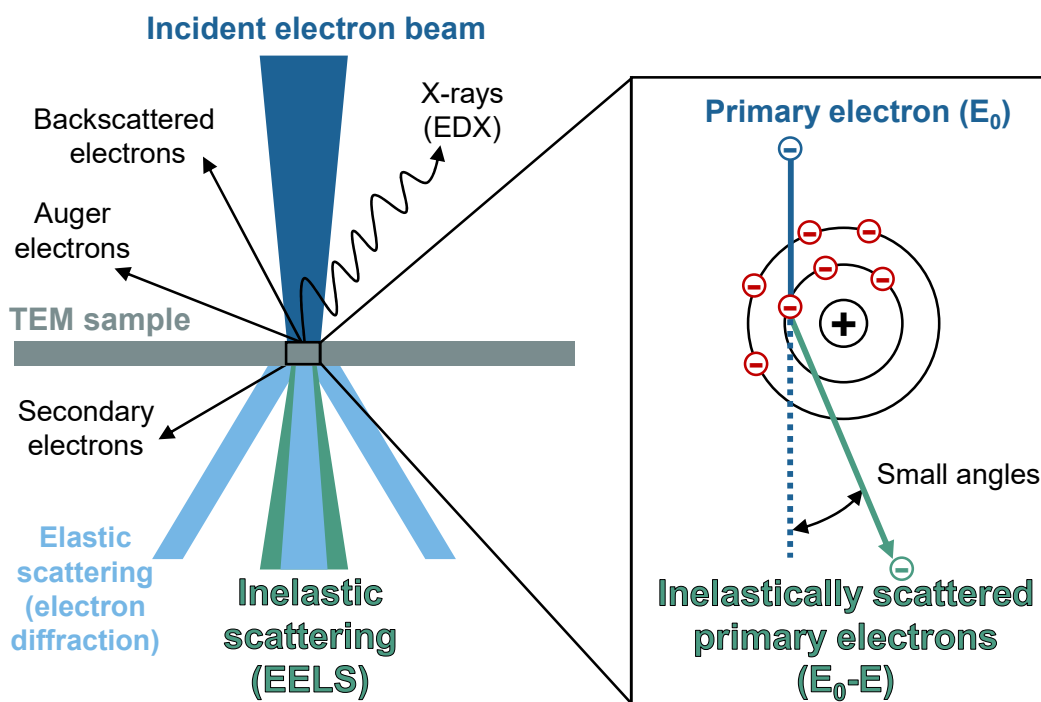


Figure 3.5. Scheme of the TEM interactions including the generation of electron loss spectroscopy signal.

In STEM, the deflection scan coils allow to focus the electron beam in a fine electron probe which can be raster-scanned over the sample. Therefore, STEM-EELS allows to acquire analytical spectrum imaging, where the combination of STEM 2D spatially-resolved electron image with EELS produces a three-dimensional dataset. As it is shown in **Figure 3.6**, an EELS spectrum is recorded from an individual position on the sample, which corresponds to a line parallel to the z-axis. Thus, spectral images can be obtained and stored at every pixel, thereby enabling the absolute correlation of the spectroscopic

and structural data at each pixel. Moreover, STEM-EELS offers a more flexible post-acquisition processing since elemental mapping can be extracted by selecting the energy-loss window corresponding to each element present in the sample (**Figure 3.6**).⁴⁻

6

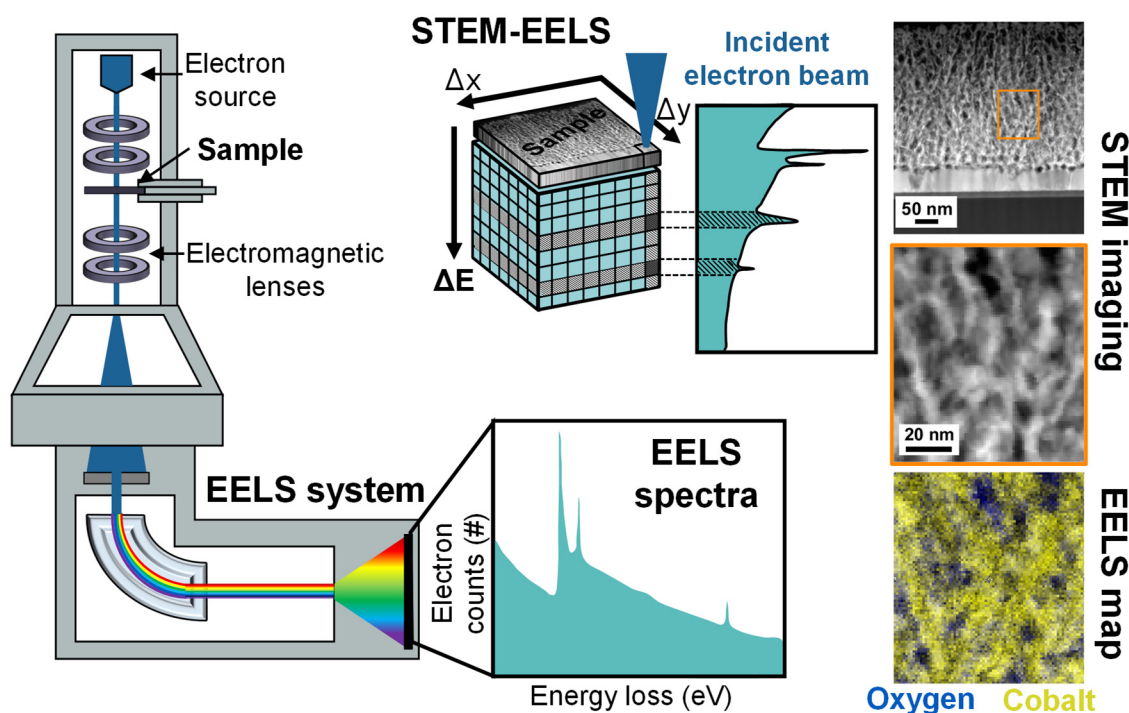


Figure 3.6. Scheme of the EELS system on a STEM together with a representation of the three-dimensional dataset. A data cube is created where two of the axes of the cube correspond to spatial information, while the third axis represents the spectrum of energy losses. The resulting data set is called spectral image. Scheme adapted from references 7 and 8.

In our case, STEM-EELS was employed to investigate the elemental-spatial distribution of Co, O and Hf throughout the thickness of Co–Pt/HfO_x heterostructures and Co–Pt microdisks. For the measurements, a lamella from each sample was prepared as described above. EELS analyses were performed on a Tecnai F20 HRTEM/STEM microscope, whereas the EELS signal was recorded while working in STEM mode at 200 kV using Gatan Wquantum SE 963 Imaging Filter (GIF).

3.2.2. X-ray diffraction and grazing incidence X-ray diffraction

The crystallographic structure of the samples was investigated on a Philips X'Pert diffractometer in Bragg-Brentano geometry using K_α radiation (**Figure 3.7**).

Diffractograms were recorded within a specific 2θ range, depending on the sample's needs, with a step size of 0.026° and a step time of 8 s.



Figure 3.7. Picture of the Philips X'pert diffractometer from the UAB's X-ray diffraction facility.

Considering the thin thickness of certain films, grazing incidence X-ray diffraction (GIXRD) was employed since it is most convenient to structurally evaluate the crystalline structure of thin films due to its surface-sensitivity. GIXRD was performed on a Bruker-AXS, model A25 D8 Discover equipped with a LinxEye XE-T detector using $\text{Cu K}\alpha$ radiation and a grazing incidence angle of 1° .

3.2.3. X-ray Absorption spectroscopy

X-ray absorption spectroscopy (XAS) is an analytical technique based on the measurement of the transitions of core electrons of an element to excited states and the continuum (Red and purple arrows, **Figure 3.8a**). At the smallest X-ray energies at which the photon can be absorbed, the core-electron will be excited to empty bound states. As shown in **Figure 3.8b**, this results in a large increase in absorption at specific X-ray photon energies, which is called absorption edge and corresponds to the difference in energy between the core level and the unoccupied states. This first spectral region is known as X-ray Absorption Near Edge Structure (XANES) and provides information about the oxidation state and the coordination environment of the absorbing atom. The oscillations beyond the XANES region constitute the Extended X-ray Absorption Fine Structure (EXAFS) (**Figure 3.8b**). These oscillations are produced by the interference of

the ejected electron from the absorbing atom and the nearest neighbors of the excited atom. EXAFS provides information about the neighbor atomic type, distance to ligands, bond length and coordination number.^{9,10}

In XAS, the excited electrons are mainly from 1s and 2p shells, implying energies of thousands of eV. For this reason, XAS experiments are mainly carried out with synchrotron sources since this allows to produce a continuous energy spectrum from hard to soft X-rays. Hard X-rays (> 4 keV) are employed to study the K-edge absorption which arises from the 1s → d transition. Alternatively, soft X-rays (0.1-2 keV) are used to excite electrons from 2p to unoccupied d orbitals (**Figure 3.8c**). L-edge XAS is one of the most used techniques for investigating the oxidation states of 3d transition metals due to the sensitivity of the edge energies position, the branching ratios and the multiplet structures to the electronic structure (i.e., oxidation state) (**Figure 3.8d**).¹¹

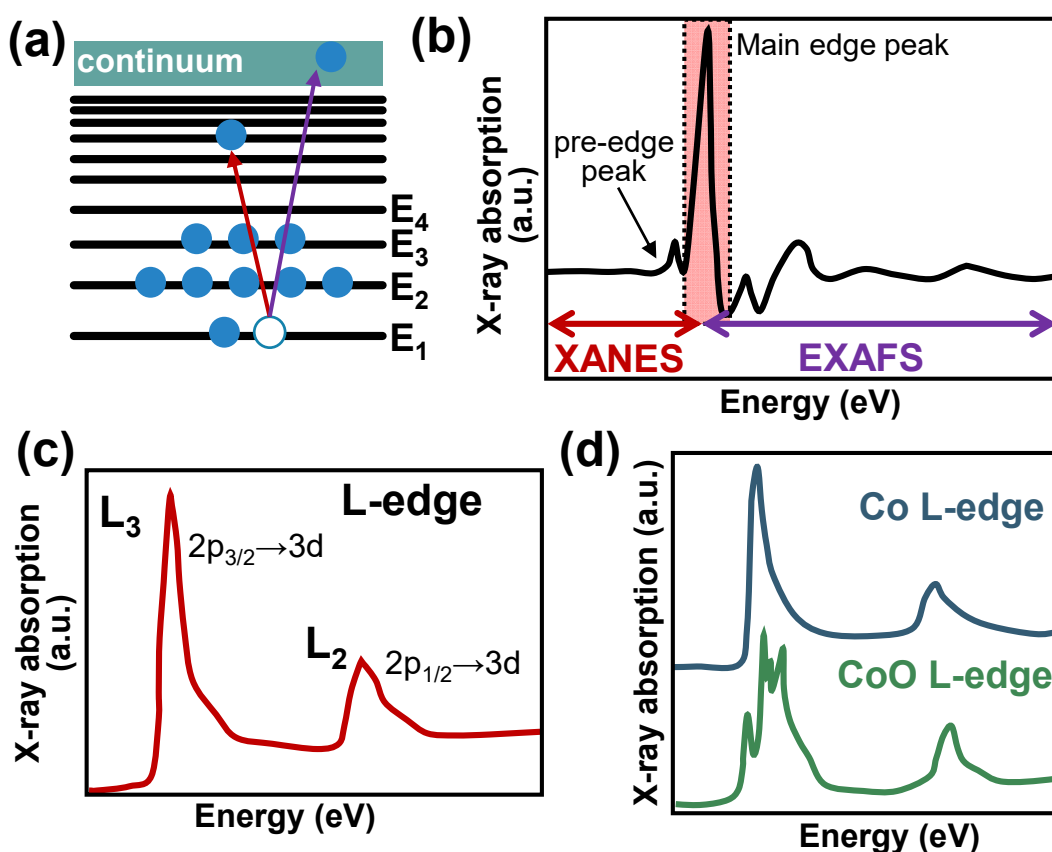


Figure 3.8. (a) Scheme of the X-ray absorption and electron excitation process, (b) Schematic of XAS including XANES and EXAFS regions. Scheme adapted from reference 9, (c) Typical metal L-edge XAS and (d) example of Co (blue) and CoO (green) L-edge XAS spectra.

In general, XAS measurements can be performed in 3 detection modes: one which is direct, the transmission mode, (which measures directly the intensities of incoming and transmitted beam), and two indirect, fluorescence yield (FY) and total electron yield (TEY) modes. The transmission mode is normally employed in XAS experiments involving hard X-rays due to the large mean free path of photons. In soft X-ray range, transmission experiments are difficult to perform due to the short attenuation length of the X-ray, implying extremely thin samples. For these reasons, FY and TEY modes are preferred in the soft X-ray range. FY and TEY are based on measuring the emitted fluorescent X-rays or the emitted secondary and Auger electrons from the sample. Owing to the short mean free path of electrons, TEY detection mode of XAS is a surface-sensitive technique, which implies that most of the detected electrons escape from the first 3-10 nm of the sample.^{9,12}

d) X-ray magnetic circular dichroism

X-ray magnetic circular dichroism (XMCD) is a variant of XAS which is based on the difference in the absorption between left and right polarized X-rays by a magnetic material in the presence of a magnetic field. XMCD originates from the difference in transition probabilities for spin-up and spin down. As it is shown in **Figure 3.9a**, when a metal is magnetized, the valence band is divided due to the exchange interaction, meaning that spin up and spin down accessible unoccupied states are not equivalent. Therefore, the observed absorption for the two light polarizations will be different, and the subtraction of the two spectra from each other results in the difference in spin population (a non-zero difference signifies a magnetic signal). From the experimental point of view, XMCD is performed by calculating the difference spectrum of two XAS taken in a magnetic field, one applying left circularly polarized light and the other with right circularly polarized light (**Figure 3.9b**). The analysis of XMCD spectra provides quantitative information of the magnetic properties for a specific element such as its spin and orbital magnetic moment. In addition, compared to other characterization techniques, XMCD possesses the advantage of element specificity, since the XMCD signal is distinctive of a particular element.^{10,13}

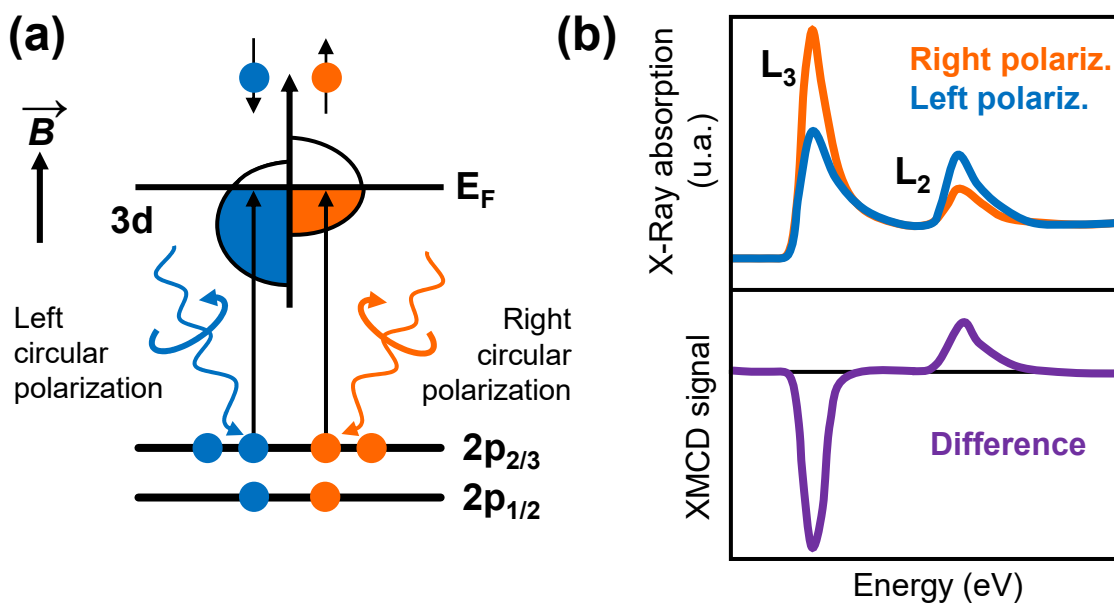


Figure 3.9. (a) Illustration of the XMCD mechanism by an example of a 3d transition metal where 2p core electrons are promoted to an uncopied 3d state at the Fermi level by circularly polarized X-rays. (b) XAS spectra at the L-edge recorded with right (orange) and left (blue) circularly polarized X-rays together with the corresponding XMCD spectra. Scheme adapted from reference 13.

XAS was employed to investigate the oxidation state of the Co–Pt microdisks at the Co $L_{2,3}$ edges. XAS measurements were performed in TEY mode using linearly polarized light at the CIRCE beamline of the ALBA Synchrotron.

Additionally, XAS measurements of nanostructured Co–Pt films were carried out in order to determine the chemical composition and oxidation state. X-ray absorption spectra were recorded at the Co $L_{3,2}$ edges, and measured in TEY mode using linearly polarized light. XMCD measurements at room (300 K) under the applied magnetic fields (20 and –20 kOe) were also performed to probe the magnetic moment of Co in the Co–Pt films. These XAS and XMCD measurements were performed at the UE46_PGM1 beamline (High-Field Diffractometer station of the synchrotron radiation source BESSY II, Helmholtz-Zentrum Berlin).

3.2.4. Magnetic measurements

a) Vibrating sample magnetometer

The magnetic properties of the nanostructured Co–Pt deposits were measured using a Vibrating sample magnetometer (VSM) from Micro sense (LOT–Quantum Design) (**Figure 3.10**). Hysteresis loops were recorded at room temperature along the parallel and perpendicular-to-plane directions, with a maximum applied magnetic field range from -20 kOe to 20 kOe.



Figure 3.10 Picture of the Micro Sense (LOT–Quantum Design) VSM.

b) Magneto-optical Kerr effect

Magnetic measurements at surface level of the nanoporous Co–Pt microdisks were performed using a magneto-optical Kerr effect (MOKE) setup from Durham Magneto Optics (**Figure 3.11**). Longitudinal (in-plane) hysteresis loops were recorded at room temperature with a laser spot focused down to around 3 μm and a maximum in-plane applied magnetic field of 2.5 kOe.

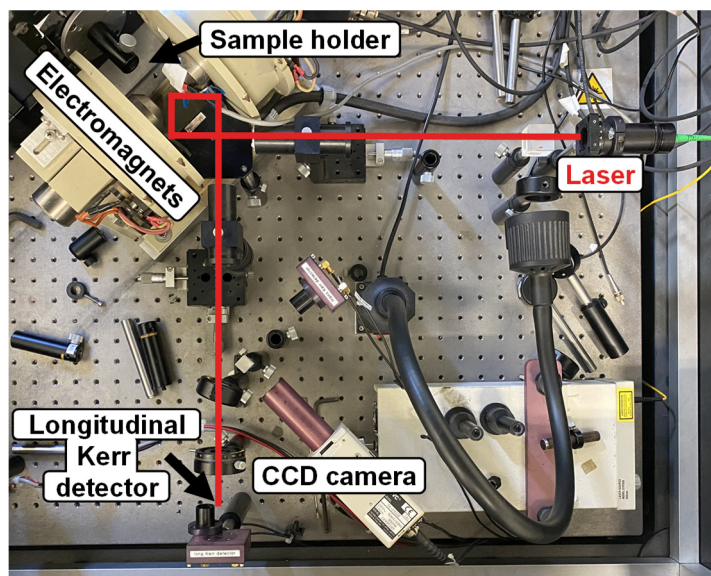


Figure 3.11. Picture of the Durham Magneto Optics MOKE set-up.

c) Magnetolectric measurements

Magnetolectric measurements refer to the recording of the magnetic properties while an electric field is being applied to the sample. To assess the ME effect produced by charge accumulation or/and magneto-ionic processes, ME measurements were all carried out by electrolyte-gating in condenser-like configuration while performing VSM or MOKE magnetometry measurements (**Figure 3.12a** and **b** respectively).

In both cases, the sample served as working electrode, a platinum wire served as counter electrode and the electrolyte consisted of an anhydrous organic solvent (propylene carbonate) containing solvated Na^+ and OH^- ions. To prepare the electrolyte, a piece of metallic sodium was immersed in a flask containing propylene carbonate. This procedure was employed to: (i) remove all traces of water to minimize the occurrence of extrinsic oxidation or corrosion events in the sample and (ii) favor the formation of EDLs, thereby increasing the electric field strength at the sample/electrolyte wall interfaces. As shown in **Figure 3.12c**, application of a negative voltage to the sample (working electrode), induces the migration of the propylene carbonate (polar solvent molecules) and solvated Na^+ ions (counter-ions). In contrast, this configuration is rearranged when the sample polarization is reverse, i.e. when negative voltage applied, solvated OH^- species migrate to the sample surface. In both scenarios, such species are accumulated between the surface of the porous sample and the electrolyte, forming the EDL and consequently

creating a very intense electric field. In contrast to the previous scheme shown in Section 1.4, where the EDL was created on a flat surface (**Figure 1.9**), in our case, the samples were mesoporous materials, resulting in a more complex structure of the EDL. Moreover, electrolyte-gating configuration was chosen since the liquid electrolyte (PC) can eventually penetrate throughout the whole 3D porous structure of the porous samples, leading to exacerbated ME effects and avoiding the occurrence of pinholes. This structure can be influenced by entropy effects, implying non-homogeneous potential distributions.¹⁴ The hysteresis loops were measured at room temperature, either with MOKE or VSM, along the sample plane while applying different DC voltages using an external Agilent B2902A power supply. In the case of Co–Pt microdisks, magnetolectric measurements were performed in a MOKE set-up (**Figure 3.12b**) and in the case of the Co–Pt/oxide heterostructures, in a VSM set-up (**Figure 3.12a**).

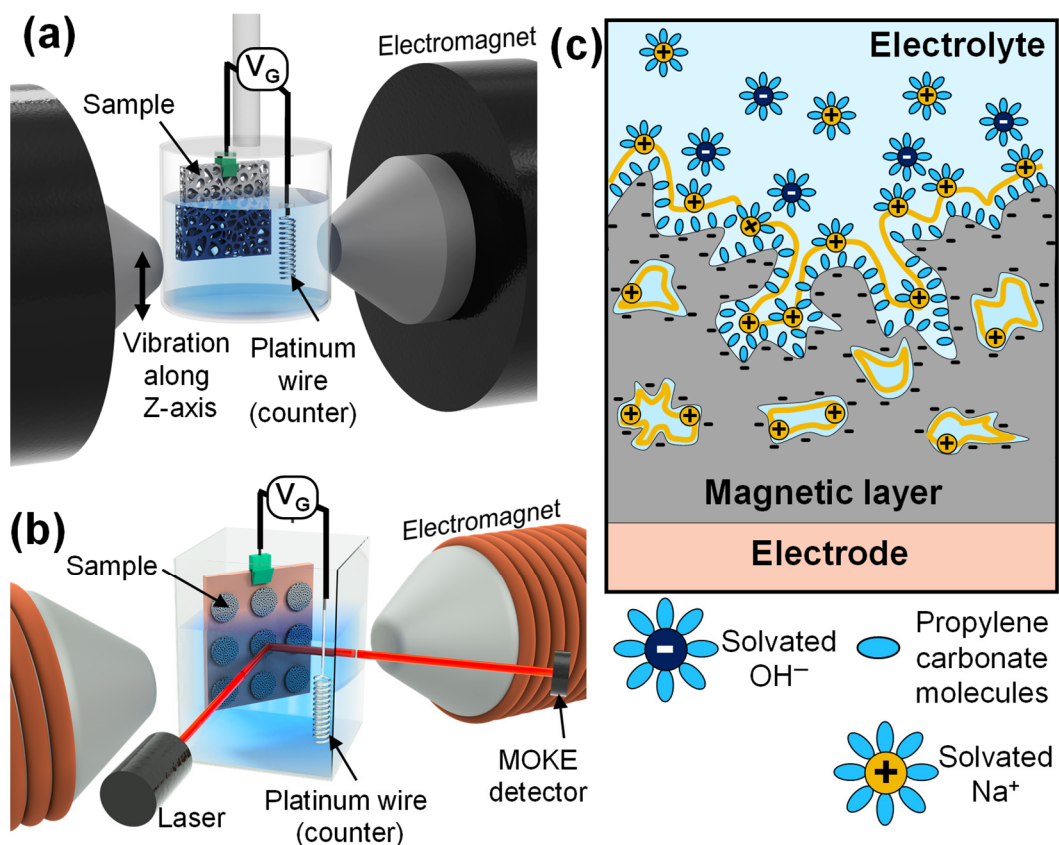


Figure 3.12. Schematic illustration of the experimental set-ups employed for the ME measurements in liquid configuration using (a) a VSM and (b) a MOKE set-up. (c) Scheme of the formation of the EDL onto the surface of a mesoporous magnetic layer (sample) and the electrolyte when the sample is subjected to a negative voltage. The electrolyte consists of propylene carbonate containing Na^+ and OH^- ions.

3.2.5. UV-Vis spectroscopy

UV-Vis spectroscopy was carried out on an HP8453 spectrophotometer (Hewlett-Packard). UV-Vis measurements were performed to investigate the evolution of $[\text{PtCl}_6]^{2-}$ complex in water with time. For that purpose, an aqueous solution of 0.0039 M $\text{Na}_2\text{PtCl}_6 \cdot 6\text{H}_2\text{O}$ was prepared and the UV-Vis transmittance spectra were recorded from 300 to 700 nm at different time intervals.

Bibliography

1. Egerton, R. F. Electron energy-loss spectroscopy in the TEM. *Reports Prog. Phys.* **72**, 016502 (2009).
2. Tan, H., Turner, S., Yücelen, E., Verbeeck, J. & Van Tendeloo, G. 2D atomic mapping of oxidation states in transition metal oxides by scanning transmission electron microscopy and electron energy-loss spectroscopy. *Phys. Rev. Lett.* **107**, 107602 (2011).
3. Ramasse, Q. M., Seabourne, C. R., Kepaptsoglou, D.-M., Zan, R., Bangert, U. & Scott, A. J. Probing the bonding and electronic structure of single atom dopants in graphene with electron energy loss spectroscopy. *Nano Lett.* **13**, 4989–4995 (2013).
4. Muller, D. A., Tzou, Y., Raj, R. & Silcox, J. Mapping sp^2 and sp^3 states of carbon at sub-nanometre spatial resolution. *Nature* **366**, 725–727 (1993).
5. Varela, M., Findlay, S. D., Lupini, A. R., Christen, H. M., Borisevich, A. Y., Dellby, N., Krivanek, O. L., Nellist, P. D., Oxley, M. P., Allen, L. J. & Pennycook, S. J. Spectroscopic imaging of single atoms within a bulk solid. *Phys. Rev. Lett.* **92**, 095502 (2004).
6. Oleshko, V. P. Electron energy-loss spectroscopy and imaging. *Ref. Modul. Chem. Mol. Sci. Chem. Eng.* **2**, 264–288 (Elsevier, 2018).
7. <https://eels.info/about/overview>.
8. <https://www.gatan.com/techniques/spectrum-imaging>.

9. Schnohr, C. S. & Ridgway, M. C. Introduction to X-ray Absorption spectroscopy. *X-ray Absorpt. Spectrosc. Semicond.* **190**, 1–26 (2015).
10. Van Bokhoven, J. A. & Lamberti, C. *X-ray absorption and x-ray emission spectroscopy: Theory and applications. X-ray absorpt. X-ray emiss. Spectrosc. Theory appl.* **1–2**, (2015).
11. Yano, J. & Yachandra, V. K. X-ray absorption spectroscopy. *Photosynth. Res.* **102**, 241–254 (2009).
12. *Neutron and Synchrotron Radiation for Condensed Matter Studies. Neutron Synchrotron Radiat. Condens. Matter Stud.* (Springer Berlin Heidelberg, 1994).
13. Van der Laan, G. & Figueroa, A. I. X-ray magnetic circular dichroism—A versatile tool to study magnetism. *Coord. Chem. Rev.* **277–278**, 95–129 (2014).
14. Ney, E. M., Hou, C.-H. & Taboada-Serrano, P. Calculation of electrical double layer potential profiles in nanopores from grand canonical monte carlo simulations. *J. Chem. Eng. Data* **63**, 2557–2566 (2018).



4

Results as
a compilation
of articles

4. Results as a compilation of articles

In this Chapter, the results obtained in the thesis are provided as a compendium of articles. A brief overview precedes each publication, while a comprehensive discussion of the results is present in the articles themselves.

4.1. Large magnetoelectric effects in electrodeposited nanoporous microdisks driven by effective surface charging and magneto-ionics

In this work, the coercivity and magnetic moment of nanoporous, as-prepared Co–Pt+CoO microdisks were drastically modified by subjecting them to an electric field (i.e. upon applying voltages of the order of +/- 10 V). A new material concept is proposed, which merges (i) enhanced electrostatic charge accumulation at the surface of the ultra-thin nanopore walls of the microdisks, and (ii) magneto-ionics, in which voltage-driven O^{2-} migration promotes a partial and controlled reduction from CoO to Co. This combination resulted in an unprecedented voltage control of the magnetic properties, which is very appealing for energy-efficient magnetic actuation.

The synthetic approach to prepare the nanoporous microdisks was based on the combination of micelle-assisted electrodeposition and photolithography. Nanoporous Co–Pt+CoO microdisks were grown in photolithographed patterned substrates by potentiostatic electrodeposition from an electrolyte containing metal chloride salts and Pluronic P123 tri-block copolymer. The block-copolymer was employed above its c.m.c. with the aim to induce nanoporosity, thus acting as structure-directing agent during the electrodeposition process. Moreover, neither pH buffers nor complexing agents were purposely added to the electrolyte to favor the introduction of oxygen in the microdisks in metal oxide state, resulting in a nanocomposite consisting of a Co-rich alloy and Co oxides. Morphological characterization revealed the formation of a mesoporous structure, both at the outer surface and along the entire thickness (300 nm) of the microdisks. Such Co–Pt/CoO structures exhibit a Co-rich composition (70 at. % Co) and a crystalline structure mainly consisting of hexagonal close packed (hcp) Co and rock-salt cubic CoO phases.

Magnetoelectric measurements were carried out by electrolyte-gating while monitoring in situ the magnetic changes in a MOKE set-up. The electric field was applied to the nanoporous Co–Pt+CoO microdisks via the formation of an EDL in an anhydrous organic

solvent (propylene carbonate) containing Na^+ and OH^- ions. A prominent reduction of H_c (88%) and a pronounced increase of Kerr signal (60%) was observed upon subjecting the microdisks to negative voltage. Such variations could be partially reversed by applying positive voltages or waiting sufficient time, even in absence of applied voltage.

The observed changes in the magnetic properties were attributed to a combination of charge accumulation and magneto-ionic effects. The large S/V ratio and the ultra-narrow pore walls of the system play a crucial role since the entire nanoporous structure is affected by the electric field and not only the outermost surface, resulting in remarkable voltage-induced effects. In addition, the oxygen present in the microdisks in the form of CoO , and the accumulated electrostatic charges effectively induce oxygen ionic motion, resulting in a partial reduction from CoO to Co , which was supported by XAS and EELS analyses.

Large magnetoelectric effects in electrodeposited nanoporous microdisks driven by effective surface charging and magneto-ionics

Cristina Navarro-Senent,^{*,†} Jordina Fornell,[†] Eloy Isarain-Chávez,[†] Alberto Quintana,[†] Enric Menéndez,[†] Michael Foerster,[‡] Lucía Aballe,[‡] Eugen Weschke,[§] Josep Nogués,^{||,⊥} Eva Pellicer,^{*,†} and Jordi Sort^{*,†,⊥}

[†]Departament de Física, Universitat Autònoma de Barcelona, E-08193 Cerdanyola del Vallès, Spain.

[‡]Alba Synchrotron Light Facility, CELLS, E-08280 Cerdanyola del Vallès, Spain

[§]Helmholtz-Zentrum Berlin für Materialien und Energie, Albert-Einstein-Strasse 15, D-12489 Berlin, Germany

^{||}Catalan Institute of Nanoscience and Nanotechnology (ICN2), CSIC and The Barcelona Institute of Science and Technology, Campus UAB, Bellaterra, E-08193 Barcelona, Spain

[⊥]ICREA, Pg. Lluís Companys 23, E-08010 Barcelona, Spain

Reproduced with permission from ACS Appl. Mater. Interfaces, 2018, 10, 44897–44905. Copyright 2020 American Chemical Society.

Large Magnetolectric Effects in Electrodeposited Nanoporous Microdisks Driven by Effective Surface Charging and Magneto-Ionics

Cristina Navarro-Senent,^{*,†} Jordina Fornell,[†] Eloy Isarain-Chávez,[†] Alberto Quintana,[†] Enric Menéndez,[†] Michael Foerster,[‡] Lucía Aballe,[‡] Eugen Weschke,[§] Josep Nogués,^{||,⊥} Eva Pellicer,^{*,†} and Jordi Sort^{*,†,⊥}

[†]Departament de Física, Universitat Autònoma de Barcelona, Cerdanyola del Vallès, E-08193 Barcelona, Spain

[‡]Alba Synchrotron Light Facility, CELLS, Cerdanyola del Vallès, E-08280 Barcelona, Spain

[§]Helmholtz-Zentrum Berlin für Materialien und Energie, Albert-Einstein-Strasse 15, D-12489 Berlin, Germany

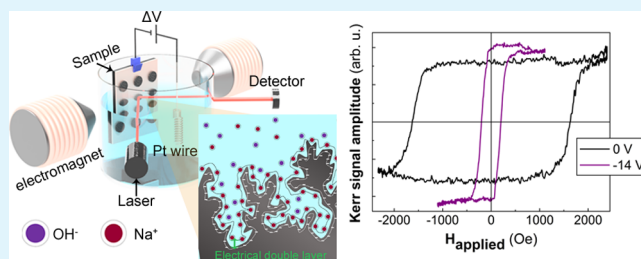
^{||}Catalan Institute of Nanoscience and Nanotechnology (ICN2), CSIC and The Barcelona Institute of Science and Technology, Campus UAB, Bellaterra, E-08193 Barcelona, Spain

[⊥]ICREA, Pg. Lluís Companys 23, E-08010 Barcelona, Spain

Supporting Information

ABSTRACT: A synergetic approach to enhance magneto-electric effects (i.e., control of magnetism with voltage) and improve energy efficiency in magnetically actuated devices is presented. The investigated material consists of an ordered array of Co–Pt microdisks, in which nanoporosity and partial oxidation are introduced during the synthetic procedure to synergetically boost the effects of electric field. The microdisks are grown by electrodeposition from an electrolyte containing an amphiphilic polymeric surfactant. The bath formulation is designed to favor the incorporation of oxygen in the form of cobalt oxide. A pronounced reduction of coercivity (88%) and a remarkable increase of Kerr signal amplitude (60%) are observed at room temperature upon subjecting the microdisks to negative voltages through an electrical double layer. These large voltage-induced changes in the magnetic properties of the microdisks are due to (i) the high surface-area-to-volume ratio with ultranarrow pore walls (sub-10 nm) that promote enhanced electric charge accumulation and (ii) magneto-ionic effects, where voltage-driven O^{2-} migration promotes a partial reduction of CoO to Co at room temperature. This simple and versatile procedure to fabricate patterned “nano-in-micro” magnetic motifs with adjustable voltage-driven magnetic properties is very appealing for energy-efficient magnetic recording systems and other magneto-electronic devices.

KEYWORDS: nanoporous material, magnetolectric actuation, Co–Pt alloy, patterned microstructures, magneto-ionic effects



1. INTRODUCTION

The advent of spintronics has revolutionized information recording strategies and has triggered the development of a number of innovative devices with an ultrahigh data storage capacity operating at ultrafast processing rates.^{1–4} However, energy consumption continues to be an important bottleneck in these devices. Conventional magnetic systems utilize magnetic fields to write information. The electric currents required to create such magnetic fields involve a significant energy loss in the form of heat dissipation (Joule effect). One method to overcome the need for external magnetic fields is to use spin-polarized currents (spin-torque effect).⁴ However, generation of spin-polarized currents is still energetically costly. The use of an applied voltage rather than magnetic fields or spin-polarized currents would represent a significant breakthrough to decrease power consumption.^{5–10}

Recent studies have reported on the possibility to tailor the magnetic properties of materials (e.g., magnetic anisotropy,

magnetization, or coercivity) with electric fields.^{6–8} There are various ways to manipulate magnetism using voltage: (i) development of single-phase multiferroics, in which magnetic and electric orders are mutually coupled;^{9,11} (ii) strain-mediated magnetolectric coupling in piezoelectric/magnetostrictive composites, where the voltage-induced strain in the piezoelectric is transmitted to the ferromagnetic counterpart via inverse magnetostriction;^{10,12–14} (iii) carrier modulation effect, where the electronic band structure (and, hence, the resulting magnetism) of ultrathin ferromagnetic films^{15–21} or magnetic semiconductors^{22–24} is modified due to the electrostatic charge accumulation at the surface; and (iv) magneto-ionics (i.e., ionic migration observed in some ferromagnetic metallic layers in direct contact with oxides such as Gd_2O_3 or

Received: October 6, 2018

Accepted: December 6, 2018

Published: December 6, 2018

HfO₂, which act as ion reservoirs by accepting or donating oxygen ions depending on the voltage polarity and strength^{25–30} or Fe₂O₃ systems, which have been exploited in multilevel memristor devices³¹). Each of these strategies suffers from its own limitations: (i) single-phase multiferroics operative at room temperature are quite scarce; (ii) strain in piezoelectric/magnetostrictive thin films is reduced due to the clamping with the substrate, and fatigue effects would also limit the endurance of an eventual strain-mediated spintronic device; (iii) surface charge accumulation in metallic films is limited by the Thomas–Fermi electric-field screening length (on the order of 0.5 nm),³² hence being only effective in ultrathin films; and (iv) magneto-ionics often requires thermal treatments (since ionic migration is thermally assisted) and it only occurs in some specific metal–metal oxide systems.^{25–30}

In this work, a new strategy to boost the effect of voltage on the magnetic properties at room temperature based on the combination of surface charge accumulation and magneto-ionic effects is reported. To this end, nanoporous Co–Pt microdisks with partly oxidized Co are prepared by electro-deposition and subsequently actuated with voltage in liquid configuration using anhydrous propylene carbonate (PC). The electric field is generated through the formation of an electrical double layer (EDL).³³ The induced nanoporosity allows the whole disks (not only the outer surface) to be magnetoelectrically active since although electric field is confined within the Thomas–Fermi screening length, the very narrow pore walls together with the use of a liquid dielectric (which can penetrate into the three-dimensional (3D) nanoporous architecture of the disks) promote a very effective accumulation of electrostatic charges in spite of the relatively large thickness of the Co–Pt microdisks (>300 nm). Remarkably, our previous works demonstrated that the coercivity of some nanoporous alloys (e.g., Cu–Ni³⁴ or Fe–Cu³⁵) can be considerably reduced with voltage (to ca. 32%), which already represented a significant improvement compared to seminal works in FePt and FePd ultrathin films, where the reported changes in coercivity were only of around 4.5%.¹⁵ In these works, the very narrow thickness of the EDL created at the interface between the sample and the electrolyte (of around 0.5 nm) is crucial since it allows the generation of very strong electric fields (on the order of tens of MV/cm) for moderate values of applied voltages (few voltage). High-density electron accumulation via EDL gating has been also demonstrated to be an effective way to enhance the ferromagnetic response of Co-doped TiO₂ epitaxial films.³⁶

Besides high surface electric charging, our work also takes advantage of magneto-ionic phenomena. So far, most works in the literature have used solid configurations (i.e., metallic ferromagnetic films adjacent to GdO_x or HfO₂ layers)^{25–30} in which oxygen ion migration has resulted in interesting magnetoelectric effects. Nevertheless, polar organic solvents (hence involving the formation of EDL) have been also utilized to promote changes of the magnetic properties of some oxide materials through controlled ion migration. For example, the saturation magnetization in CuFe₂O₄ and ZnFe₂O₄ films was varied at room temperature by electrochemically driven Li-ion exchange.³⁷ Similar changes were observed in Ni–Co with an adjacent HfO₂ layer when voltage was applied through an EDL.³⁸

Inspired by the above approaches (i.e., the benefit of nanoporosity to enhance charge accumulation and the use of an EDL to induce magneto-ionic effects at room temperature

in oxide materials), here we investigate the effects of voltage on the magnetic properties of nanoporous Co–Pt/CoO composite micropatterned structures. We have selected the Co–Pt system as the metallic counterpart for several reasons: (i) it constitutes the basis of some materials currently used in magnetic storage media (due to its high anisotropy and high coercivity, even with a limited amount of Pt in the alloy composition),^{39,40} (ii) magnetoelectric effects due to charge accumulation have been predicted in Co–Pt by means of density functional calculations,²⁰ (iii) it is known that Co–Pt is prone to incorporate oxygen in its structure during electro-deposition under specific conditions,^{41–43} and (iv) the orbital moment of Co–Pt and, thus, its anisotropy are known to be quite sensitive to the degree of oxidation.⁴⁴ The study was performed on patterned microdisks prepared by optical lithography and micelle-assisted electrodeposition as a first step toward the miniaturization of magnetoelectric devices and to eventually promote a further change of coercivity with voltage due to the enhanced surface-area-to-volume ratio.

The synthetic method to prepare the nanoporous disks is based on combining micelle-assisted electrodeposition with optical lithography. Micelle-assisted electrodeposition uses block-copolymer micelles as a soft template^{45,46} for inducing nanoporosity during the growth of the alloy within the photolithographed areas (as depicted in Figure 1a). The electrolyte contains neither a pH buffering agent nor a complexing agent so as to favor the growth of nanocomposite layers consisting of a Co-rich alloy and Co oxides. In the absence of pH buffering substances, solution alkalization at the cathode causes hydroxide/oxide precipitation. This way, oxygen can be introduced in the film in a metal oxide form. The designed composition and morphology lead to outstanding magnetoelectric/magneto-ionic effects: the coercivity (H_C) is reduced by 88% and the Kerr signal amplitude at saturation (designated as A_{Kerr}) increases by 60% by subjecting the nanoporous Co–Pt disks to a negative voltage. The initial values of H_C and A_{Kerr} tend to be progressively recovered after the applied voltage is removed. Observation of these effects in lithographed structures (not only in continuous porous films, as in previous works^{34,35}) paves the way toward the development of magneto-ionic voltage-controlled micrometer-sized devices.

2. RESULTS AND DISCUSSION

2.1. Morphology and Structure of the Electrodeposited Nanoporous Co–Pt/CoO Microdisks.

Nanoporous Co–Pt microdisks with $55 \pm 2 \mu\text{m}$ in diameter and $309 \pm 10 \text{ nm}$ in thickness were synthesized by electrodeposition from a chloride electrolyte on photolithographed Cu/Ti/Si substrates (see the Experimental Section). A representative scanning electron microscopy (SEM) image of a couple of nanoporous Co–Pt microdisks is shown in Figure 1b. When a single microdisk was imaged at a higher magnification, a morphology consisting of acicular grains with a large amount of small pores between them (i.e., mesoporosity) was observed on top (Figure 1c). This acicular morphology has often been reported in dense electrodeposited Co-based alloys (Co–Ni, Co–Mo, Co–Pt).^{47,48} Interestingly, here, the needlelike morphology remains in spite of the perturbation caused by the micelles during cations discharge and electrocrystallization. Further structural analysis was carried out by transmission electron microscopy (TEM), where the cross section of the Co–Pt microdisks reveals the occurrence of tiny nanopores of

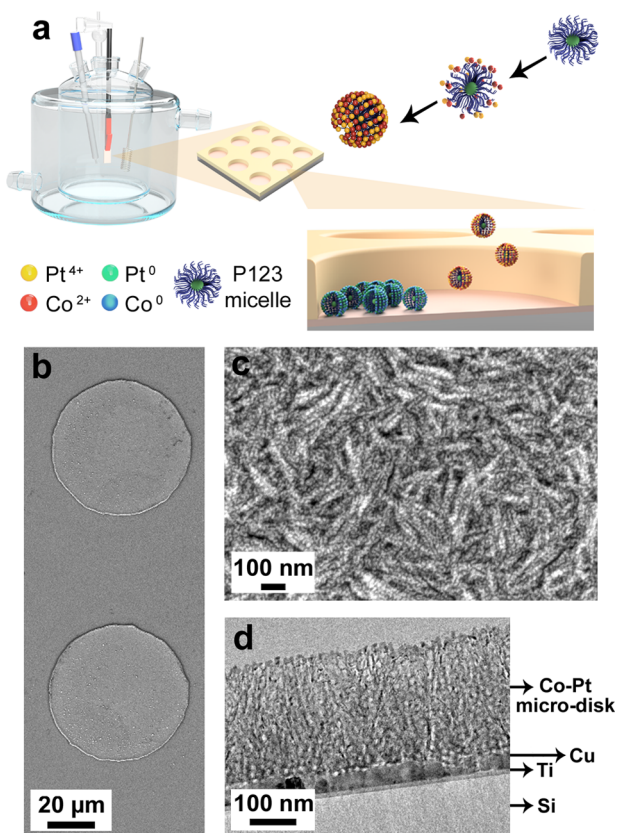


Figure 1. (a) Scheme of the micelle-assisted electrodeposition of Co–Pt/CoO on photolithographed substrates in a three-electrode electrochemical cell, wherein the dissolved metal species coordinate to the hydrophilic shell domains of the Pluronic P-123 triblock micelles; the metallic cations reduce in the conductive voids of the patterned substrate. (b) Scanning electron microscopy (SEM) image of two nanoporous Co–Pt microdisks. (c) High-resolution SEM image of a microdisk surface. (d) Cross-section transmission electron microscopy (TEM) image of a microdisk.

less than 10 nm in diameter all along the thickness of the disks, confirming that nanoporosity fully develops from the bottom

to the top of the microdisks (Figure 1d). A columnar-like growth was also apparent from magnified cross-section TEM images (Figure 2a). Compositional analyses of the microdisks by energy-dispersive X-ray (EDX) spectroscopy (see the Supporting Information, Figure S1) revealed an average composition of $\text{Co}_{70}\text{Pt}_{30}$ (in at. %) when only the metallic fraction of the deposit was considered. Furthermore, a significant amount of oxygen (20 at. %) was also detected by EDX, thus confirming the presence of metal oxides in the motifs. The elemental atomic percentages in the microdisks are shown in Table S1 of the Supporting Information. High-resolution transmission electron microscopy (HRTEM) also revealed that the microdisks are nanocrystalline. Lattice fringes were observed in clusters of around 5–10 nm (Figure 2b), which correspond to the thickness of the pore walls. According to selected area electron diffraction (SAED) analysis (Figure 2c), the nanoporous Co–Pt microdisks consist mainly of a mixture of three phases: (i) hexagonal closed-packed (hcp) Co (space group $P6_3/mmc$), (ii) cubic CoO phase (space group $Fm\bar{3}m$), and (iii) intermetallic Co_3Pt (space group $Fm\bar{3}m$). Note that the interplanar distances (d_{hkl}) of the rings assigned to the hcp-Co phase were slightly shifted toward higher values with respect to those of pure hcp-Co, suggesting that a fraction of Pt was dissolved in the hcp-Co lattice.

2.2. Magnetoelectric Measurements. The effect of an externally applied electric field on the magnetic properties of the nanoporous Co–Pt/CoO microdisks was investigated by subjecting the sample to different constant voltages and measuring the hysteresis loops by magneto-optic Kerr effect (MOKE). As depicted schematically in Figure 3a, the sample was placed in an electrolytic cell, which contained a Pt wire as the counter electrode and anhydrous propylene carbonate (PC) with Na^+ and OH^- ions as the electrolyte. Anhydrous PC is liquid enough at room temperature to properly penetrate into the pores and wet the whole sample and is broadly used not only in battery applications^{49,50} but also in magneto-electrically actuated systems.^{15,34,35,51,52} Na^+ and OH^- ions were formed after making residual water in the PC react with metallic Na. This procedure was aimed at: (i) removing any traces of water to minimize uncontrolled oxidation of the Co–

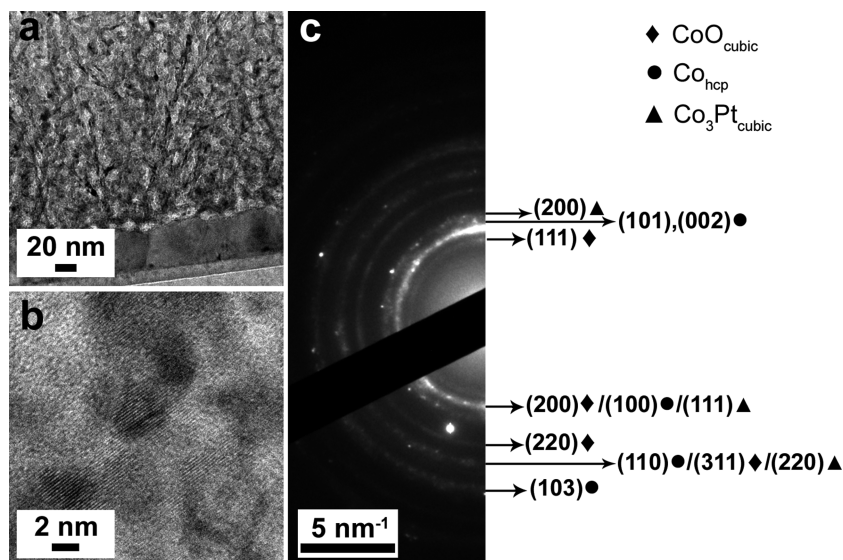


Figure 2. (a) TEM and (b) HRTEM images of the cross section of a nanoporous Co–Pt microdisk. (c) Corresponding SAED pattern.

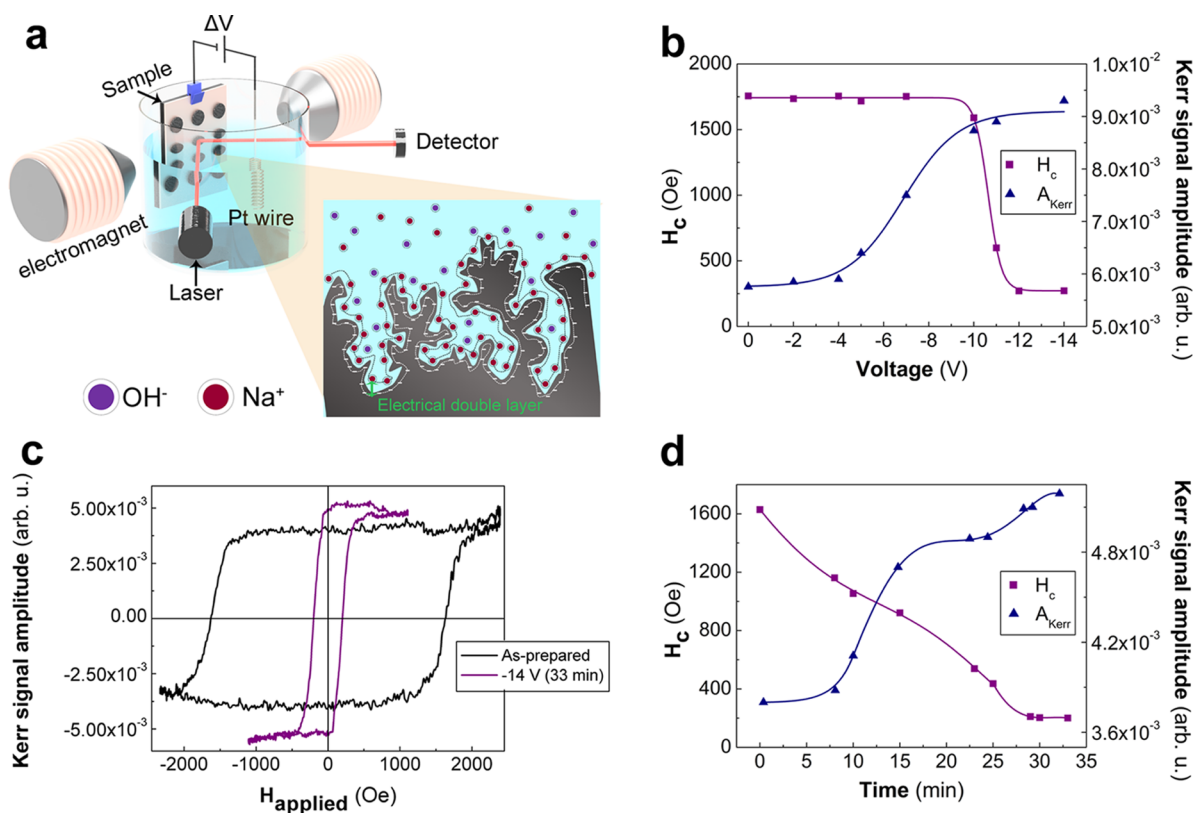


Figure 3. (a) Schematic drawing of the experimental setup used for the magneto-electric measurements together with an illustration of the formation of the electrical double layer (EDL) at the interface between the nanopores and the electrolyte when the sample is subjected to a negative voltage adapted from ref 34. (b) Dependence of the coercivity (H_C) and Kerr amplitude signal at saturation (designated as A_{Kerr}) on the applied negative voltage for a fixed time of 10 min at each voltage value. (c) Representative hysteresis loops of the nanoporous Co–Pt/CoO microdisks measured at 0 V (black loop) and after applying -14 V for 33 min (purple loop). (d) Dependence of H_C and A_{Kerr} on the time during which a fixed voltage -14 V was applied. The lines in panels (b) and (d) are guides to the eye.

Pt alloy and (ii) promoting the formation of the EDL, thus enhancing the magnitude of the electric field at the nanopore wall–electrolyte interface (Figure 3a). A current vs voltage profile compatible with the charge and discharge of the electric double layer was observed in the cyclic voltammetry curves taken in the electrolyte used to investigate microdisks' performance (Figure S4 of the Supporting Information).

First, hysteresis loops were recorded by focusing the laser spot onto a nanoporous Co–Pt disk, applying different negative voltages ranging from 0 to -14 V after waiting for 10 min at each voltage value. The dependence of H_C and A_{Kerr} on the applied voltage is shown in Figure 3b (the corresponding hysteresis loops are plotted in Figure S2 of the Supporting Information). Note that the Kerr signal amplitude is, in a first approximation, proportional to the magnetic moment. Substantial effects were observed after overcoming threshold voltages of -5 and -10 V for A_{Kerr} and H_C , respectively. Remarkably, H_C was reduced by 85% (from 1756 to 271 Oe), whereas A_{Kerr} increased by 60% with respect to its initial value. A time effect must be also considered since the time was accumulative due to the stepwise increase of voltage.

In a second series of measurements, carried out on a different sample, voltage was fixed at -14 V, and hysteresis loops were recorded varying the amount of time during which the voltage was applied (Figures 3c and S2 in the Supporting Information). Clear narrowing of the hysteresis loops was again observed after a few minutes, yielding a maximum

relative variation of 88% in H_C (from 1629 to 202 Oe) and a relative change of 30% in A_{Kerr} after 33 min (Figure 3d). Note that the relative variations in H_C and A_{Kerr} tend to level off after 27 min.

Next, the recovery process was investigated while keeping the sample immersed in the electrolyte. After having applied -14 V for 33 min, voltage was withdrawn, and after 3 h at 0 V, H_C increased by 109% (from 202 to 424 Oe, recovering up to 26% of the initial value), whereas A_{Kerr} decreased, tending to approach the initial value at 0 V. After 1 day at 0 V, H_C increased up to 607 Oe, showing a recovery of 37% of the initial value (see the Supporting Information, Figure S3). A further increase of H_C was obtained after long-term waiting at 0 V ($H_C = 1400$ Oe after 1 month), evidencing the slow dynamics of the recovery process at 0 V. The observed nontotal recovery at 0 V proves that the mechanism responsible for the observed magnetic changes involves some structural changes in the sample, and the induced effects can only be erased by applying positive voltages. Faster reversibility in the H_C and A_{Kerr} trends was attained by applying positive voltages. The coercivity increased up to 772 Oe applying $+2$ V for 10 min, and $H_C = 860$ Oe was measured after applying $+10$ V for 10 min (recovering 52% of the initial value). Unfortunately, degradation and polymerization of the propylene carbonate at the surface of the porous alloy were observed for voltages above $+10$ V, hence hampering further analysis at positive voltages by MOKE due to lack of reflectivity. It is important to emphasize that similar variations

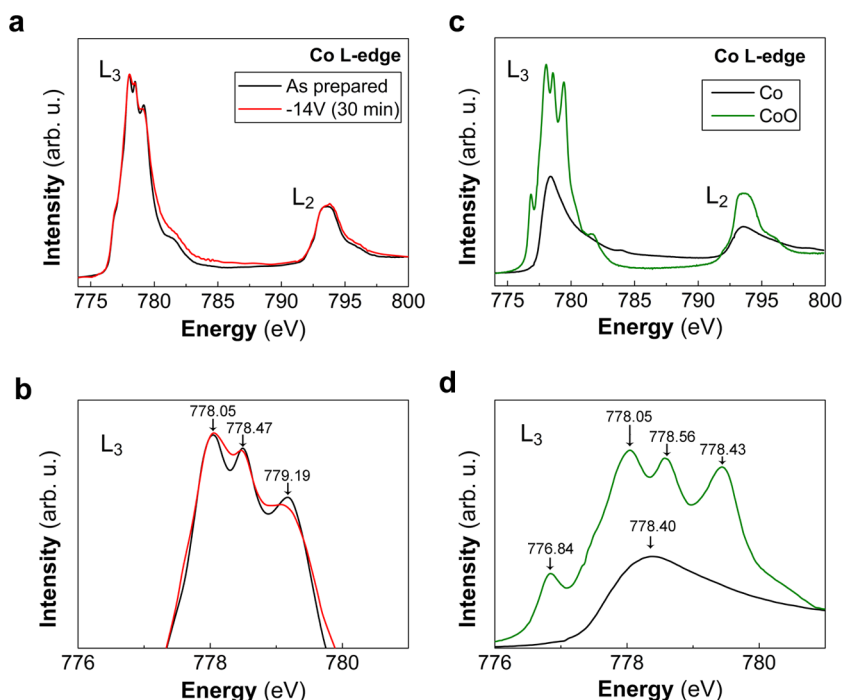


Figure 4. (a) Cobalt L-edge X-ray absorption spectra (XAS) of the nanoporous Co–Pt microdisks before (black curve) and after (red curve) applying -14 V for 10 min. (b) Zoom-in of the cobalt L_3 -edge where the energy position of the main peaks is indicated. (c) Cobalt $L_{2,3}$ -edges XAS spectra for reference samples (in black: 20 nm-thick Co thin, capped with 2 nm of Ta, grown by molecular beam epitaxy on top of a $\langle 100 \rangle$ -oriented MgO single crystal; in green: CoO (cobalt(II) oxide, 95%) powders from Alfa Aesar). (d) Zoom-in of the cobalt L_3 -edge for the two reference samples with the corresponding energies of the main peaks indicated.

on the magnetic properties with voltage were obtained by performing the same magneto-electric measurements on the same sample several months later, demonstrating the long lifetime of the nanoporous Co–Pt microdisks.

Given the nanoporous nature of the investigated material, one plausible physical origin for the observed changes in H_C could be eventual variations in the magnetic anisotropy energy (MAE) due to the effective electric charge accumulation at the surface of the pore walls. In fact, density functional theory calculations for the Co–Pt system have predicted a linear dependence of the MAE on the electric field,^{6,20,53} which could lead to variations in H_C . However, there are several aspects that indicate that the effects observed here cannot be simply ascribed to changes in the electronic band structure of Co–Pt induced by voltage. First, according to the theory, the response of the magnetocrystalline anisotropy (therefore H_C) to an applied voltage should be rather instantaneous and fully reversible (i.e., the dynamics of the system should be much faster than what is observed). Second, no significant changes in A_{Kerr} are to be expected due to changes in the MAE. Third, our previous works on voltage-actuated nanoporous Cu–Ni and Fe–Cu alloys (with minimized oxygen content) led to relative variations in H_C of at most 32%.^{34,35} Finally, important variations in A_{Kerr} occur already at lower applied voltages (-5 V) than the changes in H_C , which start to be visible at -10 V (see Figure 3b). Thus, an additional process is likely to dominate over the voltage-driven modification of the MAE related to the surface electric field. Given the presence of large amounts of oxygen in the as-prepared deposits, pronounced O^{2-} migration (magneto-ionic effect)^{25–30,43} is probably induced by voltage. The interplay between several additional possible magneto-electric mechanisms in oxide materials immersed in electrolytes (e.g., $\gamma\text{-Fe}_2\text{O}_3$) has been discussed

by several authors.⁵⁴ Although redox reactions due to the use of aqueous electrolytes should be essentially ruled out in the present study, some minor effect stemming from elastic strain on the magnetic properties (due to the alteration of the atomic bonding caused by the charge accumulation) could still be present in our case, given the nanoporous nature of the investigated sample. Nevertheless, although *ab initio* studies predict variations in the magnetic properties around several percents due to magnetoelastic effects,⁵⁵ the reported experimental changes so far have been between 0.5 and 3%, much lower than in our results.^{56,57} This, together with the in-depth structural characterization reported in the following sections, indicates that magneto-ionics is the most prominent mechanism responsible for the large magneto-electric effects observed in our system.

2.3. Soft X-ray Absorption Characterization. To demonstrate the magneto-ionic origin of the obtained results, further chemical characterization by X-ray absorption spectroscopy (XAS) spectromicroscopy was performed on a single microdisk at the CIRCE beamline of the ALBA Synchrotron at the Co $L_{2,3}$ edges (Figure 4). The XAS spectrum before voltage application exhibits a multiplet structure at the L_3 edge and an asymmetric contribution at the L_2 edge. This pattern is basically consistent with the CoO reference XAS⁵⁸ (see Figure 4c) although the relative intensity of the various peaks in the L_3 multiplet structure is not the same in the Co–Pt/CoO nanoporous disks and the CoO reference sample. This, together with the absence of a prominent L_3 prepeak at around 776 eV (which is a fingerprint of pure CoO), suggests the coexistence of CoO with metallic Co, in agreement with the SAED characterization, where both metallic and oxide phases were encountered (Figure 2c).

After applying -14 V for 40 min and removing the sample from the electrolyte (since XAS was performed ex situ, 30 min elapsed before starting the XAS measurements), the multipeak structure at the Co L_3 edge tends to smear out compared to the untreated sample (see Figure 4b). This suggests that after negative voltages, the amount of metallic Co increases at the expense of the CoO (note that metallic Co does not show the multipeak structure, Figure 4c,d).⁵⁸ The partial reduction from CoO to Co is consistent with the increase of the Kerr amplitude signal shown in Figure 3 since nanostructured CoO is likely paramagnetic at room temperature (note that bulk CoO has a Néel temperature of around 291 K).^{59,60}

2.4. Electron Energy Loss Spectroscopy (EELS) Characterization. Further characterization by electron energy loss spectroscopy (EELS) was employed to investigate the voltage-driven modifications of the spatial distribution of cobalt and oxygen in the Co–Pt microdisks at a local length scale. For this, a lamella was prepared by focused ion beam (FIB) and treated with voltage (see the Experimental Section). A scanning transmission electron microscopy (STEM) image of a cross-section of the film is shown in Figure 5a,b together

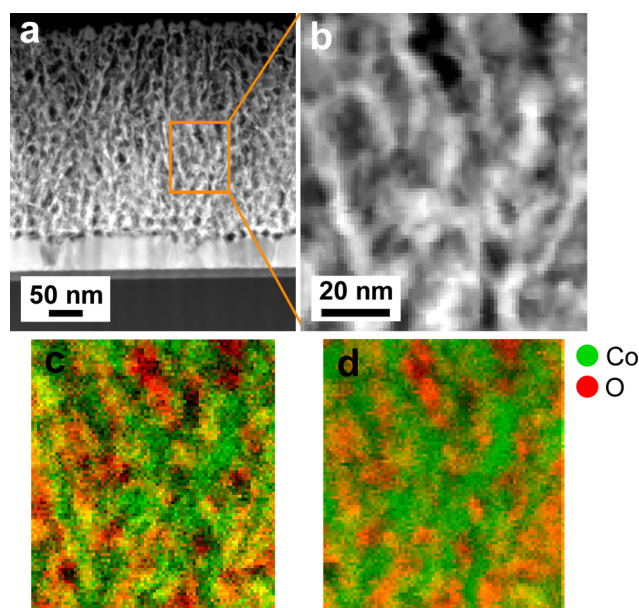


Figure 5. (a) STEM image of a cross section of a nanoporous Co–Pt microdisk and (b) zoomed detail of the region enclosed in the orange box. The corresponding cobalt (green) and oxygen (red) EELS mappings are shown in (c) for the as-prepared sample and (d) after applying -14 V for 40 min.

with the corresponding Co (green) and O (red) EELS mappings in the as-prepared state (Figure 5c) and after applying -14 V (Figure 5d). In the as-prepared sample, green regions are less defined and often superimposed to red pixels (rendering a yellowish color). The green regions are metallic Co, whereas the yellowish-like regions (superposition of green and red) correspond to CoO. Note that there are some red areas as well (without being superimposed to green), which correspond to the pores filled with tetraethyl orthosilicate (TEOS), which was used during the STEM lamella preparation (see the Experimental Section). After the microdisk is subjected to -14 V, Co-rich regions become more clearly visible and tend to expand due to the voltage-driven O and Co redistribution, which results in enlarged Co metallic

regions for negative voltages, in agreement with the XAS results (Figure 4).

The partial reduction from CoO to metallic Co can explain the decrease of coercivity. First, it is unlikely that the newly formed Co (after application of negative voltages) becomes readily alloyed with Pt, and pure Co is known to typically exhibit lower H_C than hcp Co–Pt (although H_C is not an intrinsic parameter and is, of course, also dependent on the actual microstructure of the investigated material). Additionally, since the Co-rich magnetic regions increase in size during the voltage treatment (eventually coalescence can occur, as indicated in Figure 6), this also induces a decrease of the

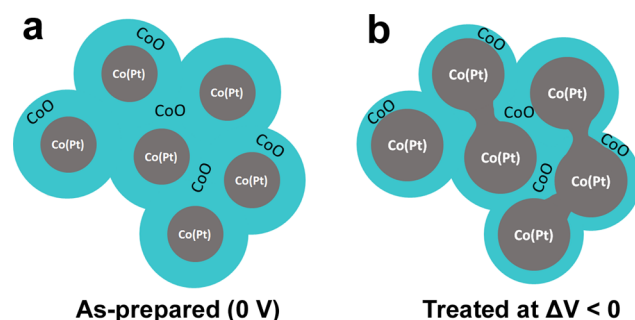


Figure 6. Schematic drawing of (a) as-prepared state (0 V) and (b) treated at $-\Delta V$ to illustrate that upon application of the negative voltage, Co(Pt) metallic regions tend to grow (and eventually become more interconnected) at the expense of CoO.

coercivity since H_C is inversely proportional to the volume of the magnetic material above the critical single-domain size.⁶¹ For isolated and isotropic Co particles, the formation of domain walls was reported above an average size of 55 nm (a bit larger critical sizes were reported for elongated particles).⁶² Although here the geometry of the alloy microdisks is much more complex than in the case of isolated particles, the interconnection and growth of the metallic counterparts within the three-dimensional nanoporous frameworks are likely to also cause a decrease of H_C .

Additionally, dipolar interactions among the different Co-rich clusters (which also cause a reduction of H_C)^{63,64} are less pronounced in the as-prepared films since CoO tends to isolate the different magnetic zones. As the thickness of the CoO regions decreases, the average distance between the ferromagnetic clusters decreases (see Figure 6b) and, consequently, H_C lowers due to the enhancement of dipolar interactions. Finally, the reduction of the amount of oxygen in the Co–Pt alloy should also decrease its orbital moment (usually linked with the anisotropy), hence also contributing to the decrease in H_C .⁴⁴

3. CONCLUSIONS

In summary, large electric-field effects have been observed in nanoporous Co–Pt/CoO microdisks prepared by micelle-assisted electrodeposition using optically lithographed substrates. The micrometer size of the disks and their nanoporous structure play an essential role in the magnetoelectric effect due to the resulting large surface-area-to-volume ratio. The presence of CoO allows for oxygen migration under the influence of the electric field. This combination allows for an unprecedented voltage control of magnetism, which is very appealing for energy-efficient magnetic actuation. Indeed, drastic changes in coercivity and the Kerr signal amplitude at

saturation are observed at room temperature by subjecting the Co–Pt/CoO disks to a negative applied voltage using an anhydrous electrolyte. Such variations are attributed to the effective electric charge accumulation at the surface of the ultrathin pore walls and the concomitant magneto-ionic effect, which results in partial reduction from CoO to Co. The reported approach can be extrapolated to other magnetic systems to foster electric-field control of magnetism in technologically relevant applications such as spintronics and magnetic actuators.

4. EXPERIMENTAL SECTION

4.1. Materials. Hydrochloric acid (HCl, 37 wt %), isopropyl alcohol (C₃H₈O, 99.9%), acetone (99.0%), absolute ethanol (99.8%), Na₂PtCl₆·6H₂O (sodium hexachloroplatinate(IV) hexahydrate, 98.0%), CoCl₂ (cobalt(II) chloride anhydrous, ≥98.0%), and Pluronic P-123 (HO(CH₂CH₂O)₂₀(CH₂CH(CH₃)-O)₇₀(CH₂CH₂O)₂₀H) block copolymer were purchased from Sigma-Aldrich. All the reagents were used as received without further purification. AZ-9260 Photoresist and AZ-400 K Developer were purchased from Merck Performance Materials GmbH. Deionized water was obtained through an EMD Millipore Simplicity Water Purification System (Millipore S.A.S., Molsheim 67120, France).

4.2. Nanoporous Co–Pt/CoO Microdisk Growth. Electrodeposition of Co–Pt was performed on prelithographed Cu (70 nm)/Ti (10 nm)/Si substrates. Prior to patterning, the substrates were degreased with acetone, isopropanol, and Milli-Q water in consecutive steps. Arrays of cylindrical holes of 50 μm in diameter and 5 μm in height were patterned by optical lithography using photoresist AZ-9260 and AZ-400 developers. Subsequently, the patterned areas were used as templates for the electrodeposition of Co–Pt microdisks. Electrodeposition was performed in a three-electrode single-compartment cell connected to a PGSTAT302N Autolab potentiostat/galvanostat (Metrohm-Autolab). A Pt spiral served as the counter electrode, and an Ag/AgCl double junction ($E = +0.210$ V standard hydrogen electrode), with 3 M KCl inner solution and 1 M NaCl outer solution, was employed as the reference electrode (Figure 1a). The electrolyte was prepared with Milli-Q water and contained 1.3 mM Na₂PtCl₆·6H₂O, 2.8 mM CoCl₂, and 1 mg/mL (1 wt %) of Pluronic P-123. The pH was adjusted to 2.1 with HCl solution. The block-copolymer P-123 was used above its critical micellar concentration⁶⁵ to ensure the formation of micelles in the aqueous electrolyte. These micelles interact with the metal ions in solution, and once adsorbed on the patterned holes of the working electrode, the discharge of the cations results in the formation of the nanoporous film (Figure 1a). Importantly, the electrolyte did not contain a pH buffering agent so as to favor the growth of a nanocomposite coating consisting of a Co-rich alloy and Co oxides. In the absence of pH buffering agents, solution alkalization at the cathode causes hydroxide/oxide precipitation. Therefore, oxygen can be incorporated in the film, forming oxides. Electrodeposition was conducted potentiostatically at -1.0 V for 350 s, under mild stirring ($\omega = 100$ rpm) and simultaneous bubbling of N₂ through the solution. The temperature of the electrolyte was kept at 25 °C by circulating water through the outer jacket of the electrolyte cell using an F12 Julabo thermostat. A representative current–time curve is shown in the Supporting Information (Figure S5). Finally, the photoresist was removed by immersing the samples in acetone, followed by a final rising in isopropanol and Milli-Q water.

4.3. Morphology and Structural Characterization. The morphology of the nanoporous Co–Pt microdisks was examined by field emission scanning electron microscopy (FE-SEM) using a Zeiss MERLIN operated at 5 kV. Compositional analysis was performed by energy-dispersive X-ray spectroscopy (EDX) using the FE-SEM operated at 15 kV. The crystal structure was investigated by means of high-resolution transmission electron microscopy (HRTEM) and selected area electron diffraction (SAED) utilizing a JEOL-JEM 2011 operated at 200 kV. Further morphological and compositional

characterization along the cross section of a microdisk was carried out by electron energy loss spectroscopy (EELS) analysis on a Tecnai F20 HRTEM/STEM microscope. TEM, STEM, and EELS analyses were performed on the cross section of the disks, from a lamella prepared by focused ion beam (FIB) (Crossbeam 1560XB from Zeiss with an ion column Canion from Orsay Physics). To prepare the lamella, the nanoporous film was capped with a 2 μm-thick TEOS layer, and a slice of material with dimensions of approximately 1×10 μm² was then cut and glued onto a TEM grid to be further thinned down to 100 nm using 5 kV and a low current (50 pA). To assess the influence of voltage on the microstructure of the nanoporous films, EELS analyses were performed before and after subjecting the lamella to -14 V for 40 min in the same electrolyte used for the magnetolectric measurements.

4.4. Soft X-ray Absorption Spectroscopy Characterization. The chemical composition and oxidation state of the nanoporous Co–Pt microdisks were determined by soft X-ray absorption spectra (XAS) (Co L_{3,2} edge), measured in total electron yield mode and using linearly polarized light, in the beamline BL24-CIRCE at the ALBA Synchrotron.⁶⁶ The XAS patterns of reference Co (20 nm-thick Co thin film, capped with 2 nm of Ta, grown by molecular beam epitaxy on top of a <100>-oriented MgO single crystal) and CoO (cobalt(II) oxide, 95%, powders from Alfa Aesar) samples were also acquired for comparison.

4.5. Magnetolectric Measurements. In-plane hysteresis loops at different values of applied DC voltage were acquired at room temperature in situ in a magneto-optical Kerr effect (MOKE) setup from Durham Magneto-Optics. An Agilent B2902A power supply was employed as the voltage source. The sample was mounted vertically on a poly(methyl methacrylate) holder placed in a quartz SUPRASIL cell filled with anhydrous propylene carbonate containing Na⁺ and OH⁻ ions. The anhydricity of the electrolyte minimized the occurrence of extrinsic oxidation or corrosion events in the Co–Pt microdisks during magnetolectric measurements. To remove any traces of residual water in the electrolyte, this was treated with metallic sodium. To prepare the electrolyte, a piece of metallic sodium was immersed in a flask containing PC (the metallic Na was in excess to the water molecules present in the PC), which was then stored in a glovebox. To be able to perform the magnetolectric measurements, the quartz cell was filled with the electrolyte using a syringe. Between each increase or decrease of the applied voltage, a minimum waiting time of 300 s was taken before the hysteresis loop was measured (in situ) to enable the electrolyte to diffuse through the nanopores and permit the formation of the electrical double layer within the entire 3D network.

■ ASSOCIATED CONTENT

Supporting Information

The Supporting Information is available free of charge on the ACS Publications website at DOI: 10.1021/acsami.8b17442.

EDX data, electron diffraction data, MOKE measurements, cyclic voltammetry experiments and electro-deposition curve (PDF)

■ AUTHOR INFORMATION

Corresponding Authors

*E-mail: Cristina.navarro@e-campus.uab.cat (C.N.-S.).

*E-mail: Eva.Pellicer@uab.cat (E.P.).

*E-mail: Jordi.Sort@uab.cat (J.S.).

ORCID

Alberto Quintana: 0000-0002-9813-735X

Eva Pellicer: 0000-0002-8901-0998

Jordi Sort: 0000-0003-1213-3639

Author Contributions

The manuscript was written through contributions of all authors. All authors have given approval to the final version of the manuscript.

Notes

The authors declare no competing financial interest.

ACKNOWLEDGMENTS

This work was funded by the European Research Council under the SPIN-PORICS 2014-Consolidator Grant (Agreement No. 648454), the Generalitat de Catalunya (2017-SGR-292 project), the Spanish Government (MAT2017-86357-C3-1-R, MAT2014-57960-C3-1-R, and associated FEDER projects), and the European Union's Horizon 2020 research and innovation program under the Marie Skłodowska-Curie grant agreement No. 665919. J.F. and E.P. acknowledge the Juan de la Cierva (IJCI-2015-27030) and Ramon y Cajal (RYC-2012-10839) fellowships, respectively, from MINECO. The ICN2 is funded by the CERCA program/Generalitat de Catalunya. ICN2 also acknowledges the support from the Severo Ochoa Program (MINECO, grant SEV-2013-0295).

REFERENCES

- (1) Žutić, I.; Fabian, J.; Sarma, S. D. Spintronics: Fundamentals and Applications. *Rev. Mod. Phys.* **2004**, *76*, 323–410.
- (2) Wolf, S. A. Spintronics: A Spin-Based Electronics Vision for the Future. *Science* **2001**, *294*, 1488–1495.
- (3) Chappert, C.; Fert, A.; Dau, F. N. V. The Emergence of Spin Electronics in Data Storage. *Nat. Mater.* **2007**, *6*, 813–823.
- (4) Dieny, B.; Sousa, R.; Herault, J.; Pappas, C.; Prenat, G.; Ebels, U.; Houssameddine, D.; Rodmacq, B.; Auffret, S.; Prejbeanu, L. B.; Cyrille, M.; Delaet, B.; Redon, O.; Ducruet, C.; Nozieres, J. P.; Prejbeanu, I. Spin-Transfer Effect and Its Use in Spintronic Components. *Int. J. Nanotechnol.* **2010**, *7*, 591–614.
- (5) Hu, J.-M.; Li, Z.; Chen, L.-Q.; Nan, C.-W. High-Density Magnetoresistive Random Access Memory Operating at Ultralow Voltage at Room Temperature. *Nat. Commun.* **2011**, *2*, No. 553.
- (6) Brovko, O. O.; Ruiz-Díaz, P.; Dasa, T. R.; Stepanyuk, V. S. Controlling Magnetism on Metal Surfaces with Non-Magnetic Means: Electric Fields and Surface Charging. *J. Phys.: Condens. Matter* **2014**, *26*, No. 093001.
- (7) Song, C.; Cui, B.; Li, F.; Zhou, X.; Pan, F. Recent Progress in Voltage Control of Magnetism: Materials, Mechanisms, and Performance. *Prog. Mater. Sci.* **2017**, *87*, 33–82.
- (8) Duschek, K.; Pohl, D.; Fähler, S.; Nielsch, K.; Leistner, K. Research Update: Magnetoionic Control of Magnetization and Anisotropy in Layered Oxide/Metal Heterostructures. *APL Mater.* **2016**, *4*, No. 032301.
- (9) Eerenstein, W.; Mathur, N. D.; Scott, J. F. Multiferroic and Magnetoelectric Materials. *Nature* **2006**, *442*, 759–765.
- (10) Wang, Y.; Hu, J.; Lin, Y.; Nan, C.-W. Multiferroic Magnetoelectric Composite Nanostructures. *NPG Asia Mater.* **2010**, *2*, 61–68.
- (11) Lu, C.; Hu, W.; Tian, Y.; Wu, T. Multiferroic Oxide Thin Films and Heterostructures. *Appl. Phys. Rev.* **2015**, *2*, No. 021304.
- (12) Brivio, S.; Petti, D.; Bertacco, R.; Cezar, J. C. Electric Field Control of Magnetic Anisotropies and Magnetic Coercivity in Fe/BaTiO₃(001) Heterostructures. *Appl. Phys. Lett.* **2011**, *98*, No. 092505.
- (13) Liu, Y.; Hu, F.-X.; Zhang, M.; Wang, J.; Shen, F.-R.; Zuo, W.-L.; Zhang, J.; Sun, J.-R.; Shen, B.-G. Electric Field Control of Magnetic Properties of Nd₂Fe₁₄B Thin Films Grown onto PMN-PT Substrates. *Appl. Phys. Lett.* **2017**, *110*, No. 022401.
- (14) Fina, I.; Quintana, A.; Padilla-Pantoja, J.; Martí, X.; Macià, F.; Sánchez, F.; Foerster, M.; Aballe, L.; Fontcuberta, J.; Sort, J. Electric-Field-Adjustable Time-Dependent Magnetoelectric Response in

Martensitic FeRh Alloy. *ACS Appl. Mater. Interfaces* **2017**, *9*, 15577–15582.

- (15) Weisheit, M.; Fahler, S.; Marty, A.; Souche, Y.; Poinson, C.; Givord, D. Electric Field-Induced Modification of Magnetism in Thin-Film Ferromagnets. *Science* **2007**, *315*, 349–351.

- (16) Koyama, T.; Chiba, D. Influence of the Magnetization Reversal Mechanism on the Electric Field Modulation of Coercivity in Pt/Co Structures. *Phys. Rev. B* **2017**, *96*, No. 224409.

- (17) Chiba, D.; Ono, T. Control of Magnetism in Co by an Electric Field. *J. Phys. D: Appl. Phys.* **2013**, *46*, No. 213001.

- (18) Chiba, D.; Fukami, S.; Shimamura, K.; Ishiwata, N.; Kobayashi, K.; Ono, T. Electrical Control of the Ferromagnetic Phase Transition in Cobalt at Room Temperature. *Nat. Mater.* **2011**, *10*, 853–856.

- (19) Maruyama, T.; Shiota, Y.; Nozaki, T.; Ohta, K.; Toda, N.; Mizuguchi, M.; Tulapurkar, A. A.; Shinjo, T.; Shiraishi, M.; Mizukami, S.; Ando, Y.; Suzuki, Y. Large Voltage-Induced Magnetic Anisotropy Change in a Few Atomic Layers of Iron. *Nat. Nanotechnol.* **2009**, *4*, 158–161.

- (20) Zhang, H.; Richter, M.; Koepf, K.; Opahle, I.; Tasnádi, F.; Eschrig, H. Electric-Field Control of Surface Magnetic Anisotropy: A Density Functional Approach. *New J. Phys.* **2009**, *11*, No. 043007.

- (21) Yang, Q.; Wang, L.; Zhou, Z.; Wang, L.; Zhang, Y.; Zhao, S.; Dong, G.; Cheng, Y.; Min, T.; Hu, Z.; Chen, W.; Xia, K.; Liu, M. Ionic Liquid Gating Control of RKKY Interaction in FeCoB/Ru/FeCoB and (Pt/Co)₂/Ru/(Co/Pt)₂ Multilayers. *Nat. Commun.* **2018**, *9*, No. 991.

- (22) Ohno, H.; Chiba, D.; Matsukura, F.; Omiya, T.; Abe, E.; Dietl, T.; Ohno, Y.; Ohtani, K. Electric-Field Control of Ferromagnetism. *Nature* **2000**, *408*, 944–946.

- (23) Chiba, D.; Matsukura, F.; Ohno, H. Electrically Defined Ferromagnetic Nanodots. *Nano Lett.* **2010**, *10*, 4505–4508.

- (24) Jiang, S.; Shan, J.; Mak, K. F. Electric-Field Switching of Two-Dimensional Van Der Waals Magnets. *Nat. Mater.* **2018**, *17*, 406–410.

- (25) Bauer, U.; Emori, S.; Beach, G. S. D. Voltage-Gated Modulation of Domain Wall Creep Dynamics in an Ultrathin Metallic Ferromagnet. *Appl. Phys. Lett.* **2012**, *101*, No. 172403.

- (26) Bauer, U.; Yao, L.; Tan, A. J.; Agrawal, P.; Emori, S.; Tuller, H. L.; Dijken, S. V.; Beach, G. S. D. Magneto-Ionic Control of Interfacial Magnetism. *Nat. Mater.* **2015**, *14*, 174–181.

- (27) Gilbert, D. A.; Grutter, A. J.; Arenholz, E.; Liu, K.; Kirby, B. J.; Borchers, J. A.; Maranville, B. B. Structural and Magnetic Depth Profiles of Magneto-Ionic Heterostructures beyond the Interface Limit. *Nat. Commun.* **2016**, *7*, No. 12264.

- (28) Baldrati, L.; Tan, A. J.; Mann, M.; Bertacco, R.; Beach, G. S. D. Magneto-Ionic Effect in CoFeB Thin Films with in-Plane and Perpendicular-to-Plane Magnetic Anisotropy. *Appl. Phys. Lett.* **2017**, *110*, No. 012404.

- (29) Bi, C.; Liu, Y.; Newhouse-Illige, T.; Xu, M.; Rosales, M.; Freeland, J. W.; Mryasov, O.; Zhang, S.; Velthuis, S. G. E. T.; Wang, W. G. Reversible Control of Co Magnetism by Voltage-Induced Oxidation. *Phys. Rev. Lett.* **2014**, *113*, No. 267202.

- (30) Duschek, K.; Petr, A.; Zehner, J.; Nielsch, K.; Leistner, K. All-Electrochemical Voltage-Control of Magnetization in Metal Oxide/Metal Nanoinclusions. *J. Mater. Chem. C* **2018**, *6*, 8411–8417.

- (31) Porro, S.; Betjka, K.; Jasmin, A.; Fontana, M.; Milano, G.; Chiolerio, A.; Fabrizio Pirri, C.; Ricciardi, C. A Multi-Level Memristor Based on Atomic Layer Deposition of Iron Oxide. *Nanotechnology* **2018**, *29*, No. 495201.

- (32) Black, C.; Welser, J. Electric-Field Penetration into Metals: Consequences for High-Dielectric-Constant Capacitors. *IEEE Trans. Electron Devices* **1999**, *46*, 776–780.

- (33) Schmickler, W. Electronic Effects in the Electric Double Layer. *Chem. Rev.* **1996**, *96*, 3177–3200.

- (34) Quintana, A.; Zhang, J.; Isarain-Chávez, E.; Menéndez, E.; Cuadrado, R.; Robles, R.; Baró, M. D.; Guerrero, M.; Pané, S.; Nelson, B. J.; Müller, C. M.; Ordejón, P.; Nogués, J.; Pellicer, E.; Sort, J. Voltage-Induced Coercivity Reduction in Nanoporous Alloy Films:

A Boost toward Energy-Efficient Magnetic Actuation. *Adv. Funct. Mater.* **2017**, *27*, No. 1701904.

(35) Dislaki, E.; Robbenolt, S.; Campoy-Quiles, M.; Nogués, J.; Pellicer, E.; Sort, J. Coercivity Modulation in Fe–Cu Pseudo-Ordered Porous Thin Films Controlled by an Applied Voltage: A Sustainable, Energy-Efficient Approach to Magnetoelectrically Driven Materials. *Adv. Sci.* **2018**, *5*, No. 1800499.

(36) Yamada, Y.; Ueno, K.; Fukumura, T.; Yuan, H. T.; Shimotani, H.; Iwasa, Y.; Gu, L.; Tsukimoto, S.; Ikuhara, Y.; Kawasaki, M. Electrically Induced Ferromagnetism at Room Temperature in Cobalt-Doped Titanium Dioxide. *Science* **2011**, *332*, 1065–1067.

(37) Dasgupta, S.; Das, B.; Li, Q.; Wang, D.; Baby, T. T.; Indris, S.; Knapp, M.; Ehrenberg, H.; Fink, K.; Kruk, R.; Hahn, H. Toward On-and-Off Magnetism: Reversible Electrochemistry to Control Magnetic Phase Transitions in Spinel Ferrites. *Adv. Funct. Mater.* **2016**, *26*, 7507–7515.

(38) Zhou, X.; Yan, Y.; Jiang, M.; Cui, B.; Pan, F.; Song, C. Role of Oxygen Ion Migration in the Electrical Control of Magnetism in Pt/Co/Ni/HfO₂ Films. *J. Phys. Chem. C* **2016**, *120*, 1633–1639.

(39) Shimatsu, T.; Sato, H.; Oikawa, T.; Inaba, Y.; Kitakami, O.; Okamoto, S.; Aoi, H.; Muraoka, H.; Nakamura, Y. High Perpendicular Magnetic Anisotropy of CoPtCr/Ru Films for Granular-Type Perpendicular Media. *IEEE Trans. Magn.* **2004**, *40*, 2483–2485.

(40) Zana, I.; Zangari, G. Electrodeposition of Co–Pt Films with High Perpendicular Anisotropy. *Electrochem. Solid State Lett.* **2003**, *6*, C153–C156.

(41) Rožman, K. Ž.; Krause, A.; Leistner, K.; Fähler, S.; Schultz, L.; Schlörb, H. Electrodeposition and Hard Magnetic Properties of Co–Pt Films in Comparison to Fe–Pt Films. *J. Magn. Magn. Mater.* **2007**, *314*, 116–121.

(42) Cortés, M.; Serrà, A.; Gómez, E.; Vallés, E. CoPt Nanoscale Structures with Different Geometry Prepared by Electrodeposition for Modulation of Their Magnetic Properties. *Electrochim. Acta* **2011**, *56*, 8232–8238.

(43) Reichel, L.; Oswald, S.; Fähler, S.; Schultz, L.; Leistner, K. Electrochemically Driven Variation of Magnetic Properties in Ultrathin CoPt Films. *J. Appl. Phys.* **2013**, *113*, No. 143904.

(44) Imperia, P.; Glaser, L.; Martins, M.; Andrezza, P.; Penuelas, J.; Alessandrovic, V.; Weller, H.; Andrezza-Vignolle, C.; Wurth, W. XMCD Studies of Co_xPt_{100-x} nanoparticles Prepared by Vapour Deposition and Chemical Synthesis. *Phys. Status Solidi A* **2008**, *205*, 1047–1051.

(45) Yamauchi, Y.; Tonegawa, A.; Komatsu, M.; Wang, H.; Wang, L.; Nemoto, Y.; Suzuki, N.; Kuroda, K. Electrochemical Synthesis of Mesoporous Pt–Au Binary Alloys with Tunable Compositions for Enhancement of Electrochemical Performance. *J. Am. Chem. Soc.* **2012**, *134*, 5100–5109.

(46) Isarain-Chávez, E.; Baró, M. D.; Pellicer, E.; Sort, J. Micelle-Assisted Electrodeposition of Highly Mesoporous Fe–Pt Nodular Films with Soft Magnetic and Electrocatalytic Properties. *Nanoscale* **2017**, *9*, 18081–18093.

(47) Pellicer, E.; Pané, S.; Sivaraman, K.; Ergeneman, O.; Suriñach, S.; Baró, M.; Nelson, B.; Sort, J. Effects of the Anion in Glycine-Containing Electrolytes on the Mechanical Properties of Electrodeposited Co–Ni Films. *Mater. Chem. Phys.* **2011**, *130*, 1380–1386.

(48) Pattanaik, G.; Zangari, G. Morphology and Magnetic Properties of Co-Rich Co–Pt Thin Films Electrodeposited on Cr Seed Layers. *J. Electrochem. Soc.* **2006**, *153*, C6–C10.

(49) Tang, K.; Fu, L.; White, R. J.; Yu, L.; Titirici, M.-M.; Antonietti, M.; Maier, J. Hollow Carbon Nanospheres with Superior Rate Capability for Sodium-Based Batteries. *Adv. Energy Mater.* **2012**, *2*, 873–877.

(50) Yan, Y.; Yin, Y.-X.; Guo, Y.-G.; Wan, L.-J. A Sandwich-Like Hierarchically Porous Carbon/Graphene Composite as a High-Performance Anode Material for Sodium-Ion Batteries. *Adv. Energy Mater.* **2014**, *4*, No. 1301584.

(51) Robbenolt, S.; Quintana, A.; Pellicer, E.; Sort, J. Large Magnetoelectric Effects Mediated by Electric-Field-Driven Nanoscale Phase Transformations in Sputtered (Nanoparticulate) and Electro-

chemically Dealloyed (Nanoporous) Fe–Cu Films. *Nanoscale* **2018**, *10*, 14570–14578.

(52) Quintana, A.; Menéndez, E.; Liedke, M. O.; Butterling, M.; Wagner, A.; Sireus, V.; Torruella, P.; Estradé, S.; Peiró, F.; Dendooven, J.; Detavernier, C.; Murray, P. D.; Gilbert, D. A.; Liu, K.; Pellicer, E.; Nogués, J.; Sort, J. Voltage-Controlled ON-OFF Ferromagnetism at Room Temperature in a Single Metal Oxide Film. *ACS Nano* **2018**, *12*, 10291–10300.

(53) Dasa, T. R.; Ignatiev, P. A.; Stepanyuk, V. S. Effect of the Electric Field on Magnetic Properties of Linear Chains on a Pt(111) Surface. *Phys. Rev. B* **2012**, *85*, No. 205447.

(54) Topolovec, S.; Jerabek, P.; Szabó, D. V.; Krenn, H.; Würschum, R. SQUID Magnetometry Combined with in Situ Cyclic Voltammetry: A Case Study of Tunable Magnetism of γ -Fe₂O₃ Nanoparticles. *J. Magn. Magn. Mater.* **2013**, *329*, 43–48.

(55) Subkow, S.; Fahnle, M. Potential Explanation of Charge Response of Magnetization in Nanoporous Systems. *Phys. Rev. B* **2011**, *84*, No. 220409.

(56) Drings, H.; Viswanath, R. N.; Kramer, D.; Lemier, C.; Weissmüller, J.; Würschum, R. Tuneable Magnetic Susceptibility of Nanocrystalline Palladium. *Appl. Phys. Lett.* **2006**, *88*, No. 253103.

(57) Ghosh, S. Charge-Response of Magnetization in Nanoporous Pd–Ni Alloys. *J. Magn. Magn. Mater.* **2011**, *323*, 552–556.

(58) Regan, T. J.; Ohldag, H.; Stamm, C.; Nolting, F.; Lüning, J.; Stöhr, J.; White, R. L. Chemical Effects at Metal/Oxide Interfaces Studied by x-Ray-Absorption Spectroscopy. *Phys. Rev. B* **2001**, *64*, No. 214422.

(59) Menéndez, E.; Modarresi, H.; Dias, T.; Geshev, J.; Pereira, L. M. C.; Temst, K.; Vantomme, A. Tuning the Ferromagnetic-Antiferromagnetic Interfaces of Granular Co–CoO Exchange Bias Systems by Annealing. *J. Appl. Phys.* **2014**, *115*, No. 133915.

(60) Menéndez, E.; Demeter, J.; Eyken, J. V.; Nawrocki, P.; Jedryka, E.; Wójcik, M.; Lopez-Barbera, J. F.; Nogués, J.; Vantomme, A.; Temst, K. Improving the Magnetic Properties of Co–CoO Systems by Designed Oxygen Implantation Profiles. *ACS Appl. Mater. Interfaces* **2013**, *5*, 4320–4327.

(61) Hadjipanayis, G. C. Nanophase Hard Magnets. *J. Magn. Magn. Mater.* **1999**, *200*, 373–391.

(62) Sato, M.; Ishii, Y. Critical Sizes of Cobalt Fine Particles with Uniaxial Magnetic Anisotropy. *J. Appl. Phys.* **1983**, *54*, 1018–1020.

(63) Kechrakos, D.; Trohidou, K. N. Magnetic Properties of Dipolar Interacting Single-Domain Particles. *Phys. Rev. B* **1998**, *58*, 12169–12177.

(64) Skomski, R.; Coey, J. M. D. *Permanent Magnetism*; Institute of Physics Publishing: Bristol, 1999.

(65) Wanka, G.; Hoffmann, H.; Ulbricht, W. Phase Diagrams and Aggregation Behavior of Poly(Oxyethylene)-Poly(Oxypropylene)-Poly(Oxyethylene) Triblock Copolymers in Aqueous Solutions. *Macromolecules* **1994**, *27*, 4145–4159.

(66) Aballe, L.; Foerster, M.; Pellegrin, E.; Nicolas, J.; Ferrer, S. The ALBA Spectroscopic LEEM-PEEM Experimental Station: Layout and Performance. *J. Synchrotron Radiat.* **2015**, *22*, 745–752.

Supporting Information

Large magnetoelectric effects in electrodeposited nanoporous micro-disks driven by effective surface charging and magneto-ionics

Cristina Navarro-Senent,^{,†} Jordina Fornell,[†] Eloy Isarain-Chávez,[†] Alberto Quintana,[†] Enric Menéndez,[†] Michael Foerster,[‡] Lucía Aballe,[‡] Eugen Weschke,[§] Josep Nogués,^{||,⊥} Eva Pellicer,^{*,†} and Jordi Sort^{*,†,⊥}*

[†]Departament de Física, Universitat Autònoma de Barcelona, E-08193 Cerdanyola del Vallès, Spain.

[‡]Alba Synchrotron Light Facility, CELLS, E-08280 Cerdanyola del Vallès, Spain

[§]Helmholtz-Zentrum Berlin für Materialien und Energie, Albert-Einstein-Strasse 15, D-12489 Berlin, Germany

^{||}Catalan Institute of Nanoscience and Nanotechnology (ICN2), CSIC and The Barcelona Institute of Science and Technology, Campus UAB, Bellaterra, E-08193 Barcelona, Spain

[⊥]ICREA, Pg. Lluís Companys 23, E-08010 Barcelona, Spain

Keywords: nanoporous material, magnetoelectric actuation, Co-Pt alloy, patterned microstructures, magneto-ionic effects.

Corresponding Author

*E-mail: Cristina.navarro@e-campus.uab.cat

*E-mail: Eva.Pellicer@uab.cat

*E-mail: Jordi.Sort@uab.cat.

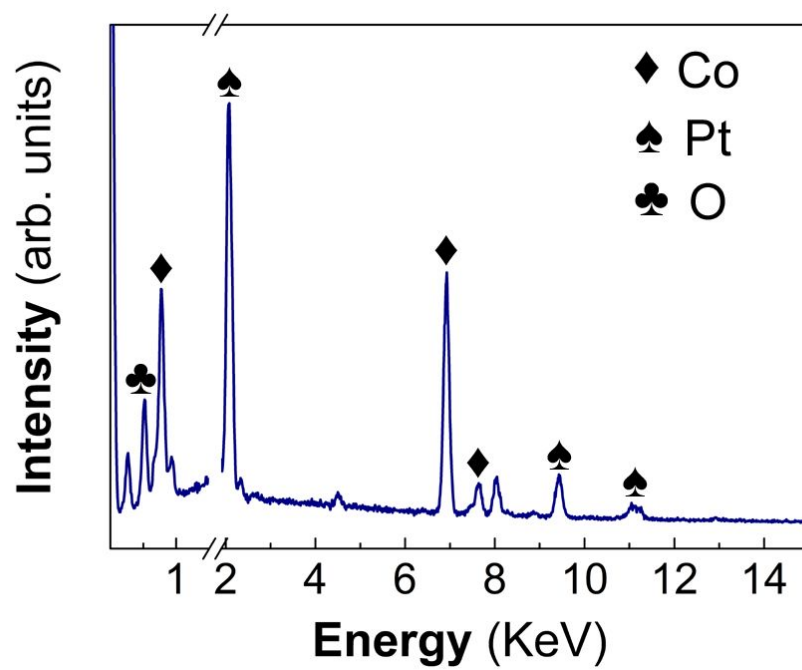


Figure S1. Energy-dispersive X-ray analysis of the nanoporous Co-Pt micro-disks.

Table S1. Elemental composition of the nanoporous Co-Pt/CoO micro-disks determined by EDX.

Element	Atomic %
Co	31
Pt	49
O	20

Table S2. Experimental values of the d_{hkl} interplanar distances (measured from the SAED rings in Figure 2c) together with the tabulated values for the different phases and the associated Miller indices. The tabulated values were obtained from the 1998 JCPDS-International Centre for Diffraction Data database (for hcp-Co and cubic CoO) and www.crystallography.net (CIF number 1524153) for Co₃Pt.

Experimental d_{hkl} spacing (Å)	Tabulated d_{hkl} spacing (Å)	h k l	Phase
2.451	2.450	1 1 1	Cubic CoO
2.110	2.118	1 1 1	Cubic Co ₃ Pt
2.126	2.122	2 0 0	Cubic CoO
2.169	2.165	1 0 0	hcp-Co
1.980	1.910	1 0 1	hcp-Co
2.074	2.023	0 0 2	hcp-Co
1.866	1.834	2 0 0	Co ₃ Pt cubic
1.501	1.500	2 2 0	Cubic CoO
1.301	1.297	2 2 0	Cubic Co ₃ Pt
1.281	1.280	3 1 1	Cubic CoO
1.310	1.252	1 1 0	hcp-Co
1.164	1.149	1 0 3	hcp-Co

The obtained d_{hkl} interplanar spacings of hcp-Co are larger than the references (i.e., tabulated values). As it is explained in the manuscript, the origin of these enlarged lattice cell parameters can be attributed to the presence of Pt in the hcp-Co phase in the form of solid solution. The covalent radius of Pt is higher than Co, resulting in larger cell parameters and, therefore, in increased d_{hkl} spacing values (https://www.webelements.com/platinum/atom_sizes.html).

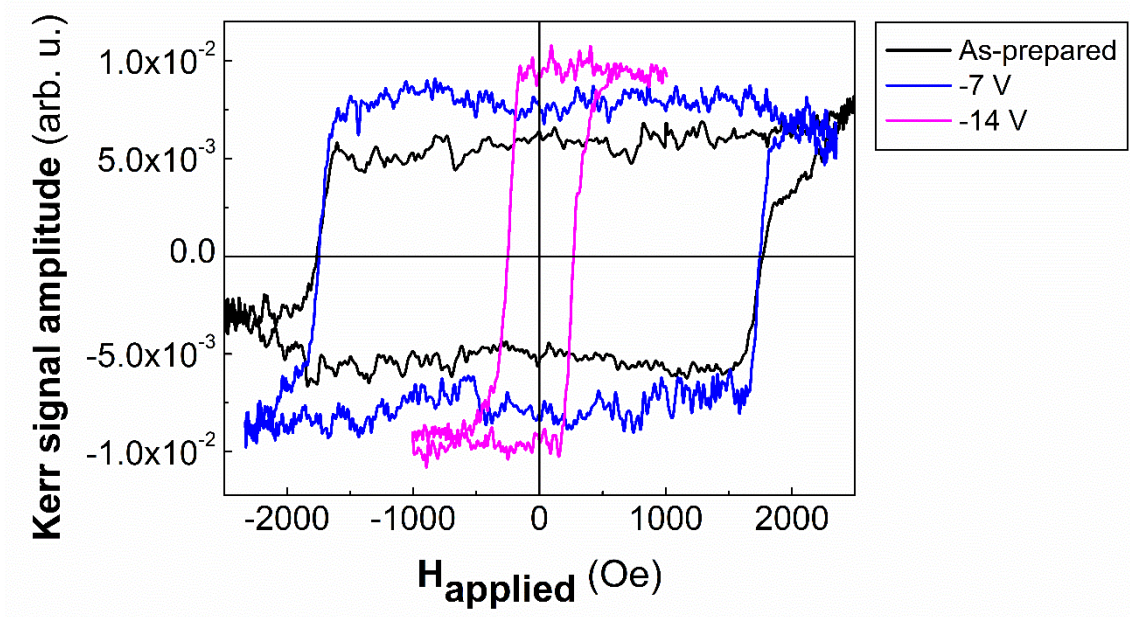


Figure S2. Hysteresis loops of a sample made of nanoporous Co-Pt/Co-O micro-disks measured in an as-prepared state (black loop) and after applying -7 V (blue loop) and -14 V (pink loop) for 10 min.

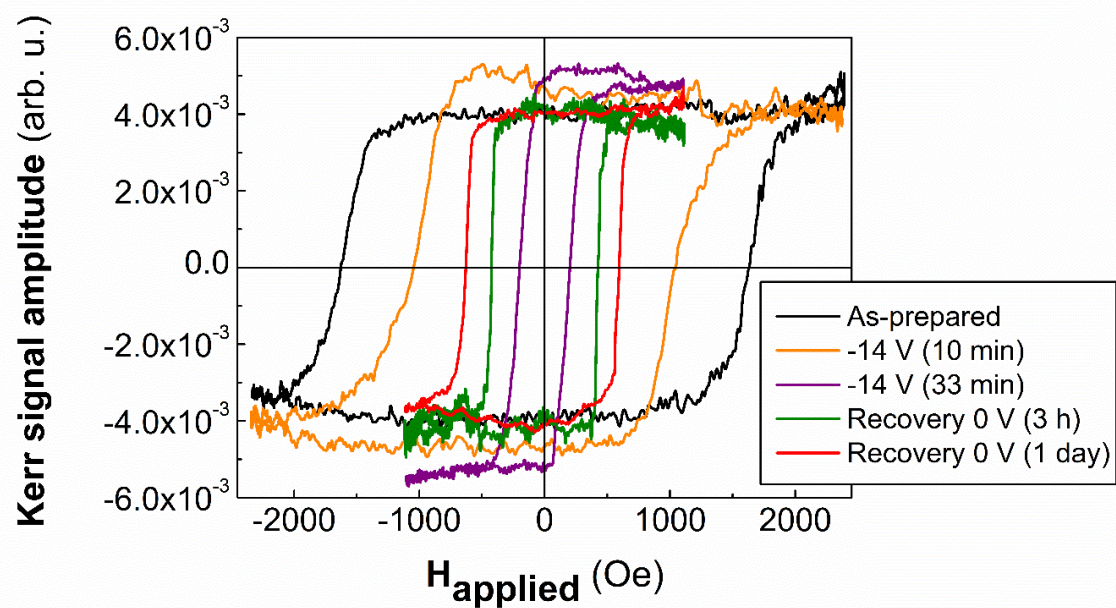


Figure S3. Hysteresis loops of the nanoporous Co-Pt/CoO micro-disks measured at 0 V (black loop), after applying -14 V for 10 min (orange loop), -14 V for 33 min (purple loop) and after recovery at 0 V for 3 h (green loop) and 1 day (red loop).

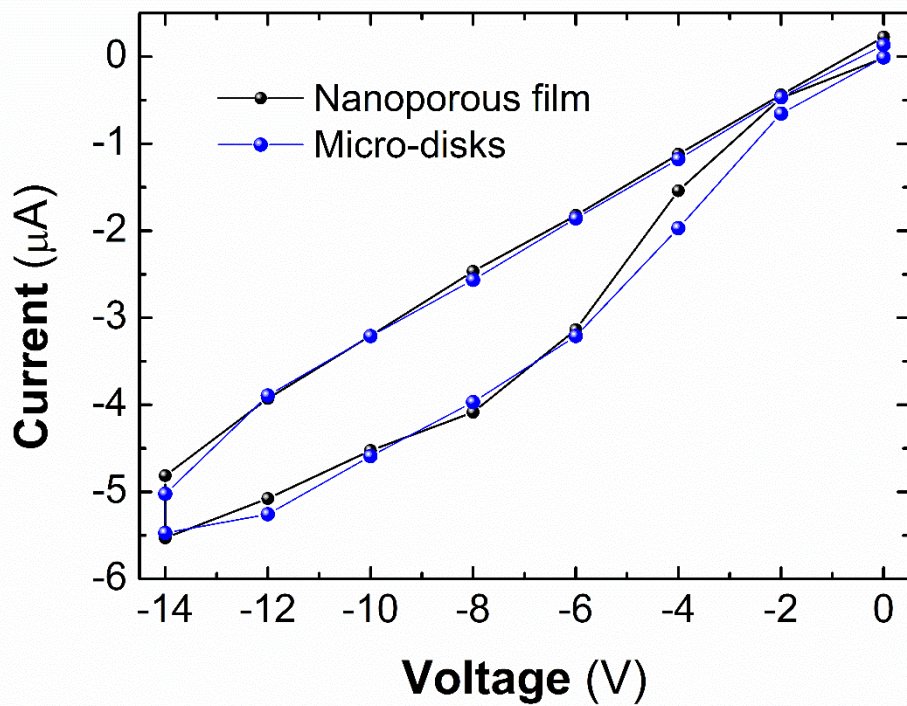


Figure S4. Cyclic voltammetry curves in anhydrous propylene carbonate with Na^+ and OH^- ions for both nanoporous Co-Pt/Co-O micros-disks and nanoporous Co-Pt films.

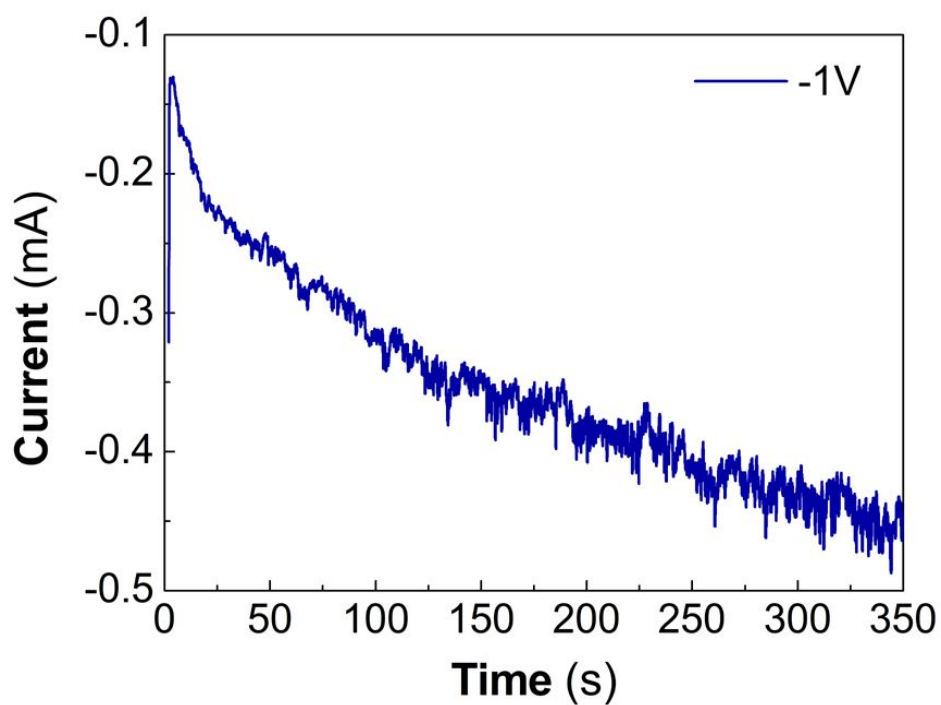


Figure S5. Potentiostatic transient corresponding to the electrodeposition of nanoporous Co-Pt on pre-lithographed Cu/Ti/Si substrates at -1 V vs. Ag/AgCl (3M KCl). Note that the y-axis is given in current instead of current density units due to the uncertainty in the estimation of the real working area.

4.2. Enhancing magneto-ionic effects in magnetic nanostructured films via conformal deposition of nanolayers with oxygen getter/donor capabilities

This study reports on the room temperature enhanced magneto-ionic phenomena in nanostructured Co–Pt+Co_xO_y/AlO_x and Co–Pt+Co_xO_y/HfO_x heterostructured films via voltage-driven oxygen motion using an anhydrous electrolyte. The material explored here is hence different from conventional metal/metal oxide bilayers for which magneto-ionic effects have previously been reported. This study shows that electrodeposited nanostructured ferromagnetic films combined with ALD oxide nanocoatings is an appealing procedure to boost magneto-ionic phenomena in heterostructured films with ultra-high metal/metal oxide interface area.

As for the previous work, nanostructured Co–Pt films were prepared by micelle-assisted electrochemical deposition from a solution containing Pluronic P123 tri-block copolymer which acted as structure-directing agent. Again, no pH buffers and complexing agents were added to the bath so as to favor the growth of nanostructured films consisting of metallic Co–Pt and Co oxides phases. Co–Pt films exhibit a homogeneous nanoroughness along the surface together with the presence of intergrain nanochannels. Subsequently, nanostructured Co–Pt films were coated with either AlO_x or HfO_x by ALD to conformally cover the nanoroughened surface of the Co–Pt films. AlO_x or HfO_x were selected due to their dissimilar oxygen affinity reported in the literature. This synthetic approach takes advantage of the nanostructuring achieved in the metallic counterpart by electrodeposition and its subsequent conformal coating with oxide nanolayers by ALD, which altogether boosts oxygen diffusion due to the high interface area between the metal and the oxide counterparts.

Magnetolectric measurements showed that H_c and magnetic moment at saturation (m_s) of Co–Pt were significantly manipulated after biasing the uncoated Co–Pt+Co_xO_y films and the Co–Pt+Co_xO_y/ALD oxide heterostructures with negative and subsequent positive voltages. An increase of m_s and a decrease of H_c were found for negative voltages,

whereas the opposite trend was observed for positive voltages. Such effect was observed in all heterostructures, namely the uncoated Co–Pt+Co_xO_y films and the ALD-coated Co–Pt+Co_xO_y films with AlO_x or HfO_x. The largest magnetoelectric effects were obtained for Co–Pt+Co_xO_y/HfO_x heterostructured films at negative voltages with an increase of m_s up to 76% and a decrease of H_c by 58%. The observed magnetoelectric changes were attributed to the reversible oxygen ion migration across the Co–Pt+Co_xO_y/oxide layer interface, resulting in variations of the Co oxidation state in the nanostructured Co–Pt+Co_xO_y film, which was investigated by XAS and XMCD. Importantly, the nature of the ALD nanocoating deposited onto the underlying Co–Pt+Co_xO_y film played an important role during the magnetoelectric measurements. HfO_x acted as an oxygen getter layer, thereby triggering magneto-ionic effects at negative voltages, and AlO_x worked as oxygen donor layer, thus promoting effects at positive voltages.

Enhancing Magneto-Ionic Effects in Magnetic Nanostructured Films via Conformal Deposition of Nanolayers with Oxygen Acceptor/Donor Capabilities

Cristina Navarro-Senent,^{*,†} Alberto Quintana,^{†,‡} Eloy Isarain-Chávez,[†] Eugen Weschke,[§] Pengmei Yu,^{||} Mariona Coll,^{||} Eva Pellicer,[†] Enric Menéndez,^{†,*} and Jordi Sort^{†,⊥,*}

[†]Departament de Física, Universitat Autònoma de Barcelona, E-08193 Cerdanyola del Vallès, Spain.

^{*}Department of Physics, Georgetown University, Washington, D.C. 20057, USA

[§]Helmholtz-Zentrum Berlin für Materialien und Energie, Albert-Einstein-Strasse 15, D-12489 Berlin, Germany

^{||}Institut de Ciència de Materials de Barcelona (ICMAB-CSIC) Campus UAB, E-08193 Bellaterra, Catalonia, Spain

[⊥]Institució Catalana de Recerca i Estudis Avançats (ICREA), Pg. Lluís Companys 23, E-08010 Barcelona, Spain

Reproduced with permission from ACS Appl. Mater. Interfaces, 2020, 12, 14484–14494. Copyright 2020 American Chemical Society.

Enhancing Magneto-Ionic Effects in Magnetic Nanostructured Films via Conformal Deposition of Nanolayers with Oxygen Acceptor/Donor Capabilities

Cristina Navarro-Senent,* Alberto Quintana, Eloy Isarain-Chávez, Eugen Weschke, Pengmei Yu, Mariona Coll, Eva Pellicer, Enric Menéndez,* and Jordi Sort*



Cite This: *ACS Appl. Mater. Interfaces* 2020, 12, 14484–14494



Read Online

ACCESS |



Metrics & More



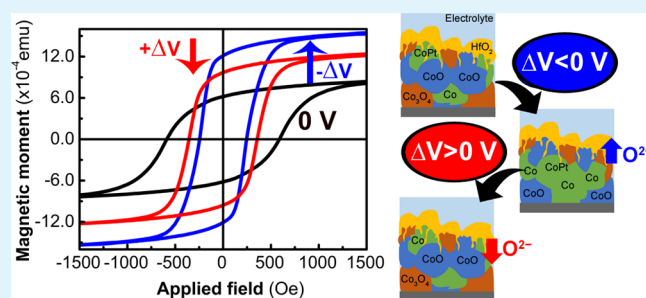
Article Recommendations



Supporting Information

ABSTRACT: Effective manipulation of the magnetic properties of nanostructured metallic alloys, exhibiting intergrain porosity (i.e., channels) and conformally coated with insulating oxide nanolayers, with an electric field is demonstrated. Nanostructured Co–Pt films are grown by electrodeposition (ED) and subsequently coated with either AlO_x or HfO_x by atomic layer deposition (ALD) to promote magneto-ionic effects (i.e., voltage-driven ion migration) during electrolyte gating. Pronounced variations in coercivity (H_C) and magnetic moment at saturation (m_S) are found at room temperature after biasing the heterostructures. The application of a negative voltage results in a decrease of H_C and an increase of m_S , whereas the opposite trend is achieved for positive voltages. Although magneto-ionic phenomena are already observed in uncoated Co–Pt films (because of the inherent presence of oxygen), the ALD oxide nanocoatings serve to drastically enhance the magneto-ionic effects because of partially reversible oxygen migration, driven by voltage, across the interface between AlO_x or HfO_x and the nanostructured Co–Pt film. Co–Pt/ HfO_x heterostructures exhibit the most significant magneto-electric response at negative voltages, with an increase of m_S up to 76% and a decrease of H_C by 58%. The combination of a nanostructured magnetic alloy and a skinlike insulating oxide nanocoating is shown to be appealing to enhance magneto-ionic effects, potentially enabling electrolyte-gated magneto-ionic technology.

KEYWORDS: magneto-ionic effects, ion migration, voltage control of magnetism, Co–Pt, nanostructured material



INTRODUCTION

Over the last decades, a great deal of effort has been made toward the development of energy-efficient materials and processes in the field of digital communication and information. Spintronics, which makes use of electronic charge and spin, has contributed to this progress with novel devices such as spin-transfer torque magnetic random-access memories, giant magnetoresistance sensors, or tunnel magnetoresistance sensors, among others.^{1,2} So far, the aforementioned devices and technologies require electric currents for their operation, which involves important energy dissipation in the form of heat (i.e., the so-called Joule heating effect). To surmount this drawback, a flurry of research has focused, in the last few years, on the voltage control of magnetism (i.e., replacing electric currents by electric fields whenever possible, therefore minimizing Joule heating effects and improving energy efficiency in these magneto-electronic devices).^{3–5}

Magneto-electric effects have been accomplished by different strategies, which include (i) strain-mediated coupling in piezoelectric–magnetostrictive heterostructured materials,^{6–8} (ii) single-phase multiferroic materials with intrinsic coupling

between ferroelectric and ferromagnetic order parameters,^{8–10} and (iii) charge carrier electronic band modulation in certain metallic ferromagnetic materials, typically Fe–Pd, Fe–Pt, Cu–Ni, or Co–Pt systems.^{11–15} Unfortunately, these approaches suffer from some drawbacks: piezoelectric response in piezoelectric–magnetostrictive devices is affected by clamping effects with the substrate and its endurance is in any case limited by fatigue-induced mechanical failure; single-phase multiferroic materials exhibit weak magneto-electric coupling and only very few of them exhibit multiferroic properties at room temperature;¹⁰ and electric charge accumulation in metallic materials occurs within the first nanometers from the metal surface because of the short electric-field screening length (the Thomas–Fermi length is $\lambda_{TF} \approx 0.5$ nm), limiting

Received: October 26, 2019

Accepted: March 4, 2020

Published: March 4, 2020



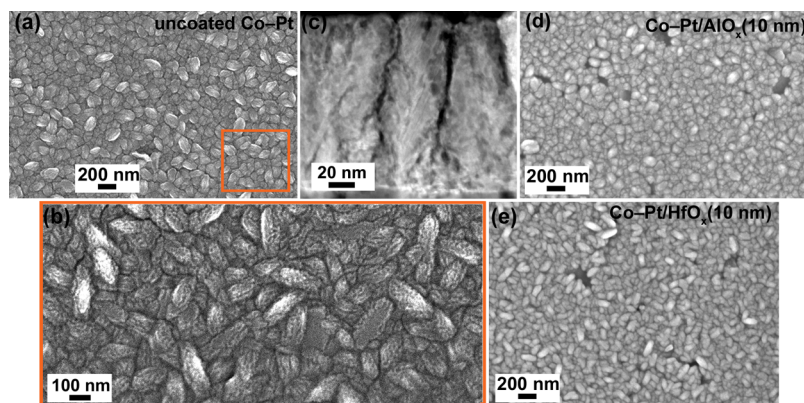


Figure 1. Top-view SEM image of the nanostructured Co–Pt film at (a) low and (b) high magnifications. In panel (b), the nanoroughened surface and intergrain porosity of nanometer size are visible. (c) STEM image of a cross section of the film. (d,e) Top-view SEM images of (d) Co–Pt/AlO_x and (e) Co–Pt/HfO_x films.

magneto-electric effects to a few nm from the surface, thereby restricting this effect to ultrathin films¹² and nanoporous magnetic alloys.^{11,14}

Alternatively, magneto-ionics is emerging as a novel pathway to tailor magnetism with voltage, which averts the above-mentioned drawbacks. Magneto-ionics relies on the motion of ions (e.g., O^{2–}^{16–21} or Li⁺^{22–24}), driven by an electric field, as an effective mechanism for controlling the oxidation–reduction processes of the ferromagnetic material. Interestingly, magnetic properties such as saturation magnetization (M_S),^{19,20,23,25} magnetic anisotropy,^{20,26} coercivity (H_C),^{16,19,25} or Dzyaloshinskii–Moriya interaction²⁷ can be successfully manipulated by electrical means taking advantage of ion diffusion. In contrast to the other magneto-electric mechanisms, magneto-ionic effects can be significant even in rather thick films. Nonetheless, thermal treatments are often required because ion diffusion is a thermally activated phenomenon.^{5,17,28}

Within magneto-ionics, most studies have focused so far on metal/metal oxide flat layers, where the voltage-induced O^{2–} migration is used to tailor magnetism. Commonly, such heterostructures comprise a magnetic material (e.g., Fe, Co, or Ni) in direct contact to a gate oxide that acts as the oxygen source/sink (e.g., GdO_x^{16,28} or HfO₂^{19,20,27,29}). The applied gate voltage can displace the O^{2–} ions from the metal oxide to the ferromagnetic layer, consequently inducing changes in H_C , M_S , magnetic anisotropy, or domain wall velocity, among others.^{16,19,20,27} Interestingly, some of these studies use liquid electrolytes (e.g., ionic liquids) to achieve large electric fields at the surface of the target material. Upon voltage application, an electric double layer (EDL) is formed at the interface between the oxide layer and the liquid electrolyte, generating rather large electric fields (because of the very narrow thickness of the EDL, which is around 0.5 nm),³⁰ thus promoting oxygen migration through the gate oxide/metal layer.^{19,20,29} Similarly, recent studies have reported changes in different magnetic parameters (magnetic anisotropy, M_S , H_C , and even magnetic phase transitions) through direct nonaqueous electrolyte gating, that is, without the assistance of gate oxide layers. In such cases, the source of oxygen is the magnetic material itself (either containing oxygen in its bulk structure or as a surface passivation layer).^{25,26,31–34}

In general, all magneto-electric phenomena are interface-driven, with thin films being the most utilized materials in voltage control of magnetism. Nevertheless, in the last decade,

enormous progress has been made in the methods to grow nanoporous materials for widespread applications in chemistry (adsorption and separation of gas molecules, chemoresistive gas sensors, energy conversion and storage, heterogeneous catalysis, etc.).^{35–37} This has triggered the idea of using nanoporous materials, which exhibit very large surface-to-volume ratios, as potential candidates for maximizing magneto-electric effects.^{11,14,25,31,38–41} Considering that magneto-ionics is an interfacial effect, where the metal/metal oxide or metal/ionic liquid interface plays a crucial role in ionic migration, nanoporous morphologies are expected to promote the diffusion of ions; notwithstanding, there are only a few reports on magneto-ionics in nanoporous/mesoporous materials and only a small fraction of them are focused on voltage-induced oxygen migration.^{25,31,38,41}

In a previous work, we demonstrated that the magnetic properties of nanoporous Co–Pt/CoO microdisks, prepared by electrodeposition (ED), can be easily modulated at room temperature upon voltage application using an anhydrous electrolyte.³¹ The accumulation of electrostatic charges at the surface of the ultranarrow pore walls and the associated voltage-driven oxygen migration (magneto-ionic effect) were mainly responsible for the observed effects. However, the amount of available oxygen was limited because it comprised only the CoO contained in the microdisks. As a result, only a reduction of H_C and an increase of the Kerr amplitude after applying a negative voltage were observed, followed by the recovery of the original values at positive voltages.³¹

In this article, we explore the enhanced voltage-induced oxygen motion in nanostructured Co–Pt/AlO_x and Co–Pt/HfO_x heterostructured films gated using an anhydrous electrolyte. First, nanostructured Co–Pt films (with intergrain porosity and a certain amount of oxygen) are prepared by micelle-assisted ED^{14,31,42,43} from a solution free from pH buffering and complexing agents to allow the formation of cobalt oxides.³¹ Subsequently, atomic layer deposition (ALD) is employed to conformally coat the nanoroughened surface and the nanochannels of the Co–Pt film either with AlO_x or HfO_x nanolayers (two oxides with oxygen vacancy mobility and dissimilar oxygen affinity^{44–47}) with high accuracy. In fact, ALD is the most suitable deposition technique to fill the intergrain nanochannels of the ferromagnetic layer with the aforementioned oxides, thus maximizing the available interface between the ferromagnetic material and the oxide. This strategy is expected to enhance the magneto-ionic effects on

the Co–Pt film, where the incorporation of an adjacent oxide nanolayer enables the control of the oxygen content in the ferromagnetic layer. Our work shows that the combination of micelle-assisted ED of a ferromagnetic nanostructured alloy with ALD of suitable oxide nanocoatings is an appealing synthesis pathway to boost magneto-ionic phenomena. The idea is applicable not only to liquid electrolyte gating but also to solid-state devices, for example, to flexible electronics (e.g., filling porous scaffolds with ionic liquid gels).^{48–50}

RESULTS AND DISCUSSION

The fabrication of the heterostructured films was conducted in two steps. First, nanostructured Co–Pt films (with some degree of intergrain porosity) were fabricated by micelle-assisted ED. This synthesis approach is employed to prepare mesoporous metals by taking advantage of micelles as a soft template (see the [Experimental Section](#) for details). [Figure 1a,b](#) shows a top-view scanning electron microscopy (SEM) image of the as-prepared nanostructured Co–Pt film. The film exhibits a homogeneous nanoparticulate morphology composed of nanometer-sized grains with visible nanostructuring inside each grain which provides a great nanoroughness along the surface ([Figure 1b](#)). More detailed structural analysis was performed by scanning transmission electron microscopy (STEM), where a characteristic columnar-like film growth and the presence of intergrain nanochannels can be appreciated ([Figure 1c](#)). STEM measurements also show that the overall film thickness is around 150 nm. Energy-dispersive X-ray (EDX) spectroscopy reveals that the O, Co, and Pt contents are approximately 38 ± 3 , 48 ± 2 , and 14 ± 1 at. %, respectively, with an average composition around $\text{Co}_{77}\text{Pt}_{23}$ considering only the metallic fraction, revealing the growth of a Co-rich alloy.

Subsequently, AlO_x and HfO_x nanolayers, with thicknesses of 10 nm, were directly deposited onto the nanostructured Co–Pt films by ALD. Top-view SEM images of the Co–Pt/ AlO_x and Co–Pt/ HfO_x composite nanostructured films are displayed in [Figure 1d,e](#), respectively. For comparison, the SEM image of the uncoated nanostructured Co–Pt film is also shown. It can be seen that the morphology of the Co–Pt films was preserved after 10 nm AlO_x and HfO_x deposition, suggesting that, as expected, ALD proceeded conformally covering the nanoroughened surface and penetrating into the intergrain channels ([Figure 1d,e](#)). Thicker coatings (20 and 80 nm) were also obtained ([Figure S1a,b](#)). As can be seen in [Figure S1b](#), 80 nm-thick coatings cause a sort of flattening of the Co–Pt film morphology probably because of the sealing of the intergrain channels.⁵¹ The thinnest coatings (10 nm) were selected for magneto-electric measurements because the insertion of HfO_x and AlO_x adds to the initial thickness of the EDL, thus progressively weakening the achievable electric field for a given voltage. To confirm the conformal coating of the nanostructure with the ALD nanolayer, electron energy loss spectroscopy (EELS) mappings were carried out on a Co–Pt/ HfO_x film ([Figure 2](#)). STEM images of a cross section of a Co–Pt/ HfO_x film are shown in [Figure 2](#), together with the corresponding Co (red) and Hf (green) EELS mapping in the interfacial area enclosed within the orange box. The EELS mappings reveal the presence of Hf inside the channels of the Co–Pt film, indicating that HfO_x coating has penetrated several tens of nm toward the interior of the Co–Pt film. EELS analyses also show the presence of both Co and Hf at the interfaces between Co–Pt and HfO_x , suggesting that mixed

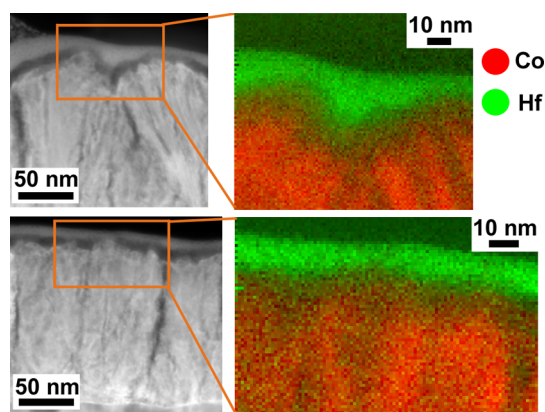


Figure 2. STEM images and Co and Hf EELS mapping of the area enclosed in the orange box of two regions of a Co–Pt/ HfO_x film. Co is in red, while Hf is in green.

cobalt/hafnium oxides may coexist within these regions. These results prove that ALD is suitable to conformally coat and fill the intergrain nanochannels of the Co–Pt film, enhancing the interface area between the Co–Pt and the HfO_x nanocoating, thus maximizing magneto-ionic effects.

The crystallographic structure of the uncoated and ALD-coated nanostructured Co–Pt films was characterized by grazing incidence X-ray diffraction (GIXRD). The diffraction pattern of the uncoated film indicates the coexistence of several phases: hexagonal close-packed (hcp) Co, face-centered cubic (fcc) Co, cubic Co_3O_4 , and cubic CoO phases (black curve, [Figure 3](#)). The presence of these cobalt oxide phases was also

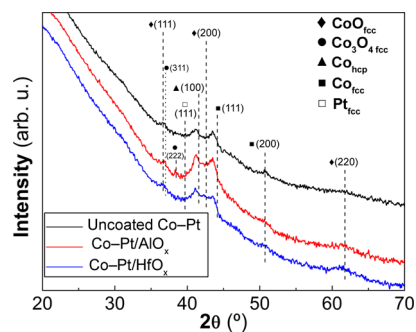


Figure 3. GIXRD patterns of the uncoated Co–Pt (black curve), Co–Pt/ AlO_x (10 nm) (red curve), and Co–Pt/ HfO_x (10 nm) (blue curve) films.

detected by EELS mappings, where the coexistence of oxygen and cobalt-rich regions was observed at the intergrains ([Figure S2](#)). Note that a slight angular shift in the hcp- and fcc-Co peaks is observed toward small angles compared to the tabulated patterns, indicating an increase in the lattice cell parameter, which is compatible with dissolution of Pt into the hcp- and fcc-Co lattices. The same crystallographic structure is seen in the patterns of the Co–Pt/ AlO_x and Co–Pt/ HfO_x heterostructured films (red and blue curves in [Figure 3](#)).^{52–54} No additional peaks attributed to Al_2O_3 or HfO_2 are observed, likely because of their amorphous-like nature.⁴³

Magnetic properties were measured prior to voltage application in a vibrating sample magnetometer (VSM) at room temperature. A decrease of m_s accompanied by a small increase of H_C was observed after coating the Co–Pt film (see the [Supporting Information](#), [Figure S3](#)). Such changes are

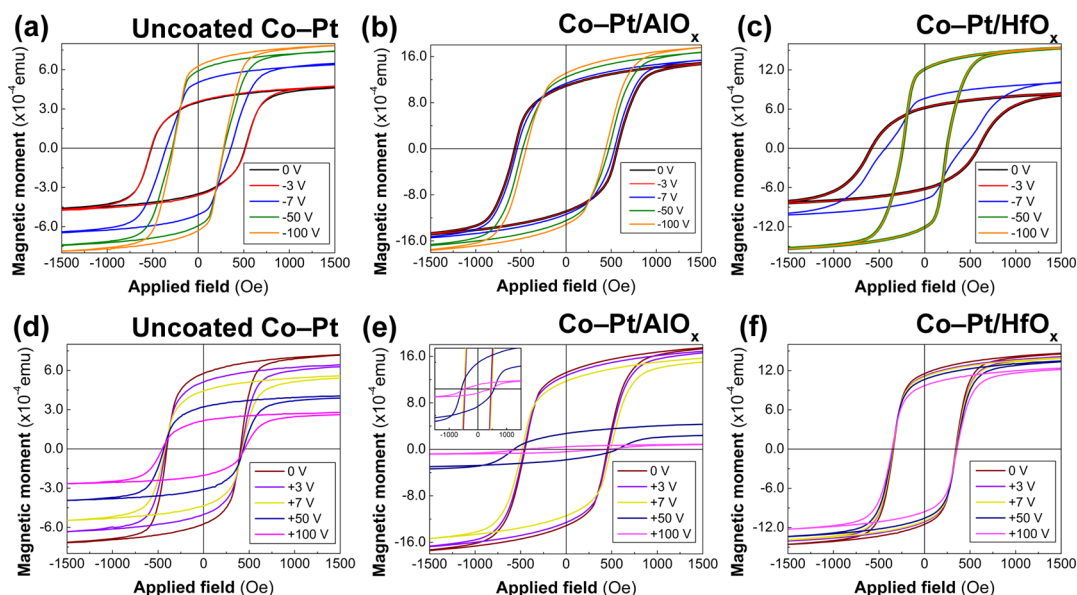


Figure 4. Room-temperature in-plane VSM measurements of (a,d) uncoated Co-Pt, (b,e) Co-Pt/ AlO_x , and (c,f) Co-Pt/ HfO_x samples after applying 0, -3, -7, -50, and -100 V and 0, +3, +7, +50, and +100 V for 90 min, respectively.

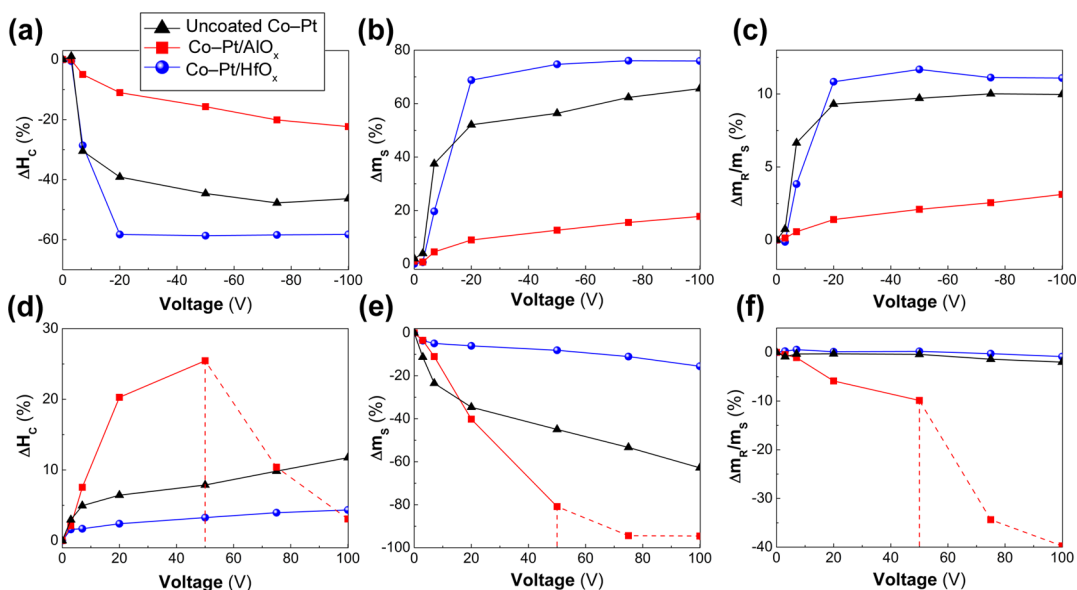


Figure 5. Dependence of the relative variation (%) of (a,d) coercivity (H_c), (b,e) magnetic moment at saturation (m_s), and (c,f) remanence to the saturation ratio (m_r/m_s) as a function of the applied negative (a-c) and positive (d-f) voltages. Dashed vertical lines denote film detachment.

ascribed to the partial oxidation of Co-Pt during the ALD process, likely occurring at the interfacial level, because the coating process involves high temperature (200 °C) for both AlO_x and HfO_x depositions and, additionally, ozone gas for the AlO_x growth.⁴³ To study the electric-field effect on the magnetic properties, hysteresis loops were measured in-plane (always in the same direction), while the films were subjected to different constant negative and positive voltages in an electrolyte. The voltage was applied using a home-made electrolytic cell containing the films as the working electrode, a Pt wire as the counter electrode, and propylene carbonate (PC), which is anhydrous, with dissolved Na^+ and OH^- ions, as the liquid electrolyte (see the [Experimental Section](#)).^{25,32}

For the magneto-electric experiments, the hysteresis loops of uncoated Co-Pt, Co-Pt/ AlO_x , and Co-Pt/ HfO_x films were recorded by applying various negative voltages ranging from 0

to -100 V, after a waiting time of 90 min at each value of voltage (Figure 4a-c, respectively). For the sake of clarity, representative loops at selected voltages are shown (see Figure S4, [Supporting Information](#), for additional data). Note that differences in the initial magnetic moment among the three samples are due to their dissimilar lateral size. As can be seen in Figure 4a-c, the loops at 0 and -3 V are virtually overlapped (black and red loops), indicating that no significant magneto-electric effects are induced at small voltages. This suggests the existence of an onset voltage, in agreement with previous results.³¹ Conversely, significant variations were observed for all three samples after overcoming the threshold voltage (-7 V, blue loop, Figure 4a-c), where m_s increases and H_c decreases as the applied voltage becomes progressively more negative. The origin of this threshold voltage is probably related to the bond-dissociation energy between O and Co.

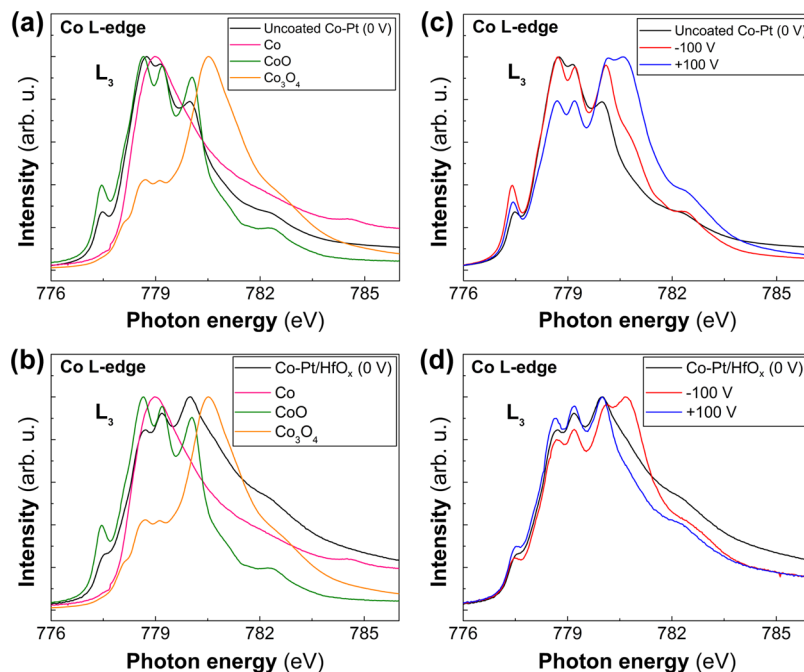


Figure 6. Zoom-in of the cobalt L_3 -edge XAS of the as-prepared (0 V, black curve) (a) uncoated Co–Pt and (b) Co–Pt/HfO_x films, together with the spectra of reference samples (pink: Co; green: CoO; orange: Co₃O₄). Evolution of cobalt L_3 -edge XAS after applying –100 V (red curve) and +100 V (blue curve) for the (c) uncoated Co–Pt and (d) Co–Pt/HfO_x films.

This threshold is the minimum energy required for creating O^{2–} ions and inducing the migration of the ions through the film.

After having applied negative voltages, the voltage was removed and the system was left for a “relaxation period” of 8 h (brown loops, Figure 4d–f). Subsequently, hysteresis loops were recorded at different positive voltages ranging from 0 to +100 V (again waiting 90 min at each value of voltage) and selected loops are plotted in Figure 4d–f (see all measured loops in Figure S4, Supporting Information). When positive voltages are applied, m_S decreases for the three samples (Figure 4d–f), even beyond the initial m_S value for the uncoated Co–Pt (initial $m_S = 5.7 \times 10^{-4}$ emu and $m_S (+100 \text{ V}) = 2.1 \times 10^{-4}$ emu), particularly, for Co–Pt/AlO_x films (initial $m_S = 16.5 \times 10^{-4}$ emu and $m_S (+50 \text{ V}) = 3.9 \times 10^{-4}$ emu) (Figure S4a,b). This already suggests that AlO_x may act as oxygen donor. In contrast, H_C increases slightly upon applying positive voltages (Figure 4d–f) but does not completely return to the initial values for Co–Pt and Co–Pt/HfO_x films (Figure S4a,c). In contrast, H_C increases almost back to its pristine value at +50 V for the Co–Pt/AlO_x films (dark blue loop, Figure S4b). Thus, Co–Pt/HfO_x films did not recover the initial state, showing only slight variations in H_C and m_S values (Figures 4f and S4c). Conversely, as can be observed in Figure 4e, the Co–Pt/AlO_x film polarized at +50 V shows an open loop because the induced magneto-electric response could not reach a stationary value in spite of the 90 min waiting time at this voltage prior to hysteresis loop acquisition. In other words, the magnetic properties of this sample kept changing over time while the loop was recorded (approximately 40 min). It should be noted that the Co–Pt/AlO_x film detached from the substrate at larger positive voltages (+75 and +100 V). Delamination was not observed in the uncoated Co–Pt and Co–Pt/HfO_x films, indicating that the Co–Pt/AlO_x coating is less stable at high positive voltages.

The results indicate that the relative variations on magnetic properties induced by the applied voltage (i.e., magneto-ionic effects) in each sample differ from one another. Figure 5 shows the relative changes in H_C and m_S and remanence to the saturation ratio (m_R/m_S) as a function of the applied voltage for the three studied samples. Remarkably, the largest variation of H_C , m_S , and m_R/m_S at negative voltages is achieved for Co–Pt/HfO_x, with a 58% reduction and 76 and 11% increases, respectively (blue curve, Figure 5a–c). Also remarkable is that, for negative voltages, a plateau is observed for the three magnetic parameters at a value between –20 and –50 V, suggesting that the voltage effect tends to saturate beyond that applied voltage. In contrast, Co–Pt/AlO_x exhibits the lowest relative variations of H_C , m_S , and m_R/m_S . Conversely, for positive voltages, Co–Pt/AlO_x shows the largest variation of H_C (25% increase), m_S (81% decrease), and m_R/m_S (10% decrease) (red curve, Figure 5d–f). Note that these values have been obtained considering the range from 0 to +50 V (i.e., excluding the +75 and +100 V points) because the sample Co–Pt/AlO_x damaged at the upper positive voltages.

In general, the same trends are observed for the three systems, that is, uncoated Co–Pt, Co–Pt/AlO_x, and Co–Pt/HfO_x films. The observed modulation in the magnetic behavior of Co–Pt is attributed to voltage-driven oxygen migration. Indeed, changes are in the same direction as those reported in the literature for the same gating polarity (note that, in our work, the Co–Pt-based films act as the gate).^{16,17,19,20,55} Negative voltages cause a decrease of H_C and an increase of m_S . The latter is consistent with a partial reduction of the Co oxides already present in the as-deposited nanostructured Co–Pt layer to metallic Co.³¹ Subsequently, when positive voltages are applied, re-oxidation of the previously formed metallic Co takes place, resulting in a decrease of m_S . For the uncoated Co–Pt film, such variations originate from voltage-driven O and Co redistributions, as previously reported.³¹ In contrast, for ALD-coated Co–Pt films, the presence of the HfO_x and

AlO_x nanolayers has a strong influence on O^{2-} migration through the Co–Pt/oxide interface depending on the voltage polarity, that is, for negative applied voltages, the relative change in H_C , m_S , and m_R/m_S is the largest for Co–Pt/ HfO_x , whereas smaller variations are observed in Co–Pt and Co–Pt/ AlO_x (Figure 5a–c). Conversely, Co–Pt/ AlO_x is the one that exhibits more pronounced magneto-electric effects for positive voltages. In other words, the ALD-coated Co–Pt films exhibit higher relative variations than their uncoated counterpart, but to achieve such enhancement, the voltage sign needs to be selected depending on the type of oxide nanocoating. This indicates that the ALD coatings enhance O^{2-} migration somehow within the Co–Pt layer. Therefore, the role of these ALD nanocoatings as oxygen acceptor/donor materials is important to understand the enhancement of the magneto-ionic effects. Considering that the origin of the observed changes relies on the reduction of CoO and Co_3O_4 to Co ,³¹ the HfO_x coating seems to facilitate the reduction of cobalt oxides upon negative voltage application (i.e., it plays an oxygen acceptor role⁴⁶). Conversely, AlO_x coating boosts the oxidation of Co at positive voltage (i.e., oxygen donor role⁴⁵). Thus, the results suggest that HfO_x is prone to accept oxygen from the Co–Pt layer, while AlO_x is instead an oxygen donor. In fact, HfO_x has been extensively used as the gate oxide material for electrical control of magnetism, where oxygen migration can occur upon voltage application.^{19,20,29,56} However, only a few studies have reported magneto-ionic effects using AlO_x ^{57,58} where instead of oxygen, Al^{3+} ions could migrate from AlO_x to the ferromagnetic film.⁵⁸ The magnetolectric changes observed for the three samples are attributed to variations in the Co oxidation state in the Co–Pt film; notwithstanding, a possible contribution from Pt could still take place and should not be completely ruled out. Recent studies have reported changes on the induced magnetic moment of Pt biased by an electric field;⁵⁹ nonetheless, such variations in our work are expected to be minor compared to the induced changes on Co.

To shed light on the voltage-driven O migration mechanism through the Co–Pt layer, X-ray absorption spectroscopy (XAS) was performed on the uncoated Co–Pt and Co–Pt/ HfO_x films at the cobalt $L_{2,3}$ edges (black curves, Figure 6a,c and b,d, respectively). For clarity, the L_2 data have been omitted from Figure 6, but it is available in the Supporting Information (Figure S5), and also, the XAS measurements of the Co–Pt/ AlO_x films have been omitted because of their aforementioned poor stability when subjected to positive voltages. Nevertheless, they can be found in Figure S6. X-ray magnetic circular dichroism (XMCD), which refers to the difference in absorption for right-handed (μ^+) and left-handed (μ^-) X-rays with circular polarization, was also performed in order to probe the magnetic moment of Co on the uncoated Co–Pt and Co–Pt/ HfO_x films (Figures S7 and 7). It should be noted that the detection depth probed by XAS in the total electron yield (TEY) mode when using soft X-rays is limited to the outermost nanometers from the surface, while VSM probes the whole film volume because it is an integrating technique.

The XAS spectrum prior to voltage application of the uncoated Co–Pt film exhibits a multiplet structure consisting of four peaks (777.4, 778.7, 779.1, and 780 eV) at the L_3 edge and a broad peak (794 eV) at the L_2 edge (black curves, Figures 6a and S5a). The pattern matches the CoO reference XAS spectrum (green curve, Figures 6a and S5a), although the three main peaks at 778.7, 779.1, and 780 eV are less

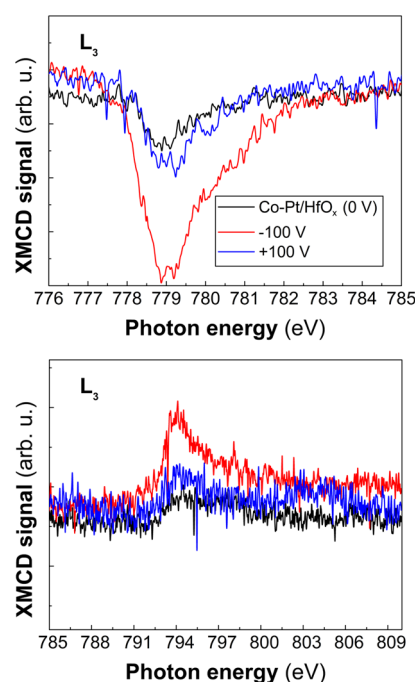


Figure 7. Zoom-in of the cobalt L_3 - and L_2 -edge XMCD signals for the Co–Pt/ HfO_x film in the pristine state (0 V, black curve) and after applying -100 V (red curve) and $+100$ V (blue curve).

pronounced in the uncoated Co–Pt film. This sample shows the XMCD signal, thus also indicating the presence of ferromagnetic metallic Co (black curve, Figure S7). Overall, the results indicate the presence of CoO and metallic Co in the uncoated Co–Pt films, in agreement with its GIXRD pattern (black curve, Figure 3). Nonetheless, the presence of small amounts of Co_3O_4 cannot be fully ruled out from XAS, and actually, a contribution from this phase in the amorphous form is envisaged in the GIXRD pattern (Figure 3). After subjecting the uncoated Co–Pt sample to -100 V (XAS was carried out ex situ, 30 min elapsed prior to starting XAS analysis), the four peaks previously observed (776.4, 778.7, 779.1, and 780.5 eV) become more pronounced at the L_3 edge (red curve, Figure 6c), while the main peak at the L_2 edge is slightly shifted toward higher photon energies (red curve, Figure S5c). This, together with the decrease in dichroic signal (red curve, Figure S7), suggests that the amount of CoO increases, whereas that of metallic Co decreases upon negative voltage application in the probed volume. When a positive voltage is applied ($+100$ V), XAS exhibits a decrease of the shoulder at 776.4 eV and the two peaks at 778.7 and 779.1 eV, which are characteristic of CoO , at the L_3 edge. Moreover, a new peak at 780.6 eV is observed at the L_3 edge, while the main peak at the L_2 edge becomes sharper (blue curve, Figure S5c). These features suggest the presence of traces of Co_3O_4 (see the orange curve of the Co_3O_4 XAS reference, Figures 6a and S5a). The results, together with the absence of dichroism in the XMCD signal (blue curve, Figure S7), indicate that the sample consists of a mixture of CoO and Co_3O_4 after the application of a strong positive voltage.

The observed changes on the XAS data for the uncoated Co–Pt films after negative voltage application seem contradictory with the obtained macroscopic magnetic measurements (Figures 4 and 5), where the value of m_S is found to increase (rather than decrease). The XAS results can be understood on

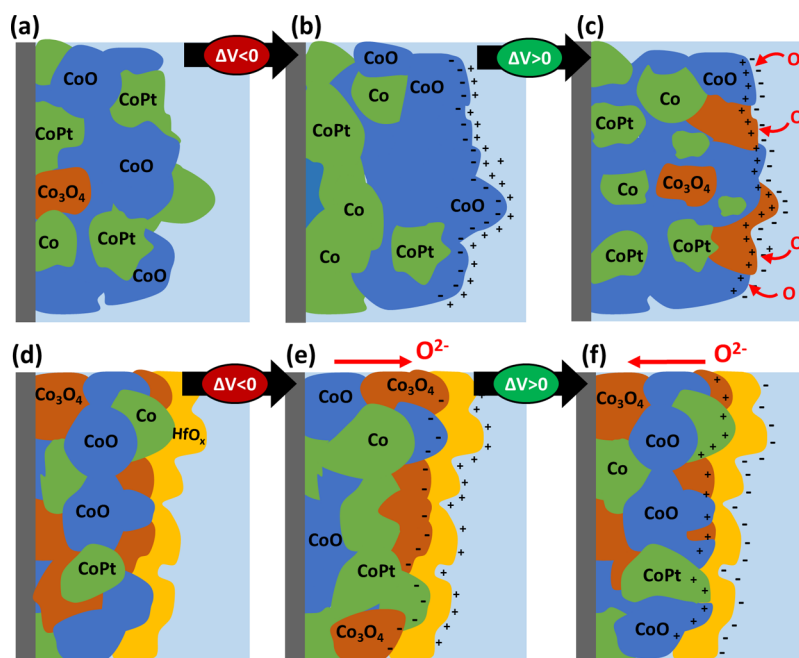


Figure 8. Schematic drawing of the distribution of cobalt phases in (a–c) uncoated Co–Pt and (d–f) Co–Pt/HfO_x films in (a,d) the pristine state (0 V), (b,e) when subjected to $-\Delta V$ and (c,f) when subjected to $+\Delta V$ in PC (depicted as light blue medium).

the basis of O migration toward the surface of the nanostructured alloy from Co₃O₄- and CoO-rich regions. First, when negative voltage is applied, O²⁻ ions from CoO and Co₃O₄ phases migrate toward the surface driven by the electric field. As a result, inner CoO is partially reduced to Co; eventually, Co₃O₄ is reduced to CoO and the outermost metallic Co clusters are partially oxidized to CoO. This scenario is schematically depicted in Figure 8a,b. Thereby, the redistribution of O across the film leads to the formation of Co-rich inner regions, which is consistent with the increase in m_s (Figures 4a and 5b), and CoO-rich regions at the surface, which is consistent with the XAS pattern (red curve, Figure 6c). Afterward, when the voltage polarity is reversed (+100 V), O²⁻ ions from Co₃O₄ are prone to migrate toward Co/CoO, oxidizing the metallic Co to CoO (Figure 8c). The decrease of the metallic Co fraction is consistent with the reduction of m_s shown in Figures 4d and 5e. Nevertheless, the XAS pattern acquired after positive voltage application shows greater presence of Co₃O₄ at the film's surface (blue curve, Figure 6c). This, together with the fact that m_s decreases even beyond its initial value (Figure S4a), suggests that an external source of oxygen coming from PC could be plausible because the amount of O within the film is limited. The origin of this excess of oxygen could be the inherent oxygen gas dissolved on the PC together with the OH⁻ ions formed during electrolyte preparation (see the Experimental Section). This would support the increase of Co₃O₄ at the surface after applying +100 V. As noted, the XAS detection depth is limited to the outermost nanometers from the surface, while VSM is an integrating technique, probing the whole film. This explains why the results gathered by both techniques seem to be contradictory, although they are not. Moreover, the increased amount of CoO and Co₃O₄ phases implies a more insulating surface, which further limits the XAS detection.

Regarding the Co–Pt/AlO_x film, the XAS spectrum of the untreated sample exhibits three main peaks (778.6, 779.2, and 779.9 eV) and a shoulder (777.6 eV) at the L₃ edge (black

curve, Figure S6a), while a broad peak (794.4 eV) is observed at the L₂ edge (black curve, Figure S6b). The XAS pattern is consistent with a mixture of metallic Co, CoO, and Co₃O₄, in agreement with the GIXRD results (Figure 3). No significant variations in the XAS spectrum are observed after subjecting the film to a negative voltage (blue curve, Figure S6). As mentioned earlier, the surface sensitivity of the XAS technique is limited to the first nanometers from the surface, while VSM-assisted magneto-electric measurements involve the whole film volume. In this case, however, only small variations in the magnetic response were observed upon negative voltage application (Figure 4b), hence it is not surprising that no drastic changes are observed by XAS either. Moreover, according to previous studies, magneto-electric effects observed after applying negative voltage could arise from Al³⁺ diffusion into the Co–Pt film.⁵⁸ XAS provides information about Co in a metallic environment or in an oxide form. This means that Co in a metallic environment would be either Co–Co, Co–Pt, or Co–Al. Considering the fact that metallic Co and Co–Al would give almost indistinguishable spectra, this explains why the XAS spectrum remains unaltered after –100 V biasing. The Co–Pt/AlO_x film was not studied by XAS after positive voltage application because it was unstable (Figure Sd–f).

As for the Co–Pt/HfO_x film is concerned, the XAS spectrum of the pristine sample at 0 V exhibits a multiplet structure consisting of four peaks (777.5, 778.7, 779.1, and 780 eV) at the L₃ edge and a peak (794.7 eV) at the L₂ edge (black curves, Figures 6b and S5b). The multiplet is rather broad, especially the peak at 780 eV, which possesses higher intensity compared to the peaks at 777.5, 778.7, and 779.1 eV. This, together with the small intensity of the XMCD signal (black curve, Figure 7), indicates that the outermost surface of the Co–Pt/HfO_x film consists of a mixture of CoO, Co₃O₄, and some traces of metallic Co, in agreement with the GIXRD analysis (blue curve, Figure 3). When negative voltage is applied, the intensities of the shoulder (777.5 eV) and the two

peaks at 778.7 and 779.1 eV on the L_3 edge slightly decrease, while the peak at 778 eV is shifted toward higher photon energies (red curve, Figure 6d). The XAS spectrum also shows a new peak at 780.7 eV at the L_3 edge, while the main peak at the L_2 edge becomes sharpened. The latter matches the main peak of Co_3O_4 reference XAS (orange curve, Figures 6b and S5d). Moreover, after subjecting the Co–Pt/ HfO_x film to -100 V, the XMCD signal exhibits higher dichroism compared to the initial state (i.e., 0 V) (red curve, Figure 7). These results suggest the coexistence of Co_3O_4 and metallic Co at the surface of Co–Pt/ HfO_x after applying negative voltage. When positive voltage is applied, the XAS spectrum exhibits a pattern similar to the initial state (0 V) at L_3 and L_2 edges (blue and black curves, respectively, Figures 6d and S5d), slight narrowing of the multiplet, and a small intensity increase of the shoulder at 777.5 eV at the L_3 edge. Additionally, XMCD shows a decrease of the dichroic signal, almost recovering the initial state (blue curve, Figure 7). These results confirm that after applying positive voltage, the surface of Co–Pt/ HfO_x films comprise CoO, metallic Co, and some traces of Co_3O_4 in a proportion which differs only slightly from the pristine state (0 V). Note that the amount of surface oxides in the Co–Pt/ HfO_x film after applying -100 V is clearly lower than that for uncoated Co–Pt, thus corroborating the role of HfO_x as a good oxygen acceptor (poorer oxygen donor).⁴⁴ Because HfO_x is prone to accept oxygen (for negative voltages) rather than to donate it back to Co–Pt (for positive voltages), the magneto-ionic effects are more pronounced under negative biasing for Co–Pt/ HfO_x .

More specifically, as depicted in Figure 8d,e, the application of negative voltage to the Co–Pt/ HfO_x system triggers the diffusion of O^{2-} ions from the Co–Pt film toward the HfO_x layer, resulting in the partial reduction of Co_3O_4 to CoO and the reduction of CoO to metallic Co. Unlike the uncoated Co–Pt films, for which O^{2-} migration was limited to the surface, oxygen ions can diffuse here within the HfO_x layer owing to the occurrence of oxygen vacancies in HfO_x .^{60–63} Nevertheless, HfO_x is able to accept oxygen only to some extent. Oxygen anions not able to enter the HfO_x lattice are involved in the oxidation of a fraction of CoO to Co_3O_4 (Figure 8e). Thus, after applying negative voltages, the Co–Pt film shows a higher presence of metallic Co and some traces of Co_3O_4 . This scenario is in accordance with the increase of m_s (Figures 4c and 5b), the changes on the XAS spectra (red curve, Figure 6d), and the increase of dichroism in the XMCD signal (red curve, Figure 7). Conversely, when the electric field polarity is inverted, the sense of O^{2-} migration is reversed. Oxygen anions are partially released from the HfO_x toward the Co–Pt film, oxidizing part of the metallic Co to CoO and CoO to Co_3O_4 (Figure 8f). In this manner, the initial state (0 V) of the Co–Pt film tends to be recovered upon positive voltage application, although not entirely. This can be inferred from the decrease of m_s (Figure S4c), which does not reach the initial state (0 V), and the slight differences on the XAS spectra (black and blue curves, Figure 6d). The results indicate that the amount of oxygen involved in the diffusion event under negative biasing does not completely diffuse back, even for large positive voltage. It is noteworthy that the observed changes in magnetism depending on the electric field polarity are in accordance with previous results reported for Co^{17,19,20} and with several studies devoted to O^{2-} migration in HfO_x under an electric field.^{64,65}

The increase (and subsequent decrease) of H_C in the three systems investigated can also be related to the reduction of CoO to Co (and the subsequent oxidation to CoO), as reported in a previous study of ours on Co–Pt/CoO composite microdisks.³¹ During negative voltage application, metallic Co regions might expand in size (Figure 8b,e). Considering that H_C is inversely proportional to the particle size within the multidomain regime,⁶⁶ it is expected that H_C will decrease with the increase of Co(Pt) region size. Conversely, the decrease of Co grain size (due to oxidation) (Figure 8c,f) would induce an increase of H_C . Dipolar interactions between the Co clusters must also be considered because H_C can be reduced (enlarged) by enhancing (diminishing) the dipolar interactions.^{67,68} As the size of Co regions increases ($-\Delta V$), the distance between clusters is presumably reduced and Co(Pt) clusters could even merge with each other (Figure 8e). Consequently, dipolar interactions would become stronger, leading to a decrease of H_C . The opposite would occur for positive voltages (Figure 8c,e). Finally, the opposite voltage-induced modulation trends for H_C and m_s could also be related to the relative influence of voltage on the effective magnetic anisotropy (K) and the saturation magnetization. Because H_C is proportional to K and inversely proportional to M_s (Stoner–Wohlfarth model in the limiting case of noninteracting single domain particles), if M_s decreases faster than K for positive voltage polarity, this would cause an increase of H_C . In our case, this seems to be the case because although we do not analyze K , there is marginal change in m_R/m_s (which is highly related to K) for the Co–Pt and Co–Pt/ HfO_x systems at positive voltage. These effects have actually been reported in the literature.²⁰ Finally, if metallic Co produced from the reduction of CoO ($-\Delta V$) does not contain Pt (presumably opposite to the initial Co–Pt metallic regions in the as-deposited film), this is expected to also cause a reduction of H_C compared to the pristine hcp Co–Pt clusters.

CONCLUSIONS

In contrast to Co–Pt films, magneto-ionic effects in Co–Pt/ AlO_x and Co–Pt/ HfO_x heterostructures are enhanced because of the oxygen acceptor/donor capabilities of the adjacent oxide nanolayers. Large variations in H_C , m_s , and m_R/m_s are obtained under negative and subsequent positive biasing. The electric field-driven migration of oxygen anions through the Co–Pt/oxide gate interface causes, in turn, variations in the Co oxidation state. These results demonstrate that coating nanostructured magnetic materials together with suitable insulating oxide nanolayers is an appealing strategy for boosting voltage-driven effects in magneto-ionic devices. In the future, we plan to operate Co–Pt/ AlO_x and Co–Pt/ HfO_x in the solid state by paying special attention to the occurrence of pinholes in the ALD layers. An investigation on the correlation between the thickness of the insulating layer and the probability of pinholes could be carried out in view of the optimum performance of the device. Likewise, the concentration of oxygen vacancies in the nonstoichiometric HfO_x should be experimentally determined and its change correlated with the applied voltage.

EXPERIMENTAL SECTION

Materials. HCl (hydrochloric acid, 37 wt %), 2-propanol ($\text{C}_3\text{H}_8\text{O}$, 99.9%), absolute ethanol (99.8%), acetone (99.0%), $\text{Na}_2\text{PtCl}_6 \cdot 6\text{H}_2\text{O}$ (98.0%), CoCl_2 ($\geq 98.0\%$), Pluronic P-123 block copolymer, PC (99.7% purity, 0.002% or 20 ppm H_2O), trimethylaluminum (TMA,

[(CH₃)₃Al]), and tetrakis(dimethylamido)hafnium (TDMAH, [(CH₃)₂N]₄Hf]) were purchased from Sigma-Aldrich. Except for PC, chemicals were used as received. Purified water was obtained from the EMD Millipore Simplicity water purification system apparatus (Millipore S.A.S.).

Sample Fabrication. Nanostructured Co–Pt films were electro-deposited on Cu (70 nm)/Ti (10 nm)/Si substrates. ED was carried out in a three-electrode cell assembled together with a PGSTAT302N Autolab galvanostat/potentiostat (from Metrohm-Autolab). Ag/AgCl was used as the reference electrode. The inner solution was 3 M KCl, and the outer solution was 1 M NaCl ($E = +0.210$ V SHE). A Pt spiral was used as the counter electrode. The films were deposited potentiostatically at -1.0 V during 600 s, under mild agitation ($\omega = 100$ rpm). The temperature of the electrolytic bath was fixed at 25 °C. The electrolyte was obtained from Milli-Q water and contained 2.8 mM CoCl₂, 1.3 mM Na₂PtCl₆·6H₂O, and 1 mg·mL⁻¹ (1 wt %) of Pluronic P-123. The pH was set to 2.1 by adding 1 M HCl solution. The concentration of P-123 was chosen to be above its critical micellar concentration⁶⁹ to induce the formation of P-123 micelles in the aqueous electrolyte. During the ED process, P-123 micelles get progressively in contact with the metal ions in solution and tend to get adsorbed on the cathode (working electrode), playing the role of a “structure-directing agent” and therefore inducing the formation of tiny pores.^{14,31,42,43} No pH buffering agent was added to the bath so as not to preclude the incorporation of oxygen in the film, and therefore the resulting nanostructured films consisted of metallic Co–Pt and Co oxide phases. The thickness of the nanostructured Co–Pt films was measured to be around 150 nm.

AlO_x and HfO_x were deposited on the nanostructured Co–Pt films by ALD using a Cambridge NanoTech Savannah 100 reactor. AlO_x coatings were obtained by alternate pulsing of TMA and ozone in the reaction chamber in the exposure mode, that is, by closing the gas exit valve for a certain amount of time to allow the precursors to diffuse into the pores and intergrain channels of the Co–Pt films. Alternatively, HfO_x deposits were prepared by combining TDMAH (heated at 75–80 °C) and deionized water as the coreactant. High purity nitrogen gas was used as the carrier and purging gas (40 and 20 sccm, respectively). In both cases, the chamber temperature was set at 200 °C. Film thickness was varied from 10 to 80 nm by modifying the number of the ALD cycles and was validated by X-ray reflectivity measurements on silicon (100) reference samples.

Morphology and Structural Characterization. Field emission SEM imaging and EDX analyses were performed on a Zeiss MERLIN operated at 5 and 15 kV, respectively. STEM images and EELS analyses were carried out on a Tecnai F20 HRTEM/STEM microscopy equipment. The crystallographic structure was investigated by means of GIXRD using a Bruker-AXS (specific model A25 D8 Discover) with a LynxEye XE-T detector using Cu K α radiation and a grazing incidence angle of 1°.

XAS and XMCD Characterization. The oxidation state of the nanostructured Co–Pt films were assessed by XAS (Co L_{3,2} edges) and acquired in the TEY mode utilizing linearly polarized light, at the UE46_PGM1 beamline (High-Field Diffractometer of the BESSY II synchrotron, Helmholtz-Zentrum Berlin). To compare with reference XAS patterns, Co L_{3,2} edge XAS spectra of Co (20 nm-thick film grown by molecular beam epitaxy on top of MgO), CoO (cobalt(II) oxide, 95%, powders purchased from Alfa Aesar), and sputtered Co₃O₄ film samples were also measured. XMCD was performed for further magnetic characterization, which acquires the difference in core-level absorption spectra (Co L_{3,2} edge) between right-handed (μ^+) and left-handed (μ^-) circularly polarized X-rays. XMCD measurements were carried out at room temperature (300 K) under the applied magnetic fields of 20 and -20 kOe.

Magneto-electric Measurements. Magnetic measurements were performed in a Micro Sense (LOT-Quantum Design) VSM at room temperature with a magnetic moment uncertainty of 0.5% and a coercivity uncertainty of ± 5 Oe. For in situ magnetoelectric measurements, a home-made electrochemical cell was attached at the end of the VSM holder. The Co–Pt-based films acted as the working electrode, a Pt wire acted as the counter electrode, and

nonaqueous PC with a small quantity of solvated Na⁺ and OH⁻ species acted as the electrolyte (i.e., nonoxidative media). These were obtained upon treating the as-purchased PC with metallic sodium in order to eliminate any traces of residual water, thus minimizing corrosion events in the sample due to the electrolyte during magneto-electric measurements. Consequently, Na⁺ and OH⁻ ions are formed, which promote the formation of the EDL and enhance the strength of the electric field in the samples.^{11,14,25,31,32} In-plane hysteresis loops were recorded applying different dc voltages ranging from 0 to -100 and 0 to $+100$ V after waiting for 90 min at every voltage value, using a power supply (model Agilent B2902A) as the voltage source. Note that the voltage was maintained during the VSM measurements. Between the two series of voltage values, the electrolyte was restored to ensure optimized performance. Relative variation in H_C , m_S , and m_R/m_S were determined as

$$\Delta y (\%) = \frac{y_f - y_i}{y_i} \times 100$$

where y is the magnetic parameter under evaluation, y_i is its value at 0 V, and y_f is the value at a given voltage. Note that y_i is different for the two series of voltage values (0 \rightarrow -100 V; 0 \rightarrow $+100$).

■ ASSOCIATED CONTENT

Supporting Information

The Supporting Information is available free of charge at <https://pubs.acs.org/doi/10.1021/acsami.9b19363>.

SEM images, VSM measurements, and XAS data (PDF)

■ AUTHOR INFORMATION

Corresponding Authors

Cristina Navarro-Senent – *Departament de Física, Universitat Autònoma de Barcelona, E-08193 Cerdanyola del Vallès, Spain*; Email: cristina.navarro.senent@uab.cat

Enric Menéndez – *Departament de Física, Universitat Autònoma de Barcelona, E-08193 Cerdanyola del Vallès, Spain*; orcid.org/0000-0003-3809-2863; Email: enric.menendez@uab.cat

Jordi Sort – *Departament de Física, Universitat Autònoma de Barcelona, E-08193 Cerdanyola del Vallès, Spain*; *Institució Catalana de Recerca i Estudis Avançats (ICREA), E-08010 Barcelona, Spain*; orcid.org/0000-0003-1213-3639; Email: jordi.sort@uab.cat

Authors

Alberto Quintana – *Departament de Física, Universitat Autònoma de Barcelona, E-08193 Cerdanyola del Vallès, Spain*; *Department of Physics, Georgetown University, 20057 Washington, D.C., United States*; orcid.org/0000-0002-9813-735X

Eloy Isarain-Chávez – *Departament de Física, Universitat Autònoma de Barcelona, E-08193 Cerdanyola del Vallès, Spain*

Eugen Weschke – *Helmholtz-Zentrum Berlin für Materialien und Energie, D-12489 Berlin, Germany*

Pengmei Yu – *Institut de Ciència de Materials de Barcelona (ICMAB-CSIC), E-08193 Bellaterra, Catalonia, Spain*

Mariona Coll – *Institut de Ciència de Materials de Barcelona (ICMAB-CSIC), E-08193 Bellaterra, Catalonia, Spain*;

orcid.org/0000-0001-5157-7764

Eva Pellicer – *Departament de Física, Universitat Autònoma de Barcelona, E-08193 Cerdanyola del Vallès, Spain*;

orcid.org/0000-0002-8901-0998

Complete contact information is available at: <https://pubs.acs.org/doi/10.1021/acsami.9b19363>

Notes

The authors declare no competing financial interest.

ACKNOWLEDGMENTS

Financial support by the European Research Council (SPIN-PORICS 2014-Consolidator Grant, agreement no. 648454), the Spanish Government (Project MAT2017-86357-C3-1-R, MAT2017-83169-R “Severo Ochoa” Programme for Centres of Excellence in R&D SEV-2015-0496 and associated FEDER), the Generalitat de Catalunya (2017-SGR-292 and 2017-SGR-1519), and the European Union’s Horizon 2020 research and innovation programme under the Marie Skłodowska-Curie grant agreement no. 665919 is acknowledged. P.Y. acknowledges the Chinese Scholarship Council CSC fellowship (201606920073).

REFERENCES

- (1) Chappert, C.; Fert, A.; Van Dau, F. N. The Emergence of Spin Electronics in Data Storage. *Nat. Mater.* **2007**, *6*, 813–823.
- (2) Dieny, B.; Sousa, R. C.; Herault, J.; Pappas, C.; Prenat, G.; Ebels, U.; Houssameddine, D.; Rodmacq, B.; Auffret, S.; Prejbeanu, L. D. B.; Cyrille, M. C.; Delaet, B.; Redon, O.; Ducruet, C.; Nozieres, J. P.; Prejbeanu, I. L. Spin-Transfer Effect and Its Use in Spintronic Components. *Internet J. Nanotechnol.* **2010**, *7*, 591–614.
- (3) Shiota, Y.; Nozaki, T.; Bonell, F.; Murakami, S.; Shinjo, T.; Suzuki, Y. Induction of Coherent Magnetization Switching in a Few Atomic Layers of FeCo Using Voltage Pulses. *Nat. Mater.* **2012**, *11*, 39–43.
- (4) Matsukura, F.; Tokura, Y.; Ohno, H. Control of Magnetism by Electric Fields. *Nat. Nanotechnol.* **2015**, *10*, 209–220.
- (5) Song, C.; Cui, B.; Li, F.; Zhou, X.; Pan, F. Recent Progress in Voltage Control of Magnetism: Materials, Mechanisms, and Performance. *Prog. Mater. Sci.* **2017**, *87*, 33–82.
- (6) Liu, M.; Obi, O.; Lou, J.; Chen, Y.; Cai, Z.; Stoute, S.; Espanol, M.; Lew, M.; Situ, X.; Ziemer, K. S.; Harris, V. G.; Sun, N. X. Giant Electric Field Tuning of Magnetic Properties in Multiferroic Ferrite/Ferroelectric Heterostructures. *Adv. Funct. Mater.* **2009**, *19*, 1826–1831.
- (7) Cherifi, R. O.; Ivanovskaya, V.; Phillips, L. C.; Zobelli, A.; Infante, I. C.; Jacquet, E.; Garcia, V.; Fusil, S.; Briddon, P. R.; Guiblin, N.; Mougín, A.; Únal, A. A.; Kronast, F.; Valencia, S.; Dkhil, B.; Barthélémy, A.; Bibes, M. Electric-Field Control of Magnetic Order above Room Temperature. *Nat. Mater.* **2014**, *13*, 345–351.
- (8) Martin, L. W.; Ramesh, R. Multiferroic and Magnetoelectric Heterostructures. *Acta Mater.* **2012**, *60*, 2449–2470.
- (9) Bibes, M.; Barthélémy, A. Multiferroics: Towards a Magnetoelectric Memory. *Nat. Mater.* **2008**, *7*, 425–426.
- (10) Izyumskaya, N.; Alivov, Y.; Morkoç, H. Oxides, Oxides, and More Oxides: High-Oxides, Ferroelectrics, Ferromagnetics, and Multiferroics. *Crit. Rev. Solid State Mater. Sci.* **2009**, *34*, 89–179.
- (11) Dislaki, E.; Robbenolt, S.; Campoy-Quiles, M.; Nogués, J.; Pellicer, E.; Sort, J. Coercivity Modulation in Fe–Cu Pseudo-Ordered Porous Thin Films Controlled by an Applied Voltage: A Sustainable, Energy-Efficient Approach to Magnetoelectrically Driven Materials. *Adv. Sci.* **2018**, *5*, 1800499.
- (12) Weisheit, M.; Fähler, S.; Marty, A.; Souche, Y.; Poinson, C.; Givord, D. Electric Field-Induced Modification of Magnetism in Thin-Film Ferromagnets. *Science* **2007**, *315*, 349–351.
- (13) Ovchinnikov, I. V.; Wang, K. L. Theory of Electric-Field-Controlled Surface Ferromagnetic Transition in Metals. *Phys. Rev. B: Condens. Matter Mater. Phys.* **2009**, *79*, 020402.
- (14) Quintana, A.; Zhang, J.; Isarain-Chávez, E.; Menéndez, E.; Cuadrado, R.; Robles, R.; Baró, M. D.; Guerrero, M.; Pané, S.; Nelson, B. J.; Müller, C. M.; Ordejón, P.; Nogués, J.; Pellicer, E.; Sort, J. Voltage-Induced Coercivity Reduction in Nanoporous Alloy Films: A Boost toward Energy-Efficient Magnetic Actuation. *Adv. Funct. Mater.* **2017**, *27*, 1701904.
- (15) Koyama, T.; Nakatani, Y.; Ieda, J. I.; Chiba, D. Electric Field Control of Magnetic Domain Wall Motion via Modulation of the Dzyaloshinskii-Moriya Interaction. *Sci. Adv.* **2018**, *4*, No. eaav0265.
- (16) Bauer, U.; Yao, L.; Tan, A. J.; Agrawal, P.; Emori, S.; Tuller, H. L.; Van Dijken, S.; Beach, G. S. D. Magneto-Ionic Control of Interfacial Magnetism. *Nat. Mater.* **2015**, *14*, 174–181.
- (17) Bi, C.; Liu, Y.; Newhouse-Illige, T.; Xu, M.; Rosales, M.; Freeland, J. W.; Mryasov, O.; Zhang, S.; Te Velthuis, S. G. E.; Wang, W. G. Reversible Control of Co Magnetism by Voltage-Induced Oxidation. *Phys. Rev. Lett.* **2014**, *113*, 267202.
- (18) Gilbert, D. A.; Olamit, J.; Dumas, R. K.; Kirby, B. J.; Grutter, A. J.; Maranville, B. B.; Arenholz, E.; Borchers, J. A.; Liu, K. Controllable Positive Exchange Bias via Redox-Driven Oxygen Migration. *Nat. Commun.* **2016**, *7*, 11050.
- (19) Zhou, X.; Yan, Y.; Jiang, M.; Cui, B.; Pan, F.; Song, C. Role of Oxygen Ion Migration in the Electrical Control of Magnetism in Pt/Co/Ni/HfO₂ Films. *J. Phys. Chem. C* **2016**, *120*, 1633–1639.
- (20) Yan, Y. N.; Zhou, X. J.; Li, F.; Cui, B.; Wang, Y. Y.; Wang, G. Y.; Pan, F.; Song, C. Electrical Control of Co/Ni Magnetism Adjacent to Gate Oxides with Low Oxygen Ion Mobility. *Appl. Phys. Lett.* **2015**, *107*, 122407.
- (21) Bauer, U.; Emori, S.; Beach, G. S. D. Voltage-Controlled Domain Wall Traps in Ferromagnetic Nanowires. *Nat. Nanotechnol.* **2013**, *8*, 411–416.
- (22) Dasgupta, S.; Das, B.; Knapp, M.; Brand, R. A.; Ehrenberg, H.; Kruk, R.; Hahn, H. Intercalation-Driven Reversible Control of Magnetism in Bulk Ferromagnets. *Adv. Mater.* **2014**, *26*, 4639–4644.
- (23) Leistner, K.; Lange, N.; Hänisch, J.; Oswald, S.; Scheiba, F.; Fähler, S.; Schlörb, H.; Schultz, L. Electrode Processes and in Situ Magnetic Measurements of FePt Films in a LiPF₆ based Electrolyte. *Electrochim. Acta* **2012**, *81*, 330–337.
- (24) Leistner, K.; Wunderwald, J.; Lange, N.; Oswald, S.; Richter, M.; Zhang, H.; Schultz, L.; Fähler, S. Electric-Field Control of Magnetism by Reversible Surface Reduction and Oxidation Reactions. *Phys. Rev. B: Condens. Matter Mater. Phys.* **2013**, *87*, 224411.
- (25) Robbenolt, S.; Quintana, A.; Pellicer, E.; Sort, J. Large Magnetoelectric Effects Mediated by Electric-Field-Driven Nanoscale Phase Transformations in Sputtered (Nanoparticulate) and Electrochemically Dealloyed (Nanoporous) Fe-Cu Films. *Nanoscale* **2018**, *10*, 14570–14578.
- (26) Zhao, S.; Zhou, Z.; Peng, B.; Zhu, M.; Feng, M.; Yang, Q.; Yan, Y.; Ren, W.; Ye, Z.-G.; Liu, Y.; Liu, M. Quantitative Determination on Ionic-Liquid-Gating Control of Interfacial Magnetism. *Adv. Mater.* **2017**, *29*, 1606478.
- (27) Diez, L. H.; Liu, Y. T.; Gilbert, D. A.; Belmeguenai, M.; Vogel, J.; Pizzini, S.; Martinez, E.; Lamperti, A.; Mohammedi, J. B.; Laborieux, A.; Roussigné, Y.; Grutter, A. J.; Arenholtz, E.; Quarterman, P.; Maranville, B.; Ono, S.; Hadri, M. S. E.; Tolley, R.; Fullerton, E.; Sanchez-Tejerina, L.; Stashkevich, A.; Chérif, S.; Kent, A.; Querlioz, D.; Langer, J.; Ocker, B.; Ravelosona, D. Nonvolatile Ionic Modification of the Dzyaloshinskii-Moriya Interaction. *Phys. Rev. Appl.* **2019**, *12*, 034005.
- (28) Gilbert, D. A.; Grutter, A. J.; Arenholz, E.; Liu, K.; Kirby, B. J.; Borchers, J. A.; Maranville, B. B. Structural and Magnetic Depth Profiles of Magneto-Ionic Heterostructures beyond the Interface Limit. *Nat. Commun.* **2016**, *7*, 12264.
- (29) Jiang, M.; Chen, X. Z.; Zhou, X. J.; Cui, B.; Yan, Y. N.; Wu, H. Q.; Pan, F.; Song, C. Electrochemical Control of the Phase Transition of Ultrathin FeRh Films. *Appl. Phys. Lett.* **2016**, *108*, 202404.
- (30) Hunter, R. J. *Foundations of Colloid Science*; Oxford University Press: New York, 2001.
- (31) Navarro-Senent, C.; Fornell, J.; Isarain-Chávez, E.; Quintana, A.; Menéndez, E.; Foerster, M.; Aballe, L.; Weschke, E.; Nogués, J.; Pellicer, E.; Sort, J. Large Magnetoelectric Effects in Electrodeposited Nanoporous Microdisks Driven by Effective Surface Charging and Magneto-Ionics. *ACS Appl. Mater. Interfaces* **2018**, *10*, 44897–44905.
- (32) Quintana, A.; Menéndez, E.; Liedke, M. O.; Butterling, M.; Wagner, A.; Sireus, V.; Torruella, P.; Estradé, S.; Peiró, F.; Dendooven, J.; Detavernier, C.; Murray, P. D.; Gilbert, D. A.; Liu,

K.; Pellicer, E.; Nogues, J.; Sort, J. Voltage-Controlled ON-OFF Ferromagnetism at Room Temperature in a Single Metal Oxide Film. *ACS Nano* **2018**, *12*, 10291–10300.

(33) Navarro-Senent, C.; Quintana, A.; Menéndez, E.; Pellicer, E.; Sort, J. Electrolyte-Gated Magnetoelectric Actuation: Phenomenology, Materials, Mechanisms, and Prospective Applications. *APL Mater.* **2019**, *7*, 030701.

(34) Molinari, A.; Hahn, H.; Kruk, R. Voltage-Control of Magnetism in All-Solid-State and Solid/Liquid Magnetoelectric Composites. *Adv. Mater.* **2019**, *31*, 1806662.

(35) Wagner, T.; Haffer, S.; Weinberger, C.; Klaus, D.; Tiemann, M. Mesoporous Materials as Gas Sensors. *Chem. Soc. Rev.* **2013**, *42*, 4036–4053.

(36) Li, W.; Liu, J.; Zhao, D. Mesoporous Materials for Energy Conversion and Storage Devices. *Nat. Rev. Mater.* **2016**, *1*, 16023.

(37) Pal, N.; Bhaumik, A. Mesoporous Materials: Versatile Supports in Heterogeneous Catalysis for Liquid Phase Catalytic Transformations. *RSC Adv.* **2015**, *5*, 24363–24391.

(38) Reitz, C.; Suchomski, C.; Wang, D.; Hahn, H.; Brezesinski, T. In Situ Tuning of Magnetization via Topotactic Lithium Insertion in Ordered Mesoporous Lithium Ferrite Thin Films. *J. Mater. Chem. C* **2016**, *4*, 8889–8896.

(39) Ghosh, S. Charge-Response of Magnetization in Nanoporous PdNi Alloys. *J. Magn. Magn. Mater.* **2011**, *323*, 552–556.

(40) Quintana, A.; Menéndez, E.; Isarain-Chávez, E.; Fornell, J.; Solsona, P.; Fauth, F.; Baró, M. D.; Nogués, J.; Pellicer, E.; Sort, J. Tunable Magnetism in Nanoporous CuNi Alloys by Reversible Voltage-Driven Element-Selective Redox Processes. *Small* **2018**, *14*, 1704396.

(41) Dubraja, L. A.; Reitz, C.; Velasco, L.; Witte, R.; Kruk, R.; Hahn, H.; Brezesinski, T. Electrochemical Tuning of Magnetism in Ordered Mesoporous Transition-Metal Ferrite Films for Micromagnetic Actuation. *ACS Appl. Nano Mater.* **2017**, *1*, 65.

(42) Isarain-Chávez, E.; Baró, M. D.; Alcantara, C.; Pané, S.; Sort, J.; Pellicer, E. Micelle-Assisted Electrodeposition of Mesoporous Fe–Pt Smooth Thin Films and Their Electrocatalytic Activity towards the Hydrogen Evolution Reaction. *ChemSusChem* **2018**, *11*, 367–375.

(43) Zhang, J.; Quintana, A.; Menéndez, E.; Coll, M.; Pellicer, E.; Sort, J. Electrodeposited Ni-Based Magnetic Mesoporous Films as Smart Surfaces for Atomic Layer Deposition: An “All-Chemical” Deposition Approach toward 3D Nanoengineered Composite Layers. *ACS Appl. Mater. Interfaces* **2018**, *10*, 14877.

(44) Foster, A. S.; Shluger, A. L.; Nieminen, R. M. Mechanism of Interstitial Oxygen Diffusion in Hafnia. *Phys. Rev. Lett.* **2002**, *89*, 225901.

(45) Aschauer, U.; Bowen, P.; Parker, S. C. Oxygen Vacancy Diffusion in Alumina: New Atomistic Simulation Methods Applied to an Old Problem. *Acta Mater.* **2009**, *57*, 4765–4772.

(46) Wang, D.; He, G.; Hao, L.; Gao, J.; Zhang, M. Comparative Passivation Effect of ALD-Driven HfO₂ and Al₂O₃ Buffer Layers on the Interface Chemistry and Electrical Characteristics of Dy-Based Gate Dielectrics. *J. Mater. Chem. C* **2019**, *7*, 1955–1965.

(47) Wang, L.-G.; Qian, X.; Cao, Y.-Q.; Cao, Z.-Y.; Fang, G.-Y.; Li, A.-D.; Wu, D. Excellent Resistive Switching Properties of Atomic Layer-Deposited Al₂O₃/HfO₂/Al₂O₃ Trilayer Structures for Non-Volatile Memory Applications. *Nanoscale Res. Lett.* **2015**, *10*, 135.

(48) Wang, C.; Zhang, H.; Li, C.; He, Y.; Zhang, L.; Zhao, X.; Yang, Q.; Xian, D.; Mao, Q.; Peng, B.; Zhou, Z.; Cui, W.; Hu, Z. Voltage Control of Magnetic Anisotropy through Ionic Gel Gating for Flexible Spintronics. *ACS Appl. Mater. Interfaces* **2018**, *10*, 29750.

(49) Zhao, S.; Zhou, Z.; Li, C.; Peng, B.; Hu, Z.; Liu, M. Low-Voltage Control of (Co/Pt)_x Perpendicular Magnetic Anisotropy Heterostructure for Flexible Spintronics. *ACS Nano* **2018**, *12*, 7167–7173.

(50) Yang, Q.; Zhou, Z.; Wang, L.; Zhang, H.; Cheng, Y.; Hu, Z.; Peng, B.; Liu, M. Ionic Gel Modulation of RKKY Interactions in Synthetic Anti-Ferromagnetic Nanostructures for Low Power Wearable Spintronic Devices. *Adv. Mater.* **2018**, *30*, 1800449.

(51) Jiang, Y.-B.; Liu, N.; Gerung, H.; Cecchi, J. L.; Brinker, C. J. Nanometer-Thick Conformal Pore Sealing Of Self-Assembled Mesoporous Silica By Plasma-Assisted Atomic Layer Deposition. *J. Am. Chem. Soc.* **2006**, *128*, 11018–11019.

(52) Darling, A. S. Cobalt–Platinum Alloys A Critical Review of Their Constitution and Properties. *Platinum Met. Rev.* **1963**, *7*, 96–104.

(53) Miller, M. S.; Schultz, A. E.; Chow, Y. M.; Heuer, L. A. Optimization of Co–Pt and Co–Cr–Pt–Ta Thin Films for Use in Magnetic Data Storage Devices. *Surf. Coat. Technol.* **1994**, *68–69*, 696–701.

(54) Lin, T. Magnetic, Recording and Structural Characteristics of Sputtered Co–Cr–Pt Films for Longitudinal Recording. *J. Magn. Mater.* **1990**, *86*, 159.

(55) Cui, B.; Song, C.; Gehring, G. A.; Li, F.; Wang, G.; Chen, C.; Peng, J.; Mao, H.; Zeng, F.; Pan, F. Electrical Manipulation of Orbital Occupancy and Magnetic Anisotropy in Manganites. *Adv. Funct. Mater.* **2015**, *25*, 864–870.

(56) Liu, Y. T.; Ono, S.; Agnus, G.; Adam, J.-P.; Jaiswal, S.; Langer, J.; Ocker, B.; Ravelosona, D.; Herrera Diez, L. Electric Field Controlled Domain Wall Dynamics and Magnetic Easy Axis Switching in Liquid Gated CoFeB/MgO Films. *J. Appl. Phys.* **2017**, *122*, 133907.

(57) Sahadevan, A. M.; Kalitsov, A.; Kalon, G.; Bhatia, C. S.; Veleev, J.; Yang, H. Electric-Field-Induced Magnetization Changes in Co/Al₂O₃ Granular Multilayers. *Phys. Rev. B: Condens. Matter Mater. Phys.* **2013**, *87*, 014425.

(58) Cheng, B.; Qin, H.; Liu, L.; Xie, J.; Zhou, G.; Chen, L.; Hu, J. Electric-Field Control of Magnetic Properties for α -Fe₂O₃/Al₂O₃ Films. *J. Phys. D: Appl. Phys.* **2018**, *51*, 235002.

(59) Miwa, S.; Suzuki, M.; Tsujikawa, M.; Matsuda, K.; Nozaki, T.; Tanaka, K.; Tsukahara, T.; Nawaoka, K.; Goto, M.; Kotani, Y.; Ohkubo, T.; Bonell, F.; Tamura, E.; Hono, K.; Nakamura, T.; Shirai, M.; Yuasa, S.; Suzuki, Y. Voltage Controlled Interfacial Magnetism through Platinum Orbits. *Nat. Commun.* **2017**, *8*, 15848.

(60) Chen, T.-J.; Kuo, C.-L. Oxygen Vacancy Formation and the Induced Defect States in HfO₂ and Hf-Silicates - A First Principles Hybrid Functional Study. *Microelectron. Reliab.* **2014**, *54*, 1119–1124.

(61) Xu, D.-P.; Yu, L.-J.; Chen, X.-D.; Chen, L.; Sun, Q.-Q.; Zhu, H.; Lu, H.-L.; Zhou, P.; Ding, S.-J.; Zhang, D.-W. In Situ Analysis of Oxygen Vacancies and Band Alignment in HfO₂/TiN Structure for CMOS Applications. *Nanoscale Res. Lett.* **2017**, *12*, 311.

(62) Tse, K.; Liu, D.; Xiong, K.; Robertson, J. Oxygen Vacancies in High-k Oxides. *Microelectron. Eng.* **2007**, *84*, 2028–2031.

(63) Perevalov, T. V.; Aliev, V. S.; Gritsenko, V. A.; Saraev, A. A.; Kaichev, V. V. Electronic Structure of Oxygen Vacancies in Hafnium Oxide. *Microelectron. Eng.* **2013**, *109*, 21–23.

(64) Goux, L.; Czarnecki, P.; Chen, Y. Y.; Pantisano, L.; Wang, X. P.; Degraeve, R.; Govoreanu, B.; Jurczak, M.; Wouters, D. J.; Altimime, L. Evidences of Oxygen-Mediated Resistive-Switching Mechanism in TiN/HfO₂/Pt Cells. *Appl. Phys. Lett.* **2010**, *97*, 243509.

(65) Nagata, T.; Haemori, M.; Yamashita, Y.; Yoshikawa, H.; Iwashita, Y.; Kobayashi, K.; Chikyow, T. Oxygen Migration at Pt/HfO₂/Pt Interface under Bias Operation. *Appl. Phys. Lett.* **2010**, *97*, 082902.

(66) Hadjipanayis, G. C. Nanophase Hard Magnets. *J. Magn. Magn. Mater.* **1999**, *200*, 373–391.

(67) Kechrakos, D.; Trohidou, K. N. Magnetic Properties of Dipolar Interacting Single-Domain Particles. *Phys. Rev. B: Condens. Matter Mater. Phys.* **1998**, *58*, 12169–12177.

(68) Skomski, R.; Coey, J. M. D. *Permanent Magnetism*; Institute of Physics Publishing: Bristol, 1999.

(69) Wanka, G.; Hoffmann, H.; Ulbricht, W. Phase Diagrams and Aggregation Behavior of Poly(Oxyethylene)-Poly(Oxypropylene)-Poly(Oxyethylene) Triblock Copolymers in Aqueous Solutions. *Macromolecules* **1994**, *27*, 4145–4159.

Supporting Information

Enhancing magneto-ionic effects in magnetic nanostructured films via conformal deposition of nanolayers with oxygen getter/donor capabilities

Cristina Navarro-Senent,^{,†} Alberto Quintana,^{†, ‡}, Eloy Isarain-Chávez,[†] Eugen Weschke,[§] Pengmei Yu,^{||} Mariona Coll,^{||} Eva Pellicer,[†] Enric Menéndez,^{†,*} and Jordi Sort^{†,⊥,*}*

[†]Departament de Física, Universitat Autònoma de Barcelona, E-08193 Cerdanyola del Vallès, Spain.

[‡]Department of Physics, Georgetown University, Washington, D.C. 20057, USA

[§]Helmholtz-Zentrum Berlin für Materialien und Energie, Albert-Einstein-Strasse 15, D-12489 Berlin, Germany

^{||}Institut de Ciència de Materials de Barcelona (ICMAB-CSIC) Campus UAB, E-08193 Bellaterra, Catalonia, Spain

[⊥]Institució Catalana de Recerca i Estudis Avançats (ICREA), Pg. Lluís Companys 23, E-08010 Barcelona, Spain

* Corresponding Authors: cristina.navarro.senent@uab.cat, enric.menendez@uab.cat, jordi.sort@uab.cat

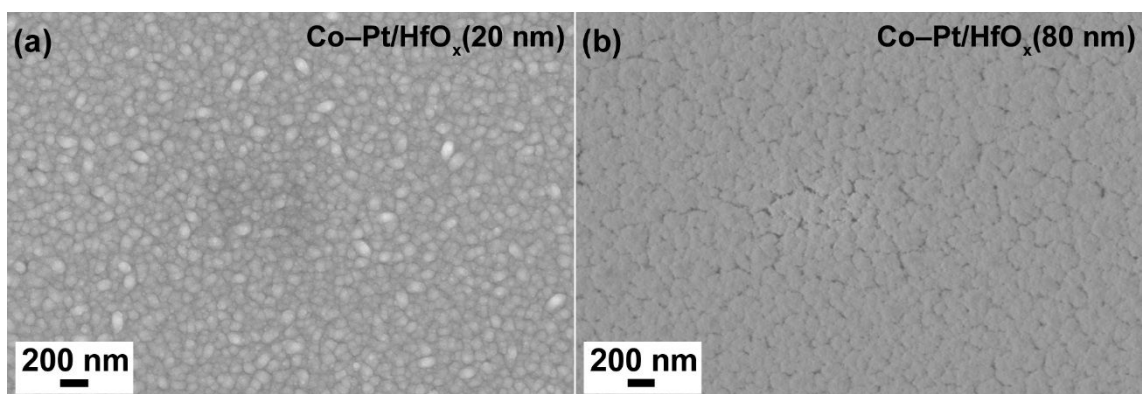


Figure S1. Scanning electron microscopy (SEM) image of an electrodeposited nanostructured Co–Pt film coated with (a) 20 nm HfO_x and (b) 80 nm of HfO_x by atomic layer deposition.

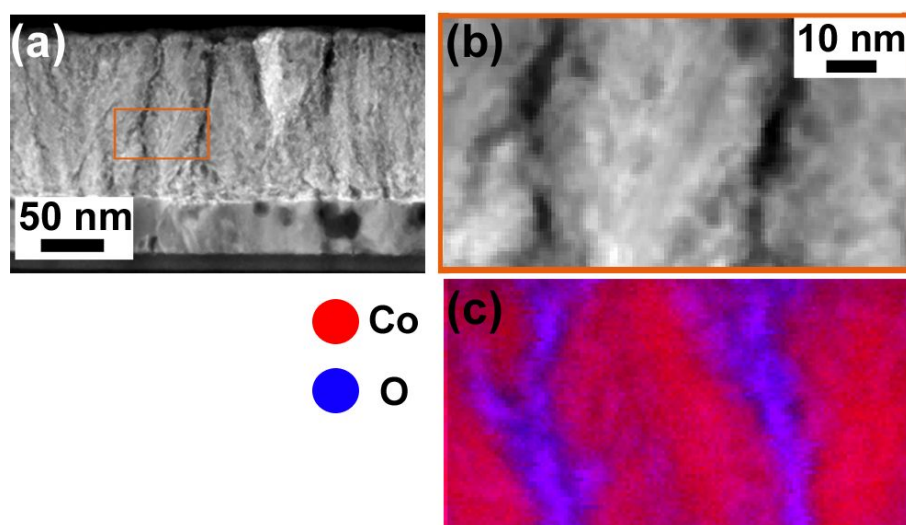


Figure S2. (a) STEM image of a cross section of uncoated Co–Pt film and (b) zoomed detail of the area enclosed in the orange square and (c) the corresponding Cobalt (red) and O (blue) EELS mapping.

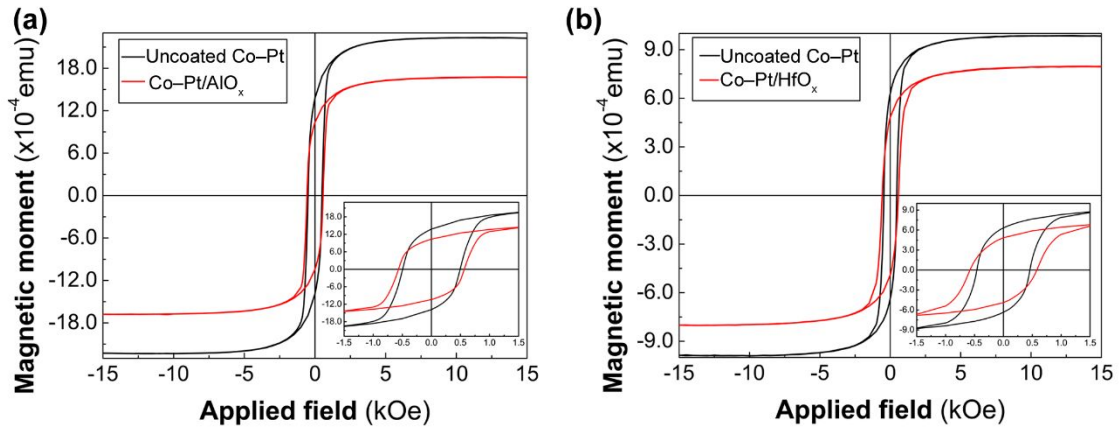


Figure S3. In-plane hysteresis loops measured by vibrating sample magnetometry (VSM) for uncoated Co-Pt (black loop) and coated Co-Pt with 10 nm of (a) AlO_x and (b) HfO_x (red loops).

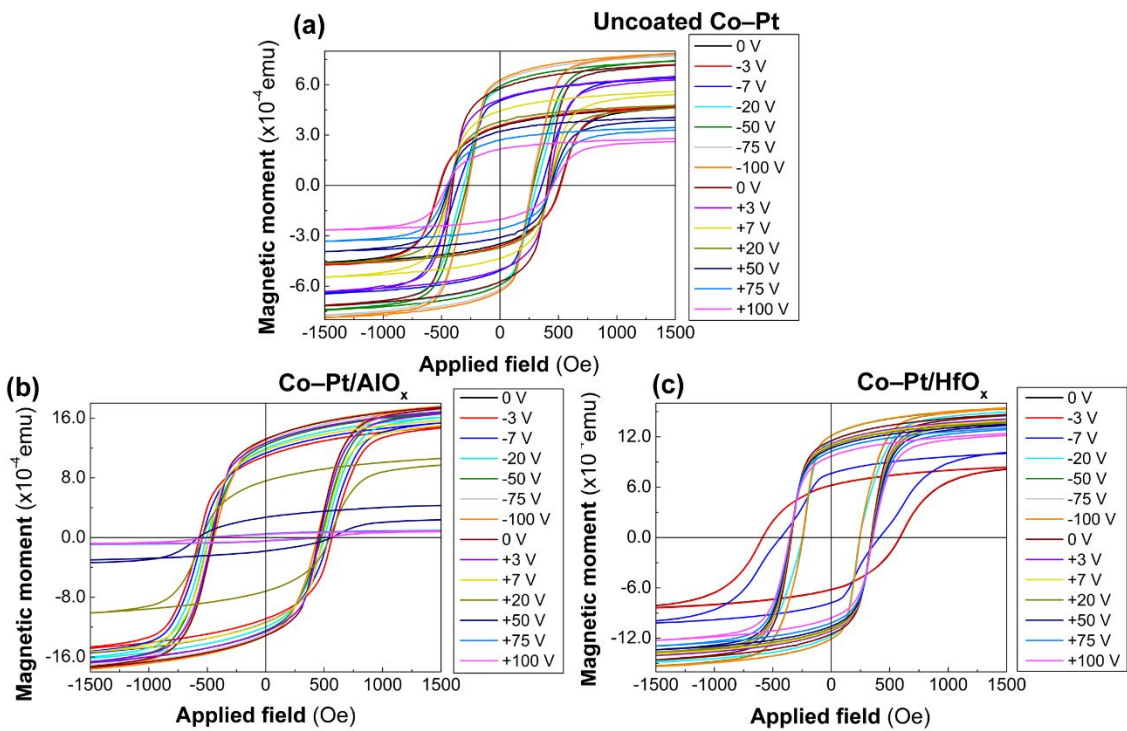


Figure S4. In-plane hysteresis loops measured by VSM for (a) uncoated Co-Pt, (b) Co-Pt/ AlO_x and (c) Co-Pt/ HfO_x films after applying 0, -3, -7, -20, -50, -75, -100, 0, +3, +7, +20, +50, +75 and +100 V in sequence.

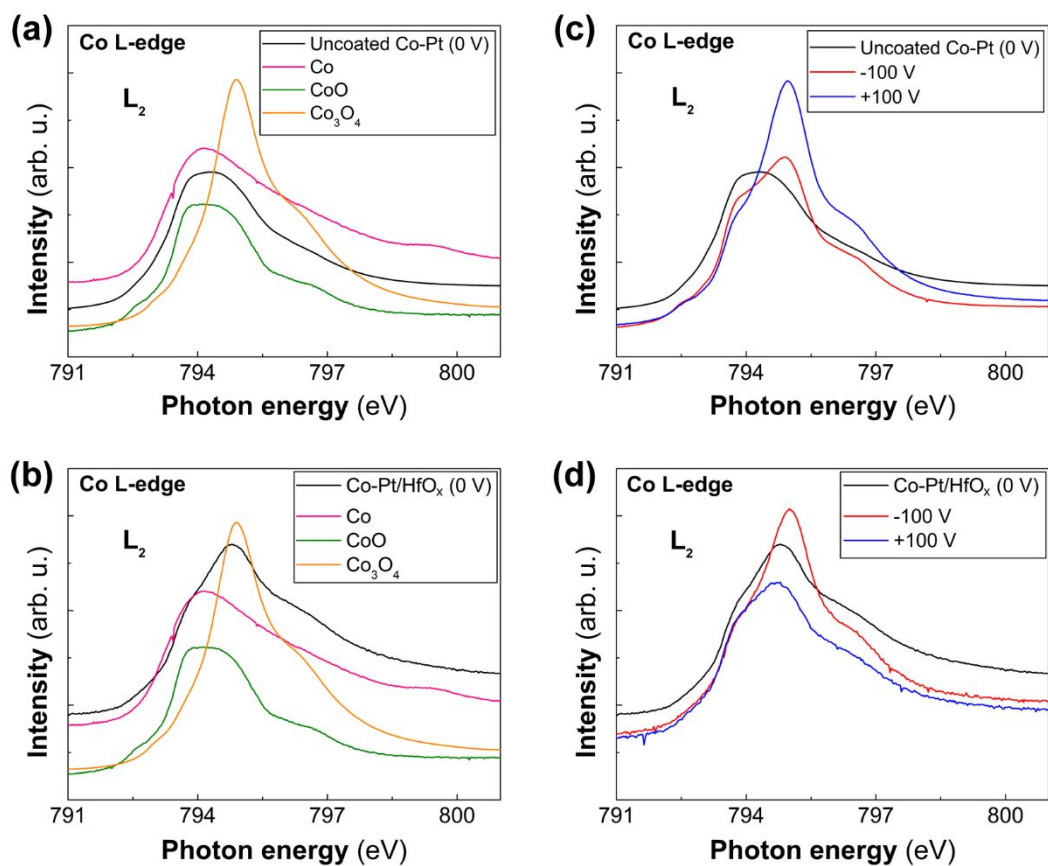


Figure S5. Cobalt L₂-edge X-ray absorption spectra (XAS) of the as-prepared (0 V, black curve) (a) uncoated Co-Pt and (b) Co-Pt/HfO₂ films, together with the spectra of reference samples (pink: Co; green: CoO; orange: Co₃O₄). Evolution of the Cobalt L₂-edge XAS after applying -100 V (red curve) and +100 V (blue curve) for (c) uncoated Co-Pt and (d) Co-Pt/HfO_x films.

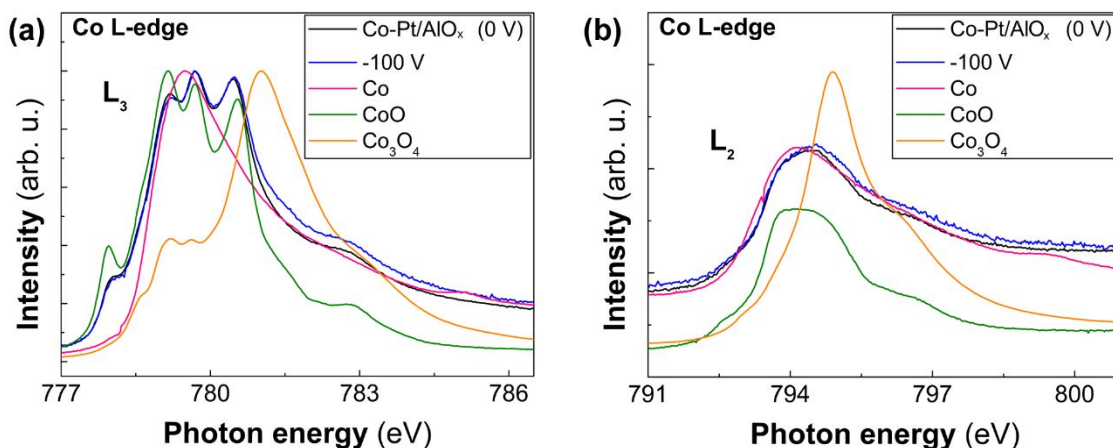


Figure S6. Zoom-in of the Cobalt (a) L_3 -edge and (b) L_2 -edge XAS spectra for the Co–Pt/ AlO_x film in the pristine state (0V, black curve) and after applying –100 V (blue curve). The XAS spectra of reference samples is shown (pink: Co; green: CoO; orange: Co_3O_4).

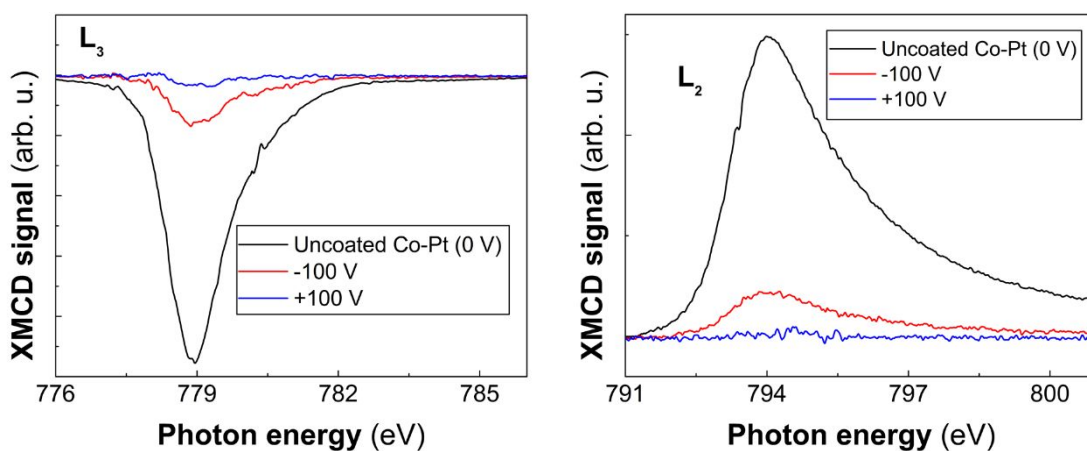


Figure S7. Zoom-in of the Cobalt L_3 (left) and L_2 (right) edges X-ray magnetic circular dichroism (XMCD) signal for the uncoated Co–Pt sample in the pristine state (0V, black curve) and after applying –100 V (red curve) and +100 V (blue curve).

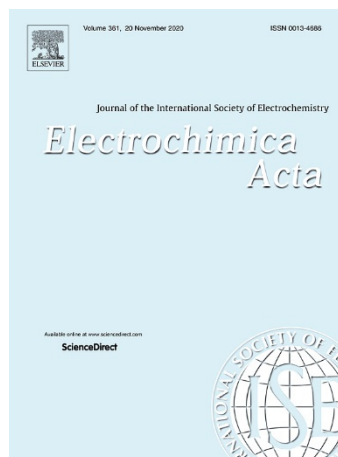
4.3. The order of addition and time matters: impact of electrolyte processing on micelle-assisted electrosynthesis of mesoporous alloys

This third study tackles the influence of the electrolyte processing over the reproducibility of mesoporous Co–Pt metallic films prepared by micelle-assisted electrodeposition. During a series of preliminary experiments, we noticed that the order of addition of the reagents to the bath and the time elapsed between its preparation and the subsequent electrodeposition experiments, had an impact over the mesoporosity of Co–Pt alloys. Specifically, we proved that the dissolution of the platinum salt (Na_2PtCl_6) in water and its storage for a period of 10 days (equilibration time) before the cobalt salt (CoCl_2) and the non-ionic surfactant P-123 were added, is crucial for reproducing the mesoporosity of the alloys.

A parametric study from various bath formulations was conducted together with a comparative detailed analysis of the resulting Co–Pt films by electron microscopy, EDX and XRD techniques.

Highly mesoporous Pt-rich Co–Pt films (10-23 at% Co) were obtained from an electrolyte involving the equilibration time, whereas Co–Pt films obtained from a freshly prepared electrolyte did not display a clear mesostructure, being this often absent. Since the corresponding cyclic voltammeteries were negatively shifted in the cathodic zone by 300 mV, the applied potentials were adjusted accordingly for deposits' growth. As a result, deposits obtained from the freshly prepared electrolyte were Co-rich (58-85 at% Co). To exclude an influence of the Co/Pt ratio of the deposits on the mesoporosity, the CoCl_2 concentration in the bath was increased by 10-fold while keeping the equilibration time. Under such conditions, deposits with higher Co contents (60-90 at%) and with a reproducible mesostructure were achieved. Mesoporosity was also evident in Co-Pt films deposited from an electrolyte in which $\text{Na}_2\text{PtCl}_6 \cdot 6\text{H}_2\text{O}$ and P-123 were first co-dissolved and the resulting dissolution stored for 10 days before CoCl_2 was added.

The results suggested that the reproducible formation of a mesoporous network is governed by the dynamics of the Pt(IV) complexes in water. UV-Vis spectroscopy showed an increase of the concentration of $[\text{PtCl}_{6-x}(\text{OH})_x]^{2-}$ complexes during the 10-day storage period. These chloroaqua complexes would originate from the progressive exchange of Cl^- and OH^- ligands, and would interact more efficiently with the poly(ethylene oxide) groups of P-123 micelles. The efficient interaction between Pt(IV) and P-123 micelles is thus key for the successful formation of long-range order mesoporosity.



The order of addition and time matters: Impact of electrolyte processing on micelle-assisted electrosynthesis of mesoporous alloys

Cristina Navarro-Senent,^{a,*} Salvador Pané,^b Jordi Sort^{a,c} and Eva Pellicer^{a,*}

^aDepartament de Física, Facultat de Ciències, Universitat Autònoma de Barcelona E-08193 Bellaterra (Cerdanyola del Vallès), Barcelona, Spain.

^bInstitute of Robotics and Intelligent Systems, Swiss Federal Institute of Technology ETH Zurich, Tannenstraße 3, 8092 Zurich, Switzerland.

^cInstitució Catalana de Recerca i Estudis Avançats (ICREA), Pg. Lluís Companys 23, E-08010 Barcelona, Spain.



The order of addition and time matters: Impact of electrolyte processing on micelle-assisted electrosynthesis of mesoporous alloys



Cristina Navarro-Senent^{a,*}, Salvador Pané^{b,*}, Jordi Sort^{a,c}, Eva Pellicer^{a,*}

^a Departament de Física, Facultat de Ciències, Universitat Autònoma de Barcelona E-08193 Bellaterra (Cerdanyola del Vallès), Barcelona, Spain

^b Institute of Robotics and Intelligent Systems, Swiss Federal Institute of Technology ETH Zurich, Tannenstraße 3, 8092 Zurich, Switzerland

^c Institució Catalana de Recerca i Estudis Avançats (ICREA), Pg. Lluís Companys 23, E-08010 Barcelona, Spain

ARTICLE INFO

Article history:

Received 9 June 2020

Revised 28 July 2020

Accepted 11 August 2020

Available online 14 August 2020

Keywords:

Electrolyte processing

Electrodeposition

Mesoporous alloys

Cobalt-platinum

Amphiphilic surfactant

ABSTRACT

Mesoporous thin films are currently awakening a considerable interest for their prospective use in applications ranging from catalysis to energy storage. Yet, some of the synthetic parameters enabling a reproducible development of mesoporosity remain uncontrolled. In this research, we demonstrate that a subtle change in the procedure for the electrolyte preparation for the electrosynthesis of mesoporous Co–Pt films is critical for reproducing the mesoporosity of the alloys. Specifically, we show that dissolution of the platinum salt ($\text{Na}_2\text{PtCl}_6 \cdot 6\text{H}_2\text{O}$) in water and storage of the solution (referred to as ‘equilibration time’) before adding the remaining reagents and additives (CoCl_2 and P-123) are imperative to consistently reproduce the films mesoporosity. Highly mesoporous Pt-rich Co–Pt films (10–23 at.% Co), with a pore diameter of 10–17 nm, were obtained from an electrolyte that involved an equilibration time, while mesoporosity was often absent in films grown from a freshly prepared electrolyte (i.e., upon dissolving all chemicals immediately before electrodeposition). The results suggest that pore formation is governed by the complexation dynamics of Pt(IV) in water, which was investigated by UV–vis spectroscopy. Namely, the concentration of hydroxochloroplatinate complexes ($[\text{PtCl}_{6-x}(\text{OH})_x]^{2-}$) originating from the exchange of Cl^- by OH^- ions increase during the equilibration time. $[\text{PtCl}_{6-x}(\text{OH})_x]^{2-}$ species would interact more favorably with the hydrophilic poly(ethylene oxide) moieties of P-123 micelles than $[\text{PtCl}_6]^{2-}$. The distinct interaction between micelles and the complexes of platinum is key for the reproducible generation of a mesoporous network. Our finding highlights the relevant role of electrolyte processing for the control of mesoporosity in metallic systems prepared by micelle-assisted electrodeposition, which we believe can be extended to many electrolytic processes.

© 2020 Elsevier Ltd. All rights reserved.

1. Introduction

Mesoporous metals and alloys have been increasingly engaging researchers during the last decade for their prospective use as critical building blocks in a wealth of applications including energy conversion, sensing, or information technologies [1,2]. Apart from exhibiting pore sizes in the range from 2 nm to 50 nm, mesoporous metals and alloys are distinguished from other mesoporous matter with high electrical and thermal conductance. Furthermore, the porous architecture can be conveniently tailored to fine-tune specific features or develop new effects. Typical processes for the synthesis of mesoporous metallic matter are hard-templating, soft-templating or solution-phase approaches [3]. The use of soft tem-

plates such as lyotropic liquid crystals [4–8] and micelle assemblies have become prevalently widespread in the last years.

Micelle assemblies were first exploited by Yamauchi and co-workers in their seminal paper describing the electrodeposition of platinum metal from diluted (1.0 wt%) non-ionic surfactant solutions [9]. The procedure was later extended to Pd [10] and bimetallic systems such as PtPd [11], PtRu [12] and PtAu [13]. Recently, our group showed that the production of high-quality mesoporous films comprising a noble metal (Pt) and a transition non-noble metal (e.g., Ni, Fe and Co), in a partially or fully alloyed state, is also feasible [14–16].

Among all methods to produce mesoporous metals and metallic alloys via soft templating, electrochemical deposition is a suitable technique to reduce the metal ions in a solution [3]. Different non-ionic surfactant assemblies have been used so far, like the commercial P-123 and F-127 Pluronics, Brij 58, as well as surfactants obtained by in-house synthesis, always above their critical micelle concentration. In addition, electrochemical deposition allows for an

* Corresponding authors.

E-mail addresses: Cristina.Navarro.Senent@uab.cat (C. Navarro-Senent), vidalp@ethz.ch (S. Pané), Eva.Pellicer@uab.cat (E. Pellicer).

spatiotemporal control over the growth of matter when electrochemical processes are forced to occur in confinement, i.e. in the porous channels of nanotemplates, or in microarrays obtained by photolithography [17,18].

While several striking outcomes have been demonstrated with electrochemical deposition, the belief that this technique is a sort of potion making, where additives are magic ingredients, persists. However, note that, despite the maturity of the technique, the synergistic role of additives in electrochemical deposition is still a largely unexplored facet. Systematic studies devoted to formulations for electroplating are scarce. For example, an often-overlooked aspect is the effect of solution preparation and handling prior to electrodeposition on the properties of the deposited material. Frequently, electrodeposition is carried out immediately after electrolyte preparation (referred to as ‘freshly prepared electrolyte’) [19–21]. Here, we noticed that, during a series of unrelated experiments regarding the electrodeposition of mesoporous alloys, the mixing order of reagents and the time elapsed between electrolyte preparation and the actual electrodeposition, was critical for the reproducibility of the final mesostructure.

Considering that reliability is fundamental for the maturity of the technology and its translation to upscaled industrial processes, here we assess the influence of electrolyte processing on the quality of mesoporous films fabricated by electrochemical deposition. Essentially, we attempt to capture the conditions that ensure homogeneous mesoporosity over the entire film surface in successive depositions or in depositions performed in different days. The Co–Pt system is selected as a case study for this purpose for several reasons. First, mesoporous Co–Pt films can be grown by electrodeposition from P-123 micelle assemblies [16]. Secondly, Co–Pt exhibits several interesting functionalities, as an electrocatalyst [22], or in magnetic microelectromechanical applications [23]. More recently, magnetoelectric effects in porous Co–Pt materials for potential use in spintronic devices have also been reported [16].

Our results indicate that the electrolytes can behave as dynamic systems, in which the order of addition and time can dramatically impact the behavior of an electrochemical process. In the presented case, prior dissolution of the platinum salt in water followed by a storage period before addition of the remaining chemicals is essential for the reproducible formation of the mesostructure during electrocrystallization. The use of freshly prepared electrolytes is discouraged since in this case the occurrence of controlled mesoporosity is elusive.

2. Experimental

2.1. Materials

Isopropyl alcohol (C₃H₈O, 99.9%), acetone (99.0%), Na₂PtCl₆·6H₂O (sodium hexachloroplatinate (IV) hexahydrate, 98.0%), CoCl₂ (cobalt(II) chloride anhydrous, ≥ 98.0%), Pluronic P-123 (HO(CH₂CH₂O)₂₀(CH₂CH(CH₃)O)₇₀(CH₂CH₂O)₂₀H) block copolymer, and HCl (hydrochloric acid, 37 wt.%) were purchased from Sigma-Aldrich. All reagents were used as received without further purification. Deionized water was obtained through an EMD Millipore Simplicity™ Water Purification.

2.2. Instrumentation

Electrodeposition was performed in a one-compartment thermostated three-electrode cell connected to a PGSTAT302N Autolab potentiostat/galvanostat (Metrohm-Autolab). A double junction Ag|AgCl ($E = +0.210$ V/SHE) reference electrode was used with 3 M potassium chloride (KCl) inner solution and 1 M sodium chloride (NaCl) outer solution. A platinum spiral was used as counter electrode. Silicon chips with sputtered titanium (20 nm)/copper

(200 nm) adhesion/seed layers were employed as working electrodes. The chip backside was made of SiO₂ to avoid electrodeposition on both sides. The platable area was 0.25 ± 0.01 cm². For cyclic voltammetry (CV) studies, a vitreous carbon rod (Metrohm) of 0.0314 cm² served as the working electrode. A single cycle was run with a lower limit of -1.3 V and an upper limit of 1.0 V vs. Ag|AgCl, at a scan rate of 50 mV s⁻¹. The potential was initially swept toward cathodic values starting from a value in which no current was recorded.

2.3. Electrode preparation and films growth

Prior to deposition, the metallized Si chips were cleaned with acetone and isopropanol, rinsed with Milli-Q water and dried with N₂. Deposition was conducted potentiostatically at potentials between -0.9 and -1.1 V (for Baths 1, 3 and 4) and between -1.0 and -1.4 V (for Bath 2) during 600 s (Table 1). Deposition was carried out under mild stirring ($\omega = 100$ rpm) while simultaneously bubbling N₂ through the solution. The temperature was set at 25 °C by making water circulate throughout the external jacket of the electrochemical cell by means of an F12 Julabo thermostat. After electrodeposition, the samples were rinsed in slightly acidic water followed by Milli-Q water and dried with argon gas.

2.4. Morphology and structural characterization

Deposit morphology and porosity was examined by field emission scanning electron microscopy (FE-SEM) on a Zeiss MERLIN operated at 5 kV. The elemental composition was determined by Energy Dispersive X-ray Spectroscopy (EDXS) at an acceleration voltage of 15 kV. ImageJ processing software was used to determine the pore size distribution in the Co–Pt films from their on-top surfaces. The crystallographic structure was examined by X-ray diffraction (XRD). XRD patterns were recorded on a Philips X'Pert diffractometer using K α radiation. Diffractograms were recorded in the 38–63° 2 θ range with a step time of 8 s and a step size of 0.026°. The mean crystallite size was calculated from the XRD patterns by applying the Scherrer's formula on the peak's width. For film thickness determinations, samples were cut mechanically using a diamond tip to be able to observe and measure the cross-sections of Co–Pt films by FE-SEM.

2.5. Study of Pt(IV) complexes evolution with time

UV–vis spectroscopy was carried out on an HP8453 spectrophotometer (Hewlett–Packard). The evolution of [PtCl₆]²⁻ complex in water with time was studied on a 0.0039 M Na₂PtCl₆·6H₂O aqueous solution. The UV–vis transmittance spectra were recorded from 300 to 700 nm at different time intervals.

3. Results and discussion

3.1. Electrolyte design and handling

Co–Pt films were prepared by electrodeposition from solutions containing Na₂PtCl₆·6H₂O, CoCl₂, and Pluronic P-123. Four electrolytes were prepared in which the ‘equilibration time’ was either implemented or not and the concentration of CoCl₂ was varied (Table 1). We define the ‘equilibration time’ as the period of time (10 days) that elapses between the dissolution of Na₂PtCl₆·6H₂O (or Na₂PtCl₆·6H₂O + P-123) in water and the addition of the other chemicals, after which electrodeposition is immediately carried out. A 10-day storage was chosen as optimum ‘equilibration time’ in order to ensure a steady-state and avoid transitory effects. For Baths 1 and 3, an aqueous solution of Na₂PtCl₆·6H₂O was prepared and stored for 10 days, followed by the addition of Pluronic P-123

Table 1

Bath composition and electrodeposition conditions utilized in Baths 1–4. In the equilibration time row, the indicated species were dissolved in water and the solution left 10 days at room temperature before $\text{CoCl}_2 + \text{P-123}$ (Baths 1 and 3) or CoCl_2 only (Bath 4) were added.

Bath	1	2	3	4
Equilibration time (10 days)	Na_2PtCl_6	–	Na_2PtCl_6	$\text{Na}_2\text{PtCl}_6 + \text{P-123}$
Bath composition and electrodeposition conditions:				
$[\text{Na}_2\text{PtCl}_6] / \text{M}$			0.0013	
$[\text{CoCl}_2] / \text{M}$	0.0028	0.0028	0.028	0.0028
$[\text{P-123}] / \text{mg mL}^{-1}$			1 (= 1 wt%)	
pH			2.3	
$T / ^\circ\text{C}$			25	
E / V	–0.9, –1.0, –1.1	–1.2, –1.3, –1.4	–0.9, –1.0, –1.1	–0.9, –1.0, –1.1
t / s			600	

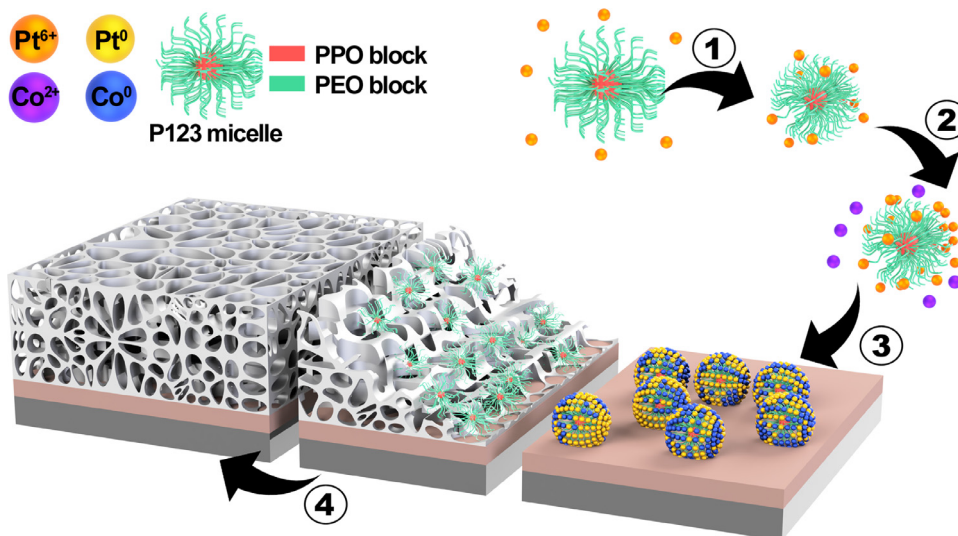


Fig. 1. Scheme of the micelle-assisted electrodeposition of mesoporous Co–Pt thin films. Step 1: P-123 micelles form spontaneously in the electrolyte. Step 2: the metal ions coordinate to the outer hydrophilic shell of the P-123 micelles. Step 3: the metallic ions reduce at the cathode by virtue of the applied potential. Step 4: P-123 surfactant is removed, leaving the mesoporous metallic Co–Pt film behind.

and CoCl_2 in that order (Fig. S1a and S1c). The concentration of CoCl_2 was 10 times higher in Bath 3 compared to Bath 1 (Table 1 and Fig. S1c). For Bath 2, an aqueous solution of $\text{Na}_2\text{PtCl}_6 \cdot 6\text{H}_2\text{O}$ was prepared, immediately followed by the addition of Pluronic P-123 and CoCl_2 , without introducing an ‘equilibration time’ (Figure S1b). Finally, a solution containing $\text{Na}_2\text{PtCl}_6 \cdot 6\text{H}_2\text{O}$ and Pluronic P-123 was prepared and stored for 10 days, after which CoCl_2 was added (Fig. S1d). The pH was adjusted to 2.3 with the addition of a few drops of HCl 1 M in all cases. The concentration of Pluronic P-123 surfactant and $\text{Na}_2\text{PtCl}_6 \cdot 6\text{H}_2\text{O}$ was 1 wt% (1 mg mL^{–1}) and 0.0013 M, respectively, in all electrolytes (Table 1). The concentration of P-123 was above its critical micelle concentration (c.m.c.) at 25 °C [24] in order to ensure the formation of micelles in the electrolyte.

In the micelle-assisted electrodeposition process, the metallic ions, which are coordinated by the hydrophilic shell domain of the P-123 micelles, migrate toward the working electrode (Steps 1 and 2, Fig. 1). Once they reach the cathode, Pt(IV) and Co(II) cations are reduced (Step 3, Fig. 1), which results in the formation of a mesoporous Co–Pt film (Step 4, Fig. 1). Therefore, the purpose of this approach is to exploit the self-assembly of P-123 molecules into micelles which gather spontaneously at the solid–liquid interface during the electrodeposition of the mesoporous Co–Pt film.

3.2. Cyclic voltammetry study

Cyclic voltammetry (CV) curves from different electrolytes were recorded, aimed at gathering information on the influence of the

equilibration time on the redox processes taking place (Fig. 2 and Fig. 3). As seen in Fig. 2, Bath 2 is characterized by a weak reduction wave around –0.3 V corresponding to platinum deposition [25], followed by a sharp increase of the current at more negative potentials. This sharp increase of the reduction current can be ascribed to hydrogen evolution which superimposes with the codeposition of Co as the scan proceeds. The potential at which current density rapidly increases is different in Baths 1 and 2. Namely, a shift of 0.3 V towards more positive values is observed for Bath 1 (inset of Fig. 2). This was an unexpected result since bath formulation and pH were identical and suggests that the equilibration time introduced in Bath 1 favors Pt deposition. As the potential is swept toward more negative values, two reduction peaks located at –0.67 V and –0.89 V are clearly observed in Bath 1, whereas they nearly overlap in Bath 2. In the anodic scan, a double oxidation peak centered at –0.3 V is detected in both cases, followed by a weaker peak around +0.75 V. The double peak is related to the oxidation of Co–Pt alloy with varying Pt/Co ratio, whereas the second weaker peak is presumably related to the oxidation of Pt [25]. The oxidation charge under the right side of the double oxidation peak is higher in Bath 2 compared to Bath 1, suggesting that the discharge of Co(II) relative to Pt(IV) increased during the cathodic scan from Bath 2.

The electrochemical fingerprint of Baths 1 and 3 can be compared in Fig. 3. Again, a shift in the potential value from which the reduction current rapidly increases is observed. This shift, however, is much less pronounced (around 0.1 V) and can be attributed to the change in concentration of Co(II) salt, which is 10 times higher

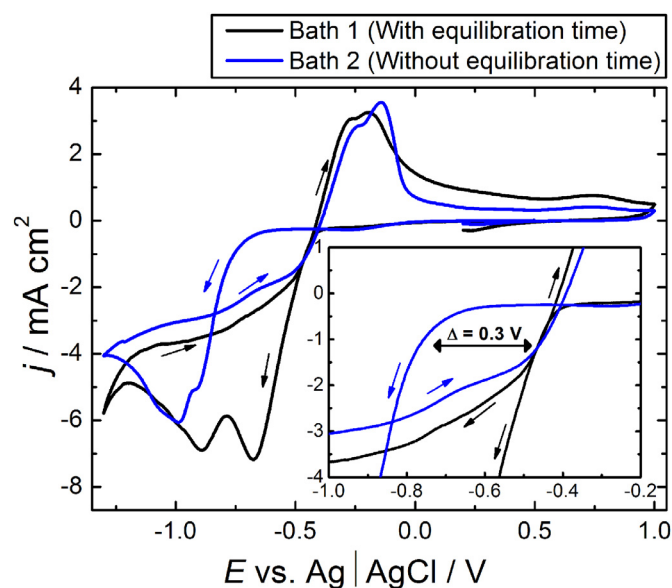


Fig. 2. CV curves recorded under stationary conditions at 50 mV s^{-1} from Bath 1 (black curve) and Bath 2 (blue curve) on vitreous carbon. (For interpretation of the references to color in this figure legend, the reader is referred to the web version of this article.)

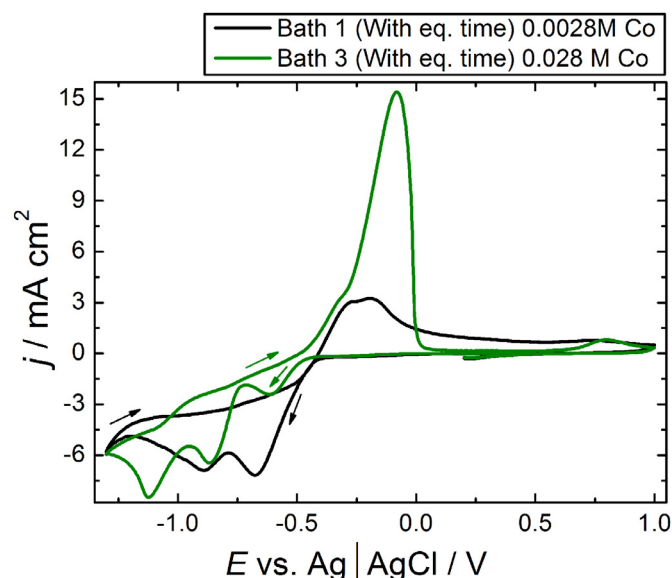


Fig. 3. CV curves recorded under stationary conditions at 50 mV s^{-1} from Bath 1 (black curve) and Bath 3 (green curve) on vitreous carbon. 'eq. time' stands for equilibration time, the concentration of CoCl_2 in each bath is indicated. (For interpretation of the references to color in this figure legend, the reader is referred to the web version of this article.)

in Bath 3. Yet, the deposition onset is detected at a more positive potential for Bath 3 compared to Bath 2 (cf. green curve in Fig. 3 and blue curve in Fig. 2). In the anodic scan, the charge under the right side of the double oxidation peak increases drastically, indicating the formation of a deposit much richer in Co in the reduction zone. According to the information acquired from the CV study, a range of potentials suitable for the potentiostatic deposition of the Co–Pt films on Cu was chosen (Fig. S2). As such, differences among the deposits resulting from the various baths were anticipated.

3.3. Morphology, porosity, and composition of the films

Fig. 4 shows FE-SEM images of the mesoporous Co–Pt thin films prepared from Bath 1 at different potentials. As shown in Fig. 4a–c, nanometer-sized pores are visible all over the surface of the films. Furthermore, the morphology and porosity were almost independent from the applied potential. Pore size was measured from the high-magnification SEM images, and the corresponding pore size distributions are shown in Fig. 4d–f. Pore diameters were in the range of 13–17 nm for films deposited at -0.9 V and -1.0 V , with the majority of pores having diameters of 15 nm and 14 nm, respectively (Fig. 4d and e). Films deposited at -1.1 V featured pore diameters in the range of 10–14 nm with a maximum at 12 nm (Fig. 4f). In contrast, Co–Pt thin films electrodeposited from Bath 2 show a completely different morphology (Fig. 5). The applied potentials were negatively shifted according to the ΔE previously observed in the CVs (Fig. 2) in order to obtain similar current densities (Fig. S2). Thin films deposited at -1.2 V showed rounded grains (Fig. 5a), while films deposited at -1.3 and -1.4 V consisted of elliptical/acicular grains (Fig. 5b and c). This transformation from rounded to acicular/elliptical shape suggest an increase of the Co content in the films. Note that this acicular morphology has often been reported in electrodeposited Co-rich Co based alloys [26,27]. In addition, an effect of the potential on the grain size is observed, where smaller grains were obtained at more positive potentials. More importantly, most of the specimens deposited from Bath 2 did not display a clear mesoporosity (Fig. 5). A mesoporous network occasionally developed in samples produced from some batches and it was clear that Bath 2 lacked reproducibility. For this electrolyte, porosity is developed at more positive potentials, although deposit morphology was distinct from that observed in the films obtained from Bath 1 (Fig. S3). The morphology of the deposit grown at -1.1 V (Fig. S3b), characterized by rounded grains with nanometer-sized pores in a cauliflower fashion, displayed a mixture of morphologies between those observed at -1.0 and -1.2 V (Fig. S3a and Fig. 5a respectively). Such intermingling morphology was probably due to the concomitant influence of applied potential and thickness (Table S1, Supporting Information). Note that the film deposited from Bath 1 at -1.1 V (23 at.% Co) and the film obtained from Bath 2 at -1.0 V (20 at.% Co) were compositionally alike, and yet they were morphologically different. Furthermore, films from Bath 2 showed a sort of edge effect characterized by a darkening of the deposit color toward the edges, which was visible at naked eye. This effect was also observed in films obtained from Bath 1 but to a much lesser extent (Table 2). A change in morphology was detected by SEM while imaging two different regions of the films produced from Bath 2 (Fig. S4a and b). The thickness of the films correlated nicely with the increase in the deposition charge as the applied potential was made more negative (Table S2). While for Bath 1 there was not a significant change in deposit morphology and pore topology with the applied potential and thickness (77–160 nm), the situation was different for Bath 2 (90–250 nm).

Elemental composition analysis by EDXS revealed an increase of the cobalt content in the deposits produced from a fixed bath as the applied potential was made more negative (Table 2), which is in agreement with the CV data. Interestingly, the films deposited from Bath 1 showed comparatively lower cobalt contents than the deposits from Bath 2 (Table 2). This result, together with the elusive generation of porosity in the latter, suggested that the presence of a high content of platinum in the films was strongly correlated to the building of an extended mesoporosity. Such correlation has been drawn in previous studies, in which proper interaction between noble metal ions of Pt and Pd and the block-copolymer micelles (Step 1, Fig. 1) is known to favor the formation of a long-range order mesostructure [10,28].

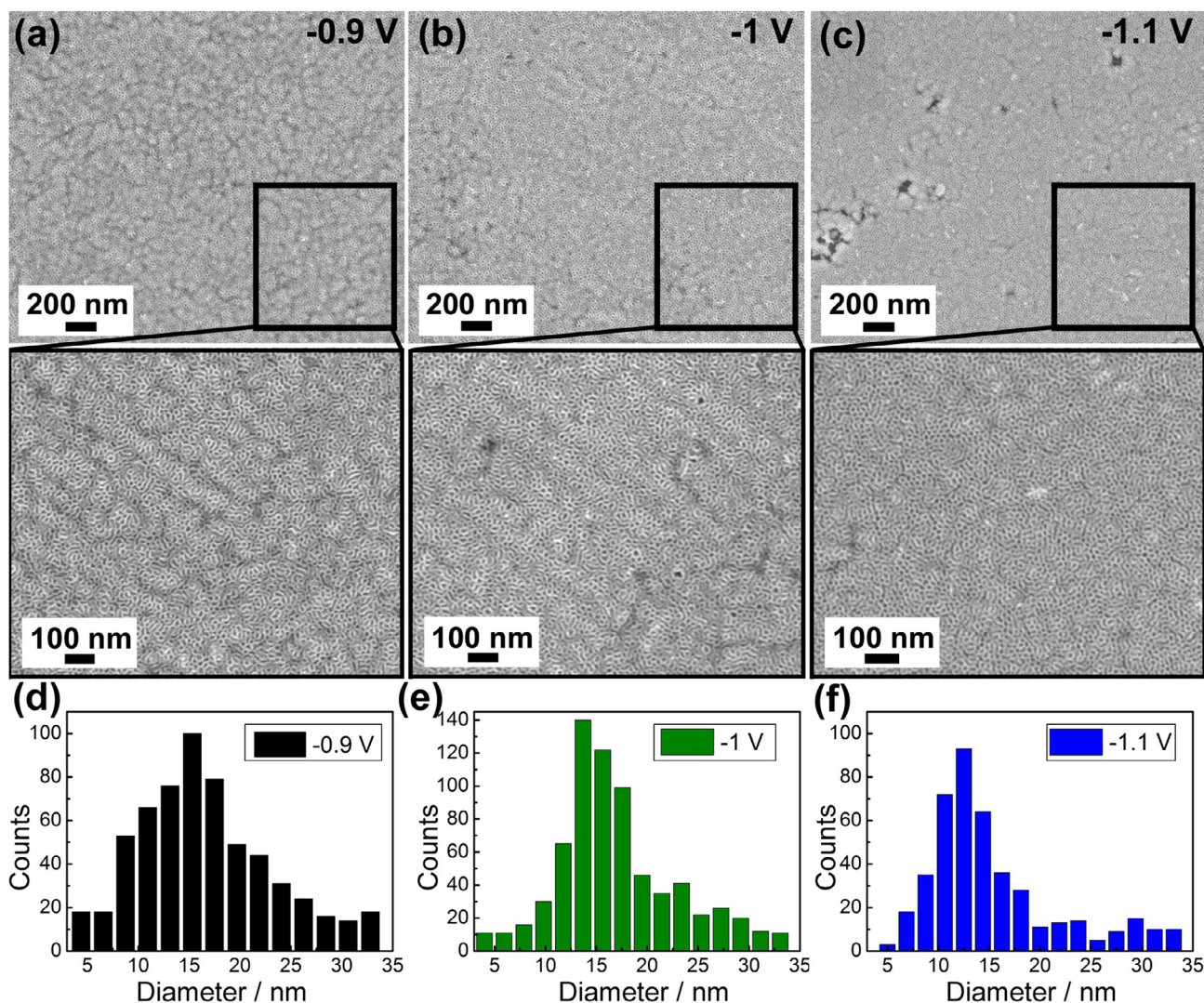


Fig. 4. Representative FE-SEM images of the Co-Pt films electrodeposited from Bath 1 at (a) -0.9 (b) -1.0 and (c) -1.1 V during 600 s. (d-f) Corresponding pore size distribution histograms.

In order to determine whether the occurrence of porosity in the deposits from Bath 1 was due to their higher Pt content or the equilibration time introduced during the electrolyte preparation, the Co(II) concentration in the electrolyte was increased by 10-fold (Bath 3, Table 1). Surprisingly, the resulting films showed a Co-rich like morphology combined with a mesoporous structure (Fig. 6), which was different from that observed in deposits from Bath 1 (Fig. 4). Importantly, the development of mesoporosity was fully reproducible unlike depositions from Bath 2. Moreover, deposits were dark gray with no apparent color gradient throughout their surface (Table 2). As for the films from Bath 2 (Fig. 5), a change from clustered rounded grains to clustered needles was observed as the potential was made more negative (Fig. 6a and c). This anticipated, again, an increase of the cobalt content. Indeed, cobalt amount was 5 at.% higher than in deposits from Bath 2 (see Table 2), thus confirming that the origin of mesoporosity in Bath 1 derived films can be ascribed to electrolyte processing and not to the Co/Pt ratio in the film. Therefore, it can be concluded that the equilibration time of Pt(IV) salt in water endows films with a reproducible mesoporosity.

Finally, the electrolyte was processed following a different procedure, in which $\text{Na}_2\text{PtCl}_6 \cdot 6\text{H}_2\text{O}$ was dissolved together with P-123 (Bath 4, Table 1) in water and stored for 10 days before CoCl_2 was

added. Thin films obtained from this bath consistently showed in consecutive depositions a flat morphology and mesoporosity analogous to those of deposits obtained from Bath 1 (Fig. 4), although with narrower pores (Fig. S5). Similarly, EDX analyses revealed an elemental composition close to deposits from Bath 1, with a difference of just 5 at.% in Co (c.f. Baths 1 and 4, Table 2). The results suggest that the addition of P-123 during the equilibration time step does not induce significant changes on the morphology, porosity and composition of the deposits. Thus, it can be concluded that the reproducible formation of the mesoporous network is ruled by the dynamics of Pt(IV) complexes. In other words, prior dissolution of the Pt salt and storage of the solution greatly controls the mesoporosity of the films.

3.4. Crystallographic structure

XRD analyses were performed to determine the crystallographic phases of the Co-Pt films prepared from Baths 1, 2 and 3 (Fig. 7a, b and c respectively).

For deposits grown from Bath 1, the main peaks located at 40.5° and 47.15° match the face-centered cubic (fcc) phase of CoPt_3 . The CoPt_3 peaks slightly shift towards higher angles as the cobalt content increases (Fig. 7a), suggesting the dissolution of Co in the fcc-

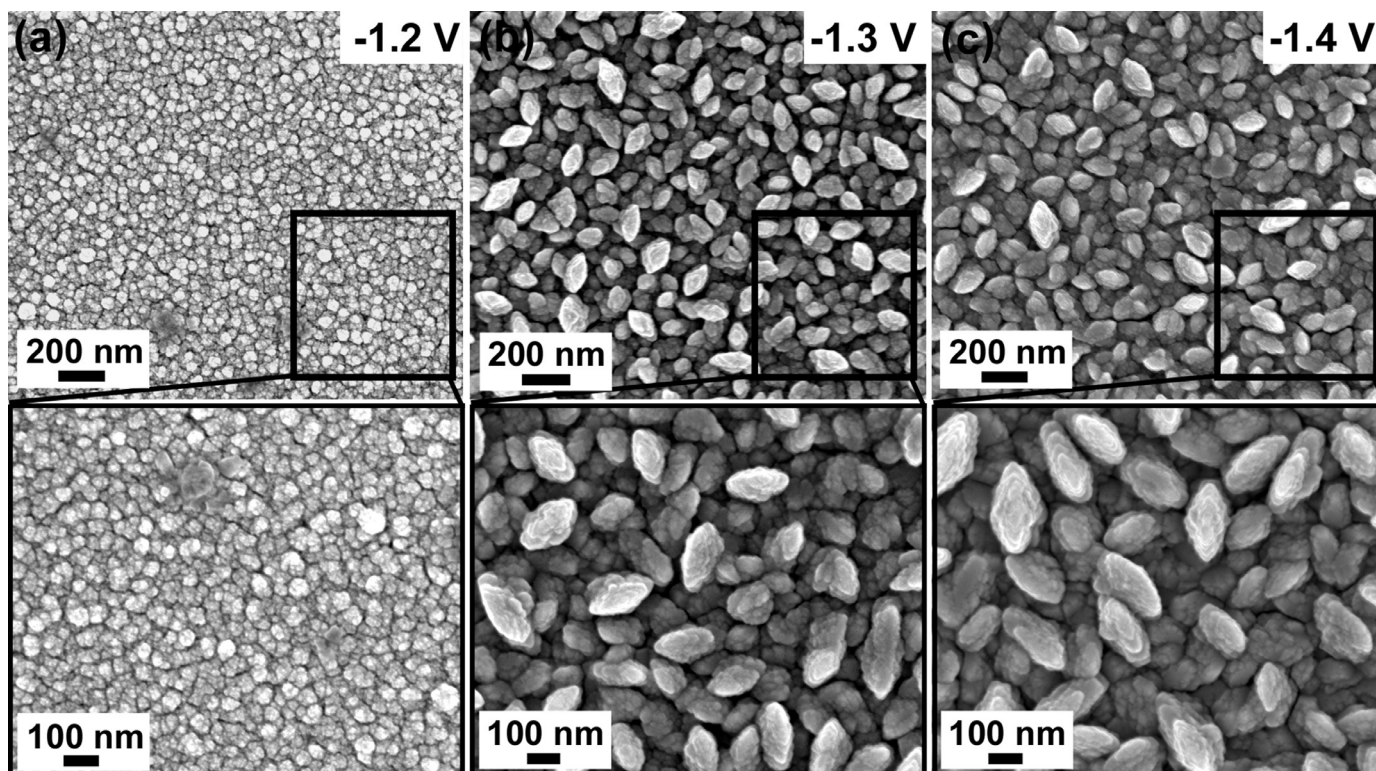











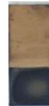


Fig. 5. Representative FE-SEM images of the Co-Pt films electrodeposited from Bath 2 at (a) -1.2 (b) -1.3 and (c) -1.4 V during 600 s.

Table 2

Cobalt content (in at.%) in the Co-Pt films deposited from the various baths and photos of the films. The orange-like color corresponds to the Cu seed-layer, which was used for the electrical connection during electrodeposition. The light gray or dark gray part corresponds to the Co-Pt film covering the remaining Cu surface.

Bath	Co at. %					
	-0.9 V	-1.0 V	-1.1 V	-0.9 V	-1.0 V	-1.1 V
1	10	15	23			
3	60	80	90			
4	15	20	28			
	-1.2 V	-1.3 V	-1.4 V	-1.2 V	-1.3 V	-1.4 V
2	58	75	85			

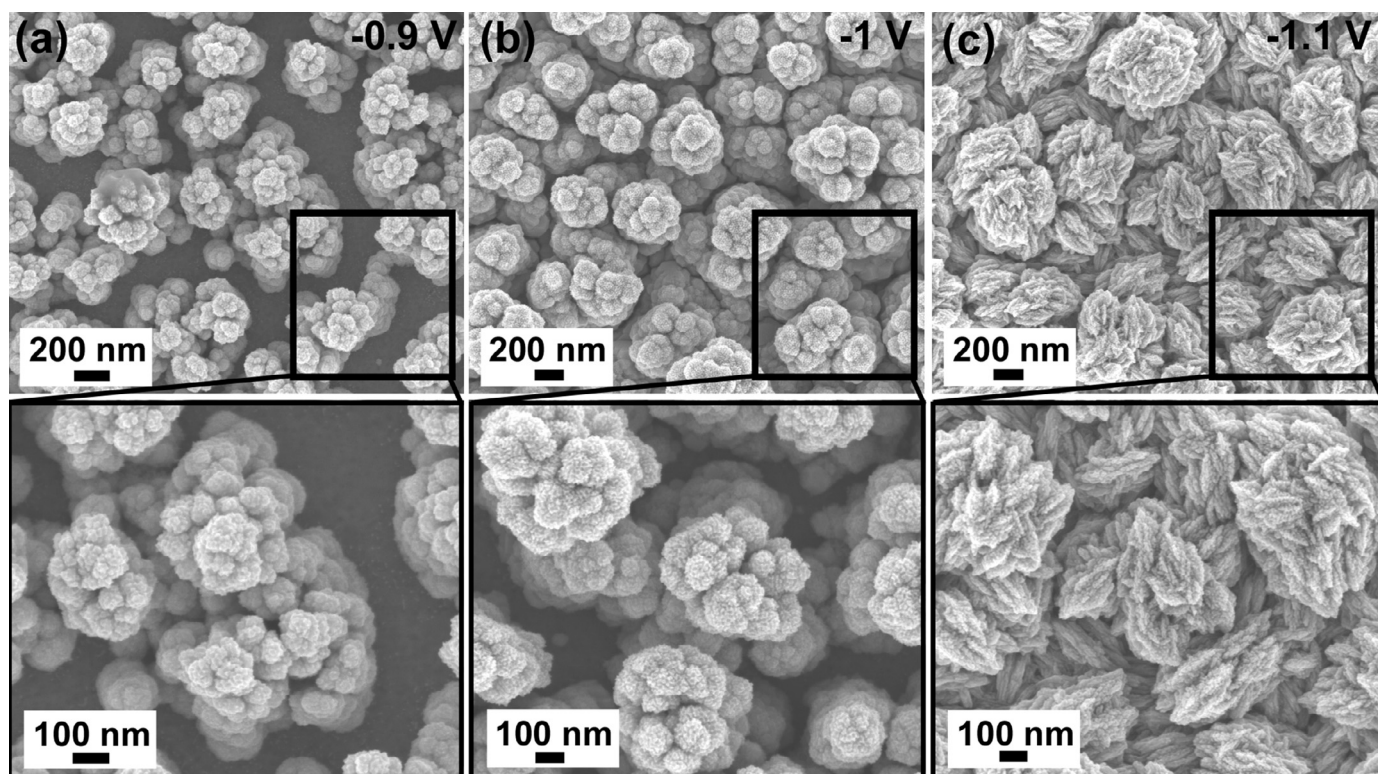


Fig. 6. Representative FE-SEM images of the Co-Pt films electrodeposited from Bath 3 at (a) -0.9 (b) -1.0 and (c) -1.1 V during 600 s.

CoPt₃ lattice. A crystallite size of 5 ± 1 nm was determined using the Scherrer's formula, as expected from the nanocrystalline nature of the films. The hexagonal close-packed (hcp) phase of Co is detected in the diffraction patterns of the Co-Pt films prepared from Bath 2, in agreement with their higher cobalt content (Fig. 7b). A shift of 0.13° toward lower angles is observed on the hcp-Co (100) peaks' position for films with 75 at.% and 85 at.% Co (red and blue curves, respectively) compared to the film with 58 at.% Co (black curve), proving that Pt is dissolved in the hcp-Co lattice. The films prepared from Bath 3 were structurally similar to those obtained from Bath 2 (Fig. 7c), although some differences in texture were noticed. In particular, the $I_{(100)}/I_{(101)}$ peak intensity ratio decreased as the cobalt content in the deposits increased (red and blue curves, Fig. 7c). Compared to the films from Bath 1, deposits grown from Bath 3 showed narrower peaks, with a crystallite size of 12 ± 1 nm. Considering that deposits from both baths (Bath 1 and 3) showed an evident and reproducible mesoporosity, this difference in the crystallite size values suggests that the formation of mesopores does not cause crystal refining. In other words, pore wall width is not correlated with crystal size, suggesting that each grown crystal is itself mesoporous.

3.5. Study of Pt(IV) complexes evolution with time

To shed light on the evolution of chemical speciation of Pt(IV) during the equilibration time and its influence on the development of film mesostructure, UV-vis spectroscopy of the $[\text{PtCl}_6]^{2-}$ species in water was performed. For this purpose, Na_2PtCl_6 was dissolved in water at a concentration of 0.0039 M and the dynamics of the resulting chloroaqua complexes was followed during several days (Fig. 8a). Note that the concentration was increased by three times to better appreciate the features in the UV-vis spectra. The obtained UV-vis spectra at 0 days (black curve) showed a shoulder at 366 nm and a small peak at 455 nm which correspond to singlet and triplet ligand-field bands, respectively, as

reported in previous works [29,30]. As shown in Fig. 8a, a decrease of both peaks' intensity is observed over time, suggesting a decrease of the amount of chloro complexes ($[\text{PtCl}_6]^{2-}$) in solution by the progressive exchange of Cl^- and OH^- ligands. This scenario is schematically depicted in Fig. 8b. During the equilibration time, Cl anions from $[\text{PtCl}_6]^{2-}$ complex are exchanged by OH^- groups from the water molecules, resulting in the formation of $[\text{PtCl}_{6-x}(\text{OH})_x]^{2-}$ complexes. This causes an increase of the concentration of H^+ in solution, which in turn causes the pH to acidify (from 3.3 to 2.6), as experimentally observed (Fig. S1a,c and d). Miolati et al. predicted a decrease in the pH of the aqueous solution due to the replacement of chlorine ligands by hydroxide ions [31]. This exchange between Cl^- and OH^- groups has been reported previously, where the dissociation of $[\text{PtCl}_6]^{2-}$ is expected to be completed up two Cl ligands [32]. The lengthy equilibration time for the completed ligand exchange is in agreement with previous research, as $[\text{PtCl}_6]^{2-}$ is known for undergoing a slow hydrolysis process [33,34]. A number of speciation models have been put forward to describe the hydrolysis of $[\text{PtCl}_6]^{2-}$ species as a function of its concentration and pH, among other parameters. For example, Miolati and Pendini assumed that chloride ions can only be exchanged by hydroxide anions [31]. Sillen and Martell [35] and Knözinger et al. [36], on the contrary, considered that the exchange with H_2O ligands takes place. In any case, the exchange between Cl^- and OH^- groups in $[\text{PtCl}_6]^{2-}$ is a more complex mechanism than the one schematically depicted in Fig. 8b. Aquo ligand exchange of chloride anions to render $\text{PtCl}_{6-x}(\text{H}_2\text{O})_x]^{-2+x}$ complexes is rapid and reversible, whereas the exchange of water and chloride by OH ligands towards $\text{PtCl}_{6-x}(\text{OH})_y(\text{H}_2\text{O})_{x-y}]^{-2+x-y}$ is considered a slow process during aging, particularly in diluted Pt(IV) solutions [34]. Interestingly, hydroxide ion ligand exchange of chloride is expected to be accelerated in presence of light according to previous studies [33,34]. Therefore, the equilibration time introduced during electrolyte preparation serves to increase the concentration of $[\text{PtCl}_{6-x}(\text{OH})_x]^{2-}$ complexes.

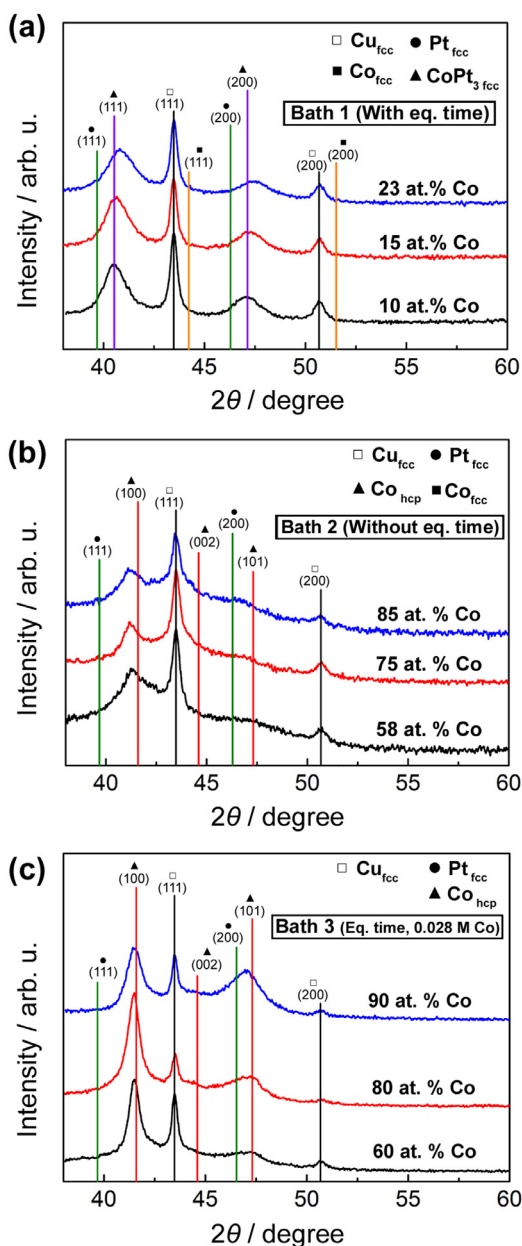


Fig. 7. XRD of the Co-Pt films electrodeposited from (a) Bath 1 at -0.9 (black), -1.0 (red) and -1.1 V (blue), (b) Bath 2 at -1.1 (black), -1.2 (red) and -1.3 V (blue) and (c) Bath 3 at -0.9 (black), -1.0 (red) and -1.1 V (blue). The fcc-Cu signal originates from the Cu seed-layer of the substrate, 'eq. time' stands for equilibration time. (For interpretation of the references to color in this figure legend, the reader is referred to the web version of this article.)

Above its c.m.c., Pluronic P-123 forms micelles in water. The core of the micelles is made of the PPO block and the shell is made of PEO units. During the electrodeposition process, the Pt(IV) species coordinate to the shell of the P-123 micelle assemblies (Fig. 1). The extent and strength of this coordination is critical for the development of mesoporosity in the deposits. Considering that the equilibration time promotes the formation of Pt(IV) chloroaqua complexes ($[\text{PtCl}_{6-x}(\text{OH})_x]^{2-}$), it is conjectured that the OH^- groups from $[\text{PtCl}_{6-x}(\text{OH})_x]^{2-}$ complex show higher affinity with the OH groups from the PEO block than Cl^- anions. A more efficient coordination between Pt(IV) and the PEO group of P-123 is thus expected for Baths 1, 3 and 4 than for Bath 2, thereby ensuring reproducible formation of a long-range order mesoporosity in the films. To support this claim, we performed a control experiment

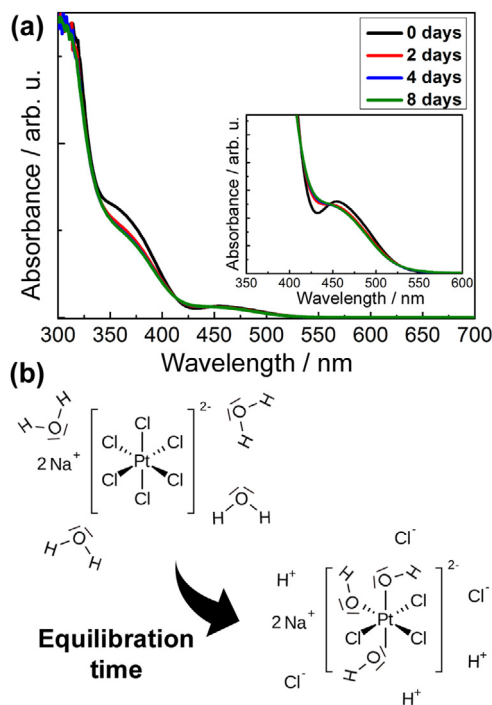


Fig. 8. (a) Time dependent evolution of UV-vis absorbance spectra of Pt(IV) complexes in water (0.0039 M) and (b) Scheme of ligand exchange taking place during the equilibration time.

in which pure Pt films were electrodeposited from one electrolyte in which the Pt(IV) salt was left to equilibrate for 10 days (Bath 5), and another one in which Pt films were grown immediately after freshly mixing the chemicals (Bath 6) (Table S2). Deposition potentials were selected according to the shift observed in the CV as for the Co-Pt baths. SEM imaging of the corresponding deposits showed that mesoporosity was present all over the film surface and in successive depositions in samples obtained from Bath 5 (Fig. 9a), whereas mesoporosity did not consistently develop in Pt films deposited from Bath 6 (Fig. 9b). For the latter, either non-porous films were obtained or mesostructured domains were occasionally observed only in some areas of the sample. In other words, the occurrence of mesoporosity from Bath 6 was non-reproducible, which verifies that the development of mesoporosity is ruled by the dynamics of Pt(IV) salt in water.

Moreover, the observed changes on the UV-vis spectra showed that 2 days of equilibration time seemed enough to secure the presence of a large concentration of $[\text{PtCl}_{6-x}(\text{OH})_x]^{2-}$ complexes in solution. Indeed, Co-Pt deposits obtained with 2 days of equilibration time showed a flat morphology and mesoporosity analogous to the films prepared using 10 days of equilibration time (Fig. S6). This result indicated that 2-day storage is also adequate for the correct formation of a mesoporous network in Co-Pt.

4. Conclusions

The impact of electrolyte processing over the mesostructure of Co-Pt films grown from an aqueous solution containing P-123 micelle assemblies is unraveled. Prior dissolution of the Pt salt (or the Pt salt + P-123) in water and storage of the resulting solution before the P-123 amphiphilic surfactant and the Co salt (or the Co salt) are added decisively impacts the reproducibility of the mesostructure formation. To ensure the formation of highly mesoporous films, storage of the Pt(IV) solution (or the Pt(IV) + P-123 solution) for a few days (2–10) is recommended. In contrast, deposits grown from freshly prepared baths were usually

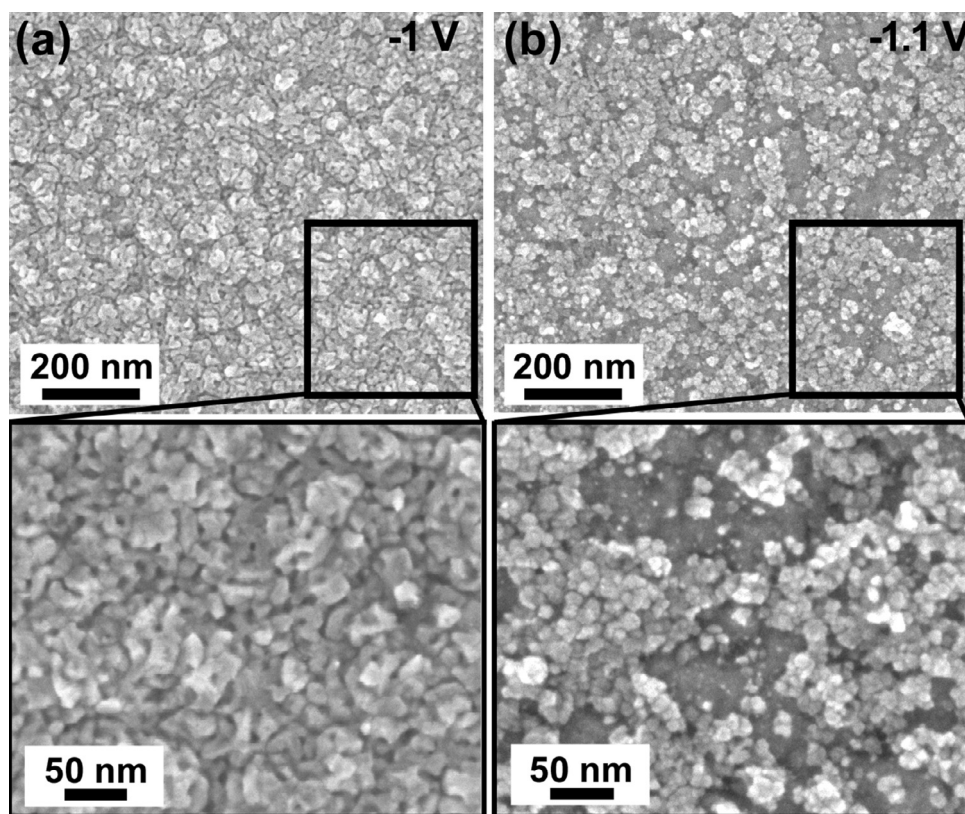


Fig. 9. Representative FE-SEM images of pure Pt films electrodeposited from a bath (a) involving an equilibration time of the Pt(IV) salt at -1.0 V for 600 s and (b) without equilibration time at -1.1 V for 600 s.

non-mesostructured, thus suggesting that the factors involving the development of mesoporosity were uncontrolled. The parametric analysis of films obtained from various baths having exactly the same formulation and pH but subject to a different electrolyte processing prior to electrodeposition clearly indicated that the Co/Pt ratio in the films could not explain why mesoporosity consistently developed in some cases and not in others. UV-vis monitoring of a Pt(IV) aqueous solution allowed us to verify that the formation of chloroaqua complexes during the storage period was key for the development of mesoporosity. We suggest that the higher affinity of the $[\text{PtCl}_{6-x}(\text{OH})_x]^{2-}$ complexes with the PEO groups of the P-123 micelle assemblies warrants the formation of compositionally homogeneous deposits with a reproducible mesoporosity. Our research highlights the significance of electrolyte processing in the electrosynthesis of mesoporous Co-Pt films and suggests that a similar protocol to guarantee the formation of mesoporous films with a high degree of reproducibility should be adopted in other systems.

Declaration of Competing Interest

The authors declare that they have no known competing financial interests or personal relationships that could have appeared to influence the work reported in this paper.

CRediT authorship contribution statement

Cristina Navarro-Senent: Investigation, Data curation, Formal analysis, Validation, Writing - original draft. **Salvador Pané:** Conceptualization, Methodology, Supervision, Writing - original draft, Writing - review & editing. **Jordi Sort:** Writing - review & editing. **Eva Pellicer:** Funding acquisition, Resources, Supervision, Writing - review & editing.

Acknowledgments

This work was funded by the Spanish Government (Project [MAT2017-86357-C3-1-R](#) and associated FEDER), the Generalitat de Catalunya (2017-SGR-292), and the European Research Council (SPIN-PORICS 2014-Consolidator Grant, Agreement n. 648454).

Supplementary materials

Supplementary material associated with this article can be found, in the online version, at [doi:10.1016/j.electacta.2020.136940](https://doi.org/10.1016/j.electacta.2020.136940).

References

- [1] S.C. Warren, U. Wiesner, Self-assembled ordered mesoporous metals, *Pure Appl. Chem.* 81 (2009) 73–84.
- [2] M.T.Y. Paul, B.D. Gates, Mesoporous platinum prepared by electrodeposition for ultralow loading proton exchange membrane fuel cells, *Sci. Rep.* 9 (2019) 4161.
- [3] V. Malgras, H. Atae-Esfahani, H. Wang, B. Jiang, C. Li, K.C.W. Wu, J.H. Kim, Y. Yamauchi, Nanoarchitectures for mesoporous metals, *Adv. Mater.* 28 (2016) 993–1010.
- [4] J.M. Elliott, P.R. Birkin, P.N. Bartlett, G.S. Attard, Microelectrodes with unique high surface areas, *Langmuir* 15 (1999) 7411–7415.
- [5] A. Foyet, A. Hauser, W. Schäfer, Double template electrochemical deposition and characterization of NiCo and NiCu alloys nanoparticles and nanofilms, *J. Solid State Electrochem* 12 (2007) 47–55.
- [6] F. Bender, R.K. Mankelov, D.B. Hibbert, J.J. Gooding, Lyotropic liquid crystal templating of groups 11 and 12 metal films, *Electroanalysis* 18 (2006) 1558–1563.
- [7] T. Xue, L.S. Loo, X. Wang, S. Kyu Kwak, J.M. Lee, Electrodeposition of mesoporous bilayers of polyaniline supported Cu_2O semiconductor films from lyotropic liquid crystalline phase, *Chem. Eng. Sci.* 80 (2012) 452–459.
- [8] S. Makino, Y. Yamauchi, W. Sugimoto, Synthesis of electro-deposited ordered mesoporous RuO_x using lyotropic liquid crystal and application toward micro-supercapacitors, *J. Power Sources* 227 (2013) 153–160.
- [9] H. Wang, L. Wang, T. Sato, Y. Sakamoto, S. Tominaka, K. Miyasaka, N. Miyamoto, Y. Nemoto, O. Terasaki, Y. Yamauchi, Synthesis of mesoporous Pt films with tunable pore sizes from aqueous surfactant solutions, *Chem. Mater.* 24 (2012) 1591–1598.

- [10] M. Iqbal, C. Li, K. Wood, B. Jiang, T. Takei, Ö. Dag, D. Baba, A.S. Nugraha, T. Asahi, A.E. Whitten, M.S.A. Hossain, V. Malgras, Y. Yamauchi, Continuous mesoporous Pd films by electrochemical deposition in nonionic micellar solution, *Chem. Mater.* 29 (2017) 6405–6413.
- [11] B. Jiang, C. Li, H. Qian, M.S.A. Hossain, V. Malgras, Y. Yamauchi, Layer-by-layer motif architectures: Programmed electrochemical syntheses of multilayer mesoporous metallic films with uniformly sized pores, *Angew. Chemie - Int. Ed.* 56 (2017) 7836–7841.
- [12] H. Wang, M. Imura, Y. Nemoto, L. Wang, H.Y. Jeong, T. Yokoshima, O. Terasaki, Y. Yamauchi, Electrochemical design of mesoporous Pt-Ru alloy films with various compositions toward superior electrocatalytic performance, *Chem. - A Eur. J.* 18 (2012) 13142–13148.
- [13] C. Li, H. Wang, Y. Yamauchi, Electrochemical deposition of mesoporous Pt–Au alloy films in aqueous surfactant solutions: Towards a highly sensitive amperometric glucose sensor, *Chem. - A Eur. J.* 19 (2013) 2242–2246.
- [14] K. Eiler, S. Suriñach, J. Sort, E. Pellicer, Mesoporous Ni-rich Ni–Pt thin films: electrodeposition, characterization and performance toward hydrogen evolution reaction in acidic media, *Appl. Catal. B Environ.* 265 (2020) 118597.
- [15] E. Isarain-Chávez, M.D. Baró, C. Alcántara, S. Pané, J. Sort, E. Pellicer, Micelle-assisted electrodeposition of mesoporous Fe–Pt smooth thin films and their electrocatalytic activity towards the hydrogen evolution reaction, *ChemSusChem* 11 (2018) 367–375.
- [16] C. Navarro-Senent, J. Fornell, E. Isarain-Chávez, A. Quintana, E. Menéndez, M. Foerster, L. Aballe, E. Weschke, J. Nogués, E. Pellicer, J. Sort, Large magnetolectric effects in electrodeposited nanoporous microdisks driven by effective surface charging and magneto-ionics, *ACS Appl. Mater. Interfaces* 10 (2018) 44897–44905.
- [17] M. Bechelany, A. Abou Chaaya, F. Frances, O. Akdim, D. Cot, U.B. Demirci, P. Miele, Nanowires with controlled porosity for hydrogen production, *Mater. Chem. A* 1 (2013) 2133–2138.
- [18] J. Zhang, S. Agramunt-Puig, N. Del-Valle, C. Navau, M.D. Baró, S. Estradé, F. Peiró, S. Pané, B.J. Nelson, A. Sanchez, J. Nogués, E. Pellicer, J. Sort, Tailoring staircase-like hysteresis loops in electrodeposited trisegmented magnetic nanowires: A Strategy toward minimization of interwire interactions, *ACS Appl. Mater. Interfaces* 8 (2016) 4109–4117.
- [19] A.H. Whitehead, J.M. Elliott, J.R. Owen, G.S. Attard, Electrodeposition of mesoporous tin films, *Chem. Commun.* 4 (1999) 331–332.
- [20] A.N. Correia, S.A.S. Machado, Electrodeposition and characterization of thin layers of Ni–Co alloys obtained from dilute chloride baths, *Electrochim. Acta* 45 (2000) 1733–1740.
- [21] A. Nicolenco, N. Tsyntsar, H. Cesiulis, Fe (III)-based ammonia-free bath for electrodeposition of Fe–W Alloys, *J. Electrochem. Soc.* 164 (2017) D590–D596.
- [22] A. Serrà, E. Gómez, E. Vallés, Facile electrochemical synthesis, using microemulsions with ionic liquid, of highly Mesoporous CoPt nanorods with enhanced electrocatalytic performance for clean energy, *Int. J. Hydrog. Energy* 40 (2015) 8062–8070.
- [23] N. Wang, D.P. Arnold, Thick electroplated Co-rich Co–Pt micromagnet arrays for magnetic MEMS, *IEEE Trans. Magn.* 44 (2008) 3969–3972.
- [24] G. Wanka, H. Hoffmann, W. Ulbricht, Phase diagrams and aggregation behavior of poly(oxyethylene)-poly(oxypropylene)-poly(oxyethylene) triblock copolymers in aqueous solutions, *Macromolecules* 27 (1994) 4145–4159.
- [25] S. Grau, M. Montiel, E. Gómez, E. Vallés, Ternary PtCoNi functional films prepared by electrodeposition: magnetic and electrocatalytic properties, *Electrochim. Acta* 109 (2019) 187–194.
- [26] E. Pellicer, S. Pané, K.M. Sivaraman, O. Ergeneman, S. Suriñach, M.D. Baró, B.J. Nelson, J. Sort, Effects of the anion in glycine-containing electrolytes on the mechanical properties of electrodeposited Co–Ni films, *Mater. Chem. Phys.* 130 (2011) 1380–1386.
- [27] G. Pattanaik, G. Zangari, Morphology and magnetic properties of Co-rich Co–Pt thin films electrodeposited on Cr seed layers, *J. Electrochem. Soc.* 156 (2006) C6–C10.
- [28] C. Wang, D. Chen, X. Jiao, Lyotropic liquid crystal directed synthesis of nanostructured materials, *Sci. Technol. Adv. Mater.* 10 (2009) 023001–023012.
- [29] L.E. Cox, D.G. Peters, E.L. Wehry, Photoaquation of hexachloroplatinate(IV), *J. Inorg. Nucl. Chem.* 34 (1972) 297–305.
- [30] A. Goursot, E. Penigault, H. Chermette, Relativistic MS $X\alpha$ calculations of the electronic structure and related Properties of $PtCl_6^{2-}$, *Chem. Phys. Lett.* 97 (1983) 215–220.
- [31] A. Miolati, U. Pardini, Beiträge zur Kenntnis der chlorierten Platinsäuren I, *Z. Anorg. Chem.* 33 (1903) 251.
- [32] G.J. Antos, A.M. Aitani, Catalytic naphtha reforming, revised and expanded, CRC Press, 2004.
- [33] H. Taube, Rates and mechanisms of substitution in inorganic complexes in solution, *Chem. Rev.* 50 (1952) 69–126.
- [34] W.A. Spieker, J. Liu, J.T. Miller, A.J. Kropf, J.R. Regalbuto, An EXAFS study of the co-ordination chemistry of hydrogen hexachloroplatinate(IV): 1. Speciation in aqueous solution, *Appl. Catal. A: Gen.* 232 (2002) 219–235.
- [35] L.G. Sillen, A.E. Martell, Stability constants of metal ion complexes, The Chemical Society, Burlington House, London, 1971 Special Publication No. 25 (Suppl. 1).
- [36] T. Mang, B. Breitschdel, P. Polanek, H. Knözinger, Adsorption of platinum complexes on silica and alumina: Preparation of non-uniform metal distributions within support pellets, *Appl. Catal. A: Gen.* 106 (1993) 239–258.

The order of addition and time matters: impact of electrolyte processing on micelle-assisted electrosynthesis of mesoporous alloys

Cristina Navarro-Senent^a, Salvador Pané^b, Jordi Sort^{a,c}, Eva Pellicer^a

^a *Departament de Física, Facultat de Ciències, Universitat Autònoma de Barcelona E-08193 Bellaterra (Cerdanyola del Vallès), Barcelona, Spain*

^b *Institute of Robotics and Intelligent Systems, Swiss Federal Institute of Technology ETH Zurich, Tannenstraße 3, 8092 Zurich, Switzerland*

^c *Institució Catalana de Recerca i Estudis Avançats (ICREA), Pg. Lluís Companys 23, E-08010 Barcelona, Spain*

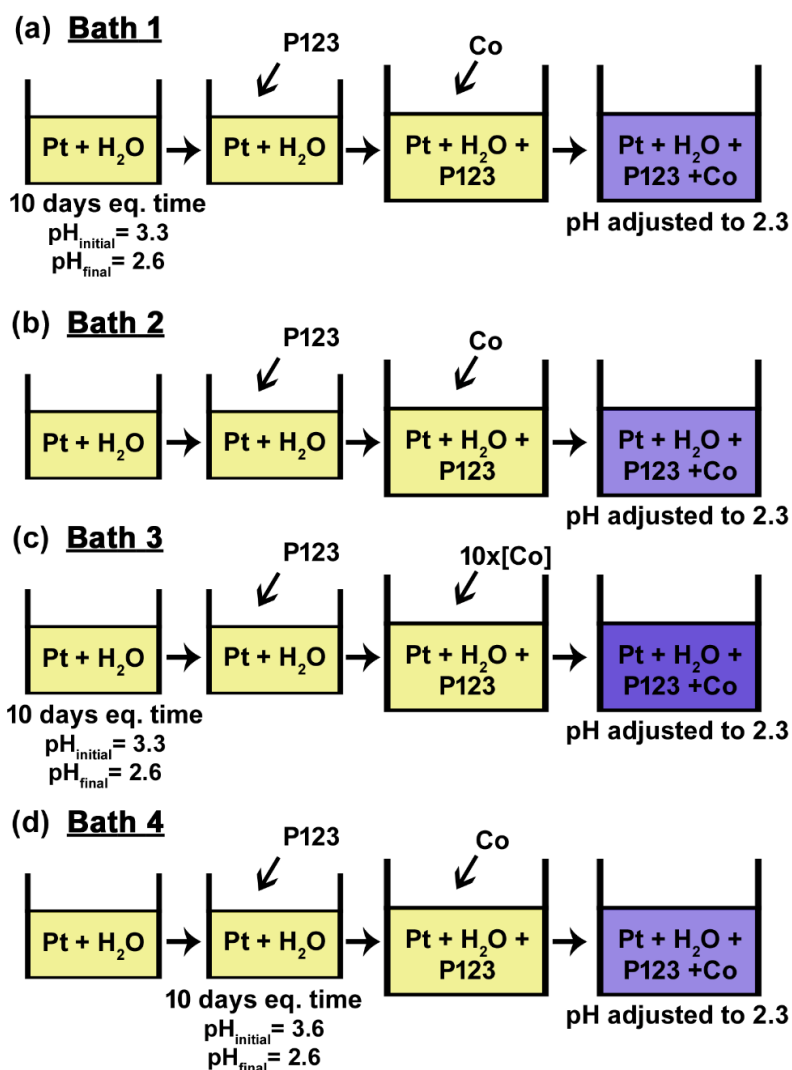


Figure S1. Scheme of the preparation procedure followed in Baths (a) 1, (b) 2, (c) 3 and (d) 4. 'eq. time' stands for equilibration time. The pH values indicated below the '10 days eq. time' are the pH value of the solution measured at day 1 and day 10, respectively.

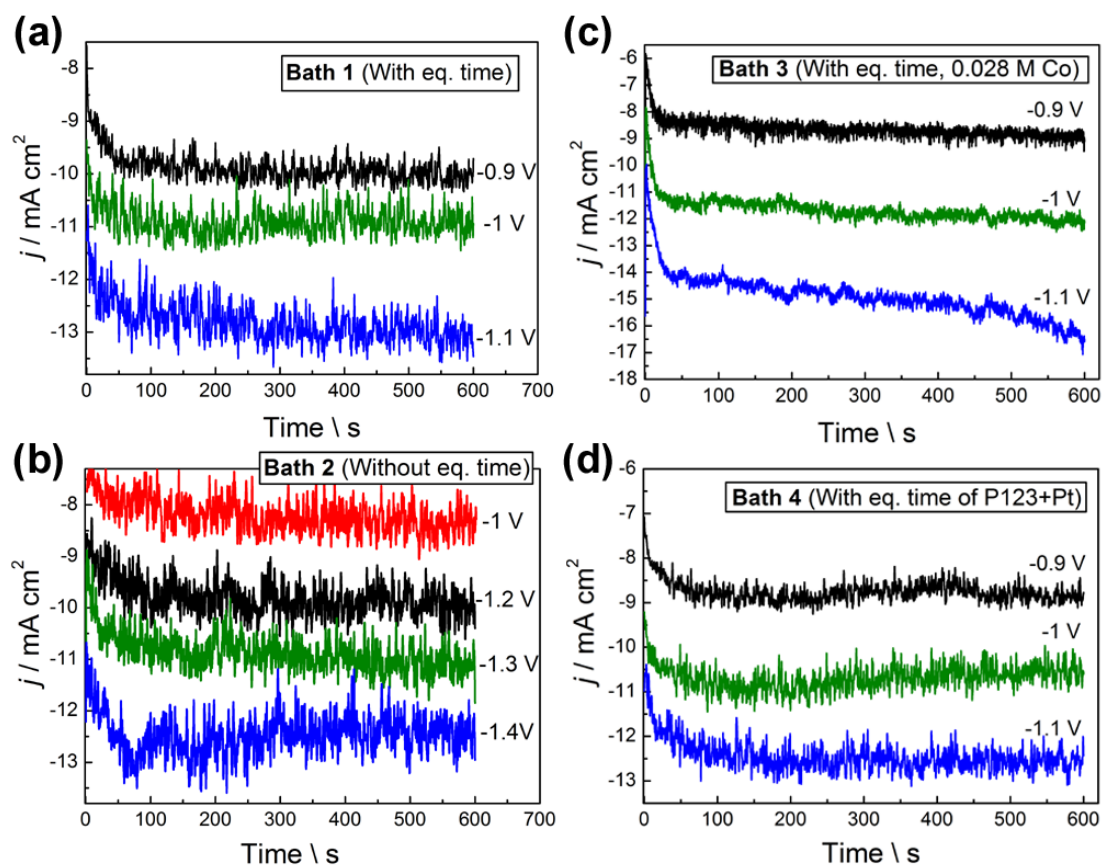


Figure S2. Representative j - t transients for Co-Pt deposition onto Cu/Ti/Si substrates at the indicated applied potentials from (a) Bath 1, (b) Bath 2, (c) Bath 3 and (d) Bath 4.

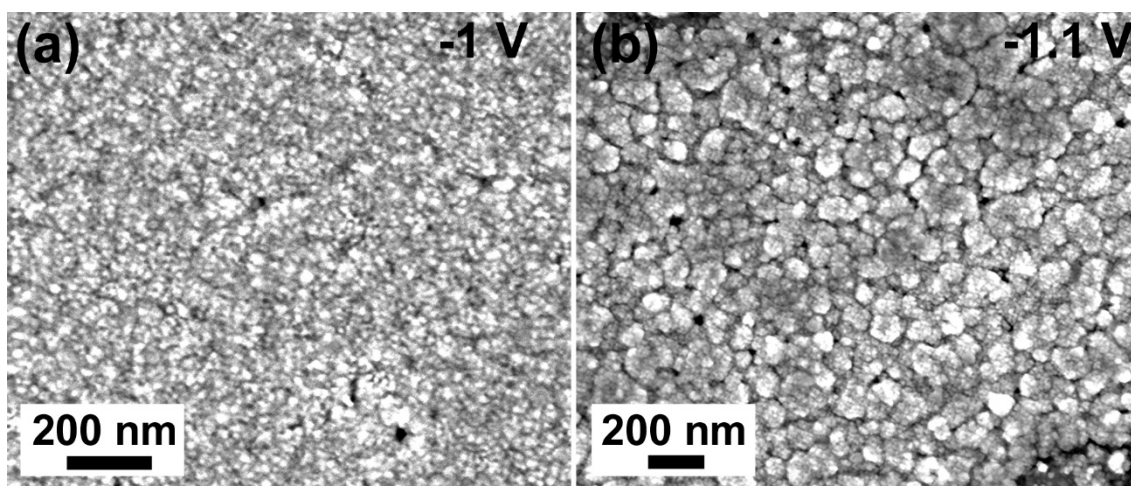


Figure S3. Representative SEM images of the Co-Pt films electrodeposited during 600 s from Bath 2 at (a) -1.0 V (20 at.% Co) and (b) -1.1 V (37 at.% Co). The average Co content is given in parentheses.

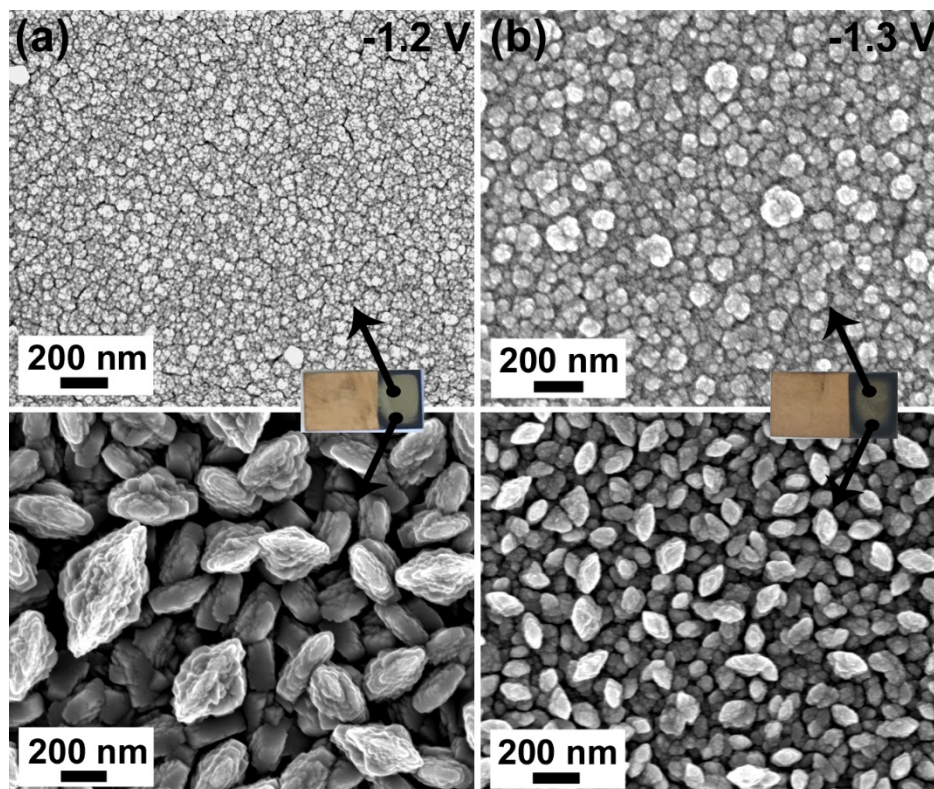


Figure S4. Representative SEM images of the Co–Pt films electrodeposited from Bath 2 at (a) –1.2 V and (b) –1.3 V, acquired from two different regions in the films, as indicated by the photos of the coatings.







Bath	Q (Coulombs)			Thickness (nm)		
	–0.9 V	–1.0 V	–1.1 V	–0.9 V	–1.0 V	–1.1 V
1				77 ± 8	122 ± 10	159 ± 8
	–1.48	–1.64	–1.92			
2				90 ± 14	156 ± 50	250 ± 35
	–1.47	–1.60	–1.85			

Table S1. Charge flowed during the electrodeposition of Co–Pt from Baths 1 and 2 and the corresponding thickness of the deposits.

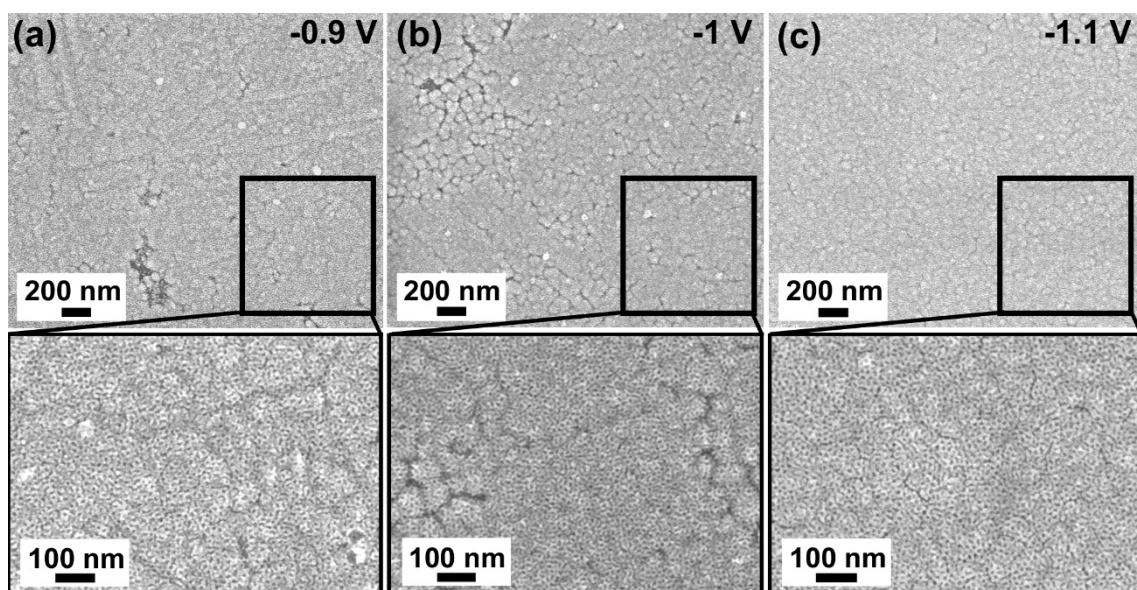


Figure S5. Representative SEM images of the Co-Pt films electrodeposited from Bath 4 at (a) -0.9 (b) -1.0 and (c) -1.1 V during 600 s.

Bath	5	6
Equilibration time (10 days)	Na_2PtCl_6	–
Bath composition and electrodeposition conditions:		
$[\text{Na}_2\text{PtCl}_6] / \text{M}$	0.0041	
$[\text{P-123}] / \text{mg mL}^{-1}$	1 (= 1 wt %)	
pH	2.3	
$T / ^\circ\text{C}$	25	
E / V	$-0.9, -1.0$	$-1, -1.1$
t / s	600	

Table S2. Bath composition and electrodeposition conditions utilized for the growth of pure Pt films from Baths 5 and 6. For Bath 5, the Pt(IV) salt was dissolved in water and the solution is left to equilibrate for 10 days at room temperature before P-123 is added.

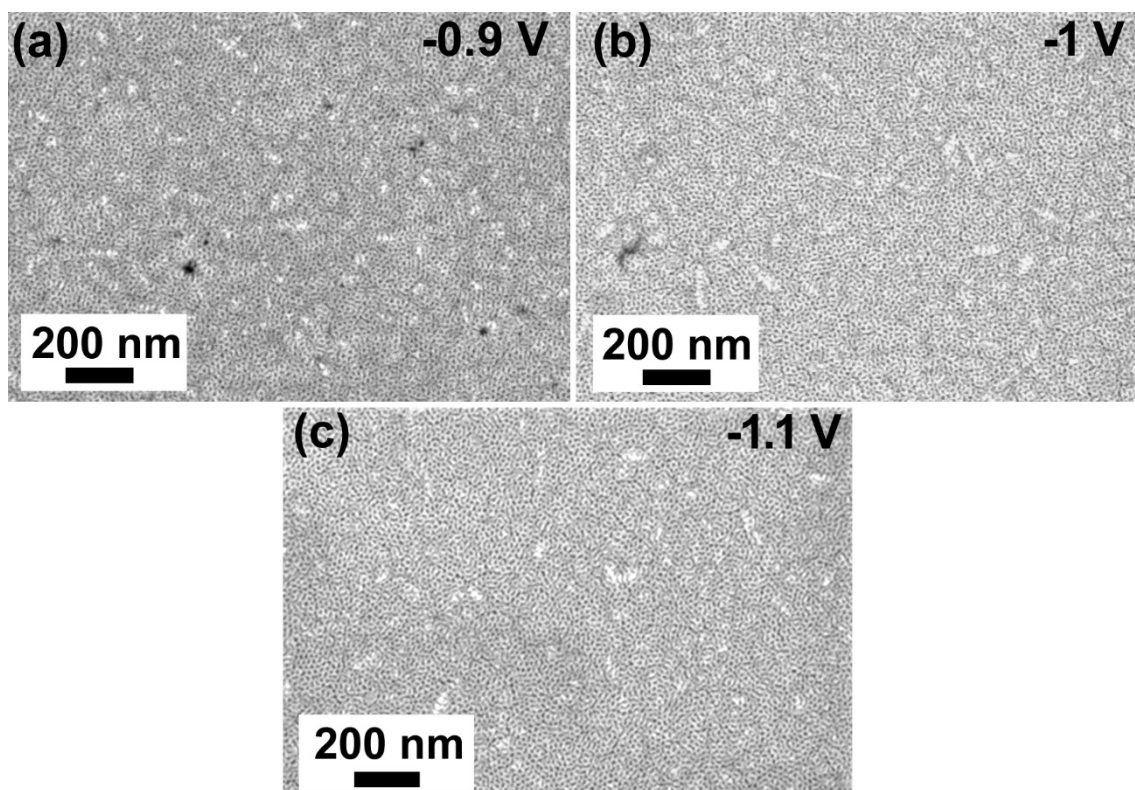


Figure S6. Representative SEM images of the Co-Pt films electrodeposited from Bath 1 at (a) -0.9 (b) -1.0 and (c) -1.1 V during 600 s using an equilibration time of 2 days.

5

Hard-magnetic,
macroporous
 $L1_0$ -ordered Co–Pt
electrodeposited
films

5. Hard-magnetic, macroporous L1₀-ordered Co–Pt electrodeposited films

For the sake of consistency, this chapter is structured as a research article.

Abstract

Macroporous L1₀-ordered Co–Pt films were successfully synthesized by electrodeposition from an aqueous sulfate-chloride electrolyte on colloidal crystal templated substrates, followed by annealing in vacuum. The colloids deposited on the substrate consisted of amidine-functionalized polystyrene spheres of 200 nm in diameter, which were self-assembled by electrophoresis. As-deposited Co–Pt films obtained after spheres removal showed a highly packed arrangement of pores of 200 nm in diameter. Structurally, the films consisted a mixture of A1-disordered face-centered cubic (fcc) solid solutions, one of them being nearly equiatomic. Upon annealing at 600 °C, the A1-disordered phases partly transformed into the L1₀-ordered (face-centered tetragonal, fct) phase, which was slightly richer in Pt (i.e., non-equiatomic). As a result, the coercivity significantly increased from 148 Oe to 1328 Oe. Importantly, the porosity of the films was preserved after annealing. Optimum annealing temperature and time were selected on the basis of a prior parametric study with electroplated dense counterparts. This work demonstrates that the combination of colloidal crystal templating and electrodeposition is a very convenient pathway towards ultra-light hard magnets with technological applications in automotive and aerospace industries, portable sensors or spectrometers, magnetic levitation systems, or magnetoelectric devices, among others.

5.1. Introduction

Hard magnetic materials are of fundamental interest for their significant performance or key role in biomedical devices, motors, generators, recording media and

microelectromechanical systems (MEMS).¹ Currently, there is an increasing demand for small size, lightweight and low-cost hard magnets due to their potential applications in spacecraft, aircraft and portable/wireless devices, among others. For this reason, there has been a flurry of research on the development of hard magnetic micro/nanomaterials.²⁻⁶ Rare-earth containing magnets (e.g. Nd-Fe-B, Sm-Co) are known as the strongest hard magnetic materials due to their high remanent magnetization and maximum energy product $(BH)_{\max}$.^{1,7} Unfortunately, rare-earth magnets are expensive and non-sustainable, suffer from high corrosion rates and their fabrication mainly relies on vacuum-based fabrication methods such as sputtering or other physical vapor deposition techniques, which are known for their high complexity and cost. In addition, they are difficult to be nanostructured or patterned into well-controlled shapes, which limits their integration in real devices.¹ Electrodeposition of rare-earth alloy magnets is a good alternative to physical deposition methods. However, their electrosynthesis from aqueous baths is not optimal due to the associated low current efficiency and incorporation of oxygen and other impurities into the films, which heavily deteriorate the hard magnetic properties.⁸⁻¹⁰ As a result, soft or semi-hard magnetic films are typically reported. Alternatively, the electrodeposition of films and nanowires from deep eutectic solvents and ionic liquids has also been demonstrated.¹¹ Yet, the resulting coercivity values are far from those achieved in sputtered films.¹²

As an alternative to rare-earth magnets, $L1_0$ -ordered alloys emerge as candidate permanent magnets owing to their high magnetocrystalline anisotropy and large coercivity. $L1_0$ -ordered alloys consist of equiatomic compositions of iron-series transition metals (e.g. Fe or Co) and heavy transition metals (e.g. Pt or Pd), which form an asymmetric face-centered tetragonal (fct) structure.^{13,14} Generally, the formation of $L1_0$ -ordered alloys (e.g. Co-Pt, Co-Pd, Fe-Pt and Fe-Pd) requires either a high-temperature deposition or a post-deposition annealing of the as-deposited A1-disordered phase to induce its structural transformation into the $L1_0$ -ordered phase. In contrast to rare-earth magnets, $L1_0$ -ordered alloys can be prepared more easily by electrochemical deposition, both in the form of continuous thin/thick films and micro/nanostructures, thus facilitating their implementation in micro-/nanosystems.^{15,16}

Co–Pt system is one of the most investigated L1₀-ordered systems. It exhibits a high uniaxial magnetocrystalline anisotropy of 4.9 erg/cm³ and (BH)_{max} of 200 kJ/m³.¹⁷ L1₀-ordered Co–Pt alloys are usually fabricated by physical vapor deposition^{18,19} or electrochemical deposition techniques,^{20–22} mostly in the form of dense thick and thin films owing to the high temperature treatment required for the L1₀-ordered phase transformation. High-temperature annealing is known to cause interdiffusion or even the collapse, for example, of arrays of substrate-supported high aspect ratio nanostructures like nanowires.²³

From the manufacturing standpoint, the electrodeposition of L1₀-ordered Co–Pt alloys has garnered significant attention because it offers good shape fidelity and easy scalability at a low cost.²⁴ The vast majority of studies have focused on the electrodeposition of thick and thin films from electrolytes containing either the dinitritodiammineplatinum (Pt(NH₃)₂(NO₂)₂)^{20,25–27} or the hexachloroplatinate salts,^{28,29} the Co precursor and a few additives. Although electrodeposition has proven effective for the fabrication of low-dimensional materials, the preparation of miniaturized L1₀-ordered Co–Pt alloy in the form of nanostructured films³⁰ and micro-/nano-structures such as nanoparticles and pillars^{31,32} has been scarcely reported.

Several approaches have been proposed so far for the preparation of porous metallic films via electrodeposition, using (i) soft templates such as hydrogen bubbles^{33,34} or block copolymers^{35,36} and (ii) hard templates like anodic alumina membranes.^{37,38} Among these, colloidal crystal templating (also known as colloidal lithography) is a cost-effective, straightforward and facile approach for the fabrication of 3D porous structures with controllable pore size. This approach relies on the self-assembly of colloidal particles of varying size (typically from hundreds to tens of nm) onto a substrate to create a pattern of colloids which serve as a soft or hard template. Several deposition techniques can be utilized to self-assemble the colloids on a surface, such as dip-coating,³⁹ spin coating⁴⁰ and electrophoretic deposition.⁴¹ In essence, colloidal crystal templating combined with electrodeposition constitute a versatile and powerful method to fabricate pseudo-ordered macro- or mesoporous alloy films, whose atomic ratio can be fine-tuned by conveniently modifying the electrodeposition parameters.^{42,43}

Taking into consideration the above, the introduction of porosity into hard magnets, as L1₀-ordered alloys, opens a new route to develop advanced magnetic materials which could find applications in several technological fields. Given their large (BH)_{max} and porous structure, these materials have a great potential for applications which require low-density magnets such as spacecraft, automobiles or microbial fuel cells technologies.^{44,45} Also, the possibility to develop magnetic composites using the porous hard magnets as a skeleton to be filled with other materials having different physical properties is of technological relevance. For instance, the pores could incorporate a soft magnetic phase, yielding an exchange spring magnet material. Alternatively, the pores could be filled with an antiferromagnetic material, giving rise to a magnetic composite exhibiting exchange bias effect, a phenomenon commonly exploited in spintronic systems, magnetic random-access memories and magnetic read heads.

Herein, we present the fabrication of macroporous, L1₀-ordered Co–Pt thin films via colloidal crystal template-assisted electrodeposition. A close-packed colloid assembly of charged amidine polystyrene (PS) spheres with 200 nm diameter size was assembled by electrophoretic deposition onto a titanium surface. Subsequently, equiatomic Co–Pt alloy was grown by potentiostatic electrodeposition from an aqueous sulfate-chloride electrolyte. Finally, selective etching of the spheres yielded a macroporous Co₅₀Pt₅₀ alloy film. For the sake of comparison, fully dense films were deposited on unpatterned Ti surfaces. Both fully dense and macroporous Co–Pt thin films were subject to a parametric study to determine the optimal conditions (temperature and time) to maximize the extent of conversion of the as-deposited fcc phase into the L1₀-ordered (fct) phase, which was followed by both grazing incidence X-ray diffraction (GIXRD) and vibrating sample magnetometry (VSM).

5.2. Experimental section

5.2.1. Cell and electrodes preparation

Electrodeposition was carried out in a one-compartment, thermostated three-electrode cell connected to a PGSTAT204 Autolab potentiostat/galvanostat (Metrohm-Autolab). A

double junction Ag|AgCl ($E = +0.210$ V/SHE) reference electrode (Metrohm AG) with 3 M KCl inner solution and 1 M Na₂SO₄ outer solution was used. A platinum spiral served as the counter electrode. Cyclic voltammetry (CV) curves were recorded on a glassy carbon electrode of 0.0314 cm² working area. For the preparation of the dense Co–Pt thin films, flat Si/Ti (150 nm) substrates were used as working electrodes. Titanium was chosen as conductive layer in order to avoid atomic interdiffusion in the Co–Pt thin films during the heat treatment. The working area was measured to be 0.25 ± 0.01 cm². For the growth of macroporous Co–Pt thin films, Si/Ti (150 nm) substrates coated with amidine functionalized PS spheres were used.

Electrophoretic deposition of the PS spheres was performed using an Agilent B2902A power supply as voltage source and a home-made 3D-printed cell consisting of poly(methyl methacrylate) (PMMA) chamber attached to a counter electrode made of platinized titanium sheet (anode). Si/Ti (150 nm) substrates (cathode) were fixed at 0.5 cm from the counter electrode (**Figure 5.1a**). Monodisperse, positively charge amidine-terminated PS sub-micrometer spheres of 200 nm in diameter were purchased from ThermoFisher. Positively charge PS spheres were selected in order to be able to negatively polarize the Ti conductive layer and avoid its passivation during the electrophoretic deposition, which otherwise would happen under positive polarization. A final aqueous solution of 0.05% w/v of the PS sphere suspension was added to the custom cell. The positively charged amidine PS spheres were deposited by applying an electric field of $40 \text{ V}\cdot\text{cm}^{-1}$ during 5 min. Subsequently, the samples were dried on a hot-plate at 80 °C for 10 min to evaporate the water.

5.2.2. Co–Pt electrodeposition

The electrolyte for Co-Pt deposition consisted of 0.002 M Na₂PtCl₆·6H₂O, 0.02 M CoSO₄ and 0.2 M NaSO₄. The pH was adjusted to 2.88 by adding a few drops of 1 M H₂SO₄ solution to the electrolyte. The films were deposited potentiostically at -0.55 V during 420 s, under mild agitation ($\omega = 100$ rpm) while simultaneously bubbling N₂ into the solution to de-aerate the electrolyte. The temperature was maintained at 25 °C by circulating water throughout the external jacket of the electrochemical cell by means of an F12 Julabo thermostat. After deposition, the dense thin films were rinsed with Milli-Q

(MQ) water and dried in air. In the case of deposition onto the electrophoretically patterned substrates, the PS spheres were selectively etched away by immersing the samples in tetrahydrofuran overnight under agitation ($\omega = 400$ rpm). The resulting macroporous films were thoroughly cleaned with acetone and isopropanol, rinsed with MQ water and finally dried with N_2 .

5.2.3. Heat treatment

Heat treatments of the as-deposited films were carried out in a home-made set-up consisting of a high-vacuum system connected to a quartz tube located inside of a 653.03 high-Temperature Furnace. Different annealing temperatures (550, 600 and 650 °C) and times (20, 60, 80 and 100 min) were applied under vacuum (pressure $< 10^{-6}$ mbar). First, the furnace was heated up to the desired temperature using a ramp rate of 5 °C/min. Then, the quartz tube containing the sample under vacuum was inserted into the furnace and kept there for certain periods (20, 60, 80 and 100 min). Finally, the furnace was left to cool down to room temperature.

5.2.4. Characterization

The morphology and composition of the fully dense and macroporous Co–Pt films were characterized on a Zeiss Merlin FE-SEM equipped with an EDX detector. GIXRD measurements were performed on a Bruker-AXS, model A25 D8 Discover equipped with a LinxEye XE-T detector using $Cu K_{\alpha}$ radiation and a grazing incidence angle of 1°. The mean crystallite size was calculated from the GIXRD patterns using the Scherrer equation. Magnetic measurements were carried out using a VSM Micro sense (LOT–Quantum Design). Hysteresis loops were recorded at room temperature along the in-plane direction, with a maximum applied magnetic field of 20 kOe.

5.3. Results & Discussion

The synthetic method adopted to prepare the macroporous Co–Pt films was colloidal crystal template-assisted electrodeposition (**Figure 5.1**). This approach relies on the use of colloidal crystal of PS spheres as soft template for inducing the macroporosity to the

Co–Pt thin film. Firstly, amidine-terminated PS spheres were assembled on the Si/Ti substrates by electrophoretic deposition (**Figure 5.1a**). Subsequently, colloidal crystal templated substrates were employed as working electrode for the electrodeposition of Co–Pt alloy (**Figure 5.1bi**). Finally, selective removal of the spheres results in a macroporous Co–Pt thin film (**Figure 5.1bii**).

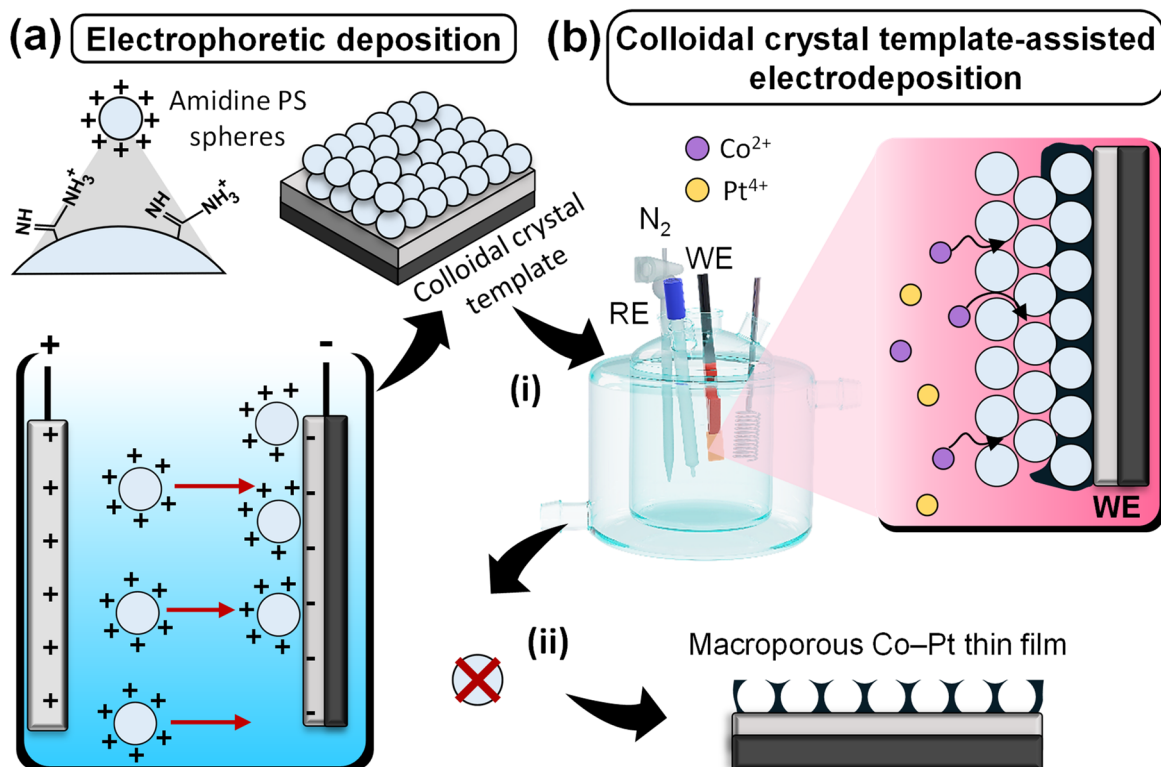


Figure 5.1. (a) Schematic drawing depicting the electrophoretic deposition of PS spheres. By applying an electric field of $40 \text{ V}\cdot\text{cm}^{-1}$, positively charged amidine-terminated PS spheres move towards the cathode, resulting in the assembly of the spheres onto the Si/Ti substrate. (b) Schematic representation of colloidal crystal template-assisted electrodeposition. (i) The colloidal crystal layer is used as template for the electrodeposition of Co–Pt alloy, (ii) followed by the removal of the PS spheres, leaving the macroporous Co–Pt film behind.

Deposition of Co–Pt alloy was conducted from a sulfate-chloride electrolyte which was adapted from an electrolyte designed for the deposition of Fe–Pt magnets.¹⁵ Interestingly, the bath was additive-free and simply contained hexachloroplatinate and cobalt sulfate salts. This bath formulation had not been used before for the synthesis of the L_{10} -ordered Co–Pt alloy by electrodeposition.^{28,29} **Figure 5.2a** shows the CV curve recorded from the electrolyte on glassy carbon. In the negative sweep, the different reduction peaks can be attributed to the discharge of Pt(IV) ions, followed by Co(II) co-

deposition and hydrogen co-evolution.⁴⁶ In the anodic scan, a main oxidation peak centered at -0.015 V and a much weaker peak at more positive potentials were recorded. According to the CV fingerprint, cathodic potentials close to the onset of Co and Pt co-deposition (roughly around -0.5 V) were selected to avoid the growth of Co-rich deposits. Deposition was conducted potentiostatically since the real working area of the colloidal crystal templated substrates could not be precisely determined (**Figure 5.2b**). For the sake of comparison, fully dense Co–Pt deposits were electroplated on unpatterned Si/Ti substrates from the same electrolyte (black curve, **Figure 5.2b**). After a parametric study of the deposition potential, a constant potential value of -0.55 V was chosen for obtaining Co–Pt deposits with equiatomic composition (**Figure 5.2b**).

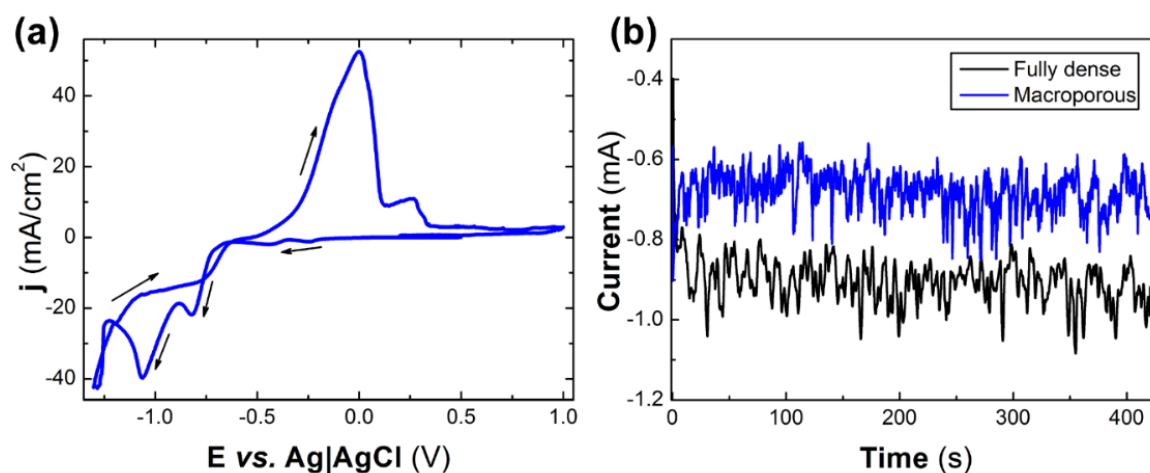


Figure 5.2. (a) CV curve recorded under stationary condition at $50 \text{ mV}\cdot\text{s}^{-1}$ from the aqueous sulfate-chloride electrolyte on vitreous carbon electrode. (b) Potentiostatic transients corresponding to the electrodeposition of the fully dense (black curve) and macroporous Co–Pt thin films (blue curve) at $-0.55 \text{ V vs. Ag|AgCl}$ (3 M KCl). Note that the y-axis is given in current instead of current density due to the uncertainty in the estimation of the real working area for the colloidal crystal templated substrates. However, the geometric areas were the same and hence, the values are strictly comparable.

Figure 5.3 shows representative FE-SEM images of the as-deposited, equiatomic, fully macroporous Co–Pt films and their dense counterparts. Dense films exhibit fine submicrometer grains with round-shape morphology and cracks that extend over the entire surface (**Figure 5.3a**). The occurrence of cracking could be attributed to severe lattice mismatch between the Ti seed-layer and the Co–Pt deposit (hexagonal close-packed *versus* face-centered cubic phases). **Figure 5.3b** shows the FE-SEM images of the

macroporous Co–Pt films after PS spheres removal. The films displayed an architecture consisting of nearly a monolayer of hemispherical randomly arranged pores. The pore size matched the diameter of the PS spheres (200 nm). Cross-sectional measurements revealed a thickness of 201 ± 7 nm for the dense films and 116 ± 4 nm for the macroporous thin films. Elemental compositional analysis revealed a composition of 49 ± 4 at% Co and 51 ± 4 at% Pt for the fully dense films, whereas macroporous films showed a composition of 52 ± 5 at% Co and 48 ± 5 at% Pt. Moreover, low amounts of oxygen were found in both cases, namely 9 at% for the fully dense films and 15 at% for the macroporous films.

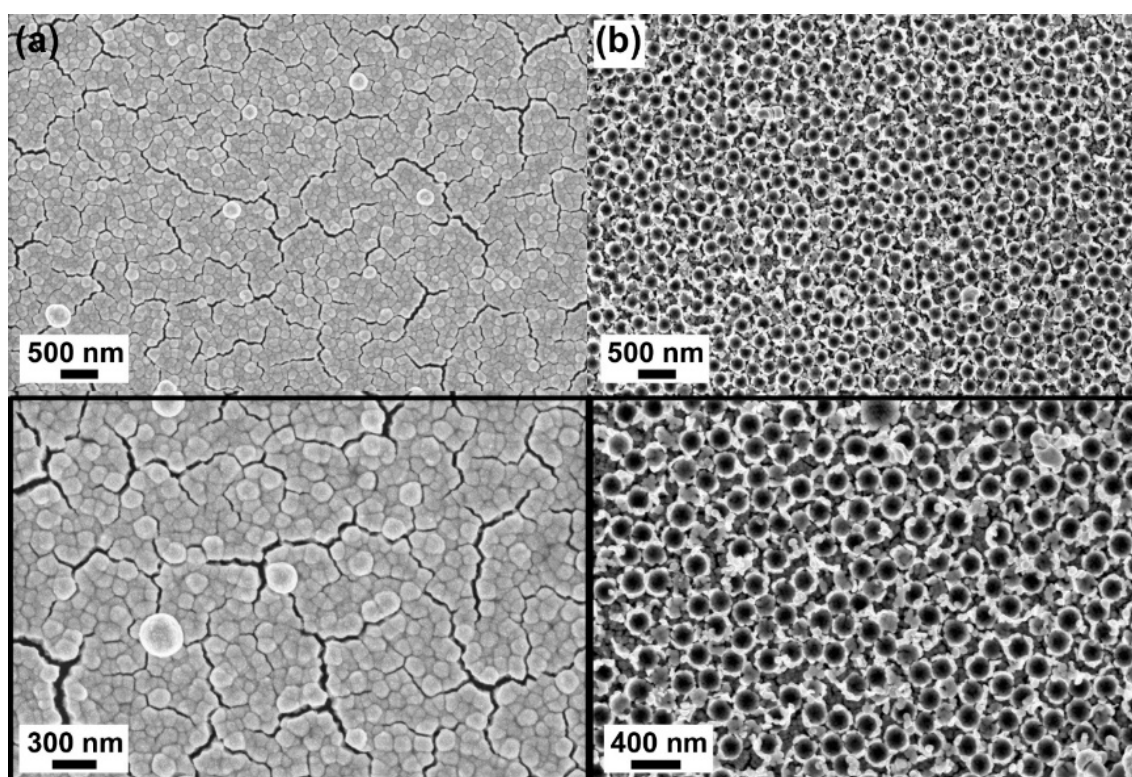


Figure 5.3. Representative low and high magnification FE-SEM images of equiatomic (a) fully dense and (b) macroporous Co–Pt thin films.

GIXRD analyses were performed to determine the crystallographic phases of fully dense and macroporous Co–Pt films both before and after annealing (**Figure 5.4a** and **b** respectively). For the sake of clarity, only the GIXRD patterns corresponding to samples annealed under optimal conditions, namely 600 °C for 100 min for the fully dense films and 600 °C for 80 min for the macroporous Co–Pt films, are shown. These are optimal annealing conditions as it will be demonstrated later in the magnetic characterization

part (**Figure 5.5** and **5.8**, respectively). In the GIXRD patterns of the as-prepared dense Co–Pt films, two main peaks, located at 41.0° and 47.4° , that matched the fcc phase of equiatomic Co–Pt (i.e., the so-called A1-disordered phase) were observed. Furthermore, the crystallite size estimated from the peak broadening at 41.0° using the Scherrer's formula was about 4 nm. After annealing at 600°C for 100 min, the corresponding GIXRD patterns showed narrower peaks at 24.2° , 33.4° , 41.6° and 48.2° , which are assigned to the fct $L1_0$ ordered phase. The crystallite size was roughly around 15 nm. These results proved that the chosen annealing conditions efficiently promote the complete rearrangement of Co and Pt atoms from the A1-disordered phase into the chemically ordered $L1_0$ structure, in concordance with the magnetic data shown below. The diffractograms of the as-deposited macroporous Co–Pt films showed two main peaks located at 41.6° and 48.0° , which is compatible with the coexistence of two A1-disordered solid solutions, one roughly stoichiometric and the other one richer in Co.²⁸ Considering that their chemical composition was 52 ± 5 at% Co and 48 ± 5 at% Pt, a solid solution richer in Pt should also be present, although it is not seen in the GIXRD pattern. This remains an open issue. The small peak observed at 44.4° matches the position of fcc/hcp-Co, while the low intensity peaks between 30° and 37.5° can be assigned to Co oxohydroxides/oxides. The films were also nanocrystalline, with a crystallite size of 5 nm as estimated using the Scherrer's formula. Upon annealing, the corresponding XRD patterns showed two main peaks located at 41.1° and 47.6° which matched the fct $L1_0$ ordered phase. These peaks, though, are shifted towards smaller angles indicating enrichment in Pt. A small peak is observed at 42.6° which matches the position of fcc-CoO phase. In addition, the cubic intermetallic CoPt_3 phase (PDF 029-0499) could also be present, having its main peaks at 40.5° and 47.1° angular positions. This phase is typically formed in non-equiatomic Co–Pt alloys with deviations of the order of 5 at%.⁴⁷ These observations are consistent with the two magnetic phases observed in the magnetic hysteresis loops, as it will be shown later (**Figure 5.7c**). The annealed macroporous samples remained nanocrystalline with an estimated crystallite size of 10 nm.

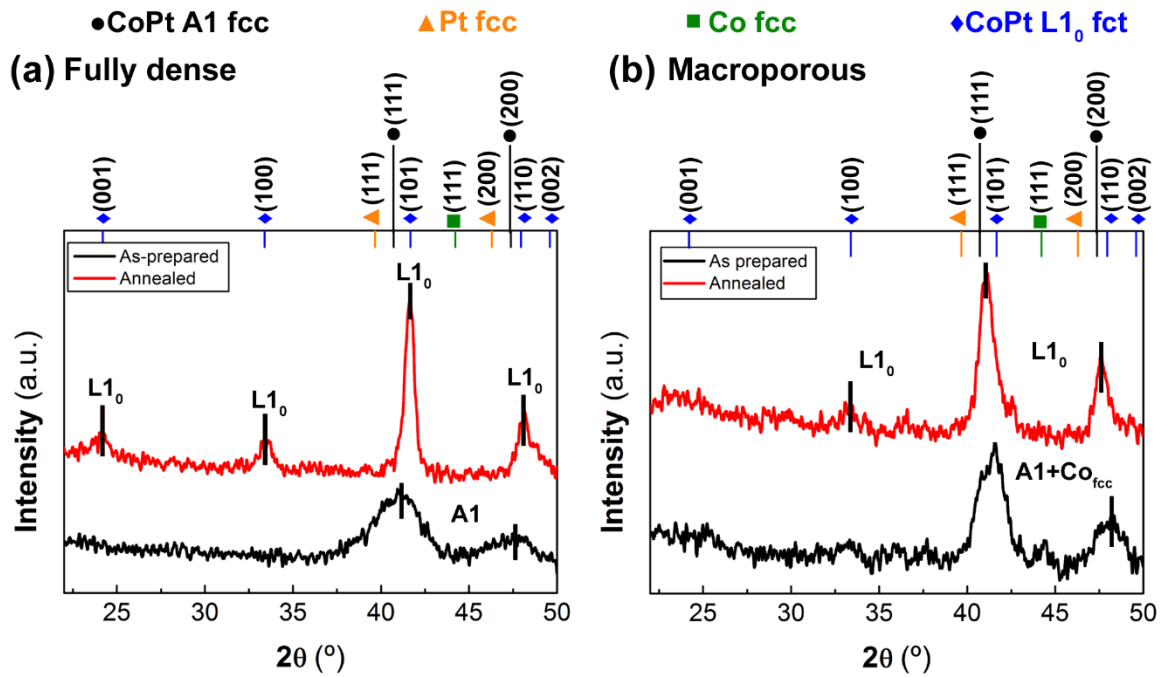


Figure 5.4. (a) XRD patterns of the equiatomic fully dense Co–Pt films in the as-prepared state (black curve) and after being annealed at 600 °C for 100 min (red curve). (b) XRD patterns of the macroporous Co–Pt films in the as-prepared state (black curve) and after being annealed at 600 °C for 80 min (red curve).

As-deposited, fully dense Co–Pt thin films were magnetically soft with a coercivity (H_C) of 85 ± 5 Oe. A first parametric study to determine the optimal annealing conditions was performed on the fully dense films (**Figure 5.5**). First, temperature was optimized for a fixed annealing time of 60 min, as seen in **Figure 5.5a**. As the annealing temperature was made higher, H_C values increased, suggesting that the disordered phase gradually converted into the L1₀-ordered phase. The H_C reached the highest value of 4.8 kOe when the dense films were annealed at 600 °C but it dropped to 2.0 kOe when the annealing temperature was set at 650 °C. From the observed results, it was concluded that 600 °C was the optimum temperature for the structural conversion from the as-deposited fcc to the fct phases. Later, annealing time was optimized while keeping the optimum temperature of 600 °C fixed (**Figure 5.5b and c**). On increasing the annealing time from 20 to 100 min, the H_C increased monotonically from 1.06 kOe after 20 min to 6.2 kOe after 100 min, and then dropped to 2.8 kOe when the film was annealed for 120 min, as shown in **Figure 5.5b**. In contrast to as-deposited dense films, annealed counterparts showed squarer hysteresis loops with a squareness ratio closer to 1, which is a characteristic of hard magnetic materials (**Figure 5.5c**). Moreover, all the annealed films

showed a nearly single-phase magnetic character except for the sample heat-treated for 100 min, which showed the additional contribution of a softer magnetic phase (pink curve **Figure 5.5c**). From these results, it was concluded that 600 °C and 100 min were the optimal annealing conditions to achieve full conversion of the as-obtained phase into the L1₀-ordered one for the dense Co–Pt thin films.

Figure 5.6 shows the FE-SEM images of the dense Co–Pt films before and after annealing at 600 °C for 100 min. Interestingly, no pronounced changes in morphology were observed after heat treatment. Yet, the grains became a bit less rounded and the width of the cracks increased (**Figure 5.6b**), which could be attributed to recrystallization induced by the annealing process.

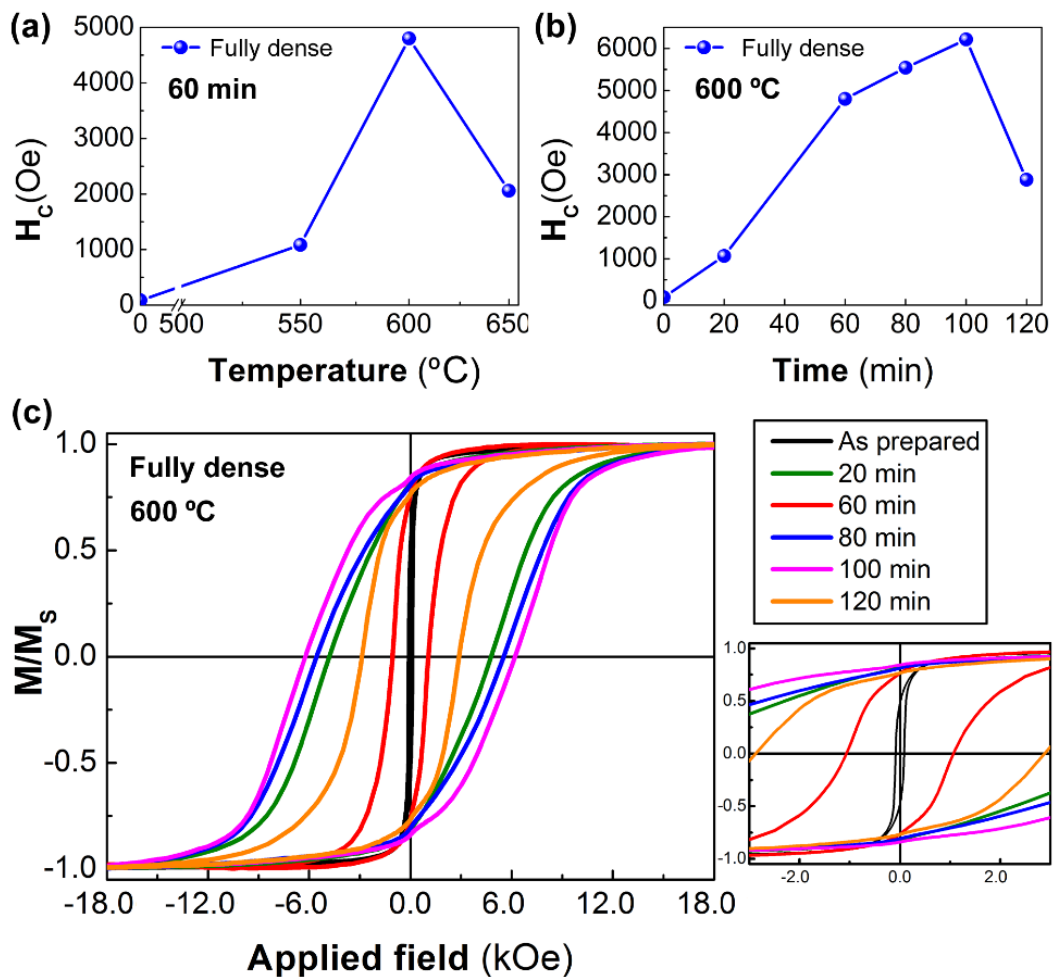


Figure 5.5. (a) Dependence of H_c on temperature for a fixed annealing time of 60 min for the equiatomic fully dense Co–Pt thin films. (b) Dependence of H_c on annealing time for a fixed temperature of 600 °C. (c) In-plane hysteresis loops of the as-prepared fully dense Co–Pt films (black curve) and annealed at 600 °C for 20, 60, 80, 100 and 120 min.

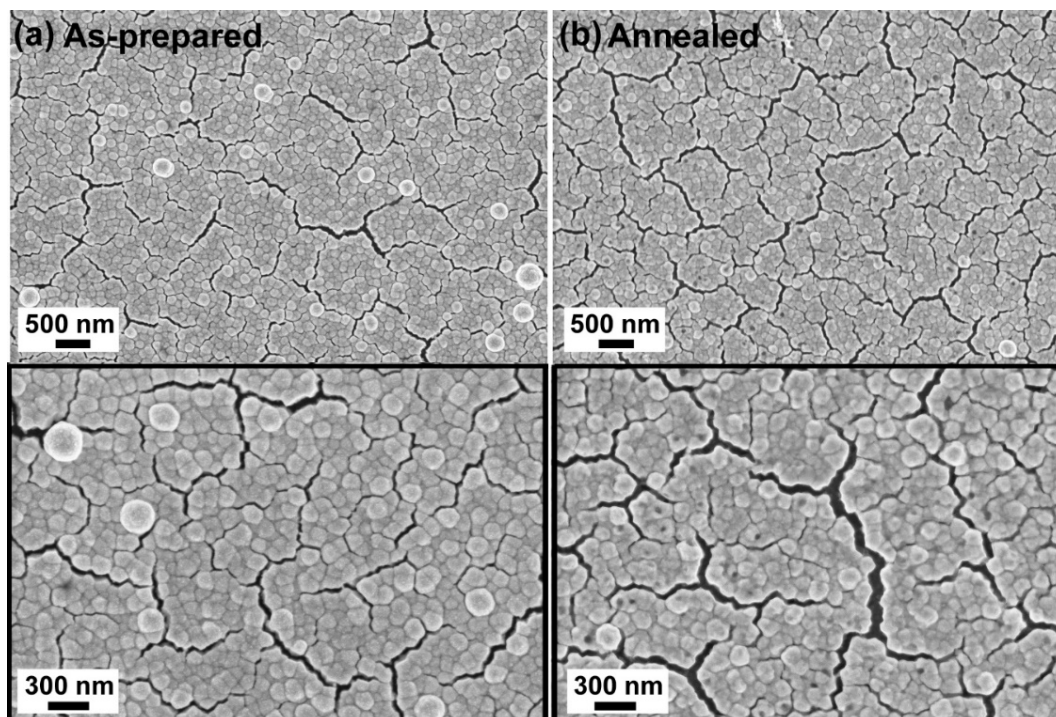


Figure 5.6. Low and high magnification FE-SEM images of the equiatomic fully dense Co-Pt thin films (a) before and (b) after annealing at 600 °C for 100 min.

As-deposited macroporous Co-Pt thin films were magnetically soft, with a slightly higher H_C (148 ± 9 Oe) compared to the fully dense films due to the hindrances imposed by the pore walls on the propagation of magnetic domain walls. Since the annealing temperature had been previously optimized for the dense films, it was decided to subject the macroporous thin films to that temperature for varying annealing times. **Figure 5.7** shows the corresponding in-plane hysteresis loops and the FE-SEM images. As the annealing time was increased, wider loops were obtained, analogous to what was observed for the dense films. An increase of the squareness ratio value, which was closer to 1 for all annealed samples except for that annealed at 600 °C during 20 min, was also observed (**Figure 5.7a**). In addition, the macroporous Co-Pt film annealed at 600 °C for 80 min showed a two-phase magnetic behavior (**Figure 5.7c**), which was anticipated by GIXRD analysis. This result could be attributed to the presence of Pt rich $L1_0$ ordered and soft magnetic $CoPt_3$ phases after the annealing treatment. Regarding the morphology, no significant variations were observed as the annealing time increased and, most importantly, porosity was preserved in all the samples after the heat treatment. Remarkably, annealing of Co-Pt films (20 nm pore size) prepared by micelle-assisted electrodeposition (see previous chapter) at 600 °C for 60 min gave rise to non-porous

deposits. This indicated collapse of the pores and underpinned the importance of the selection of the proper pore size to avoid pores collapse during heat-treatment of films at relatively high temperatures.

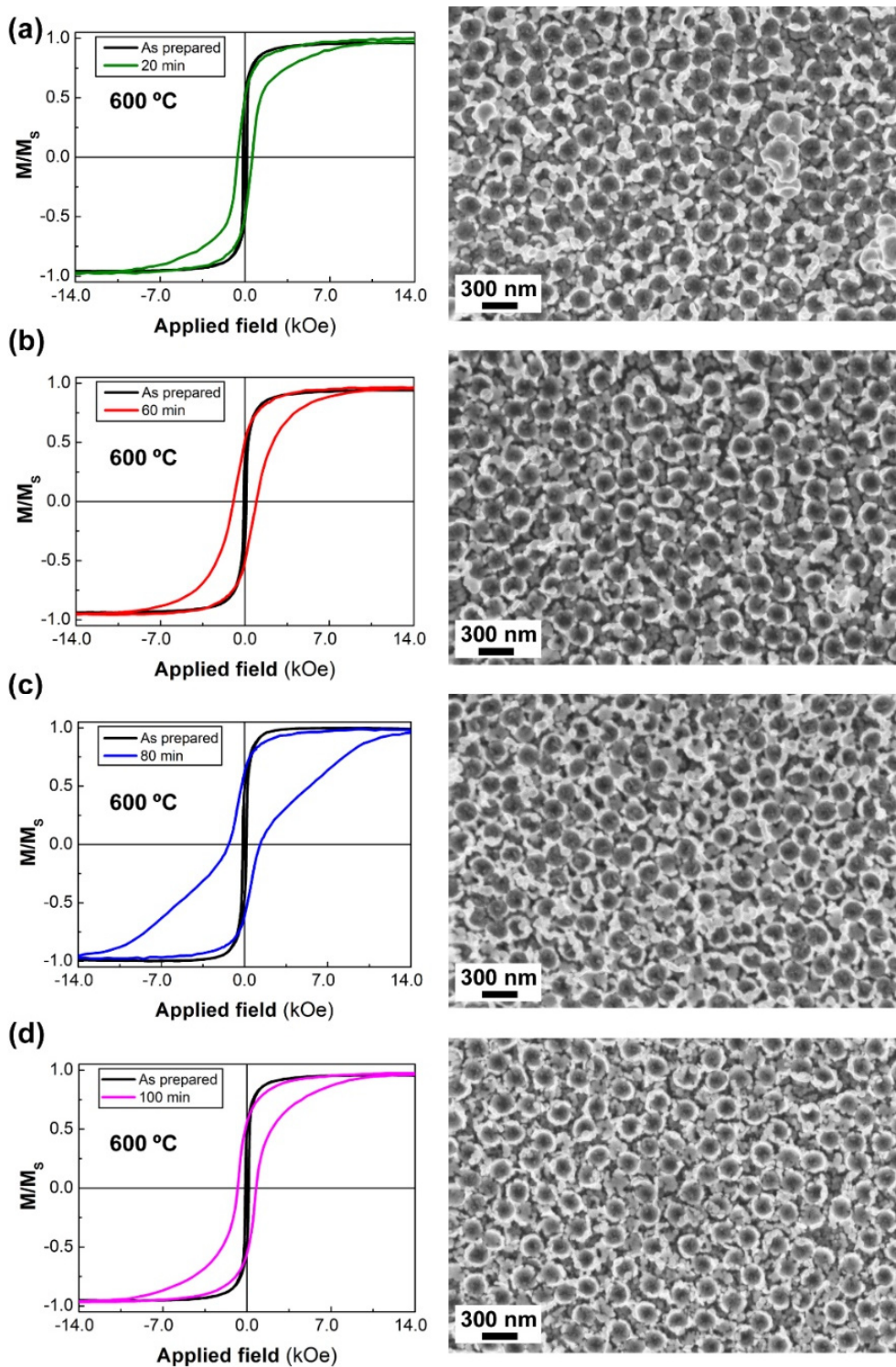


Figure 5.7. In-plane hysteresis loops of the as-prepared macroporous Co-Pt films (black curve) and after annealing at 600 °C for (a) 20 (b) 60 (c) 80 and (d) 100 min and their corresponding FE-SEM images.

Figure 5.8a shows the trend in H_C as a function of the annealing time ($T_{\text{annealing}} = 600\text{ }^\circ\text{C}$) for the macroporous Co–Pt thin films. As the annealing time increased, H_C augmented progressively and reached a maximum of 1328 Oe after 80 min. Afterwards, H_C dropped to 770 Oe when the annealing time was extended to 100 min. In any case, the increase in H_C was much less pronounced than for the fully dense counterparts, suggesting that (i) the as-deposited macroporous films were structurally different from the dense counterparts as it was evidenced by GIXRD, (ii) the conversion of the as-deposited fcc phase into the fct one did not take place to the same extent, (iii) the transformation resulted in a mixture of Pt rich $L1_0$ ordered and CoO phases, or (iv) other phenomena like diffusion of the Ti from the seed layer into the Co–Pt films occurred upon annealing. As can be seen in **Figure 5.8b** and **c**, macroporosity was preserved across the film surface after the heat treatment. Yet, less rounded macropores were found after annealing which could be attributed to the deformation of the pore wall.

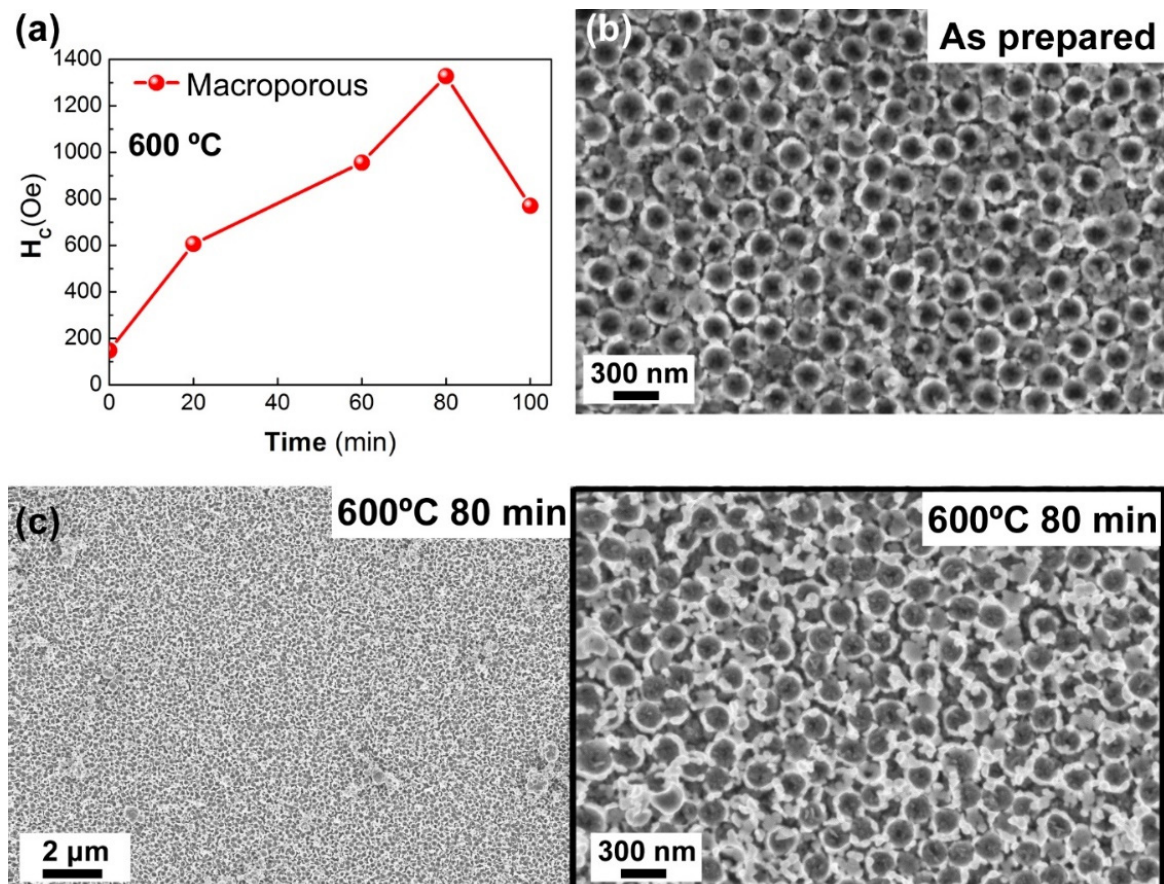


Figure 5.8. (a) Dependence of H_C on annealing time for a fixed temperature of $600\text{ }^\circ\text{C}$ for the macroporous Co–Pt thin films. FESEM of (b) as-prepared and (c) annealed macroporous Co–Pt films at $600\text{ }^\circ\text{C}$ for 80 min.

5.4. Conclusions

In conclusion, macroporous, semi-hard magnetic $L1_0$ -ordered Co–Pt thin films were prepared by colloidal crystal template-assisted electrodeposition from an aqueous sulfate-chloride electrolyte followed by annealing. A parametric study of the optimal annealing conditions taking electrodeposited fully dense counterparts as a reference revealed that a maximum H_c value of 1328 Oe was achieved after annealing at 600 °C for 80 min. Importantly, the selected pore size (200 nm) secured the preservation of the porosity upon annealing. GIXRD analyses evidenced the polycrystalline structure of the as-deposited macroporous films, which showed a mixture of A1-disordered Co–Pt solid solutions. In turn, the existence of different magnetic and crystallographic phases (hard magnetic Pt-rich $L1_0$ ordered and soft-magnetic $CoPt_3$ phases) was seen in the annealed macroporous films. This study demonstrates that the combination of electrodeposition and colloidal templating technique is a suitable strategy for fabricating hard magnetic porous films. These materials are appealing as low-density magnets or magnetic composites with a great potential for implementation in spacecraft, automobiles, or magnetoelectric devices.

References

1. Chin, T.-S. Permanent magnet films for applications in microelectromechanical systems. *J. Magn. Magn. Mater.* **209**, 75–79 (2000).
2. Kervendal, E. A., Kirk, D. R. & Meinke, R. B. Spacecraft radiation shielding using ultralightweight superconducting magnets. *J. Spacecr. Rockets* **46**, 982–988 (2009).
3. Gich, M., Casas, L., Roig, A., Molins, E., Sort, J., Suriñach, S., Baró, M. D., Muñoz, J. S., Morellon, L., Ibarra, M. R. & Nogués, J. High-coercivity ultralight transparent magnets. *Appl. Phys. Lett.* **82**, 4307–4309 (2003).
4. Janulevicius, M., Klimkevičius, V., Mikoliunaite, L., Vengalis, B., Vargalis, R., Sakirzanovas, S., Plausinaitiene, V., Zilinskas, A. & Katelnikovas, A. Ultralight magnetic nanofibrous $GdPO_4$ aerogel. *ACS Omega* **5**, 14180–14185 (2020).

5. Chen, N. & Pan, Q. Versatile fabrication of ultralight magnetic foams and application for Oil–Water separation. *ACS Nano* **7**, 6875–6883 (2013).
6. Li, Y., Liu, Q., Hess, A. J., Mi, S., Liu, X., Chen, Z., Xie, Y. & Smalyukh, I. I. Programmable ultralight magnets via orientational arrangement of ferromagnetic nanoparticles within aerogel hosts. *ACS Nano* **13**, 13875–13883 (2019).
7. Arnold, D. P. & Naigang Wang. Permanent magnets for MEMS. *J. Microelectromechanical Syst.* **18**, 1255–1266 (2009).
8. Chen, J. & Rissing, L. Electroplating hard magnetic SmCo for magnetic microactuator applications. *J. Appl. Phys.* **109**, 07A766 (2011).
9. Xie, M. Electrodeposition of Sm-Co alloy films with nanocrystalline/amorphous structures from a sulphamate aqueous solution. *Int. J. Electrochem. Sci.* **12**, 11330–11342 (2017).
10. Kang, L., Cui, C., Yang, W., Zhang, Y. & Guo, M. The properties and microstructure of Nd-Fe-B nanowires fabricated by electrochemical deposition using porous Alumina templates. *Mater. Chem. Phys.* **242**, 122470 (2020).
11. Xu, X., Sturm, S., Zavasnik, J. & Rozman, K. Z. Electrodeposition of a rare-earth iron alloy from an ionic-liquid electrolyte. *ChemElectroChem* **6**, 2860–2869 (2019).
12. Cojocar, P., Magagnin, L., Gomez, E. & Vallés, E. Using deep eutectic solvents to electrodeposit CoSm films and nanowires. *Mater. Lett.* **65**, 3597–3600 (2011).
13. Kashyap, A., Skomski, R., Solanki, A. K., Xu, Y. F. & Sellmyer, D. J. Magnetism of L1₀ compounds with the composition MT (M=Rh, Pd, Pt, Ir and T=Mn, Fe, Co, Ni). *J. Appl. Phys.* **95**, 7480–7482 (2004).
14. Skomski, R. Phase formation in L1₀ magnets. *J. Appl. Phys.* **101**, 09N517 (2007).
15. Rhen, F. M. F. & Coey, J. M. D. Electrodeposition of coercive L1₀ FePt magnets. *J. Magn. Magn. Mater.* **322**, 1572–1575 (2010).
16. Huang, Y. H., Okumura, H., Hadjipanayis, G. C. & Weller, D. CoPt and FePt nanowires by electrodeposition. *J. Appl. Phys.* **91**, 6869 (2002).

17. Dempsey, N. M. in *Nanoscale Magn. Mater. Appl.* 661–683 (Springer US, 2009). doi:10.1007/978-0-387-85600-1_22
18. Visokay, M. R. & Sinclair, R. Direct formation of ordered CoPt and FePt compound thin films by sputtering. *Appl. Phys. Lett.* **66**, 1692–1694 (1995).
19. Ristau, R. A., Barmak, K., Lewis, L. H., Coffey, K. R. & Howard, J. K. On the relationship of high coercivity and L1₀ ordered phase in CoPt and FePt thin films. *J. Appl. Phys.* **86**, 4527–4533 (1999).
20. Oniku, O. D., Qi, B. & Arnold, D. P. Electroplated thick-film cobalt platinum permanent magnets. *J. Magn. Magn. Mater.* **416**, 417–428 (2016).
21. Garraud, A., Oniku, O. D. & Arnold, D. P. Influence of temperature on the magnetic properties of electroplated L1₀ CoPt thick films. *J. Appl. Phys.* **117**, 17C718 (2015).
22. Ewing, J., Wang, Y. & Arnold, D. P. High-current-density electrodeposition using pulsed and constant currents to produce thick CoPt magnetic films on silicon substrates. *AIP Adv.* **8**, 056711 (2018).
23. Wang, S.-J., Chen, C.-H., Chang, S.-C., Uang, K.-M., Juan, C.-P. & Cheng, H.-C. Growth and characterization of tungsten carbide nanowires by thermal annealing of sputter-deposited WC_x films. *Appl. Phys. Lett.* **85**, 2358–2360 (2004).
24. Lou, H. H., & Huang, Y. *Electroplating. Encyclopedia of Chemical Processing. Encycl. Chem. Process.* (CRC Press, 2006).
25. Oniku, O. D., Qi, B. & Arnold, D. P. Electroplated L1₀ CoPt thick-film permanent magnets. *J. Appl. Phys.* **115**, 17E521 (2014).
26. Rhen, F. M. F., Backen, E. & Coey, J. M. D. Thick-film permanent magnets by membrane electrodeposition. *J. Appl. Phys.* **97**, 113908 (2005).
27. Berkh, O., Rosenberg, Y., Shacham-Diamand, Y. & Gileadi, E. Electrodeposited near-equiatomic CoPt thick films. *Electrochem. Solid-State Lett.* **11**, D38 (2008).
28. Hosoiri, K., Wang, F., Doi, S. & Watanabe, T. Preparation and characterization of electrodeposited Co-Pt binary alloy film. *Mater. Trans.* **44**, 653–656 (2003).

29. Georgescu, V. & Daub, M. Magnetism and magnetoresistance in electrodeposited (L1₀) CoPt superlattices. *J. Optoelectron. Adv. Mater.* **7**, 853–858 (2005).
30. Wang, F., Hosoiri, K., Doi, S., Okamoto, N., Kuzushima, T., Totsuka, T. & Watanabe, T. Nanostructured L1₀ Co–Pt thin films by an electrodeposition process. *Electrochem. commun.* **6**, 1149–1152 (2004).
31. Yasui, N., Imada, A. & Den, T. Electrodeposition of (001) oriented CoPt L1₀ columns into anodic alumina films. *Appl. Phys. Lett.* **83**, 3347–3349 (2003).
32. Hannour, A., Bardotti, L., Prével, B., Tournus, F., Mailly, D., Bucher, J.-P. & Nafidi, A. Nanostructured L1₀-CoPt dot arrays with perpendicular magnetic anisotropy. *Mater. Lett.* **193**, 108–111 (2017).
33. Li, Y., Jia, W.-Z., Song, Y.-Y. & Xia, X.-H. Superhydrophobicity of 3D porous copper films prepared using the hydrogen bubble dynamic template. *Chem. Mater.* **19**, 5758–5764 (2007).
34. Zhang, J., Baró, M. D., Pellicer, E. & Sort, J. Electrodeposition of magnetic, superhydrophobic, non-stick, two-phase Cu–Ni foam films and their enhanced performance for hydrogen evolution reaction in alkaline water media. *Nanoscale* **6**, 12490–12499 (2014).
35. Wang, L. & Yamauchi, Y. Strategic synthesis of trimetallic Au@Pd@Pt core–shell nanoparticles from poly(vinylpyrrolidone)-based aqueous solution toward highly active electrocatalysts. *Chem. Mater.* **23**, 2457–2465 (2011).
36. Jiang, B., Li, C., Malgras, V., Imura, M., Tominaka, S. & Yamauchi, Y. Mesoporous Pt nanospheres with designed pore surface as highly active electrocatalyst. *Chem. Sci.* **7**, 1575–1581 (2016).
37. Wang, H., Jeong, H. Y., Imura, M., Wang, L., Radhakrishnan, L., Fujita, N., Castle, T., Terasaki, O. & Yamauchi, Y. Shape- and size-controlled synthesis in hard templates: sophisticated chemical reduction for mesoporous monocrystalline Platinum nanoparticles. *J. Am. Chem. Soc.* **133**, 14526–14529 (2011).
38. Pérez-Page, M., Yu, E., Li, J., Rahman, M., Dryden, D. M., Vidu, R. & Stroeve, P.

- Template-based syntheses for shape controlled nanostructures. *Adv. Colloid Interface Sci.* **234**, 51–79 (2016).
39. Gu, Z.-Z., Fujishima, A. & Sato, O. Fabrication of high-quality opal films with controllable thickness. *Chem. Mater.* **14**, 760–765 (2002).
 40. Jiang, P., Prasad, T., McFarland, M. J. & Colvin, V. L. Two-dimensional nonclose-packed colloidal crystals formed by spincoating. *Appl. Phys. Lett.* **89**, 011908 (2006).
 41. Rogach, A. L., Kotov, N. A., Koktysh, D. S., Ostrander, J. W. & Ragoisha, G. A. Electrophoretic deposition of latex-based 3D colloidal photonic crystals: a technique for rapid production of high-quality opals. *Chem. Mater.* **12**, 2721–2726 (2000).
 42. Braun, P. V. & Wiltzius, P. Electrochemically grown photonic crystals. *Nature* **402**, 603–604 (1999).
 43. Bruce, D. W., O'Hare, D. & Walton, R. I. *Porous Materials. Porous Mater.* (John Wiley & Sons, Ltd, 2010).
 44. Li, F., Wang, D., Liu, Q., Wang, B., Zhong, W., Li, M., Liu, K., Lu, Z., Jiang, H., Zhao, Q. & Xiong, C. The construction of rod-like polypyrrole network on hard magnetic porous textile anodes for microbial fuel cells with ultra-high output power density. *J. Power Sources* **412**, 514–519 (2019).
 45. Jones, S. M. Aerogel: Space exploration applications. *J. Sol-Gel Sci. Technol.* **40**, 351–357 (2006).
 46. Eiler, K., Suriñach, S., Sort, J. & Pellicer, E. Mesoporous Ni-rich Ni–Pt thin films: Electrodeposition, characterization and performance toward hydrogen evolution reaction in acidic media. *Appl. Catal. B Environ.* **265**, (2020).
 47. Sun, X., Jia, Z. Y., Huang, Y. H., Harrell, J. W., Nikles, D. E., Sun, K. & Wang, L. M. Synthesis and magnetic properties of CoPt nanoparticles. *J. Appl. Phys.* **95**, 6747–6749 (2004).



6

General discussion

6. General discussion

Energy consumption remains a compelling issue in the IT industry, especially in the case of data centers, which rely on the use of magnetically actuated memory devices (e.g. HDDs and MRAMs). So far, magnetic data is mainly written using electric currents (either to generate the magnetic field or to produce spin polarized currents), which causes huge energy losses through heat dissipation. In recent years, ME actuation has emerged as a promising strategy to control magnetism while boosting energy efficiency in a wide range of applications such as magnetic recording and spintronics. This strategy relies on the control of magnetism by means of electric fields, resulting in the replacement of electric current by voltage. In this regard, various routes to tackle the E-field control of magnetism have been proposed: intrinsic magnetic/electric coupling in single-phase multiferroics, strain-mediated ME coupling in extrinsic magnetostrictive/piezoelectric heterostructures, charge accumulation in ferromagnetic/dielectric interfaces, and electrochemical processes (including potential-induced faradaic reactions, electrochemical hydrogenation, and ion intercalation). In all the cases, the ME coupling is of interfacial nature since interfaces play a crucial role in the response of magnetic materials to external electrical stimuli. Consequently, most of the studies reported so far to address the E-field control of magnetism (especially those dealing with charge or electrochemical effects) use ferromagnetic thin films, due to their large S/V ratio. In this sense, porous, roughened and nanostructured materials are expected to increase the ME effect to a large extent. The introduction of porosity into magnetic materials makes it possible to migrate from magneto-ionic thin films to 3D structures, which is rated as a proof-of-concept to develop voltage-assisted magnetic storage media, as alternative to spin-transfer torque effects or thermally-assisted recording media.

Among available ME materials, the Co–Pt system is proposed as candidate in the literature because (i) alloys consisting of transition metal and noble metal combinations typically exhibit strong ME effects ascribed to charge accumulation and (ii) its orbital momentum and anisotropy are quite susceptible to the degree of oxidation. In addition, under certain synthetic conditions, it is possible to incorporate oxygen in its structure

(particularly by electrodeposition). Therefore, Co–Pt based materials emerge as excellent candidates for investigating ME effects via charge accumulation and magneto-ionic mechanisms. From the fabrication perspective, different methods can be employed for the preparation of Co–Pt based materials. Of these, the versatility, simplicity, low cost, and ease of operation of electrodeposition makes it tremendously competitive over vacuum-based methods. Furthermore, porosity can be introduced almost at will in the electrodeposited alloys using different approaches such as soft and hard templating. Conversely, the introduction of porosity via vacuum-based methods alone is rather challenging. Some works have reported the preparation of porous films via sputtering alone by tuning the deposition angle or the Ar^+ gas pressure in the chamber. However, in such cases, porosity is induced in an inhomogeneous manner and only to some extent.

Inspired by the features mentioned above, 3D porous Co–Pt based materials were exploited in this thesis from two distinct perspectives: (i) the assessment of their ME properties via charge accumulation and/or ion migration effects and in parallel (ii) their fabrication via electrodeposition combined with other techniques (namely, optical and colloidal lithographies for substrate patterning).

Specifically, mesoporous Co–Pt based materials of hundreds of nm in thickness were prepared by micelle-assisted electrodeposition for subsequent ME studies in liquid configuration. Electrodeposition from an aqueous solution containing a surfactant forming micelles is a very convenient strategy to prepare mesoporous alloys with an interconnected pore architecture. In this thesis, electrodeposition was combined with other techniques such as optical lithography and atomic layer deposition to obtain advanced ME materials. As a result, arrays of mesoporous Co–Pt microdisks and nanostructured Co–Pt/ALD oxide thin films were obtained. For both sorts of structures, the aqueous electrolyte employed for their growth contained neither a pH buffer nor a complexing agent on purpose. The goal was to favor the incorporation of oxygen in the deposit or, in other words, to promote the deposition of a Co-rich Co–Pt alloy together with Co oxides. Accordingly, Co–Pt+Co_xO_y composite films were obtained.

ME actuation of the samples was performed via the electrolyte-gating approach at room temperature, which exploits the formation of the EDL to create a high electric field at the electrolyte/sample interface due to the narrow dielectric layer thickness of the EDL. Liquid

electrolytes are desirable for large S/V ratio materials (or 3D materials) where the electrolyte can be in contact with the entire sample surface, avoiding current leakage, which is a common reason for failure in solid state dielectrics. Electrolyte-gating was carried out in a water-free aprotic organic solvent (anhydrous propylene carbonate) to avoid the occurrence of corrosion. Although it can be assumed that propylene carbonate is capable to penetrate inside the pores towards the substrate, we cannot guarantee that the porous Co–Pt+Co_xO_y composite was fully wetted. Further studies could be carried out to evaluate the degree of infiltration of the propylene carbonate inside the material. To trace magnetic property changes during electrochemical polarization in liquid, magneto-optic Kerr effect and VSM were utilized for the microdisks and the Co–Pt/ALD films, respectively. The samples were fit into a small Eppendorf in a two-electrode configuration.

By applying electric fields, a reduction of 88% in H_C and an increase of 60% in Kerr amplitude was successfully achieved in mesoporous Co–Pt+CoO microdisks. Elemental and spectroscopy analyses led to the conclusion that the observed ME effects were due to the synergy of two contributions: electric charge accumulation at the ultra-narrow pore walls of the microdisks and, (ii) voltage-driven O²⁻ migration (magneto-ionic effect) which caused the partial reduction of CoO to Co.

Following the same concept, H_C and m_S were effectively modulated in nanostructured Co–Pt+Co_xO_y, Co–Pt+Co_xO_y/AlO_x and Co–Pt+Co_xO_y/HfO_x films upon biasing with either negative or positive voltages. Similar to the previous research, negative voltages decreased H_C and increased m_S, while positive voltages induced the reverse trend in all the samples. The largest magneto-ionic effects were observed for Co–Pt+Co_xO_y/HfO_x heterostructured films with an increase of m_S up to 76% and a decrease of H_C by 58%. Opposite to the previous study, though, the observed changes in the magnetic properties were fully ascribed to a magneto-ionic mechanism. Namely, the ME variations arose from the reversible oxygen ion migration across the Co–Pt+Co_xO_y/ALD oxide interface, resulting in changes of the Co oxidation state, as confirmed by spectroscopy measurements. Interestingly, the observed variations depended significantly on the type of ALD nano-coating. HfO_x acted as an oxygen receptor layer, thus boosting magneto-

ionic effects at negative voltages, whereas AlO_x served as an oxygen donor layer, therefore promoting effects at positive voltages.

Overall, we have therefore demonstrated two different approaches to modulate the magnetic properties of Co–Pt based nanomaterials by electric fields through electrolyte-gating. The first strategy relies on a combined surface charging and magneto-ionics effect, wherein the oxygen was sourced in the Co–Pt microdisk itself, namely, in the CoO counterpart. Consequently, only changes in H_c and Kerr amplitude were obtained by applying negative voltages and then the original values were recovered after reversing the voltage polarity. Therefore, the cobalt valency change was non-volatile, which suggests the possibility to have voltage-programmable magnetic states. This could have applications in neuromorphic computing, where analogous and cumulative effects induced by selective voltage application are desirable. Yet, the switching speeds were in the range of minutes, which is an aspect that needs to be improved. In contrast, the second strategy relies on blending nanostructured Co–Pt+ Co_xO_y thin films and ALD oxide nanolayers (HfO_x and AlO_x) to enhance magneto-ionic performance. In this study, the adjacent HfO_x or AlO_x nanolayers acted as the main O^{2-} reservoir, resulting in larger variations of the magnetic properties.

In the abovementioned works, Co–Pt based materials were composed of a mixture of metallic Co–Pt and Co oxides phases in order to study their ME response via charge accumulation and magneto-ionic effects. Besides ME effects, we also drew our attention on the electrochemical fabrication pathways towards fully metallic meso/macroporous Co–Pt based materials which could find alternatives applications besides ME devices. Past efforts on electrodeposited Co–Pt coatings have largely focused on thin films and micro/nanostructures, while the electrodeposition of macro/mesoporous fully metallic Co–Pt based materials remained largely overlooked.

Mesoporous metal matrices are increasingly important for many applications and therefore the study of the factors influencing the quality of the final structure is timely and rather uncommon. Often, plating electrolytes are somehow "magic" mixtures, and in many cases, the exact formulation is a well-kept secret, at least for the commercial versions. Thus, trying to understand in detail the mechanism of interaction between the individual components is important. Micelle-assisted electrodeposition is a soft-

templating technique that relies on the dissolution of amphiphilic surfactants (above their c.m.c.) in aqueous solutions to induce the formation of micelles acting as a structure-directing agent during deposition. Despite the available literature in the field, systematic studies devoted to find out the key parameters enabling the development of long-range order mesoporosity are scarce. With the aim to capture the optimal conditions to reproducibly obtain a homogeneous mesoporosity in Co–Pt films, a parametric study of various chloride-based baths was performed. Interestingly, previous dissolution of the platinum salt, followed by their storage (referred to as equilibration time) before the cobalt salt and the nonionic P-123 surfactant are added, ensures the reproducible formation of the mesostructure. We could demonstrate that the aging of the hexachloroplatinate solution had a direct effect on the cyclic voltammetry recorded from the electrolyte and on the final morphology of the Co–Pt film. Although it is already known in the literature that the exchange rates of Pt(IV) complexes are slow, we deemed important to remind the scientific community about this fact and its implication in the case of electrodeposited mesoporous alloy films. Spectroscopy analyses confirmed that the reproducible formation of the mesoporous network is ruled by the dynamics of the Pt (IV) complexes in water and the consequently more efficient interaction with the outer hydrophilic groups of the P-123 micelles. SEM images revealed that homogeneous mesoporous Co-rich Co–Pt films with a pore diameter of 10–17 nm could be obtained from electrolytes involving an equilibration time in both successive depositions and in different batches. In contrast, Co–Pt deposits prepared from a fresh electrolyte (obtained upon dissolving all the chemicals at the same time) did not consistently show a reproducible mesoporous network.

Finally, we capitalized on the current trend towards ultra-light materials to produce hard magnetic macroporous Co–Pt thin films. In this case, electrodeposition and colloidal crystal templating technique were combined to meet this goal. Equiatomic Co–Pt alloy was electrodeposited from an aqueous sulfate-chloride electrolyte by potentiostatic electrodeposition. After selective etching of the colloids, as-deposited Co–Pt films exhibited a highly packed arrangement of pores of 200 nm in diameter. As-deposited macroporous films were magnetically soft, nanocrystalline and structurally composed of a mixture of A1-disordered fcc solid solutions, one of them being nearly equiatomic.

Upon annealing at 600 °C, the A1-disordered phases partly transformed into the L1₀-ordered fct phase, which was slightly richer in Pt, plus small fractions of CoO and CoPt₃. In turn, VSM loops revealed a two-phase magnetic behaviour in the annealed macroporous films which was attributed to the presence of hard magnetic Pt-rich L1₀ ordered and soft-magnetic CoPt₃ phases. Moreover, H_c significantly increased from 148 Oe to 1328 Oe after annealing at 600 °C. Importantly, the larger pores obtained throughout this strategy are less prone to collapse during the annealing process, enabling the formation of the L1₀-ordered phase while maintaining the porous arrangement. Magnetoelectric studies on these hard-magnetic Co–Pt films are planned as future work.

In summary, the exploitation of the magnetic and ME properties of porous Co–Pt based materials obtained through electrochemical pathways has been the driving force and the major focal point of this thesis. We demonstrated that ME effects via charge accumulation and magneto-ionics are significantly enhanced with the utilization of porous Co–Pt based structures. It is also envisaged that the developed synthetic protocols could be extended to other materials to advance in the field of 3D magneto-ionics.

7

Conclusions

7. Conclusions

The main conclusions extracted from this thesis are summarized in the bullet points below:

- Porous Co-rich Co–Pt+Co_xO_y based materials have been successfully fabricated by electrodeposition from a chloride-based bath containing the P-123 amphiphilic surfactant. The concentration of the surfactant was above its c.m.c. to favour the formation of micelles, which acted as a soft template during deposition. The bath did not contain pH buffers and/or complexing agents in order to favour the incorporation of oxygen in the films, yielding a nanocomposite consisting of a Co-rich Co–Pt alloy and Co_xO_y phases.
- ME properties of the porous Co–Pt+Co_xO_y based materials were studied via non-aqueous electrolyte gating approach at room temperature. This approach was chosen to exploit the formation of the EDL to generate large electric fields at the electrolyte/sample interface. The liquid electrolyte approach was advantageous considering the high S/V ratio of the Co–Pt+Co_xO_y based materials, which allowed the electrolyte to penetrate the interior of the pores and maximize magnetoelectric interfacial effects.
- Arrays of mesoporous Co–Pt+Co_xO_y microdisks were prepared by electrodeposition on photolithographed substrates. Again, the high surface area of the motifs led to enhanced ME effects. Specifically, H_C and the overall Kerr signal could be remarkably modulated by subjecting the microdisks to negative voltages. After reversing the voltage polarity, the original values were recovered. The observed effects were ascribed to charge accumulation at the surface of the pore walls and magneto-ionic effects (voltage-driven oxygen ion migration).
- In Co–Pt+Co_xO_y/HfO_x and Co–Pt+Co_xO_y/AlO_x heterostructured films, the nanostructuring achieved by the micelle-assisted electrodeposition and the subsequent conformal nanocoating by ALD allowed to maximize the available interface between the ferromagnetic material and the oxide nanolayer. Consequently, large magneto-ionic effects were observed in all heterostructures,

i.e., uncoated Co–Pt+Co_xO_y and ALD-coated Co–Pt+Co_xO_y films. Drastic changes in H_C and m_S were observed after biasing with negative and subsequent positive voltages. The most significant ME response was observed for Co–Pt+Co_xO_y/HfO_x heterostructure at negative voltages. The observed ME variations were attributed to the E-field oxygen migration through the Co–Pt+Co_xO_y/oxide gate interface. ALD-coated Co–Pt+Co_xO_y films exhibit higher variations than uncoated Co–Pt+Co_xO_y, where HfO_x and AlO_x nanocoatings showed dissimilar role as oxygen acceptor/donor materials depending on the voltage polarity. HfO_x facilitated magneto-ionics effects upon negative voltage application (*i.e.* it acts as an oxygen acceptor). Contrarily, AlO_x exhibit an oxygen donor role, showing higher magneto-ionics effects upon positive voltage application.

- From the synthetic viewpoint, a parametric study from various bath formulations revealed that electrolyte processing is critical for the precise control of mesoporosity in Co–Pt thin films. To ensure the formation of a mesoporous network, previous dissolution of the hexachloroplatinate salt and their storage for a few days (before the P-123 amphiphilic surfactant and the Co salt are added) were implemented prior to deposition. Conversely, non-mesostructured Co–Pt films were often obtained from freshly prepared baths. The observed results showed that the aging the hexachloroplatinate solution has a key effect on the reproducible development of the mesoporosity. The correct formation of the mesostructure is governed by the dynamics of the Pt (IV) complexes in water and the effective interaction of newly formed hydroxochloroplatinate complexes with the outer hydrophilic groups of the P-123 micelles.
- Hard magnetic macroporous Co–Pt thin films have been successfully fabricated by electrodeposition and colloidal crystal templating. XRD analysis revealed the polycrystalline structure of as-deposited macroporous films, which a mixture of equiatomic A1-disordered Co–Pt solid solutions. After annealing at 600 °C, the A1-disordered phases partly transformed into the L1₀-ordered phase (which was slightly richer in Pt), as a result, H_C increased from 148 to 1328 Oe. Such increase was attributed to the existence of different magnetic and crystallographic phases

(hard magnetic Pt-rich $L1_0$ ordered and soft-magnetic CoPt_3 phases). ME studies on these samples are planned for the near future.



8

Future perspectives

8. Future perspectives

Considering the results described in this Thesis, several future research lines can be outlined:

- The use of alternative liquid dielectrics for the electrolyte-gating actuation, such as ionic liquids (e.g. DEME-TFSI) or other electrolytes (e.g. LiPF₆-ethylene carbonate). This would allow inducing higher E-fields through the formed EDL and investigating magnetoelectric effects likely at lower applied voltages.
- In analogy to the work carried out on Co–Pt+Co_xO_y/ALD gate oxide, fully metallic mesoporous Co–Pt thin films could be coated with either AlO_x or HfO_x by ALD to induce magneto-ionic effects.
- To optimize the synthesis of hard magnetic macroporous Co–Pt electrodeposited films so that they only consist of fcc equitatomic A1-disordered phase (i.e., single-phase material). After electrodeposition, the annealing conditions (temperature and time) could be optimized to achieve full transformation of the A1-disordered phase into the L1₀-ordered phase, and consequently, the highest possible values of coercivity would be obtained. Eventually, ME studies could be performed on these newly synthesized hard magnetic macroporous Co–Pt films.
- The use of the hard magnetic macroporous L1₀-ordered Co–Pt electrodeposited films as skeleton to be filled with other materials. A soft magnetic phase (e.g. permalloy) could be incorporated as a coating on the Co–Pt macropores to develop a spring magnet. Alternatively, Co–Pt could be impregnated with an antiferromagnetic phase (e.g. CoO or NiO) to trigger the exchange bias effect.
- Colloidal crystal template-assisted electrodeposition could be combined with photolithography to synthesized hard magnetic macroporous Co–Pt patterned structures, which could be appealing materials for a variety of applications.

9

Curriculum Vitae

9. Curriculum vitae

Cristina Navarro Senent

Contact information

Address Microscopy Service, Sciences building C2/-193 Universitat Autònoma de Barcelona
City, State 08193 Bellaterra, Spain
e-mail cristina.navarro.senent@uab.cat
Web address <https://jsort-icrea.uab.cat/htm/navarro-senent.htm>

Education

2017–Currently **PhD in Materials Science**
Universitat Autònoma de Barcelona, Barcelona, Spain
Group: Smart nanoengineered Materials, Nanomechanics and Nanomagnetism (Gnm³)
Supervisor: Prof. Jordi Sort and Dr. Eva Pellicer

2016–2017 **Master in advanced Nanoscience and Nanotechnology, Specialisation in Nanomaterials**
Universitat Autònoma de Barcelona, Barcelona, Spain
Master thesis: Self-assembled monolayers based on carbon nanotubes for the impedimetric sensing of PAHs
Supervisor: Dr. José Muñoz and Dr. Marta Mas-Torrent

2011–2016 **Bachelor degree in Nanoscience and Nanotechnology**
Universitat Autònoma de Barcelona, Barcelona, Spain
Degree thesis: pH responsive self-assembly of polystyrene-block polyvinylpyridine micelles and cucurbit[7]uril on gold surfaces.
Supervisor: Arántzazu González Campo
Place: Functional Nanomaterials & Surfaces Group, Institut de Ciència de Materials de Barcelona (Barcelona), Spain

Experience

Mar-Jul 2016 **Research Fellow in Nanomaterials Departament**
Leitat Technological Center, Barcelona, Spain

Languages

Spanish Mother tongue
Catalan Proficient user
English Proficient user

Publications

J. Munoz J, **C. Navarro-Senent**, N. Crivillers and M. Mas-Torrent. Study of carbon nanotube-rich impedimetric recognition electrode for ultra-low determination of polycyclic aromatic hydrocarbons in water. *Microchim Acta* 2018,185, 255. **I.F.= 6.232** (2019)

C. Navarro-Senent*, J. Fornell, E. Isarain-Chávez, A. Quintana, E. Menéndez, M. Foerster, L. Aballe, E. Weschke, J. Nogues, E. Pellicer*, and J. Sort*. Large magnetoelectric effects in electrodeposited nanoporous microdisks driven by effective surface charging and magneto-ionics. *ACS Appl. Mater. Interfaces*, 2018, 10, 44897–44905. **I.F.= 8.758** (2019)

C. Navarro-Senent, A. Quintana, E. Menéndez, E. Pellicer and J. Sort*. Electrolyte-gated magnetoelectric actuation: Phenomenology, materials, mechanisms, and prospective applications. *APL Mater.* 2019, 7, 030701. **I.F.= 4.060** (2019)

C. Navarro-Senent*, A. Quintana, E. Isarain-Chávez, E. Weschke, P. Yu, M. Coll, E. Pellicer, E. Menéndez* and J. Sort*. Enhancing magneto-ionic effects in magnetic nanostructured films via conformal deposition of nanolayers with oxygen getter/donor capabilities. *ACS Appl. Mater. Interfaces*, 2020, 12, 14484–14494. **I.F.= 8.758** (2019)

C. Navarro-Senent*, S. Pané, J. Sort and E. Pellicer*. The order of addition and time matters: Impact of electrolyte processing on micelle-assisted electrosynthesis of mesoporous alloys. *Electrochim. Acta*, 2020, 358, 136940. **I.F.= 6.215** (2019)

K. Eiler*, J. Fornell, **C. Navarro-Senent**, E. Pellicer and J. Sort*. Tailoring magnetic and mechanical properties of mesoporous single-phase Ni–Pt films by electrodeposition. *Nanoscale*, 2020, 12, 7749–7758. **I.F.= 6.895** (2019)

A. Nicolenco, **C. Navarro-Senent**, J. Sort. Nanoporous Composites with converse magnetoelectric effects for energy-efficient applications. Reference Module in Materials Science and Materials Engineering, 2021.

Congresses

- May 2018 **C. Navarro-Senent**, J. Fornell, E. Isarain-Chávez, A. Quintana, J. Nogués, E. Pellicer, J. Sort. *Magnetoelectric effects in lithographed nanoporous Co-Pt dots*.
↳ IW-MAG'18 – Barcelona, Spain. Oral contribution
- June 2018 **C. Navarro-Senent**, J. Fornell, E. Isarain-Chávez, A. Quintana, J. Nogués, E. Pellicer, J. Sort. *Magnetoelectric properties of nanoporous Co-Pt dots synthesized by micelle-assisted electrodeposition on lithographed substrates*.
↳ SMT32 2018 – San Sebastian, Spain. Poster
- July 2018 **C. Navarro-Senent**, J. Fornell, E. Isarain-Chávez, A. Quintana, J. Nogués, E. Pellicer, J. Sort. *Electric-field effect on the magnetic properties of nanoporous Co-Pt patterned microstructures*.
↳ Thermec'2018 – Paris, France. Poster
- November 2019 **C. Navarro-Senent**, A. Quintana, E. Isarain-Chávez, E. Weschke, P. Yu, M. Coll, E. Pellicer, E. Menéndez, J. Sort. *Boosting magneto-ionic effects in magnetic mesoporous films through conformal oxygen getter/donor nanocoatings*.
↳ MMM2019 – Las Vegas, United States. Oral contribution

Managerial activities

JPHD2019. 4th Scientific Meeting of BNC-b Students

Type of activity: Co-organizer of the meeting

Place: Institut de Ciència de Materials de Barcelona (ICMAB) and Catalan Institute of Nanoscience and Nanotechnology (ICN2)

Date: 6-7 June 2019

Attendance at courses

20-26 February 2018 **Introduction to scanning electron microscopy for material and life science**
↳ Servei de Microscòpia – Universitat Autònoma de Barcelona (UAB), Barcelona, Spain

19-23 March 2018 **Introduction to transmission electron microscopy for material and life science**
↳ Servei de Microscòpia – Universitat Autònoma de Barcelona (UAB), Barcelona, Spain

26-30 March 2018 **3rd e-Minds Training Course: Electrochemical processing methodologies and corrosion protection for devices**, COST Action MP1407
↳ Hotel Sungarden – Siófok, Hungary

17-28 September 2018 **European School of Magnetism 2018**
↳ ACMiN, AGH University of Science and Technology–Kraków, Poland

12 February, 24 April 2019 **Becoming a Scientific Writer: Putting Why before How**
↳ Universitat Autònoma de Barcelona (UAB), Barcelona, Spain

Courses delivered

- Theoretical sessions: Electron microscopy – Material Characterization Techniques, **Master in Advanced and Nanotechnology**
Course: 2018-2019
University: Universitat Autònoma de Barcelona (UAB)
5h
- Practical sessions: SEM, and theoretical sessions: Electron microscopy – Material Characterization Techniques, **Master in Advanced and Nanotechnology**
Course: 2019-2020
University: Universitat Autònoma de Barcelona (UAB)
13h

Prizes

- **1st Poster Award** in the "3rd Scientific Meeting of BNC-b Students" (Barcelona, Spain, November 2017).
- **Best Poster Prize** at the European School on Magnetism 2018 "Magnetism by light" (Kraków, Poland, September 2018).
- **2nd Prize** and **Best Presenter Prize by the audience** in the UAB's "4 Minute Thesis" competition.

Skills and Expertise

Electron Microscopy Field Emission Scanning Electron Microscopy (FESEM), Energy-dispersive X-ray spectroscopy (EDS), Transmission Electron Microscopy (TEM), Profilometry.

Image Processing Image J, Digital Micrograph

Other techniques Autolab potentiostat/galvanostat, Vibrating sample magnetometer (VSM), X-Ray Diffraction (XRD)

Graph and Data

Analysis Origin Pro, X'Pert HighScore